Carbon Based Thin Film Electrodes as Model Systems for the Electrocatalytic Hydrogenation of Unsaturated Organics

A thesis presented to

The University of Dublin, Trinity College Dublin

for the degree of

Doctor of Philosophy in Chemistry

by

Christian Schröder

Trinity College Dublin
Coláiste na Tríonóide, Baile Átha Cliath
The University of Dublin

Under the supervision of

Professor Paula E. Colavita

School of Chemistry, Trinity College Dublin

2025

Declaration

I declare that the work in this thesis has not been previously submitted as an exercise for a degree to this or any other university and is entirely my own work. Due acknowledgement and references are given to the work of others where appropriate.

I agree to deposit this thesis in the University's open access institutional repository or allow the library to do so on my behalf, subject to Irish Copyright Legislation and Trinity College Library conditions of use and acknowledgement.

I consent the examiner retaining a copy of the thesis beyond the examining period, should they so wish (EU GDPR May 2018).

Christian Schröder, February 2025

If you believe in something

and put it in your mind,

it can be realised

- Eliud Kipchoge

Acknowledgments

I want to start these acknowledgments by expressing my deepest gratitude to Professor Paula E. Colavita, for allowing me to pursue my PhD under her supervision. The pandemic forced me to change my plans, which turned out to be my luck, as I ended up in Trinity College. Paula made sure I had everything I needed to start the PhD journey, and over the last four years, and a bit extra, it was her guidance and her belief in me that made this thesis possible. There are so many things for which I am grateful to her that it would fill to much space here. All I will say here is Thank you for everything you have done for me.

This thesis would not exist if it would not be for all the help, guidance and support I got from so many great people. Thank you to Kim McKelvey for all the help with the SECCM and all the discussions about results, despite of the time difference between Ireland and New Zealand. Professor Tatiana Perova provided access to the Raman instrument and was always there to help with measurements and data analysis, which was invaluable. To Igor Shvets for providing access to the XPS instrument. A big thank you to Cormac McGuinness for teaching me the theoretical and the practical side of how to use the XPS, without which many of the results would not be possible. Here I also want to mention his PhD student Lee, who helped me so much around the instrument. To Niall McEvoy for use of the CVD furnace and the scanning Raman. Thank you to Chris Murray for allowing me to use the optical microscope and helping me with many other things. To Riley Gatensby for providing evaporated metal films. To Karsten Rode for helping with the XRR measurements. Thank you to everyone else in CRANN, AMBER and Trinity who helped me over the last four years. To our collaboration partner, Dr. Tristan Petit at the HZB in Berlin and his research group for the collaboration involving MXenes and Synchrotron measurements.

To everyone in the school of chemistry who helped with so many things along the way. I can honestly say that this would not have been possible without you. To Peter for helping with orders and dealing with suppliers when needed, thank you so much. To Mark for going out of his way to help with deliveries, gas cylinders or liquid nitrogen. To Manuel and John for help with the various measurements and instrumentations and for all the help solving all kinds of problems big or small without hesitation. Thank you. Big thank you to Sinead, Ann-Marie and Ben for dealing with everything administrative and doing more than necessary to help. To Beatriz and to Noelle for all the help before and during the teaching labs.

Thank you to my final year student Kiaya for her contribution to this work. While I supervised just one student myself, I had the privilege to support more students that I want to thank here to. Pietro, Larry, Lua, Nina, Zijian and Emma, it was my honour to work with you.

To all members of the Colavita group, everyone in the office and all other fellow PhD students, who were not just colleagues but also became friends, you made the last four years the amazing journey it has. I am grateful, I got to share this journey with all of you, there are some people that I want to mention here.

A massive thank you to Silvia, for making sure we keep the lab organised, but more than that for inviting me to her home when we got stuck in Ireland for Christmas, for the many coffee chats and for so much more. Hugo, I would need to thank you for so many things. For teaching me so much, helping me find around Trinity and especially CRANN. For the many Rugby games watched and so much more. I could not have asked for a better Postdoc to start my PhD. Thank you to Marc, for the science discussions that helped solve so many problems and gave rise to new ideas. Having you with me made me a better scientist. My grant-mate Filippo, the last four years had its ups and downs but I am thankful I got to share it with you. Thank you to Lua, working with you is a privilege. Without you there would be no Dynamic-Duo and I am grateful that I got to be a part of your journey in Trinity. And thank you for making sure our group did socialise every now and then. Maida, thank you for all the help along the way and for organising regular food events. Sonsoles, the office would not be the same without you. Thank you for offering emotional support whenever needed. Thank you, Chloé, for keeping me company through the many long hours, late nights and weekends in the office, when I wrote this thesis. It was good to not be alone in those times. To Sam, although our time together was short, I am glad I met you. To all of you and everyone else that is not mentioned here, thank you for making this journey enjoyable and a time I am always going to remember.

A special thank you to Professor Bund, my master professor. His belief in my potential and his encouragement helped me decide to pursue a PhD. When I started my Master in Ilmenau I could not have imagined where this would lead me. I owe so much of this to the support and education I received from Professor Bund and his entire team.

To my family, especially my parents without whom I would not be here today. thank you for always believing in me, guiding me, and providing me with the strength to pursue my dreams. Thank you for your unwavering support over the last years and getting me to this point. To my brother who always supported me and always had an open ear. I am grateful for you and all you have done. A massive thank you to my grandparents, whose quiet strength and enduring love have been a constant source of inspiration. This work is based on the foundation you've provided, and the values you've instilled in me.

To the everyone at Poolbeg Parkrun, thank you for the community. Thank you to my friends, who supported me in so many different ways. Thank you for taking my mind of the thesis, keeping me grounded and always being there for me. A big thank you to my girlfriend who always believed in me, even when I doubted myself. And again, thank you to everyone who helped me get to this point. I will be forever grateful.

Summary

On the transition away from fossil fuels towards a more sustainable economy electrocatalysis can play a crucial role. One example of this is the electrocatalytic hydrogenation of unsaturated organic molecules, which provides a route to store energy from renewable sources as fuels and chemicals. Additionally, the electrocatalytic hydrogenation has the potential to enable the use of biomass as a sustainable carbon feedstock, further reducing the need for fossil resources. For the ECH to become a real alternative, the development of new electrocatalysts is essential.

The electrocatalytic hydrogenation generates the required hydrogen in-situ from the electrolyte, which makes catalysts in the hydrogen evolution reaction materials of interest in the electrocatalytic hydrogenation. Precious metals deliver a high activity, but their scarcity, high cost and tendency to catalyst poisoning makes them less desired in the electrocatalytic hydrogenation. As a result, transition metals and materials derived from them, like transition metal dichalkogenides are receiving increased attention. However, these materials come with different challenges, like corrosion in the conditions used for the ECH or low electric conductivity. Carbon and carbon based materials can be used to overcome some of these drawbacks and thereby allowing the effective use of these materials in the ECH. Carbon is chemically stable in a wide range of conditions, abundantly available and its chemistry can be tailored for specific applications. In electrocatalysis carbon can be used as a metal-free electrode material, as a catalyst support or for encapsulation. This thesis will explore all three of these applications.

The opening section will give the motivation behind this work by looking at the current reliance of fossil resources today. From there, the electrocatalytic hydrogenation will be introduced followed by a discussion of potential electrocatalytic materials based on non-precious metals. The role of carbon in electrochemistry particularly in electrocatalytic application will be highlighted. The three use cases of carbon - metal-free electrodes, catalyst support and encapsulation - will be looked at, along with the use of model electrode systems. Finally, the aims of the thesis will be outlined. The second chapter looks at the materials and methods used and introduces the theory behind the main techniques of this work.

The first result chapter, Chapter 3, focuses on the synthesis and characterisation of metal-free nitrogenated carbon films. For this, the synthesis procedure present in the group

was updated to ensure reliable synthesis of nitrogenated carbon films. The two step synthesis allowed control over the distribution of nitrogen sites and the graphitisation. The electrochemical performance of the nitrogenated films was investigated in the HER and the ECH. While only a poor activity was found, the results helped a better understanding of the ECH.

In Chapter 4 the nitrogenated carbon films synthesised in the previous chapter were used as support for molybdenum disulfide, a material with promising activity in the HER. The heterostructures were synthesised via a CVD process using a close proximity "microreactor" setup. After the characterisation of the materials, the activity in the HER and ECH of the heterostructures was investigated. The heterostructures showed promising activity in the ECH, which can be the basis of future studies.

Carbon encapsulation of copper was investigated in Chapter 5. Varying mass loadings of carbon were deposited on sputtered copper films. After a comprehensive characterisation the electrochemical activity of the films was investigated. And a negligible effect of the carbon was found for the HER, which was attributed to the microroughness of the copper film. While the electrocatalytic activity did not seem affected by the carbon, a positive effect on the selectivity towards benzyl alcohol was found. The cause for which could not be finally explained.

In Chapter 6 the use of the carbon thin films as substrates in nano-electrochemistry measurements using scanning electrochemical cell microscopy (SECCM), which will be briefly introduced, will be shown. An extended characterisation of the carbon films will be shown. Two projects within the group will be used to show the potential of the carbon films in correlative electrochemistry of nanomaterials.

To conclude the work, design principles derived from the results will be discussed together with general insights in the ECH and the role that carbon materials can play. After, that, promising future research directions will be discussed.

Table of Contents

List of Abbreviations

a-C	Amorphous Carbon
AFM	Atomic Force Microscopy
BE	Binding Energy
CNT	Carbon Nano Tube
CO_2RR	Carbon dioxide Reduction Reaction
CV	Cyclic Voltammetry
CVD	Chemical Vapour Deposition
DC	Direct Current
DLC	Diamond Like Carbon
ECH	Electrocatalytic Hydrogenation
EDS	Energy Dispersive X-ray Spectroscopy
FE	Faradaic Efficiency
FID	Flame Ionization Detector
GC	Glassy Carbon
HER	Hydrogen Evolution Reaction
HOPG	Highly Oriented Pyrolytic Graphite
IMFP	Inelastic Mean Free Path
ITO	Indium Tin Oxide
KE	Kinetic Energy
KF	Kleinflansch
KPI	Key Performance Indicator
LSV	Linear Sweep Voltammetry
M@C	Carbon Encapsulated Metal
MFC	Mass Flow Controller
MWCNT	Multiwalled Carbon Nano Tubes
NC	Nano Crystalline
N-GO	Nitrogen doped Graphene Oxide
NHE	Normal Hydrogen Electrode
OER	Oxygen Evolution Reaction
OOR	Organic Oxidation Reaction
ORR	Oxygen Reduction Reaction
PVD	Physical Vapour Deposition

QRCE	Quasi-reference Counter Electrode
RHE	Reversible Hydrogen Electrode
RMS	Root Mean Square
RSF	Relative Sensitivity Factor
SECCM	Scanning Electrochemical Cell Microscopy
SEM	Scanning Electron Microscopy
SHE	Standard Hydrogen Electrode
STXM	Scanning Transmission X-Ray Microscopy
ta-C	Tetrahedral amorphous Carbon
TEM	Transmission Electron Microscopy
TEY	Total Electron Yield
TMDC	Transition Metal Dichalkogenides
TOF	Turn Over Frequency
UV	Ultraviolet
XPS	X-ray Photoelectron Spectroscopy
XRR	X-ray Reflectivity

List of Figures

Chapter I

Chapter II

Chapter III

Chapter IV

Chapter V

Chapter VI

Appendix

List of Tables

Chapter I

Chapter III

Chapter IV

Chapter V

Chapter I

1. Introduction

This chapter will introduce the motivation behind this thesis, by looking at the global use of fossil resources and the challenges associated with replacing them. Electrochemical methods and their use in sustainable technologies will be introduced followed by electrocatalytic hydrogenation as a promising technology. Subsequently, the discussion will review the rationale for novel catalyst materials and the different roles that carbon materials can play in electrocatalysis will be highlighted. Finally, the aims of the thesis will be discussed in the context of the above discussion.

1.1. Global energy picture

1.1.1. Increasing energy demand

The global demand for energy is continuously rising. There are several factors contributing to this increased demand. Developing countries needing more energy to power their economic growth, new technologies, like artificial intelligence requiring large amounts of electricity and a growing population, 10.4 billion people expected by the end of the century, according to the UN,[1] are some of the reasons for this. This can be seen in the development of the primary energy production (shown in Figure 1a), which increased from 57000 TWh in 1970 to 172000 TWh in 2023. This primary energy, the unprocessed input into the energy system, is and has been largely supplied by fossil resources, with over 90% supplied by oil, gas and coal, as shown in Figure 1b. Until 2023 the percentage of fossil resources has decreased to just above 80%, but due to the increasing energy demand, the total amount still increased. Since the 2010s contributions of renewable energy sources like wind and solar energy started to increase. A similar trend is seen for biofuels, with an almost tenfold increase from 2000 to 2023.

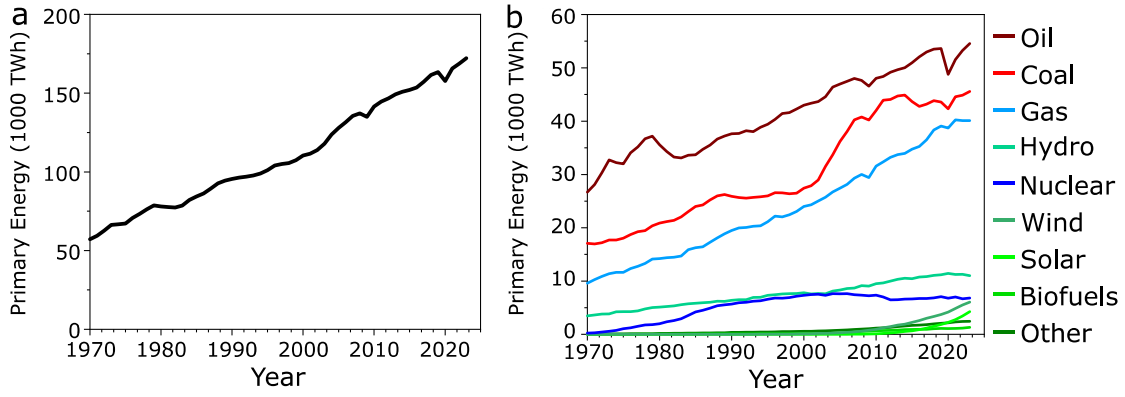

Figure 1.1 (a) Global primary energy consumption from 1970 to 2023. (b) Global primary energy consumption by energy source.[2]

The energy picture gets more complex, looking not just at the primary energy sources, but also at the use of the energy. There are generally three main sectors of energy use, transport, residential and industrial. In 2022 in the European Union the use of primary energy in these sectors was 31%, 27% and 25%, respectively.[3] The form energy used is not the same for the different sectors. In transport, most of the energy comes from gasoline and diesel, used to power cars and trucks. In contrast, households use energy mainly in the form of

electricity, with some fossils used for heating applications. Industry does use fossil resources to generate heat and supply the energy needed for the different processes. Industry does also require fossil fuels as a reactant and carbon feedstock in the petrochemical industry. This diverse use of energy makes the shift away from fossil fuels a challenging task, as a universal solution will be hard to find, and individual solutions are needed for each use. The next section explores the reasons why turning away from fossil fuels is needed.

1.1.2. Dependence and problems of fossil fuels

Fossil resources have been the fuel for industrialisation and are the basis for the standard of living we have. Over the last years the problems associated with the excessive use and the dependence of fossil fuels have become obvious. Industries and societies need a constant supply of fossil fuels to cover the energy demand. As the fossil resources are globally not evenly distributed, some countries will benefit from this dependence. Figure 2 shows the production of fossil fuels in the major production nations over the years. European countries, other than Norway, are reliant on imports of fossil fuels, which can lead to potential conflicts between political and economic goals, as dependence on imports make countries susceptible to political pressure from suppliers.

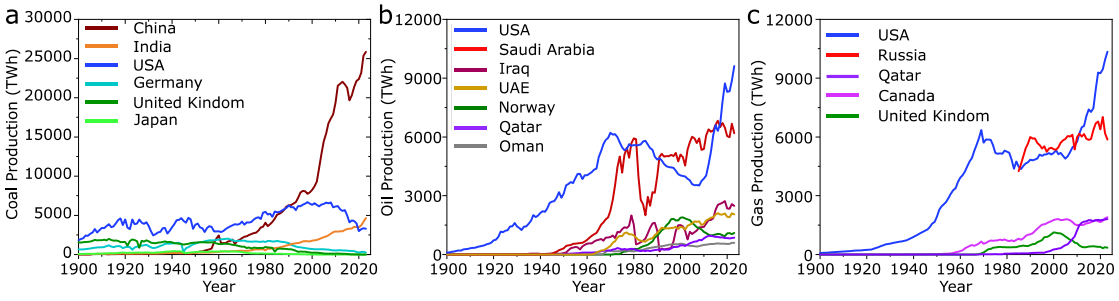

Figure 1.2 Production of Fossil fuels (a) Coal, (b) Oil and (c) Gas Of the major production nations per year.[4]

The challenges linked to the use of fossil fuel are not just political. Emissions from combustion of fossil fuels in form of CO_2 and other greenhouse gases have been recognized as a main contributor of climate change, leading to more extreme weather events and higher temperatures around the globe.

Emissions do not just affect the climate and the environment, but also the population. Exposure to emissions, for example of vehicles, can have adverse health effects. Air

pollution, through particulates, fumes and other combustion products have been found to cause asthma, cardiovascular diseases, lung cancer and more. Exposure to emission from combustion of fossil fuels can have a negative impact on every organ in the human body.[5] These reasons highlight the need to find alternative sources of energy, to allow for healthy and peaceful societies in the future.

1.1.3. Fossil resources as raw material

The use of fossil fuels is not limited to energy applications. Fossil resources are also a raw material and carbon feedstock for a variety of chemicals used in everyday life. This includes reagents for medication and food additives, starting materials for polymers as well as dyes, lubricants and resins.[6] The processing of crude oil to an end product involves multiple steps. In a first step the crude oil is separated in its fractions.[7] A scheme of this is shown in Figure 1.3. In the refinery, the fractions are separated by their boiling point, resulting in mixtures of hydrocarbons with a similar carbon content. This ranges from short chained gaseous products, like methane or butane, to the solid residue bitumen and asphalt. In this refining process the typical transportation fuels like gasoline, kerosene and diesel are obtained, too.

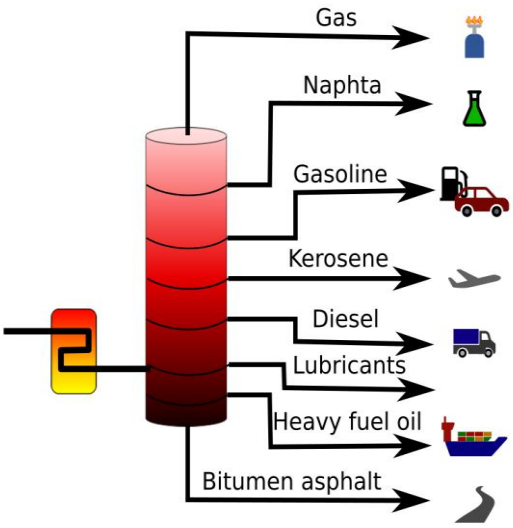

Figure 1.3 Schematic of crude oil refining with typical fractions obtained.[7, 8]

For petrochemical products, naphtha and the short chain hydrocarbons, like methane, propane and ethane are of high interest. The fractions are separated, and their individual components extracted. Through different chemical processes, these feedstocks are

transformed and turned into base chemicals and further processed into chemical intermediates and final products, used for a variety of applications, with about 95% of manufactured goods relying on or containing petrochemical products.[9] Figure 1.4 shows a flow diagram of the processing of fossil resources to the end products. This diagram is not a complete list, but rather used to highlight the variety and the omnipresence of petrochemical derived products nowadays. The processes employed to convert the feed to chemicals are often carried out under high pressure and high temperatures. This energy input is often achieved through fossil fuels, making them not just a source of energy but also a raw material for petrochemical reactions.

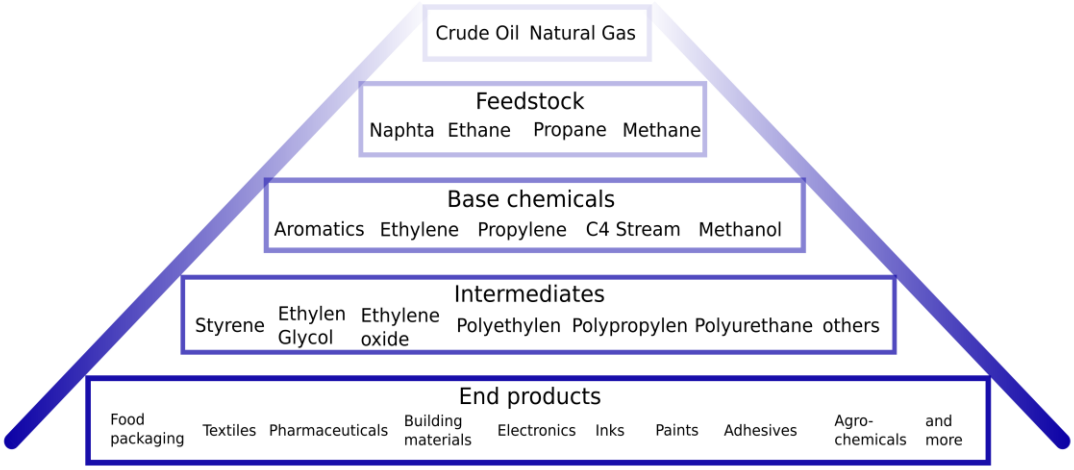

Figure 1.4 Schematic of processing from fossil resources to consumer products (not a complete list).[9-11]

This shows that fossil resources are not just an important energy source but also a huge carbon feedstock of raw materials. In 2022 in the European Union, 3286 PJ of fossil fuels were used as raw materials.[3] To replace fossil fuels both a sustainable source of energy and a sustainable carbon feedstock will be needed.

1.1.4. Expansion of renewable energy

Fossil resources are still the main source of electricity around the globe,[12] with coal being the most important, as seen in Figure 1.5. Oil plays only a small role when it comes to electricity generation, with a contribution of around 3%. Natural gas is still increasing in importance for electricity generation, as it is seen as a transition technology away from oil and coal, as it offers higher efficiency. Renewable energy sources, relatively constant from

1970 to 2000, started to increase, contributing to around 27% of all electricity produced globally in 2019. In the EU, the contribution of renewables is even higher.

Renewables include hydro, solar, wind and biofuels and waste. While renewable energy sources are needed for the transition away from fossil fuels, they bring their own challenges that need to be overcome. Efficient power generation by solar power needs shining of the sun. This includes not just fluctuations during day and night, but also over the course of the year. In addition, geographic limitations are also to be considered. The sun must irradiate in the right angle to allow efficient power generation. This makes regions in the global north and in the global south (*ca.* above and below 60°), undesirable for solar electricity generation.[13, 14] For wind energy, areas of sufficient wind are needed. This often requires the addition of power transmission over long distances, requiring an expansion of the power grid.

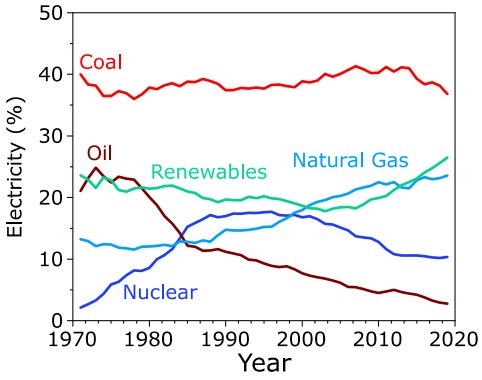

Figure 1.5 Electricity production by energy source globally from 1971 to 2019.[12]

These limitations are made more complex by the need of acceptance within society, as in many cases e.g. civil resistance against wind parks is encountered. Expanding hydro power is often associated with interference with natural ecosystems and while many new concepts to expand hydro power with limited interference are explored, challenges will remain.

In the case of wind and solar power, and to a lesser extent in hydro power, generation of electricity is dependent on external influences. As mentioned above, solar power generation fluctuates during the day and depends on the presence of clouds. Wind is not a constant stream, and power shortfalls due to windless days or weak winds must be mitigated too. Hydropower is less exposed to short term fluctuations, but even water levels in reservoirs can decrease in periods of drought, limiting the potential for power generation. These limitations can be overcome with investment and engineering, but fossil fuels are used for more than just energy generation.

1.1.5. Electrochemistry for sustainability

For many applications electrochemistry could become the key to harvest the full potential of renewable energy sources. Electrochemical methods can be used for energy storage and conversion and be adapted to specific applications. In general, electrochemistry is focused on the interplay between chemical reactions and an external electrical potential.

1.1.5.1. Energy storage for renewable energies

Batteries are a widely used technology for electrochemical energy storage. In a battery, electrons are stored in the anode during charging, depleting the cathode of electrons, generating a potential difference between them. During discharge, electrons flow from the anode to the cathode, freeing positive ions to be transported through the electrolyte and a separator towards the cathode, where they react with the electrons (Figure 1.6).[15] Through different cell chemistries and sizes, batteries can be used to power small devices, like mobile phones or laptops, or be used for large scale storage for electrical grid applications.

Batteries are a well-established technology, that have been used since the 19th century. Many different cell chemistries have been explored and used over the decades and, today, Li-ion batteries are often used for a wide range of devices. Through the expansion of electric vehicles, based on batteries, they can help to replace fossil fuels in the transport sector, if electricity is generated in a renewable way. They can also be used for grid storage, where they store excess energy from wind and solar and feed it back into the grid on demand.

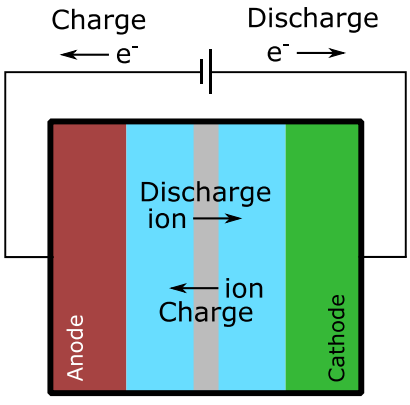

Figure 1.6 Schematic of a battery cell.

The potential of batteries in a sustainable future cannot be denied, there are however limitations to their use. In aviation, weight is a crucial factor: the energy density of today's batteries is below 1 MJ/kg[16] i.e. less competitive than gasoline or kerosene which have energy density of around 45 MJ/kg.[17] Even accounting for the relatively low efficiency of internal combustion engines of 40%,[18, 19] the energy density of typical batteries remain inferior to what is achievable with conventional fuels. A realistic look at aviation without the need for kerosene from fossil sources requires so called sustainable aviation fuels. This shows that batteries, while useful and irreplaceable in various applications, will not be able to replace fossil sources by themselves; they are rather, one of the components that will help to replace fossil fuels and will need to be integrated with other technologies.

1.1.5.2. Energy conversion

Energy conversion is another route for applying electrochemical solutions towards a sustainable future. The electrical energy is not stored as electrical energy, as it is the case for batteries, but the energy is converted into chemical energy. These chemicals can then be fed into the existing infrastructure, either as fuel or as chemicals.

Water electrolysis for the generation of hydrogen is one of these technologies. A scheme of an electrolyser is shown in Figure 1.7. The hydrogen can then be used for internal combustion, as a reagent for chemical reactions or for electricity generation in a fuel cell. In general, the generation of hydrogen is the main goal in water electrolysis, and oxygen is seen as a side product. Hydrogen, generated through renewable sources, is seen as an essential chemical and fuel for a sustainable future.

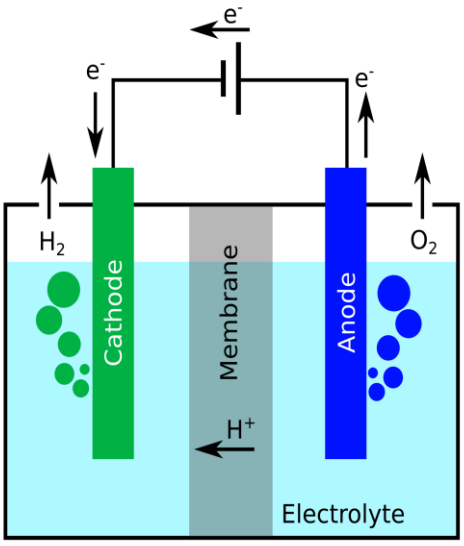

Figure 1.7 Schematic of a water electrolyser.

The hydrogen evolution reaction (HER) is occurring at the cathode of an electrolyser and is a well-studied reaction.[20-22] In acidic media the HER follows multiple steps. In a first step adsorbed hydrogen, H_{ads}, is formed at the electrode, by reaction of a proton with an electron. This is called the Volmer step (1). The adsorbed hydrogen can either react with a second adsorbed hydrogen in the so called Tafel step (2), or with another proton from solution in the Heyrovsky step (3). The chemical equations of this are shown below.

$$H_3O^+ + e^- \rightarrow H_{ads} \quad (1.1)$$

$$2\,H_{ads} \rightarrow H_2 \quad (1.2)$$

$$H_{ads} + H_3O^+ + e^- \rightarrow H_2 + H_2O \quad (1.3)$$

Catalyst materials are needed for the HER to take place with high voltage efficiency. A catalyst for the HER needs to be able to activate and bind adsorbed hydrogen. However, there needs to be a balance so as not to bind the hydrogen too strongly to allow for evolution of hydrogen gas as a product. A graphical representation of that is given in the volcano plot, graphing the exchange current densities of different materials against the free enthalpy of hydrogen adsorption. This was first proposed by Trasatti who used experimental data on the HER to illustrate the relationship.[22] Nørskov et al. then replaced the metal hydride bond strength on the x-axis with the Gibbs free enthalpy of hydrogen adsorption obtained from computational results, ΔG_{H*}.[21] This is shown below. Platinum gives the highest exchange current densities with an optimal strength of hydrogen adsorption that is close to zero. Thus, Pt is the state-of-the--art electrocatalyst in the HER and fuel cell applications.

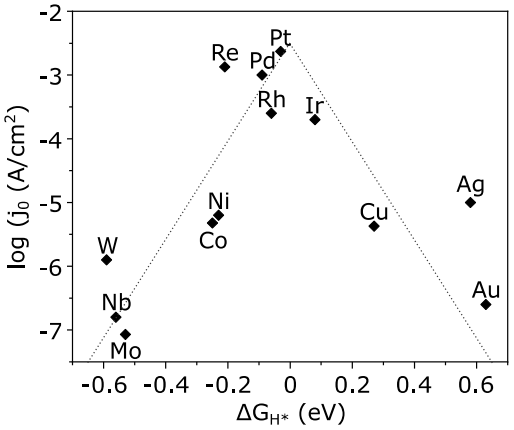

Figure 1.8 Volcano Plot showing the exchange current density in the HER as a function of the Gibbs free enthalpy of hydrogen adsorption. (Data taken from Nørskov et al.[21]).

The anodic reaction in water electrolysis is the oxygen evolution reaction (OER). As the oxygen is produced at the electrode, hydronium ions (or water in alkaline media) are generated which are transported to the cathode to sustain the HER. As is the case for the HER, the OER requires catalyst materials, with the best performing materials today being iridium oxide and ruthenium oxide.[23-25] The chemical equations for acidic (1.4) and alkaline(1.5) OER are shown below.

$$2\,H_2O \rightarrow 4\,H^+ + 4e^- + O_2 \quad (1.4)$$

$$4\,OH^- \rightarrow 2\,H_2O + 4\,e^- + O_2 \quad (1.5)$$

The OER has a thermodynamic potential of 1.23 V vs. RHE.[26] This means, that for water electrolysis a voltage of at least 1.23 V is required. However, the overpotentials, the actual potential needed to run these reactions, associated with this reaction significantly increases the voltage required for water electrolysis. The oxygen produced via the electrocatalytic process is often seen as only a side product, therefore this high voltage is a challenge when it comes to the energy efficiency of hydrogen production. Electrooxidation of organic molecules in organic oxidation reactions (OOR) have been proposed to replace the OER to potentially lower the required voltage of electrolysis.[27, 28] This has the added benefit of obtaining a chemical products that can be used in industrial applications at the anode side. Here, an organic compound is oxidised at the anode, often with a lower thermodynamic potential compared to the OER. This can lower the energy demand to produce hydrogen as well as producing chemical products at the anode.

Hydrogen is not the only product that can be generated at the cathode of an electrolyser. Different electroreductions have been proposed to render electrochemical energy conversions economically competitive. Examples are the reduction of alkynes to alkanes and alkenes;[29] or the hydrogenation of aldehydes and ketones to alcohols,[30] as discussed below. The reduction of CO_2 (CO2RR) to methane, ethylene or ethanol is another technology often proposed and investigated.[31] This technology is taking CO_2, removing it from the atmosphere or straight from a point source and turns it into chemicals and fuels. One of the challenges of CO2RR is the supply of CO_2, as the content in the atmosphere is too low for efficient reactions. This brings the need of CO_2 capturing at the source of the generation.[32] Another way to overcome this problem is by letting nature capture the CO_2 and then use the generated biomass and subsequently use the biomass as a carbon feed.

Viable electrochemical conversions could replace a variety of petrochemical processes. As this means that it is possible to run them on a smaller scale compared to typical petrochemical reactions, the conversions can be operated at the source of the raw material and/or in a decentralized manner. This can not only lower the energy demand of conversions, but also allow to introduce biomass as a sustainable carbon feedstock. The high cost of transport currently makes the conversion of biomass derived chemicals not feasible or cost-effective and, as a result, waste biomass is generally only burned and used for thermal energy production. The next section looks as biomass as a sustainable carbon feedstock and how biomass can be used for electrochemical conversions.

1.2. Biomass as sustainable carbon feedstock

Biomass is renewable organic material from plants and animals. This includes wood and wood waste, Agricultural crops and waste, municipal waste and animal manure.[33] In general biomass is directly or indirectly a product of photosynthesis. Most plant based biomass contains, to some degree, intertwined structures of cellulose, hemicellulose and lignin.[34]

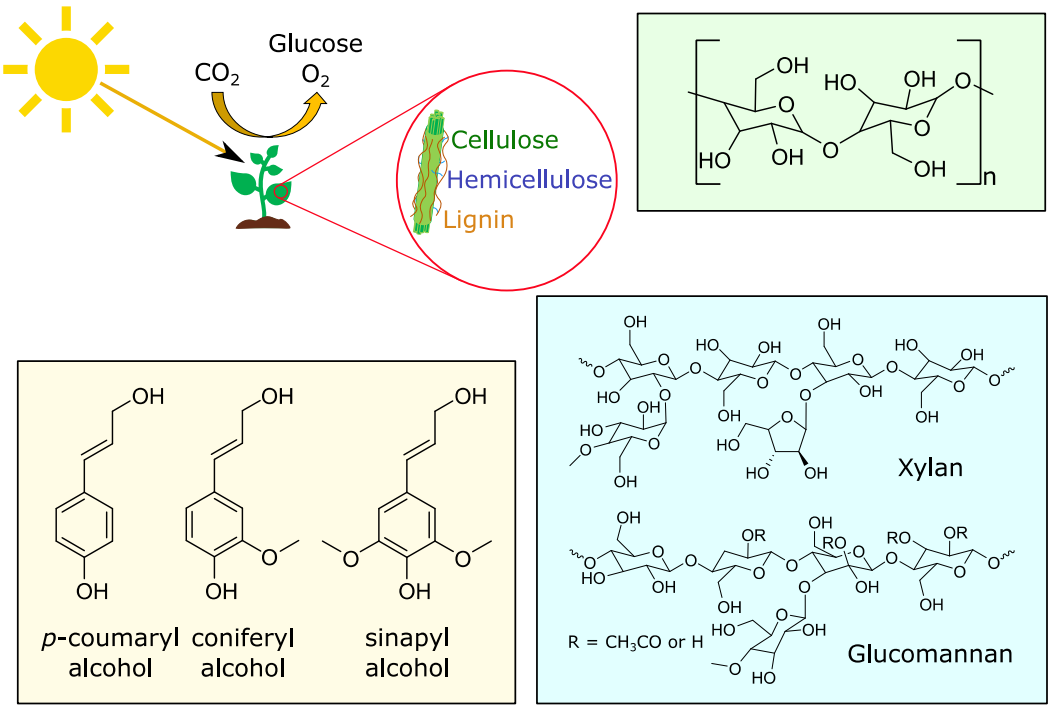

Figure 1.9 Scheme of generation of biomass through Photosynthesis and the chemical structure of cellulose, hemicellulose and the three main components of lignin.

Biomass is the only alternative to fossil oil as a source for carbon based chemicals and fuels.[35] The use of biomass for energy applications is not a new idea, as even the burning of wood falls under this category. In 2023 biomass contributed about 5% to the total primary energy consumption in the United States of America.[36]

1.2.1. Biomass for energy applications

There are two main ways of employing biomass:[36, 37] one is the direct combustion of biomass for heat production, and the second is the conversion of the biomass for production of solid, liquid and gaseous fuels. These conversions can be carried out using biological, chemical or thermochemical methods. Biological conversion includes the production of bioethanol and bio methanol through fermentation and anaerobic digestion. Bioethanol is already widely used as a biofuel, with unleaded fuel containing up to 10% bioethanol, for example in Europe, the USA and Australia. The production of bioethanol is mainly based on starch and sugar containing crops, especially corn and sugar beets. If agricultural land is used to produce fuels, conflicts between energy and food production could arise, therefore there is much interest in finding novel processes for cost-effective production from alternative crops or biomass sources. Fermentation can be carried out using cellulose and hemicellulose-based feeds;[38] however in this case a pretreatment of the biomass is needed to hydrolyse the biopolymers into glucose monomers, which can then be fermented. The fermentation occurs as shown in the equation below.

$$C_6H_{12}O_6 \rightarrow 2C_2H_5OH + 2CO_2 \qquad (1.6)$$

A significant drawback of fermentation processes is that, as only cellulose and hemicellulose can be fermented, the lignin, i.e. a significant portion of the biomass, cannot be utilised or exploited. In addition to this, the fermentation of one molecule of glucose produces two molecules of ethanol and two molecules of carbon dioxide. When looking at bioethanol as a carbon feedstock for chemicals, a loss of a third of the carbon content to CO_2 as a side product is highly undesirable. Biodiesel is a biofuel produced from chemical conversion of biomass through transesterification of vegetable oils and other fats and greases into fatty acid methyl esters.[39] This biodiesel can be used directly to replace conventional diesel fuel.

In the Billion Ton Report 2016[40] the US DoE looked at the potential of biomass for fuel production. The authors reported a potential between 1.2 and 1.5 billion dry tons of biomass in the USA by 2040 which, under the assumptions of the report (80 gallons of biofuel per dry ton of biomass), would yield 96-120 billion gallons (363 to 454 billion litres) of biofuel. In comparison, in 2023 the USA consumed about 140 billion gallons (530 billion litres) of gasoline, a number which is expected to further increase in coming years.[41] Bioethanol has energy density of about 23.6 MJ/L (29.9 MJ/kg), i.e. a lower energy content compared to the 34.7 MJ/L (46.7 MJ/kg) of conventional gasoline.[42] Thus, the energy delivered of biofuel under these assumptions is estimated to be about 10.7 EJ in the most optimistic scenario, which is well short of the about 18.4 EJ used in 2023. In the Billion Ton Report 2023 the authors reported however that the US could supply enough biomass in a sustainable way to fuel their aviation needs with sustainable fuels.[43]

The picture drawn by these predictions, shows that the existing technologies are not sufficient for utilizing biomass in a sustainable economy. This highlights the need for new approaches to biomass processing/valorisation, as for example through thermo-chemical conversion, which is the combination of a pyrolysis step with a chemical treatment step. This can be used to produce solid, liquid and gaseous fuels, utilizing not only cellulose and hemicellulose but also lignin. Especially as Lignin contains almost 40% of the energy stored within biomass, while only contributing to 10 – 25% of the mass.[35] Electrochemical processing offers an alternative route to the chemical treatment of biomass to produce chemicals and fuels.[44]

1.2.2. Pyrolysis and bio-oil upgrading

Pyrolysis is the thermochemical conversion of biomass under reduced oxygen atmosphere. The process yields solid, gaseous and liquid products. The solid fraction is called bio-char and is a carbon rich solid. As it is highly porous, it finds application as adsorbent or as support material in electrochemical applications.[45] The gaseous fraction, the biogas, contains CO_2, CO, methane and different short chain hydrocarbons;[46] these can be separated and then introduced into the natural gas stream.

The char and the combustible components of the biogas can also be used to generate the heat required for the pyrolysis process. Bio-oil is formed upon condensation of the vapour phase; this phase can be used for direct heating and electricity generation or used for

upgrading to fuels and chemicals. The distribution of the three fractions, and their composition is dependent on the biomass feed as well as on the pyrolysis process. Scott and Piskorz investigated the distribution of the different fractions depending on the temperature of pyrolysis.[47] They reported that the highest percentage of bio-oil is obtained at an optimum temperature of 500°C.

Bio-oil is a complex mixture of oxygenated hydrocarbons and a significant amount of water. As the biomass all consists to some degree of the three biopolymers, certain compounds are generally found in bio-oil.[48, 49] A selection of these compounds is shown in Figure 1.10. These compounds are different aromatic alcohols and aldehydes, as well as different oxygenated compounds. The wide range of organic compounds found in bio-oil - over 300 in the bio-oil from the pyrolysis of wood - show the potential it holds as a sustainable carbon feedstock for transportation fuels and chemicals.[50, 51]

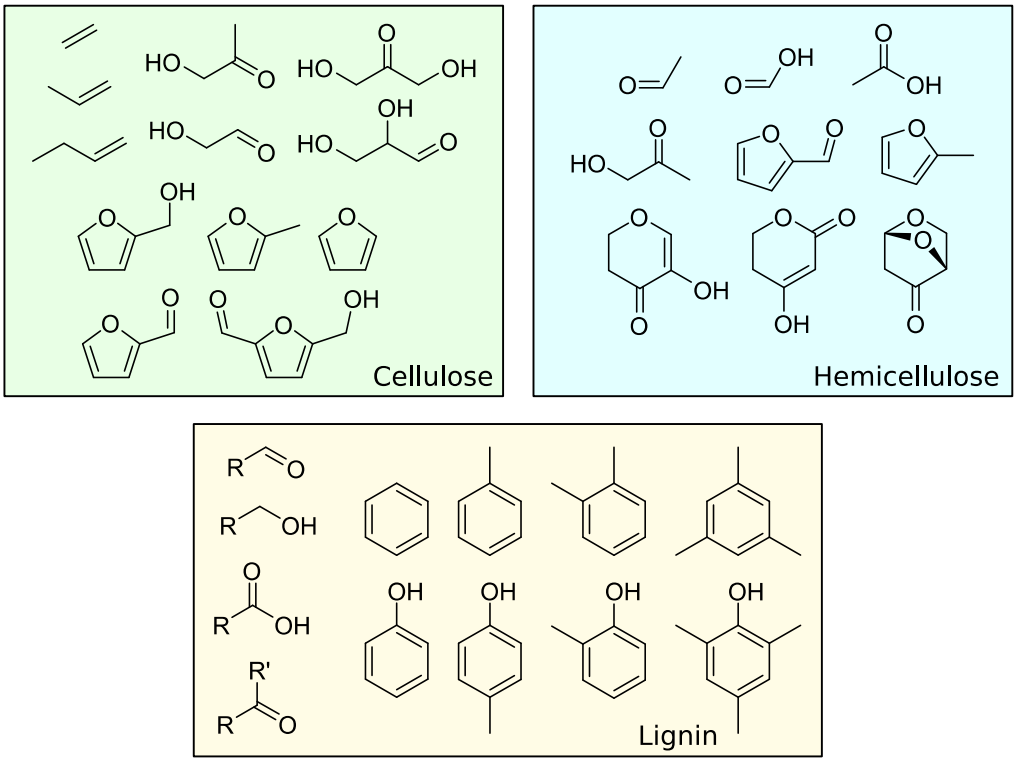

Figure 1.10 Selection of organic molecules generated during pyrolysis of lignocellulosic biomass, separated by starting polymer.[52, 53]

Bio-oil is not stable and is prone to aging, making it challenging to store, transport and utilize.[54] This ageing is caused by a variety of reactions, like polymerization, esterification, dimerization, hydration, and others. Such processes can lead to phase separation, change in carbonyl content, higher water content and an increase in viscosity.[55, 56] Many of the

reactions responsible for aging occur through carbonyl groups, like aldehydes.[57] Through hydrogenation of these aldehydes, the bio-oil can be stabilized for storage and transportation. Different routes for stabilising and upgrading biomass have been proposed, from deoxygenation to polymerisation. One promising route is the hydrogenation of oxygenated compounds. This can be used to stabilise the bio-oil, increase the heating value or in general be used for the synthesis of chemicals and fuels.

1.3. Electrocatalytic hydrogenation

1.3.1. General mechanism

Conventional hydrogenation reactions are widely used in the chemical industry. They do require high pressure, high temperature and a supply of pure hydrogen. In addition to the high energy demands associated with these operational conditions, these reactions are usually only viable in large scale plants located in the proximity of oil refineries. The transportation costs required with bringing biomass to these centralized locations make standard hydrogenation processes incompatible with sustainable use of biomass.

Electrocatalytic hydrogenation (ECH) is an alternative to conventional hydrogenation, with the potential to significantly reduce energy requirements. In the ECH, hydrogen is generated in-situ at the electrode, thus reducing the energy demands of thermal activation of H_2 and the need for external hydrogen inputs altogether.[58] ECH is carried out at moderate conditions and in aqueous media; this lowers the required energy input as well as the demands on reactor design and performance. The driving force behind ECH is an externally applied potential, which can be achieved using renewable electricity. Variations in the applied potential can in principle moderate the activity and selectivity of the reaction, allowing flexibility in the hydrogenation process.

The first step of the ECH is the generation of adsorbed hydrogen at the electrode surface (1.7),[59] which is identical to the Volmer step of the HER, placing the HER in competition with the ECH. The adsorbed hydrogen reacts then with the unsaturated organic adsorbed on the electrode to form the hydrogenated product (1.9). In addition to this, hydrogenolysis can occur as well (1.11). The hydrogenation of the organic follows the same steps as in conventional heterogenous catalysis, with the big different that the activated hydrogen is produced in situ from water and not from the breaking of a hydrogen molecule. The chemical equations for the ECH of an unsaturated compound can be written as follows:

$$H_3O^+ + e^- \rightarrow H_{ads} \quad (1.7)$$

$$Y = Z \rightarrow (Y = Z)_{ads} \quad (1.8)$$

$$(Y = Z)_{ads} + 2H_{ads} \rightarrow (HY - ZH)_{ads} \quad (1.9)$$

$$(HY - ZH)_{ads} + 2H_{ads} \rightarrow HY - ZH \quad (1.10)$$

$$(HY - ZH)_{ads} + 2H_{ads} \rightarrow YH_2 + ZH_2 \quad (1.11)$$

The ECH can be used on a variety of functionalities, carbon-carbon double and triple bonds, aldehydes, ketones and even nitro groups.[60] Carbonyl groups are of high interest in the upgrading of biomass:[35] they are at the origin of several bio-oil ageing reactions and are also important intermediates for the synthesis of many high-value chemicals. Some carbonyl compounds used for studies of electrocatalytic hydrogenation are shown in Table 1.1.

Table 1.5 Organic carbonyl compounds used in literature for electrocatalytic hydrogenation studies.

Functional Group	Product	Reference
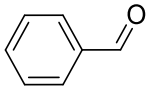 Benzaldehyde	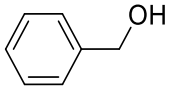 Benzyl Alcohol	61-63
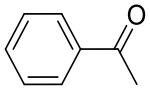 Acetophenone	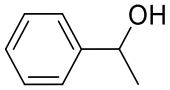 1-Phenyl-ethanol	64, 65
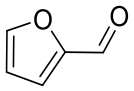 Furfural	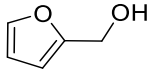 Furfuryl Alcohol	66
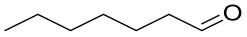 Heptanal	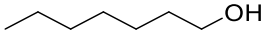 Heptanol	66
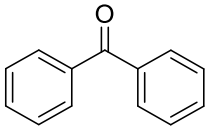 Benzophenone	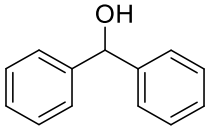 Diphenylmethanol	64

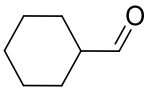 Cyclohexane carboxaldehyde	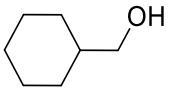 Cyclohexyl methanol	66
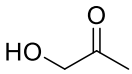 Hydroxy acetone	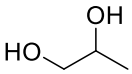 Propylene glycol	67
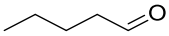 Pentanal	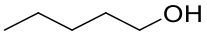 Pentanol	68

1.3.2. Benzaldehyde as model compound

Due to the complex nature of real bio-oil, the investigation of hydrogenation processes can be challenging. For this reason, many studies investigating the catalytic performance of hydrogenation processes, use diagnostic compounds such as benzaldehyde and furfural to provide a mechanistic understanding and for optimisation purposes. Benzaldehyde is the simplest aromatic aldehyde, with only one carbonyl group that can be hydrogenated to the corresponding alcohol. It is also relatively soluble when compared to other aromatic compounds, thus making it a good model organic substrate for the fundamental study of catalytic hydrogenations.

In the case of benzaldehyde, the ECH occurs through two consecutive additions of adsorbed hydrogen at the electrode, yielding benzyl alcohol. The intermediate, the ketyl radical of benzaldehyde can undergo a combination with a second radical, yielding hydrobenzoin, as shown in the reaction pathways in Figure 1.11. The presence of the two products shows the importance of understanding the process of the reaction, to obtain, if possible, a high selectivity towards one of the products.

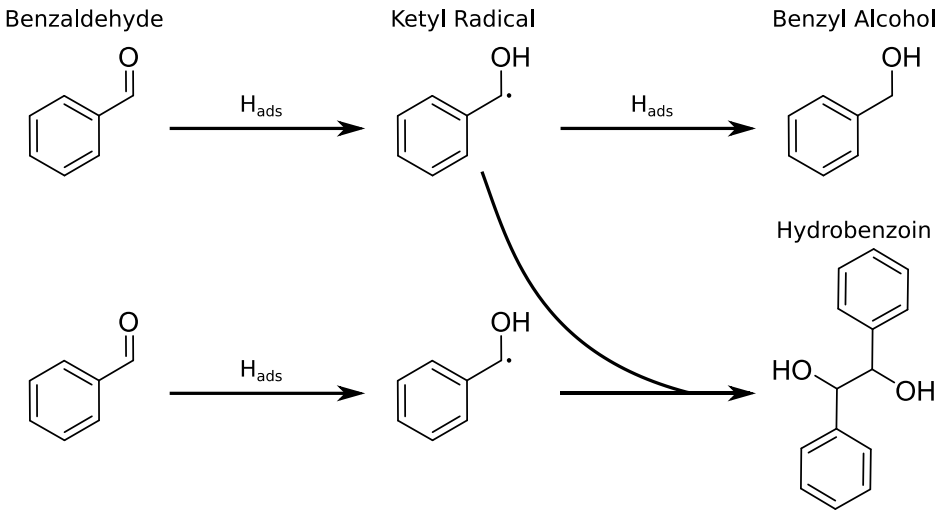

Figure 1.11 ECH reactions of benzaldehyde resulting in the full hydrogenation product benzyl alcohol and the dimerization product hydrobenzoin.

Different studies have been performed, to understand what conditions lead to dimerization and which lead to full hydrogenation of the aldehyde. Cantu et al. investigated the ECH mechanism of aliphatic and aromatic aldehydes on different catalyst materials.[68] They proposed different possible routes via which hydrogenation can take place. A first pathway involved reaction of an adsorbed hydrogen with the adsorbed organic as previously described; the authors called this a concerted hydrogenation. In contrast to this, the sequential hydrogenation pathway is proposed, where the organic is first reduced by addition of an electron before protonation takes place. What the authors found was that the preferred pathway is expected to change with applied potential, with the sequential electron-proton addition becoming more favourable at more cathodic potentials. This reaction mechanism has been previously reported by Chan-Shing et al. where the authors called the addition of an adsorbed hydrogen the ECH, and the sequential electron-proton addition an electronation-protonation reaction.[69] Andrews et al. found that the hydrogenation of benzaldehyde at more cathodic potentials leads to increased formation of the dimerization product, especially on non-precious metals.[70] This increased production of hydrobenzoin can be explained by the change in reaction mechanism, where an increased production of ketyl radical leads to faster rates of dimerization. The effect of applied potential on the ECH of benzaldehyde has been investigated by Lopez-Ruiz et al.[61] at varying potentials; their work proposes that changes in surface coverage of benzaldehyde and hydrogen are the reason for changes in observed reaction orders. The fact that base metals lead to production of dimerization products, and precious metals do not, has been investigated by Anibal et al.[71] In their work, the authors investigated the ECH

of benzaldehyde on different metals and proposed that benzaldehyde undergoes decarbonylation reactions on Pt. This in turn leads to CO poisoning of the catalyst surface and consequent lower rates of dimerization. All these studies show that the reaction conditions of the ECH, namely pH, applied potential, concentration of organic, to name a few are important for careful control over product distribution/selectivity.

In addition to the reaction conditions, the choice of electrocatalyst material is important for the performance of the ECH. Especially, as in addition to the dimerization, the HER is the other main competing reaction. This is due to the fact, that the ECH at low overpotentials requires adsorbed hydrogen to be present at the surface, which can also lead to the evolution of hydrogen through the HER. This is often unwanted in the ECH, as it lowers the faradaic efficiency. The competition with the HER, and especially the requirement of adsorbed hydrogen can however be used to design catalyst materials for the ECH, by screening materials used in other electrocatalytic applications and especially the HER.[72]

1.3.3. Electrocatalysts for the ECH

In many cases of electrocatalysis, precious metals give the best performance, and e.g. platinum is the state-of-the-art catalysts for the HER.[20] In the ECH, palladium and other precious metals have been reported to have excellent activity.[63, 66] Nonetheless, while the activity of precious metals is almost unrivalled by other materials, they do suffer from serious drawbacks. Precious metals are scarce and expensive, which is a problem, when it comes to scaling up a technology like the ECH. The disadvantages of precious metals are not just of economic nature. These materials are susceptible to catalyst poisoning and deactivation through different processes,[73] which can be particularly problematic for the processing of heterogeneous feeds of biomass origin. Importantly, Pt has been shown to be poisoned and its catalytic activity inhibited by the adsorption of carbon monoxide which can form from surface decomposition of carbonylated compouds.[74, 75] Also, metal nanoparticles used in electrocatalysis are known to undergo the so called Ostwald ripening:[76] this is the growth of metal nanoparticles by dissolution of small particles and subsequent redeposition onto bigger ones[77] and leads to a decrease in the electrocatalyst active surface area. Ostwald ripening can be inhibited by the choice of support material however it is a problematic degradation mechanism for Pt-group nanoparticle electrocatalysts.[78]

Due to the challenges linked to precious metals, transition metals have garnered more significant attention for electrocatalytic applications.[66, 70, 72, 79] In general, the activity of transition metals is lower compared to precious metals, but this lower activity, especially in the HER can potentially be advantageous for the ECH.[66, 70, 80] In the reduction of carbon dioxide, copper is a widely used catalyst, owing to its ability to catalyse C-C coupling reactions.[81] Other transition metals, which have been investigated and reported are silver and nickel.[82] The lower activity compared to precious metals is also usually offset by the price, which is a fraction compared to that of precious metals. However, the stability of non-precious metals is often a major challenge and poses limitations to operational conditions in a range of reactions. In acidic media, and under the conditions typically used for the ECH of bio-oil, transition metals can corrode. A variety of strategies have therefore been developed to bypass these problems and fabricate catalyst materials based on transition metals.

Transition metal oxides, carbides and nitrides have been reported to catalyse the HER and ECH reactions. A special case of carbides are MXenes, a layered carbide material. MXenes have gained much attention for applications in capacitors and there are also reports of promising electrocatalytic activity in the HER.[83] Another class of materials are transition metal dichalcogenides (TMDCs), which be synthesized as 2D or 3D nanostructured materials. One TMDC often reported, especially for the HER is MoS_2, which consists of low-cost raw materials and can deliver good performance in the HER.[84]

All these catalyst materials are rarely used in bulk form. Metals, especially precious metals are more often used as nanoparticles, dispersed on a conductive support material. Similar strategies are chosen for MXenes and TMDCs. The dispersion on a conductive support allows the use of semiconducting materials, like MoS_2, and the reduction of needed catalyst material. In many applications the support chosen is a carbon-based material. Especially graphitic materials are often used, due to their electrical conductivity and (electro)chemical stability. The variety of carbon materials, discussed later in this chapter, and the possibility to tune the chemical composition, makes carbon a promising material in electrocatalysis.

1.3.4. Evaluation of catalyst materials

To be able to evaluate the performance of a catalyst material it is necessary to define key performance indicators (KPIs) and usually a combination of KPIs is needed to establish an overall assessment of performance. An important property of an electrocatalyst in electrolyser applications is its production rate, which is the amount of chemical product generated, normalised by electrode area and electrolysis time as in equation (1.12):

$$\text{Production Rate}\left(\frac{\text{mol}}{\text{h cm}^2}\right) = \frac{n_{\text{product}}}{t_{\text{electrolysis}} \cdot A} \tag{1.12}$$

Where $n_{Product}$ is the amount of a product produced during the electrolysis, $t_{electrolysis}$ is the time of electrolysis and A is the electrode area. The production rate can be calculated for benzyl alcohol and hydrobenzoin in the case of the ECH of benzaldehyde, or for hydrogen for the HER.

Similar to the rate at which products are generated is the rate at which benzaldehyde is electro-reduced or consumed. While this generally would be defined by the amount of benzaldehyde consumed per time and area, in this work the reduction rate is calculated using the sum of products as a proxy for the consumption of benzaldehyde. The reason for this is the fact that after analysis the carbon balance does not fully add up, making this definition a good approximation:

$$\text{Reduction Rate}\left(\frac{\text{mol}}{\text{h cm}^2}\right) = \frac{n_{\text{Benzyl Alcohol}} + 2 * n_{\text{Hydrobenzoin}}}{t_{\text{Electrolysis}} \cdot A} \tag{1.13}$$

This expression includes the sum of the production rate of benzyl alcohol and twice the production rate of hydrobenzoin, as two benzaldehyde molecules are reduced to yield one mole of the dimer product.

The faradaic efficiency (FE) is an indicator for how much of the charge passed is used for electrocatalytic hydrogenation reactions, as opposed to hydrogen evolution. In the case of benzaldehyde hydrogenations, two electrons are needed for generating either of the possible products, so that the equation for the FE is:

$$\text{F. E. (\%)} = \frac{n_{\text{Product}}}{\frac{Q}{F} \cdot 0.5} \tag{1.14}$$

Where Q is the charge passed during the electrolysis, and F is Faraday's constant (96485.3321 C/mol). In the absence of additional side faradaic reactions, it is usually

assumed that the balance of the total charge is accounted for by the HER as the only competing process.

As the FE already provides an indicator of selectivity between the ECH and the HER as the only competing process, the term selectivity in this work, as well as others', is used to describe the selectivity towards a specific product of organic hydrogenation. As only two products were obtained from the electrolysis experiments, in the case of benzaldehyde, the selectivity is calculated according to the equation below:

$$\text{Selectivity}\ (\%) = \frac{n_{\text{Benzyl Alcohol}}}{n_{\text{Benzyl Alcohol}} + n_{\text{Hydrobenzoin}}} \tag{1.15}$$

The above KPIs are calculated for all materials used in this work. Finally, another important performance indicator that can be calculated, and that is used in chapter 5, is the turnover frequency (TOF). The TOF is similar to the production rate or reduction rate, with the difference that the rate is normalised to the surface coverage/concentration of active sites. Calculation of TOF values therefore requires that the identity of the catalytic site be known or at least assumed, as shown below:

$$\text{TOF}(s^{-1}) = \frac{n_{\text{Benzyl Alcohol}} + 2 \cdot n_{\text{Hydrobenzoin}}}{t_{\text{electrolysis}} \cdot n_{\text{catalyst}}} = \frac{\text{Reduction rate}}{\Gamma_{\text{catalyst}}} \tag{1.16}$$

Where Γ_{catalyst} indicates the surface density of active sites (mol/cm^2). This expression indicates how much benzaldehyde is reduced per unit time, with the same approximations as for the reduction rate (1.13), (frequency of production per site) and can be adapted to calculate the turnovers specific of benzyl alcohol or hydrobenzoin. Finally, it is important to note that all of the above KPIs are generally dependent on applied voltage/current conditions for electrolysis under potential/current control.

Using the above KPIs it is possible to evaluate the performance of a catalyst material for the ECH. A material for the ECH should show a high production rate with high faradaic efficiency and a high selectivity for one of the two products. These KPIs give a good indication of the activity of a catalyst material but are not the only descriptors relevant for catalytic material. One additional property relevant for catalytic materials is the stability, during application and storage. Another relevant property is the sustainability of the material. This includes the synthesis, as well as the recyclability of the catalyst material.

1.4. Carbon-based electrocatalyst materials

Carbon materials and nanomaterials find widespread use in electrochemical applications. For instance, state of the art lithium-ion batteries employ a graphite anode, exploiting the ability of the carbon material to reversibly intercalate and deintercalated Li-ions into the carbon lattice. Carbon has many advantageous properties for electrochemical and electrocatalytic applications: graphite and graphitized materials are conductive and (electro)chemically relatively stable; carbon is widely available and environmentally benign; finally, the variety of carbon morphologies and allotropes, together with the possibility to tune chemical composition for specific applications, make carbon a sought-after material in electrocatalysis.

1.4.1. Different allotropes of carbon

As mentioned above, carbon can be found in different allotropes and morphologies, which all exhibit unique properties. Diamond and graphite are the two main allotropes and are shown in Figure 1.12. Diamond consists of tetrahedrally-bonded carbon centres covalently bonded to carbon atoms via σ-bonds, making diamond one of the hardest natural occurring materials. Diamond has an excellent thermal conductivity together with a poor electric conductivity[85] and is a wide band gap semiconductor (E_{gap} = 5.47 eV); these properties make it an interesting material for many applications under extreme conditions, for example as exit windows for high power lasers[86] or monochromators at Synchrotron facilities.[87]

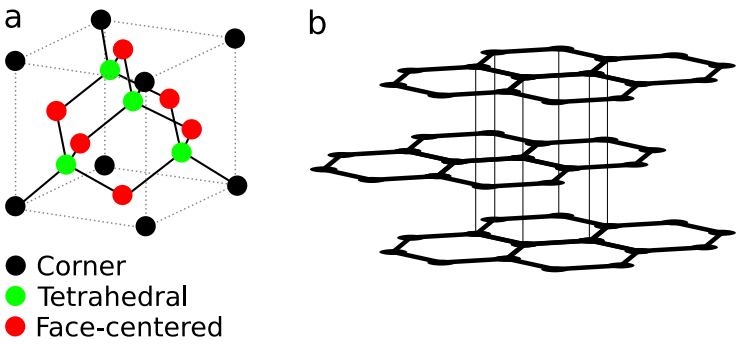

Figure 1.12 Chemical structure of (a) Diamond and (b) Graphite. (Adapted from Kobashi[88] and Bernal and Bragg[89]).

Graphite consists of trigonally bonded carbon centres (sp^2) forming extended 2D layers of six-membered rings of π-bonded C-C atoms.[89] Van der Waals interactions between these 2D layers result in the 3D crystal structure of graphite. This leads to anisotropy in the thermal, electronic and mechanical properties of graphite; for instance, electric conductivity along the planes is higher, as the layers have a delocalised π-electron system, but poor in the direction perpendicular to the planes.[90] The 2D layers can be shifted against each other under shear stress, which makes graphite a good lubricant.[91] The layered structure is also the reason for the ability of graphite to intercalate ions, for example in Li-ion batteries,[92] as the weak coupling between the layers results in facile lattice expansion in the direction perpendicular to the planes (*c*-axis). This thesis focuses on carbon materials rich in sp^2 centres, as these graphitized materials are most often used as electrodes/conductive supports in electrochemistry; for this reason, some of the common graphitic materials are discussed below in greater detail.

1.4.2. Graphitic carbon materials

Single layers of graphite are called graphene; this material was first isolated in 2004[93] and its discovery was awarded with a Noble prize. Initial work was carried out on graphene obtained from mechanical exfoliation of highly ordered pyrolytic graphite (HOPG). At present, it is also possible to obtain graphene from CVD processes,[94] from liquid exfoliation[95] and from oxidation-reduction chemical and/or electrochemical methods.[96] Graphene is a promising candidate for different applications due to its unique properties.[97] It is light and has an excellent specific surface area. It exhibits excellent electronic conductivity with a tuneable band gap. The mechanical strength of graphene makes it also interesting for wearable electronics applications. Derived from graphene different allotropes of carbon have been discovered and synthesised. Carbon nanoribbons are single layer graphene, with a quasi-one-dimensional structure.[98] They have a width of usually less than 100 nm and a much larger length. Carbon nanotubes (CNTs) are formed of sp^2 carbon in a tubular shape, with a one-dimensional structure; they can be single walled or multiwalled and exhibit metallic or semiconducting properties depending on their structure.[99] CNTs have a large specific surface area, which makes them a widely used material in electrocatalytic applications. Further graphitic carbon materials, which are just mentioned for completeness, are fullerenes,[100] nanofibers,[101] nano-onions[102] and nano-cubes.[103]

Glassy carbon (GC) is based on sp^2 carbon, but in contrast to graphite does not possess a high crystallinity.,[104] GC cannot be graphitized at elevated temperatures.[105] GC has short-range order present in the form of partially planar structures; there is however no long-range order, giving rise to glass-like properties, e.g. its mode of fracture. GC is formed typically from pyrolysis of carbonaceous resins and polymers.[106] It is highly conductive and is therefore frequently used in electrode applications; it usually shows reasonable electrochemical inertness and a wide potential window in aqueous electrolytes[107] which has led to its frequent use in electroanalytical applications and as electrocatalyst support.

Amorphous carbons (a-C) are carbon materials that possess neither long- nor short-range order.[108] a-C can be synthesized to display a wide range properties, depending on the ratio of sp^2 and sp^3 carbon present, as shown in Figure 11. For high ratios of sp^3, the term used is either tetrahedral amorphous carbon (ta-C) or diamond-like carbon (DLC), as many of the properties in these materials (electronic, mechanical, chemical) are similar to those of diamond. Higher ratios of sp^2 carbon are present in materials termed as a-C, which can instead approach the properties of nanocrystalline graphitic carbons. Although the properties of a-C vary with chemical composition, amorphous carbons are generally (electro-)chemically inert and exhibit low friction coefficients, which is beneficial when used as tribological coatings,[109] which explains interest in mechanical applications of these materials for e.g. hard-drives, joint replacements, stents etc. The presence of sp^2 centres can also result in acceptable conductivity for electrode applications, which coupled with their ease of fabrications, e.g. via physical deposition methods, has led our group and others to investigate their performance in e.g. biosensing or electrode array fabrication.[110-114] In contrast to glassy carbon, a-C undergoes chemical changes at elevated temperatures forming graphitic materials.[115-117] This graphitisation will be used in this thesis to generate graphitic carbon films used for electrocatalytic studies.

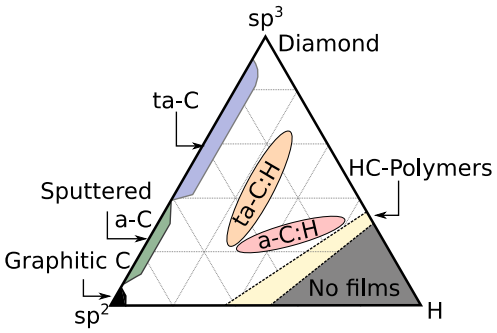

Figure 1.13 Different carbon materials depending on sp^2, sp^3 and hydrogen content. Reworked from Ferrari and Robertson.[118]

Furthermore, it is possible to integrate amorphous- and graphitic-carbon to fabricate/synthesize heterostructured materials that leverage synergies between the carbon phase and a metallic or oxide phase. In this thesis, carbon materials will be used in three different ways for electrocatalysis studies: as metal free and heteroatom-doped carbon, as a support for a second catalytic material and as encapsulation layer for metals. The following sections will introduce the reader to the electrocatalytic applications of these materials.

1.4.2.1. Metal-free heteroatom-doped carbon

Metal-free carbon materials are promising candidates for electrocatalytic applications. Consisting of a low cost material which is widely available and abundant, carbon can be tailored towards specific applications.[119] Pure carbon materials, as previously mentioned, tend to display good chemical and electrochemical stability in aqueous solutions, which makes them relatively inert as electrodes.[120] There are however different strategies to modulate the intrinsic activity of carbon via the introduction of defects,[120-122] or introduction of heteroatom functionalities, for example with boron, nitrogen, sulphur or phosphorous, which have all been investigated in the electrocatalysis of a wide range of reactions of importance for energy and sustainability.

Heteroatom doping can change the electronic properties and electrical conductivity of graphitic carbon materials. Introduction of sulphur into the carbon lattice has been shown to increase electron-donor properties and the conductivity of the material.[123] Boron doping of CNTs, has been shown to change the electronic structure from semiconducting to metallic.[124] Doping with heteroatoms can further introduce adsorption sites for reactants and intermediates into the carbon. The adsorption changes are often the result of the acidity/basicity of the introduced functional sites. This has been shown for e.g. sulphur doped carbon in the adsorption of Cd^{+2} ions.[125] The authors reported on a pH effect in the adsorption, whereby increasing the pH to values above 3 the adsorbent surface is expected to have a negative charge through deprotonation, thus resulting in better adsorption of positively charged cadmium ions. Computational data of P-doping of CNTs suggests increased adsorption of acceptor molecules, like NO_2, compared to bare CNTs.[126] Nitrogen sites in carbon, e.g. pyridinic-N, can act as a Lewis base, allowing for adsorption of CO_2 by acid/-base interactions.[127]

These changes in the carbon properties make heteroatom doped carbons promising candidates for different electrocatalytic applications, like the ORR, where boron doped nanotubes[128] and P-doped xerogels[129] were shown to have good activity. An improved activity through heteroatom doping can also be seen in the HER. Zheng et al.[130] reported a computational study, lowering the Gibbs free enthalpy of hydrogen adsorption of graphene doped with N and P to 0.08 eV, from 1.85 eV for bare graphene. An improved HER activity has also been reported for boron doped graphene, by Sathe et al.[131] A similar improvement was reported for N-doped graphene;[132] Tian et al. showed that nitrogen doped graphene offers improved HER performance compared to pure graphene. Wei et al. synthesised metal free carbon materials derived from bacteria.[133] The obtained materials were reported to have large specific surface areas and contained nitrogen and phosphorus and showed improved HER performance. Similar strategies have been used for carbon nanotubes, where an improved HER activity through nitrogen doping was reported.[134]

Nitrogen doping has been more intensively studied compared to the other heteroatoms, because it is easily introduced into the carbon lattice and N-doped carbons were reported to exhibit improved electrocatalytic activity compared to pure carbon.[122, 135] This work will investigate nitrogen-doped carbons, for this reason this section will look more specifically at synthesis routes, effects of different nitrogen sites in the carbon lattice and applications in electrocatalysis.

Different routes for the synthesis of N-doped graphitic carbons have been investigated. In general, two ways are possible. Nitrogen can be introduced into the graphite lattice during synthesis of the carbon material or afterwards as a post-synthetic modification. Examples for both approaches can be found in literature. Choi et al.[136] reported a solvothermal reduction of hexachlorobenzene with pentachloro pyridine, resulting in an amorphous nitrogen doped carbon. N-doped amorphous carbon can further be synthesised by sputter deposition, introducing N_2 gas into the deposition process. This has previously been shown by our group,[114, 116, 117, 137] and will be used in this work. Adding NH_3 to the gas stream during the CVD growth of graphene and carbon nanotubes results in N-doped carbons.[135] Choosing a nitrogen containing precursor for the CVD process, for example phthalocyanine, also results in the growth of N-doped nanotubes.[138] Synthesis of porous nitrogen containing carbon materials was reported by our group, through the introduction of melamine as a nitrogen source during the synthesis of the materials.[139] Liu et al. used urea as a nitrogen source, combining it with formaldehyde to synthesise a nitrogen-

containing porous carbon. Further strategies include the generation of N-doped carbons from biomass, for example through a hydrothermal treatment of glucose with nitrogen containing molecules or proteins.[140, 141] Post-synthesis surface modifications to achieve nitrogen doping have also been investigated in the literature. Our group has previously reported nitrogenation through ammonia treatment at elevated temperatures of graphitised carbon films,[116, 117, 137] which will also be used within this work. Treatments with ammonia gas at elevated temperatures have also been reported to nitrogenate carbon black and Ketjen black.[142] Using a reactive ammonia plasma to generate nitrogen sites has been reported by the group of Duesberg, for pyrolytic carbon,[143] reduced graphene oxide,[144] and graphene.[145] Another possibility is the nitrogenation through ion bombardment which has been used effectively for mechanistic studies.[146]

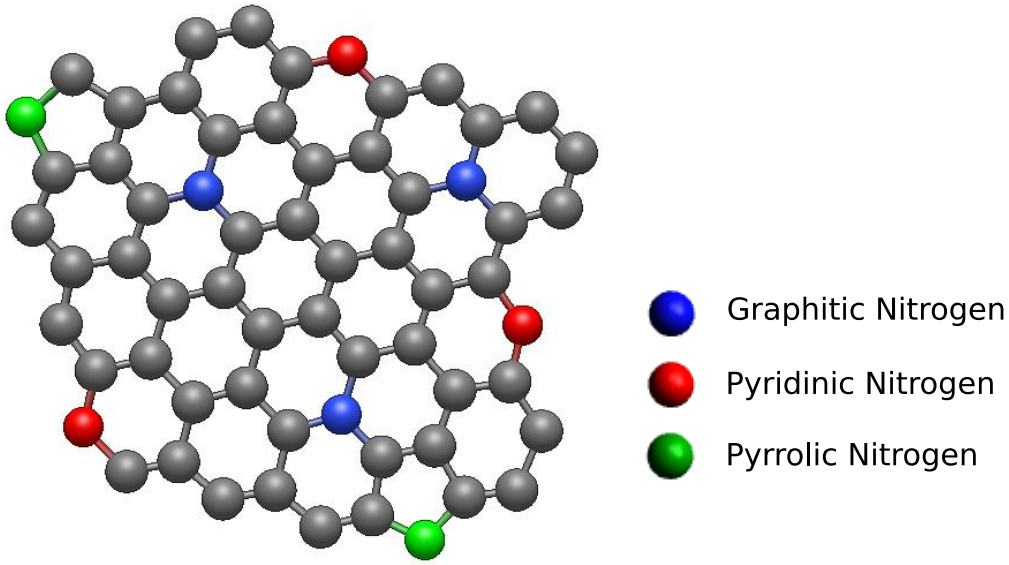

Figure 1.14 Nitrogen doped carbon lattice with graphitic (blue), pyridinic (red) and pyrrolic (green) nitrogen sites.

Within a graphitic carbon lattice, nitrogen can be present as different sites/functionalities.[135] This is shown in Figure 1.14. If a nitrogen substitutes a carbon atom within the graphene lattice, it is called graphitic ($N_{Graphitic}$) or substitutional nitrogen. A nitrogen bound to two carbons forming a six membered ring at the edge or at a vacancy in the lattice is called pyridinic ($N_{Pyridinic}$). Pyrrolic nitrogen ($N_{Pyrrolic}$), which is also present at edges and vacancies, is involved in the formation of a five-membered ring. In general, nitrogen in the graphitic lattice will lead to local increased polarity, which leads to higher wettability of the carbon and more favourable adsorption properties in comparison with bare carbons.[147] Nitrogen contains one more electron compared to carbon, which it can donate to the pi system, therefore nitrogenation processes are often observed to increase the conductivity of graphitic carbon materials. N-doped carbons have been shown to

exhibit an improved HER activity compared to nitrogen-free carbon.[122] DFT calculations have shown, that N-doped carbons have for the HER favourable hydrogen adsorption properties in contrast to bare carbon, this decrease in the Gibbs free energy of the Hydrogen adsorption has been reported by Deng et al.[148] The different nitrogen sites do however have different properties and different effects on the carbon.

Graphitic nitrogen acts as a N-dopant in the carbon lattice.[149-151] $N_{Graphitic}$ sites have a slightly positive charge, as they donate the extra electron into the π-system of the carbon.[151, 152] The slightly positive charge of the nitrogen leads to a slightly negative charge in the surrounding carbon atoms. This partial positive charge shifts their π-states from the Fermi level to higher energies, in the unoccupied region.[153] With the free electron pair that graphitic nitrogen sites possess, $N_{Graphitic}$ imparts Lewis basicity on the neighbouring carbons, allowing for adsorption of molecules through Lewis-acid/-base interactions.

If a nitrogen forms a pyridinic site, it acts similar to a p-dopant in semiconductors:[150] the nitrogen will have a slightly negative charge[152, 153] with the surrounding carbons being partially positively charged. This positive charge on the carbon leads to occupied states being bound more strongly, shifting to deeper energies from the Fermi level.[153] $N_{Pyridinic}$ has a free electron pair, thus acting as a Brønsted-base.[154] The presence of the free electron pair can be linked to increased reactivity and favourable adsorption on the $N_{Pyridinic}$ site,[154] which can be protonated/deprotonated in aqueous solutions depending on the pH. This can have an impact on the electrocatalytic activity, as previously reported by our group for the ORR.[137] Pyrrolic nitrogen on the other hand has been shown to have a nearly negligible doping effect.[150]

1.4.2.2. Carbon-supported electrocatalysts

Electrocatalyst materials are often used on a carbon support. For the hydrogen evolution reaction, Pt nanoparticles supported on carbon are the state-of-the-art catalyst.[155] Electrocatalysts based on nanomaterials offer many benefits, like a high specific surface area, many low-coordinated surface atoms and enhanced charge transfer kinetics, to name a few.[156] Metals supported on carbon are also used to investigate the ECH.[157] Andrews et al. used carbon cloth impregnated with metal nanoparticles to investigate the electrocatalytic activity of different metals.[70] The carbon does not just support the electrocatalyst and offer conductivity, it can also affect stability and activity of the

materials. Speder et al. looked at the degradation of Pt/C on Vulcan and on Ketjen black[158] and the authors found an increased stability on the Ketjen black-supported material. O'Hayre et al.[146, 159-162] investigated the stability of precious metal nanoparticles on carbon supports and reported increased stability through nitrogen modification.

Molybdenum disulphide and other 2D materials with promising electrocatalyst performances in the HER, are often used on a carbon support, by leveraging the good conductivity and, the high specific surface area of the carbon.[163] In literature, many reports look at the design and synthesis of MoS_2 on carbon for the HER,[164] and other electrocatalytic applications. MoS_2/carbon heterostructures have shown good electrocatalytic activity,[165] and will be investigated in this work for the ECH of benzaldehyde. Multiple designs and synthesis routes have been reported to obtain MoS_2/carbon heterostructures. In many of these reports, nitrogen doping was shown to have a positive effect on the growth, the stability or the electrocatalytic activity of the heterostructures.

Cao et al.[163] used a hydrothermal method growing MoS_2 nanosheets on multi-walled CNTs (MWCNT). A hydrothermal method was also used by Xiang et al.[166] to synthesise MoS_2 nanosheets on carbon cloth. Growth of MoS_2 on nitrogen doped CNTs in a wet chemical synthesis was reported by Li et al.[167] The report shows an improved growth of MoS_2 on the N-CNTs, which the authors attribute to higher wettability of the nitrogen-doped carbon and interactions between the anionic precursor and the N-dopants in the carbon. For all these materials an improved HER activity was reported. CVD methods have also been reported to grow MoS_2 on (graphitic) carbon materials. Chen et al.[168] used a process using molybdenum chloride and sulphur, to form MoS_2 on carbon nano fibres. Another CVD process was reported by Gnanasekar et al.[169] MoO_3 was used as the source of molybdenum, which reacts in the vapour phase with sulphur powder to form MoS_2 growing on a graphene substrate. By this method vertically aligned nanosheets of MoS_2 were obtained, yielding good activity in the HER. The combination of MoO_3 as the precursor and sulphur vapour produced in a second hot zone has been used by different groups to grow MoS_2 on different substrates.[170-172] This method will also be used in this work.

1.4.2.3. Carbon encapsulation

Carbon can further be used to encapsulate metals and metal nanoparticles for electrocatalytic applications. This approach has different benefits. Encapsulation of platinum can inhibit the poisoning of the metal, for example by methanol.[173] For transition metals, carbon encapsulation can increase the stability of the metal core,[174] thereby allowing the use of transition metals, like iron, in electrocatalytic applications.[175]

The increased stability of carbon encapsulated metals (M@C) is achieved through minimizing interactions between metal cores, thereby inhibiting agglomeration,[174] and/or through protecting the metal core from the ambient environment, avoiding oxidation and corrosion. This has been shown by Fronczak et al.[176] for carbon encapsulated iron particles, where the authors reported the corrosion resistance of the Fe@C particles in different acids. Stability of Ni nanoparticles encapsulated in graphene was reported by Ai et al.[177] Bao et al. investigated encapsulated nanoparticles of iron, cobalt and an alloy of the two in the ORR,[175, 178] OER[179] and the HER.[148] The authors report electrochemical stability of M@C structures in conditions, that would lead to corrosion of the bare metals. This indicates that the carbon shell protects the metal from the electrolyte, while still maintaining electrocatalytic activity.

In the HER, the carbon shell has been reported to further regulate the Gibbs free energy of hydrogen adsorption.[180] Thereby not just maintaining the electrocatalytic activity of the metal core, but increasing it through synergistic effects. This has been shown, computationally and experimentally by Bao et al.[181] The authors reported in their work a ΔG_{H^*} close to zero for encapsulated particles of a nickel cobalt alloy. This is a Gibbs free energy significantly lower than the bare carbon shell ($\Delta G_{H^*} \approx 1.3$ eV) and higher compared to the bare alloy nanoparticle ($\Delta G_{H^*} \approx -0.3$ eV). Similar results were obtained by Fei et al.[182] They investigated cobalt nanoparticles embedded in N-doped carbon and show that the heterostructured catalyst exhibits improved HER activity compared to the bare metal nanoparticle. The results were also shown by Ma et al.[183] for alloyed nanoparticles of Co, Mo and P encapsulated in carbon. In addition to stable HER in a wide range of pH values, was the synergistic effect on ΔG_{H^*} shown, through computational data. Nonetheless, there is uncertainty as to the exact role of the carbon shell in electrocatalytic processes and the exact nature of the active site in the above reactions remains highly debated, as recently discussed by Yoo et al.[184]

1.4.3. Use of model electrode systems

All these strategies and applications of carbon have been investigated and reported in electrocatalysis. This is due to the aforementioned benefits and variety of carbon materials. In many cases it is however difficult to separate changes in intrinsic activity from those contributions arising from structural modifications. CNTs are usually grown with metal catalysts,[185] and therefore a clear understanding of the activity of the carbon in contrast to the dispersed metal is difficult. As these 3D structures have high specific surface areas, increased activity attributed to the material might only be due to this increased specific area. For this reason, model electrodes are often used to deconvolute the intrinsic activity of catalyst materials from nanostructure/porosity and mass transport effects.[186]

Guo et al. used model carbon electrodes in the ORR and reported pyridinic nitrogen as the active sites for oxygen adsorption.[187] A similar approach was used by Favaro et al., using highly oriented pyrolytic graphite (HOPG) implanted with nitrogen and argon.[188] Here the authors proposed that an increased activity of the treated HOPG compared to the pristine HOPG stems from morphological and chemical changes, namely the nitrogen sites. The approach of model systems has been previously used in our group to look at the contribution of different nitrogen sites in the ORR at different pH.[137] In the work, Behan et al. found that the activity of different nitrogen sites changes with the pH, which has been linked to the pKa of the pyridinic sites.

Model systems are however not only used for carbon materials. Zhou et al. used HOPG supported platinum model electrodes to test the methanol oxidation.[159] The authors report that Pt grown on N-doped HOPG is more dispersed with smaller particle size compared to Pt grown on undoped HOPG. Further an increased activity and stability was reported in the methanol oxidation, due to the N doping. Pylypenko et al. studied the stability of Pt-Ru nanoparticles on N-doped HOPG and found an increased stability through the nitrogen doping, compared to the undoped carbon.[189, 190] In this case, the synthesis of the metal was done through sputtering and not through electrodeposition. For undoped and low-dopant concentration, changes in the metal morphology and agglomeration were found after cycling the electrodes in acidic electrolyte. The authors linked this increased stability to mitigation of migration processes of the metal through the nitrogen sites.

In addition to the investigation of chemical changes, model systems allow for investigation of mechanisms by giving controlled geometries and known mass transport effects. On flat

and relatively smooth electrodes, the influence of mass transport is known. Thus, activities observed in materials can be deconvoluted from mass transport effects. Porosity and roughness can influence the observed behaviour of electrodes. Porous electrodes of a material are known to exhibit higher capacitances and Tafel slopes compared to a smooth version of the material.[191] Because of this the observed behaviour might lead to the wrong conclusions if the exact geometries/nanostructure are not considered. This shows the benefit of using model electrode systems when designing carbon based electrocatalyst materials.

1.5. Aims of the thesis

Electrochemical technology plays a major role in the transition to a more sustainable economy. Electrocatalytic applications allow the synthesis of chemicals and fuels using renewable energy. With this the full potential of biomass as a source of energy and carbon feedstock can be unfolded. The ECH requires active electrocatalysts and many materials have been explored in the literature. In many of these materials carbon plays a crucial role.

The aim of this thesis is to explore the role carbon and carbon-based materials can play in the electrocatalytic hydrogenation of benzaldehyde. The use of model electrode geometries will allow to derive intrinsic activities of the materials. Further an understanding of the effect of different reaction conditions on the ECH activity will be built. Evaluation of materials will be done based on the selectivity, faradaic efficiency and production/reduction rate. The design of a custom made electrolysis cell will be shown as well. The materials synthesised and investigated in this thesis include:

- Nitrogen doped carbon thin films with a controlled nitrogen distribution and graphitisation, in Chapter 3.
- Molybdenum disulphide grown on the nitrogenated carbon thin films in Chapter 4.
- Copper encapsulated by amorphous carbon of varying thickness in Chapter 5.
- In Chapter 6 the annealed carbon films are used as a substrate in correlative SECCM. On the basis of two examples the benefits of the carbon films for this application is highlighted

Design and synthesis of the materials will be carried out and a comprehensive characterisation with microscopic and spectroscopic techniques will be done.

To end the thesis the conclusions and findings will be summarised, and an outlook on future work and research directions will be given. In addition, further applications of the synthesised materials will be shown.

The results of this research have in part been communicated to the scientific community through peer-review articles in well-recognised journals and through international conference presentations.

References

1. United Nations. Global Issues Population. https://www.un.org/en/global-issues/population#:~:text=The%20world%20population%20is%20projected,and%2010.4%20billion%20by%202100.
2. Our World in Data Energy consumption by source, World. https://ourworldindata.org/grapher/energy-consumption-by-source-and-country (accessed 22/11/2024).
3. European Union. Energy statistics - an overview 2024. https://ec.europa.eu/eurostat/statistics-explained/index.php?title=Energy_statistics_-_an_overview.
4. Ritchie, H.; Rosado, P., Fossil fuels. OurWorldinData.org, 2017.
5. Schraufnagel, D. E.; Balmes, J. R.; Cowl, C. T.; De Matteis, S.; Jung, S. H.; Mortimer, K.; Perez-Padilla, R.; Rice, M. B.; Riojas-Rodriguez, H.; Sood, A.; Thurston, G. D.; To, T.; Vanker, A.; Wuebbles, D. J., Air Pollution and Noncommunicable Diseases: A Review by the Forum of International Respiratory Societies' Environmental Committee, Part 2: Air Pollution and Organ Systems. *Chest* **2019,** *155* (2), 417-426.
6. Werpy, T.; Petersen, G.; Aden, A.; Bozell, J.; Holladay, J.; White, J.; Manheim, A.; Eliot, D.; Lasure, L.; Jones, S., Top Value Added Chemicals From Biomass. Volume 1 - Results of Screening for Potential Candidates From Sugars and Synthesis Gas. *US Department of Energy* **2004**, 76.
7. Gary, J. H.; Handwerk, G. E., *Petroleum Refining Technology and Economics*. Marcel Dekker, Inc.: 1984.
8. U.S. Energy Information Administration. Oil and petroleum products explained 2023. https://www.eia.gov/energyexplained/oil-and-petroleum-products/refining-crude-oil-the-refining-process.php.
9. CEFIC Petrochemical europe Essential materials for a sustainable future. https://www.petrochemistry.eu/.
10. ICIS How petrochemicals are used today. https://fta-globalassets.s3-eu-west-1.amazonaws.com/documents/forms/ppf-pdf/icis-petrochemicals-flowchart.pdf (accessed 25/11/2024).
11. Canada Energy Regulator Market Snapshot: Petrochemical products in everyday life. https://www.cer-rec.gc.ca/en/data-analysis/energy-markets/market-snapshots/2018/market-snapshot-petrochemical-products-in-everyday-life.html (accessed 25/11/2024).
12. InternationalEnergyAgency. World Energy Balances: Overview 2024. https://www.iea.org/reports/world-energy-balances-overview/world.
13. Saadatmand, M.; Gharehpetian, G. B.; Moghassemi, A.; Guerrero, J. M.; Siano, P.; Alhelou, H. H., Damping of Low-Frequency Oscillations in Power Systems by Large-Scale PV Farms: A Comprehensive Review of Control Methods. *IEEE Access* **2021,** *9*, 72183-72206.
14. Zhang, H. L.; Baeyens, J.; Degrève, J.; Cacères, G., Concentrated solar power plants: Review and design methodology. *Renewable and Sustainable Energy Reviews* **2013,** *22*, 466-481.
15. Borah, R.; Hughson, F. R.; Johnston, J.; Nann, T., On battery materials and methods. *Materials Today Advances* **2020,** *6*, 100046.
16. Placke, T.; Kloepsch, R.; Dühnen, S.; Winter, M., Lithium ion, lithium metal, and alternative rechargeable battery technologies: the odyssey for high energy density. *Journal of Solid State Electrochemistry* **2017,** *21* (7), 1939-1964.

17. Mazloomi, K.; Gomes, C., Hydrogen as an energy carrier: Prospects and challenges. *Renewable and Sustainable Energy Reviews* **2012,** *16* (5), 3024-3033.
18. Leach, F.; Kalghatgi, G.; Stone, R.; Miles, P., The scope for improving the efficiency and environmental impact of internal combustion engines. *Transportation Engineering* **2020,** *1*, 100005.
19. Albatayneh, A.; Assaf, M. N.; Alterman, D.; Jaradat, M., Comparison of the Overall Energy Efficiency for Internal Combustion Engine Vehicles and Electric Vehicles. *Environmental and Climate Technologies* **2020,** *24* (1), 669-680.
20. Bockris, J. O. M.; Ammar, I. A.; Huq, A. K. M. S., The Mechanism of the Hydrogen Evolution Reaction on Platinum, Silver and Tungsten surfaces in Acid Solutions. *The Journal of Physical Chemistry* **1957,** *61* (7), 879-886.
21. Nørskov, J. K.; Bligaard, T.; Logadottir, A.; Kitchin, J. R.; Chen, J. G.; Pandelov, S.; Stimming, U., Trends in the Exchange Current for Hydrogen Evolution. *Journal of The Electrochemical Society* **2005,** *152* (3), J23.
22. Trasatti, S., Work function, electronegativity, and electrochemical behaviour of metals: III. Electrolytic hydrogen evolution in acid solutions. *Journal of Electroanalytical Chemistry and Interfacial Electrochemistry* **1972,** *39* (1), 163-184.
23. Trasatti, S., Electrocatalysis by oxides — Attempt at a unifying approach. *Journal of Electroanalytical Chemistry and Interfacial Electrochemistry* **1980,** *111* (1), 125-131.
24. Naito, T.; Shinagawa, T.; Nishimoto, T.; Takanabe, K., Recent advances in understanding oxygen evolution reaction mechanisms over iridium oxide. *Inorganic Chemistry Frontiers* **2021,** *8* (11), 2900-2917.
25. McCrory, C. C. L.; Jung, S.; Peters, J. C.; Jaramillo, T. F., Benchmarking Heterogeneous Electrocatalysts for the Oxygen Evolution Reaction. *Journal of the American Chemical Society* **2013,** *135* (45), 16977-16987.
26. Giordano, L.; Han, B.; Risch, M.; Hong, W. T.; Rao, R. R.; Stoerzinger, K. A.; Shao-Horn, Y., pH dependence of OER activity of oxides: Current and future perspectives. *Catalysis Today* **2016,** *262*, 2-10.
27. Du, L.; Sun, Y.; You, B., Hybrid water electrolysis: Replacing oxygen evolution reaction for energy-efficient hydrogen production and beyond. *Materials Reports: Energy* **2021,** *1* (1), 100004.
28. Chen, Z.; Wei, W.; Song, L.; Ni, B.-J., Hybrid Water Electrolysis: A New Sustainable Avenue for Energy-Saving Hydrogen Production. *Sustainable Horizons* **2022,** *1*, 100002.
29. Wang, Z.; Garg, A.; Wang, L.; He, H.; Dasgupta, A.; Zanchet, D.; Janik, M. J.; Rioux, R. M.; Román-Leshkov, Y., Enhancement of Alkyne Semi-Hydrogenation Selectivity by Electronic Modification of Platinum. *ACS Catalysis* **2020,** *10* (12), 6763-6770.
30. Sauter, W.; Bergmann, O. L.; Schröder, U., Hydroxyacetone: A Glycerol-Based Platform for Electrocatalytic Hydrogenation and Hydrodeoxygenation Processes. *ChemSusChem* **2017,** *10* (15), 3105-3110.
31. Zhu, D. D.; Liu, J. L.; Qiao, S. Z., Recent Advances in Inorganic Heterogeneous Electrocatalysts for Reduction of Carbon Dioxide. *Advanced Materials* **2016,** *28* (18), 3423-3452.
32. Appel, A. M.; Bercaw, J. E.; Bocarsly, A. B.; Dobbek, H.; DuBois, D. L.; Dupuis, M.; Ferry, J. G.; Fujita, E.; Hille, R.; Kenis, P. J. A.; Kerfeld, C. A.; Morris, R. H.; Peden, C. H. F.; Portis, A. R.; Ragsdale, S. W.; Rauchfuss, T. B.; Reek, J. N. H.; Seefeldt, L. C.; Thauer, R. K.; Waldrop, G. L., Frontiers, Opportunities, and Challenges in Biochemical and Chemical Catalysis of CO2 Fixation. *Chemical Reviews* **2013,** *113* (8), 6621-6658.

33. McKendry, P., Energy production from biomass (part 1): overview of biomass. *Bioresource Technology* **2002,** *83* (1), 37-46.
34. Biswas, R.; Uellendahl, H.; Ahring, B. K., Wet Explosion: a Universal and Efficient Pretreatment Process for Lignocellulosic Biorefineries. *BioEnergy Research* **2015,** *8* (3), 1101-1116.
35. Garedew, M.; Lin, F.; Song, B.; DeWinter, T. M.; Jackson, J. E.; Saffron, C. M.; Lam, C. H.; Anastas, P. T., Greener Routes to Biomass Waste Valorization: Lignin Transformation Through Electrocatalysis for Renewable Chemicals and Fuels Production. *ChemSusChem* **2020,** *13* (17), 4214-4237.
36. U.S. Energy Information Administration. Biomass explained 2024. https://www.eia.gov/energyexplained/biomass/#:~:text=All%20biomass%20can%20be%20burned,biomass%20includes%20pyrolysis%20and%20gasification.
37. Field, C. B.; Campbell, J. E.; Lobell, D. B., Biomass energy: the scale of the potential resource. *Trends in Ecology & Evolution* **2008,** *23* (2), 65-72.
38. Pulidindi, I. N.; Kimchi, B. B.; Gedanken, A., Can cellulose be a sustainable feedstock for bioethanol production? *Renewable Energy* **2014,** *71*, 77-80.
39. Meher, L. C.; Vidya Sagar, D.; Naik, S. N., Technical aspects of biodiesel production by transesterification—a review. *Renewable and Sustainable Energy Reviews* **2006,** *10* (3), 248-268.
40. U.S. Department of Energy (DoE) *2016 BILLION-TON REPORT Advancing Domestic Resources for a Thriving Bioeconomy*; OAK RIDGE NATIONAL LABORATORY: 2016.
41. U.S. Energy Information Administration. How much gasoline does the United States consume? 2024. https://www.eia.gov/tools/faqs/faq.php?id=23&t=10#:~:text=In%202023%2C%20U.S.%20finished%20motor,U.S.%20gallons%20in%20a%20barrel).
42. U.S. Department of Energy (DoE). Alternative Fuels Data Center. https://afdc.energy.gov/fuels/properties.
43. U.S. Department of Energy (DoE) *2023 Billion-Ton Report: An Assessment of U.S. Renewable Carbon Resources*; Oak Ridge National Laboratory: 2023.
44. Lucas, F. W. S.; Grim, R. G.; Tacey, S. A.; Downes, C. A.; Hasse, J.; Roman, A. M.; Farberow, C. A.; Schaidle, J. A.; Holewinski, A., Electrochemical Routes for the Valorization of Biomass-Derived Feedstocks: From Chemistry to Application. *ACS Energy Letters* **2021,** *6* (4), 1205-1270.
45. Davies, G.; El Sheikh, A.; Collett, C.; Yakub, I.; McGregor, J., Chapter 5 - Catalytic carbon materials from biomass. In *Emerging Carbon Materials for Catalysis*, Sadjadi, S., Ed. Elsevier: 2021; pp 161-195.
46. Di Blasi, C., Modeling chemical and physical processes of wood and biomass pyrolysis. *Progress in Energy and Combustion Science* **2008,** *34* (1), 47-90.
47. Scott, D. S.; Piskorz, J., The continuous flash pyrolysis of biomass. *The Canadian Journal of Chemical Engineering* **1984,** *62* (3), 404-412.
48. Lu, X.; Gu, X., A review on lignin pyrolysis: pyrolytic behavior, mechanism, and relevant upgrading for improving process efficiency. *Biotechnology for Biofuels and Bioproducts* **2022,** *15* (1), 106.
49. Jiang, G.; Nowakowski, D. J.; Bridgwater, A. V., Effect of the Temperature on the Composition of Lignin Pyrolysis Products. *Energy & Fuels* **2010,** *24* (8), 4470-4475.
50. Czernik, S.; Bridgwater, A. V., Overview of Applications of Biomass Fast Pyrolysis Oil. *Energy & Fuels* **2004,** *18* (2), 590-598.
51. Pinheiro Pires, A. P.; Arauzo, J.; Fonts, I.; Domine, M. E.; Fernández Arroyo, A.; Garcia-Perez, M. E.; Montoya, J.; Chejne, F.; Pfromm, P.; Garcia-Perez, M., Challenges

and Opportunities for Bio-oil Refining: A Review. *Energy & Fuels* **2019,** *33* (6), 4683-4720.
52. Gu, X.; Ma, X.; Li, L.; Liu, C.; Cheng, K.; Li, Z., Pyrolysis of poplar wood sawdust by TG-FTIR and Py–GC/MS. *Journal of Analytical and Applied Pyrolysis* **2013,** *102*, 16-23.
53. Zhang, X.; Lei, H.; Chen, S.; Wu, J., Catalytic co-pyrolysis of lignocellulosic biomass with polymers: a critical review. *Green Chemistry* **2016,** *18* (15), 4145-4169.
54. Cai, J.; Rahman, M. M.; Zhang, S.; Sarker, M.; Zhang, X.; Zhang, Y.; Yu, X.; Fini, E. H., Review on Aging of Bio-Oil from Biomass Pyrolysis and Strategy to Slowing Aging. *Energy & Fuels* **2021,** *35* (15), 11665-11692.
55. Black, S.; Ferrell, J. R., Accelerated aging of fast pyrolysis bio-oil: a new method based on carbonyl titration. *RSC Advances* **2020,** *10* (17), 10046-10054.
56. Black, S.; Ferrell, J. R., III, Determination of Carbonyl Groups in Pyrolysis Bio-oils Using Potentiometric Titration: Review and Comparison of Methods. *Energy & Fuels* **2016,** *30* (2), 1071-1077.
57. Baehr, C.; Smith, G. J.; Sleeman, D.; Zevaco, T. A.; Raffelt, K.; Dahmen, N., Aldehydes and ketones in pyrolysis oil: analytical determination and their role in the aging process. *RSC Advances* **2022,** *12* (12), 7374-7382.
58. Lessard, J., Electrocatalytic Hydrogenation. In *Encyclopedia of Applied Electrochemistry*, Kreysa, G.; Ota, K.-i.; Savinell, R. F., Eds. Springer New York: New York, NY, 2014; pp 443-448.
59. Chapuzet, J. M.; Lasia, A.; Lessard, J., Electrocatalytic hydrogenation of organic compounds. *Electrocatalysis* **1998,** *155*.
60. Liu, C.; Wu, Y.; Zhao, B.; Zhang, B., Designed Nanomaterials for Electrocatalytic Organic Hydrogenation Using Water as the Hydrogen Source. *Accounts of Chemical Research* **2023,** *56* (13), 1872-1883.
61. Lopez-Ruiz, J. A.; Sanyal, U.; Egbert, J.; Gutiérrez, O. Y.; Holladay, J., Kinetic Investigation of the Sustainable Electrocatalytic Hydrogenation of Benzaldehyde on Pd/C: Effect of Electrolyte Composition and Half-Cell Potentials. *ACS Sustainable Chemistry & Engineering* **2018,** *6* (12), 16073-16085.
62. Singh, N.; Sanyal, U.; Ruehl, G.; Stoerzinger, K. A.; Gutiérrez, O. Y.; Camaioni, D. M.; Fulton, J. L.; Lercher, J. A.; Campbell, C. T., Aqueous phase catalytic and electrocatalytic hydrogenation of phenol and benzaldehyde over platinum group metals. *Journal of Catalysis* **2020,** *382*, 372-384.
63. Song, Y.; Sanyal, U.; Pangotra, D.; Holladay, J. D.; Camaioni, D. M.; Gutiérrez, O. Y.; Lercher, J. A., Hydrogenation of benzaldehyde via electrocatalysis and thermal catalysis on carbon-supported metals. *Journal of Catalysis* **2018,** *359*, 68-75.
64. Villalba, M.; del Pozo, M.; Calvo, E. J., Electrocatalytic hydrogenation of acetophenone and benzophenone using palladium electrodes. *Electrochimica Acta* **2015,** *164*, 125-131.
65. Sáez, A.; García-García, V.; Solla-Gullón, J.; Aldaz, A.; Montiel, V., Electrocatalytic hydrogenation of acetophenone using a Polymer Electrolyte Membrane Electrochemical Reactor. *Electrochimica Acta* **2013,** *91*, 69-74.
66. Lopez-Ruiz, J. A.; Andrews, E.; Akhade, S. A.; Lee, M.-S.; Koh, K.; Sanyal, U.; Yuk, S. F.; Karkamkar, A. J.; Derewinski, M. A.; Holladay, J.; Glezakou, V.-A.; Rousseau, R.; Gutiérrez, O. Y.; Holladay, J. D., Understanding the Role of Metal and Molecular Structure on the Electrocatalytic Hydrogenation of Oxygenated Organic Compounds. *ACS Catalysis* **2019,** *9* (11), 9964-9972.
67. Carroll, K. J.; Burger, T.; Langenegger, L.; Chavez, S.; Hunt, S. T.; Román-Leshkov, Y.; Brushett, F. R., Electrocatalytic Hydrogenation of Oxygenates using Earth-

Abundant Transition-Metal Nanoparticles under Mild Conditions. *ChemSusChem* **2016,** *9* (15), 1904-1910.
68. Cantu, D. C.; Padmaperuma, A. B.; Nguyen, M.-T.; Akhade, S. A.; Yoon, Y.; Wang, Y.-G.; Lee, M.-S.; Glezakou, V.-A.; Rousseau, R.; Lilga, M. A., A Combined Experimental and Theoretical Study on the Activity and Selectivity of the Electrocatalytic Hydrogenation of Aldehydes. *ACS Catalysis* **2018,** *8* (8), 7645-7658.
69. Chan-Shing, E. S.; Boucher, D.; Lessard, J., The electrochemical reduction of α-nitrocumene in a protic and basic medium on large surface area (porous) electrodes: electronation-protonation or electrocatalytic hydrogenation? *Canadian Journal of Chemistry* **1999,** *77* (5-6), 687-694.
70. Andrews, E.; Lopez-Ruiz, J. A.; Egbert, J. D.; Koh, K.; Sanyal, U.; Song, M.; Li, D.; Karkamkar, A. J.; Derewinski, M. A.; Holladay, J.; Gutiérrez, O. Y.; Holladay, J. D., Performance of Base and Noble Metals for Electrocatalytic Hydrogenation of Bio-Oil-Derived Oxygenated Compounds. *ACS Sustainable Chemistry & Engineering* **2020,** *8* (11), 4407-4418.
71. Anibal, J.; Malkani, A.; Xu, B., Stability of the ketyl radical as a descriptor in the electrochemical coupling of benzaldehyde. *Catalysis Science & Technology* **2020,** *10* (10), 3181-3194.
72. Moutet, J.-C., ELECTROCATALYTIC HYDROGENATION ON HYDROGEN-ACTIVE ELECTRODES. A REVIEW. *Organic Preparations and Procedures International* **1992,** *24* (3), 309-325.
73. Moulijn, J. A.; van Diepen, A. E.; Kapteijn, F., Catalyst deactivation: is it predictable?: What to do? *Applied Catalysis A: General* **2001,** *212* (1), 3-16.
74. Jung, N.; Cho, Y.-H.; Ahn, M.; Lim, J. W.; Kang, Y. S.; Chung, D. Y.; Kim, J.; Cho, Y.-H.; Sung, Y.-E., Methanol-tolerant cathode electrode structure composed of heterogeneous composites to overcome methanol crossover effects for direct methanol fuel cell. *International Journal of Hydrogen Energy* **2011,** *36* (24), 15731-15738.
75. Chung, D. Y.; Kim, H.-i.; Chung, Y.-H.; Lee, M. J.; Yoo, S. J.; Bokare, A. D.; Choi, W.; Sung, Y.-E., Inhibition of CO poisoning on Pt catalyst coupled with the reduction of toxic hexavalent chromium in a dual-functional fuel cell. *Scientific Reports* **2014,** *4* (1), 7450.
76. Parthasarathy, P.; Virkar, A. V., Electrochemical Ostwald ripening of Pt and Ag catalysts supported on carbon. *Journal of Power Sources* **2013,** *234*, 82-90.
77. Alemán, J. V.; Chadwick, A. V.; He, J.; Hess, M.; Horie, K.; Jones, R. G.; Kratochvíl, P.; Meisel, I.; Mita, I.; Moad, G.; Penczek, S.; Stepto, R. F. T., Definitions of terms relating to the structure and processing of sols, gels, networks, and inorganic-organic hybrid materials (IUPAC Recommendations 2007). *Pure and Applied Chemistry* **2007,** *79* (10), 1801-1829.
78. Padgett, E.; Yarlagadda, V.; Holtz, M. E.; Ko, M.; Levin, B. D. A.; Kukreja, R. S.; Ziegelbauer, J. M.; Andrews, R. N.; Ilavsky, J.; Kongkanand, A.; Muller, D. A., Mitigation of PEM Fuel Cell Catalyst Degradation with Porous Carbon Supports. *Journal of The Electrochemical Society* **2019,** *166* (4), F198.
79. Roylance, J. J.; Kim, T. W.; Choi, K.-S., Efficient and Selective Electrochemical and Photoelectrochemical Reduction of 5-Hydroxymethylfurfural to 2,5-Bis(hydroxymethyl)furan using Water as the Hydrogen Source. *ACS Catalysis* **2016,** *6* (3), 1840-1847.
80. Kwon, Y.; Birdja, Y. Y.; Raoufmoghaddam, S.; Koper, M. T. M., Electrocatalytic Hydrogenation of 5-Hydroxymethylfurfural in Acidic Solution. *ChemSusChem* **2015,** *8* (10), 1745-1751.
81. Garza, A. J.; Bell, A. T.; Head-Gordon, M., Mechanism of CO2 Reduction at Copper Surfaces: Pathways to C2 Products. *ACS Catalysis* **2018,** *8* (2), 1490-1499.

82. Kuang, Y.; Feng, G.; Li, P.; Bi, Y.; Li, Y.; Sun, X., Single-Crystalline Ultrathin Nickel Nanosheets Array from In Situ Topotactic Reduction for Active and Stable Electrocatalysis. *Angewandte Chemie International Edition* **2016,** *55* (2), 693-697.
83. Seh, Z. W.; Fredrickson, K. D.; Anasori, B.; Kibsgaard, J.; Strickler, A. L.; Lukatskaya, M. R.; Gogotsi, Y.; Jaramillo, T. F.; Vojvodic, A., Two-Dimensional Molybdenum Carbide (MXene) as an Efficient Electrocatalyst for Hydrogen Evolution. *ACS Energy Letters* **2016,** *1* (3), 589-594.
84. Cao, Y., Roadmap and Direction toward High-Performance MoS2 Hydrogen Evolution Catalysts. *ACS Nano* **2021,** *15* (7), 11014-11039.
85. Wort, C. J. H.; Balmer, R. S., Diamond as an electronic material. *Materials Today* **2008,** *11* (1), 22-28.
86. Seal, M., Applications exploiting the extreme properties of diamonds. *Materials Science and Engineering: B* **1992,** *11* (1), 167-171.
87. Shvyd'ko, Y.; Blank, V.; Terentyev, S., Diamond x-ray optics: Transparent, resilient, high-resolution, and wavefront preserving. *MRS Bulletin* **2017,** *42* (6), 437-444.
88. Kobashi, K., *Diamond films: chemical vapor deposition for oriented and heteroepitaxial growth*. Elsevier: 2010.
89. Bernal, J. D.; Bragg, W. L., The structure of graphite. *Proceedings of the Royal Society of London. Series A, Containing Papers of a Mathematical and Physical Character* **1924,** *106* (740), 749-773.
90. Dutta, A. K., Electrical Conductivity of Single Crystals of Graphite. *Physical Review* **1953,** *90* (2), 187-192.
91. Savage, R. H., Graphite Lubrication. *Journal of Applied Physics* **1948,** *19* (1), 1-10.
92. Winter, M.; Besenhard, J. O.; Spahr, M. E.; Novák, P., Insertion Electrode Materials for Rechargeable Lithium Batteries. *Advanced Materials* **1998,** *10* (10), 725-763.
93. Novoselov, K. S.; Geim, A. K.; Morozov, S. V.; Jiang, D.; Zhang, Y.; Dubonos, S. V.; Grigorieva, I. V.; Firsov, A. A., Electric Field Effect in Atomically Thin Carbon Films. *Science* **2004,** *306* (5696), 666-669.
94. Muñoz, R.; Gómez-Aleixandre, C., Review of CVD Synthesis of Graphene. *Chemical Vapor Deposition* **2013,** *19* (10-11-12), 297-322.
95. Coleman, J. N., Liquid Exfoliation of Defect-Free Graphene. *Accounts of Chemical Research* **2013,** *46* (1), 14-22.
96. Achee, T. C.; Sun, W.; Hope, J. T.; Quitzau, S. G.; Sweeney, C. B.; Shah, S. A.; Habib, T.; Green, M. J., High-yield scalable graphene nanosheet production from compressed graphite using electrochemical exfoliation. *Scientific Reports* **2018,** *8* (1), 14525.
97. Sengupta, J.; Hussain, C. M., Graphene-based field-effect transistor biosensors for the rapid detection and analysis of viruses: A perspective in view of COVID-19. *Carbon Trends* **2021,** *2*, 100011.
98. Kawai, S.; Saito, S.; Osumi, S.; Yamaguchi, S.; Foster, A. S.; Spijker, P.; Meyer, E., Atomically controlled substitutional boron-doping of graphene nanoribbons. *Nature Communications* **2015,** *6* (1), 8098.
99. Dai, H., Carbon nanotubes: opportunities and challenges. *Surface Science* **2002,** *500* (1), 218-241.
100. Kroto, H. W.; Heath, J. R.; O'Brien, S. C.; Curl, R. F.; Smalley, R. E., C60: Buckminsterfullerene. *Nature* **1985,** *318* (6042), 162-163.
101. De Jong, K. P.; Geus, J. W., Carbon Nanofibers: Catalytic Synthesis and Applications. *Catalysis Reviews* **2000,** *42* (4), 481-510.
102. Bartelmess, J.; Giordani, S., Carbon nano-onions (multi-layer fullerenes): chemistry and applications. *Beilstein Journal of Nanotechnology* **2014,** *5*, 1980-1998.

103. Srinivasan, V.; Kathiravan, A.; Kathiresan, M.; Krishnan, G.; Jhonsi, M. A., Facile synthesis of carbon nanocubes and its applications for sensing antibiotics. *Journal of Photochemistry and Photobiology A: Chemistry* **2020,** *403*, 112855.
104. Jenkins, G. M.; Kawamura, K., Structure of Glassy Carbon. *Nature* **1971,** *231* (5299), 175-176.
105. Yamaguchi, T., Galvanomagnetic properties of glassy carbon. *Carbon* **1963,** *1* (1), 47-50.
106. Uskoković, V., A historical review of glassy carbon: Synthesis, structure, properties and applications. *Carbon Trends* **2021,** *5*, 100116.
107. Benck, J. D.; Pinaud, B. A.; Gorlin, Y.; Jaramillo, T. F., Substrate Selection for Fundamental Studies of Electrocatalysts and Photoelectrodes: Inert Potential Windows in Acidic, Neutral, and Basic Electrolyte. *PLOS ONE* **2014,** *9* (10), e107942.
108. Fitzer, E.; Kochling, K.-H.; Boehm, H. P.; Marsh, H., Recommended terminology for the description of carbon as a solid (IUPAC Recommendations 1995). *Pure and Applied Chemistry* **1995,** *67* (3), 473-506.
109. Yao, L.; He, J., Recent progress in antireflection and self-cleaning technology – From surface engineering to functional surfaces. *Progress in Materials Science* **2014,** *61*, 94-143.
110. Sun, B.; Colavita, P. E.; Kim, H.; Lockett, M.; Marcus, M. S.; Smith, L. M.; Hamers, R. J., Covalent Photochemical Functionalization of Amorphous Carbon Thin Films for Integrated Real-Time Biosensing. *Langmuir* **2006,** *22* (23), 9598-9605.
111. Hamblin, D. N.; Qiu, J.; Haubold, L.; Swain, G. M., The performance of a nitrogen-containing tetrahedral amorphous carbon electrode in flow injection analysis with amperometric detection. *Analytical Methods* **2015,** *7* (11), 4481-4485.
112. Jarošová, R.; Rutherford, J.; Swain, G. M., Evaluation of a nitrogen-incorporated tetrahedral amorphous carbon thin film for the detection of tryptophan and tyrosine using flow injection analysis with amperometric detection. *Analyst* **2016,** *141* (21), 6031-6041.
113. Heikkinen, J. J.; Kaarela, T.; Ludwig, A.; Sukhanova, T.; Khakipoor, S.; Kim, S. I.; Han, J. G.; Huttunen, H. J.; Rivera, C.; Lauri, S. E.; Taira, T.; Jokinen, V.; Franssila, S., Plasma etched carbon microelectrode arrays for bioelectrical measurements. *Diamond and Related Materials* **2018,** *90*, 126-134.
114. Behan, J. A.; Stamatin, S. N.; Hoque, M. K.; Ciapetti, G.; Zen, F.; Esteban-Tejeda, L.; Colavita, P. E., Combined Optoelectronic and Electrochemical Study of Nitrogenated Carbon Electrodes. *The Journal of Physical Chemistry C* **2017,** *121* (12), 6596-6604.
115. Murphy, D. M.; Cullen, R. J.; Jayasundara, D. R.; Doyle, R. L.; Lyons, M. E. G.; Colavita, P. E., Heterogeneous Charge Transfer at the Amorphous Carbon/Solution Interface: Effect on the Spontaneous Attachment of Aryldiazonium Salts. *The Journal of Physical Chemistry C* **2013,** *117* (44), 22768-22777.
116. Behan, J. A.; Mates-Torres, E.; Stamatin, S. N.; Domínguez, C.; Iannaci, A.; Fleischer, K.; Hoque, M. K.; Perova, T. S.; García-Melchor, M.; Colavita, P. E., Untangling Cooperative Effects of Pyridinic and Graphitic Nitrogen Sites at Metal-Free N-Doped Carbon Electrocatalysts for the Oxygen Reduction Reaction. *Small* **2019,** *15* (48), 1902081.
117. Behan, J. A.; Hoque, M. K.; Stamatin, S. N.; Perova, T. S.; Vilella-Arribas, L.; García-Melchor, M.; Colavita, P. E., Experimental and Computational Study of Dopamine as an Electrochemical Probe of the Surface Nanostructure of Graphitized N-Doped Carbon. *The Journal of Physical Chemistry C* **2018,** *122* (36), 20763-20773.
118. Ferrari, A. C.; Robertson, J., Interpretation of Raman spectra of disordered and amorphous carbon. *Physical Review B* **2000,** *61* (20), 14095-14107.

119. Guo, W.; Yu, L.; Tang, L.; Wan, Y.; Lin, Y., Recent Advances in Mechanistic Understanding of Metal-Free Carbon Thermocatalysis and Electrocatalysis with Model Molecules. *Nano-Micro Letters* **2024,** *16* (1), 125.
120. Zhao, Z.; Chen, H.; Zhang, W.; Yi, S.; Chen, H.; Su, Z.; Niu, B.; Zhang, Y.; Long, D., Defect engineering in carbon materials for electrochemical energy storage and catalytic conversion. *Materials Advances* **2023,** *4* (3), 835-867.
121. Wang, W.; Shang, L.; Chang, G.; Yan, C.; Shi, R.; Zhao, Y.; Waterhouse, G. I. N.; Yang, D.; Zhang, T., Intrinsic Carbon-Defect-Driven Electrocatalytic Reduction of Carbon Dioxide. *Advanced Materials* **2019,** *31* (19), 1808276.
122. Dai, L., *Carbon-based metal-free catalysts: design and applications*. John Wiley & Sons: 2018.
123. Shaheen Shah, S.; Abu Nayem, S. M.; Sultana, N.; Saleh Ahammad, A. J.; Abdul Aziz, M., Preparation of Sulfur-doped Carbon for Supercapacitor Applications: A Review. *ChemSusChem* **2022,** *15* (1), e202101282.
124. Wirtz, L.; Rubio, A., Band structure of boron doped carbon nanotubes. *AIP Conference Proceedings* **2003,** *685* (1), 402-405.
125. Saka, C.; Teğin, İ.; Kahvecioğlu, K., Sulphur-doped carbon particles from almond shells as cheap adsorbent for efficient Cd(II) adsorption. *Diamond and Related Materials* **2023,** *131*, 109542.
126. Cruz-Silva, E.; Lopez-Urias, F.; Munoz-Sandoval, E.; Sumpter, B. G.; Terrones, H.; Charlier, J.-C.; Meunier, V.; Terrones, M., Phosphorus and phosphorus–nitrogen doped carbon nanotubes for ultrasensitive and selective molecular detection. *Nanoscale* **2011,** *3* (3), 1008-1013.
127. Kumar, K. V.; Preuss, K.; Lu, L.; Guo, Z. X.; Titirici, M. M., Effect of Nitrogen Doping on the CO2 Adsorption Behavior in Nanoporous Carbon Structures: A Molecular Simulation Study. *The Journal of Physical Chemistry C* **2015,** *119* (39), 22310-22321.
128. Cheng, Y.; Tian, Y.; Fan, X.; Liu, J.; Yan, C., Boron Doped Multi-walled Carbon Nanotubes as Catalysts for Oxygen Reduction Reaction and Oxygen Evolution Reactionin in Alkaline Media. *Electrochimica Acta* **2014,** *143*, 291-296.
129. Wu, J.; Yang, Z.; Sun, Q.; Li, X.; Strasser, P.; Yang, R., Synthesis and electrocatalytic activity of phosphorus-doped carbon xerogel for oxygen reduction. *Electrochimica Acta* **2014,** *127*, 53-60.
130. Zheng, Y.; Jiao, Y.; Li, L. H.; Xing, T.; Chen, Y.; Jaroniec, M.; Qiao, S. Z., Toward Design of Synergistically Active Carbon-Based Catalysts for Electrocatalytic Hydrogen Evolution. *ACS Nano* **2014,** *8* (5), 5290-5296.
131. Sathe, B. R.; Zou, X.; Asefa, T., Metal-free B-doped graphene with efficient electrocatalytic activity for hydrogen evolution reaction. *Catalysis Science & Technology* **2014,** *4* (7), 2023-2030.
132. Tian, Y.; Ye, Y.; Wang, X.; Peng, S.; Wei, Z.; Zhang, X.; Liu, W., Three-dimensional N-doped, plasma-etched graphene: Highly active metal-free catalyst for hydrogen evolution reaction. *Applied Catalysis A: General* **2017,** *529*, 127-133.
133. Wei, L.; Karahan, H. E.; Goh, K.; Jiang, W.; Yu, D.; Birer, Ö.; Jiang, R.; Chen, Y., A high-performance metal-free hydrogen-evolution reaction electrocatalyst from bacterium derived carbon. *Journal of Materials Chemistry A* **2015,** *3* (14), 7210-7214.
134. Davodi, F.; Tavakkoli, M.; Lahtinen, J.; Kallio, T., Straightforward synthesis of nitrogen-doped carbon nanotubes as highly active bifunctional electrocatalysts for full water splitting. *Journal of Catalysis* **2017,** *353*, 19-27.
135. Inagaki, M.; Toyoda, M.; Soneda, Y.; Morishita, T., Nitrogen-doped carbon materials. *Carbon* **2018,** *132*, 104-140.
136. Choi, C. H.; Park, S. H.; Chung, M. W.; Woo, S. I., Easy and controlled synthesis of nitrogen-doped carbon. *Carbon* **2013,** *55*, 98-107.

137. Behan, J. A.; Iannaci, A.; Domínguez, C.; Stamatin, S. N.; Hoque, M. K.; Vasconcelos, J. M.; Perova, T. S.; Colavita, P. E., Electrocatalysis of N-doped carbons in the oxygen reduction reaction as a function of pH: N-sites and scaffold effects. *Carbon* **2019,** *148*, 224-230.
138. Choi, H. C.; Park, J.; Kim, B., Distribution and Structure of N Atoms in Multiwalled Carbon Nanotubes Using Variable-Energy X-Ray Photoelectron Spectroscopy. *The Journal of Physical Chemistry B* **2005,** *109* (10), 4333-4340.
139. Iannaci, A.; Ingle, S.; Domínguez, C.; Longhi, M.; Merdrignac-Conanec, O.; Ababou-Girard, S.; Barrière, F.; Colavita, P. E., Nanoscaffold effects on the performance of air-cathodes for microbial fuel cells: Sustainable Fe/N-carbon electrocatalysts for the oxygen reduction reaction under neutral pH conditions. *Bioelectrochemistry* **2021,** *142*, 107937.
140. White, R. J.; Yoshizawa, N.; Antonietti, M.; Titirici, M.-M., A sustainable synthesis of nitrogen-doped carbon aerogels. *Green Chemistry* **2011,** *13* (9), 2428-2434.
141. Baccile, N.; Antonietti, M.; Titirici, M.-M., One-Step Hydrothermal Synthesis of Nitrogen-Doped Nanocarbons: Albumine Directing the Carbonization of Glucose. *ChemSusChem* **2010,** *3* (2), 246-253.
142. Zahoor, A.; Christy, M.; Hwang, Y. J.; Lim, Y. R.; Kim, P.; Nahm, K. S., Improved electrocatalytic activity of carbon materials by nitrogen doping. *Applied Catalysis B: Environmental* **2014,** *147*, 633-641.
143. Nolan, H.; McEvoy, N.; Keeley, G. P.; Callaghan, S. D.; McGuinness, C.; Duesberg, G. S., Nitrogen-doped pyrolytic carbon films as highly electrochemically active electrodes. *Physical Chemistry Chemical Physics* **2013,** *15* (42), 18688-18693.
144. Nolan, H.; Mendoza-Sanchez, B.; Ashok Kumar, N.; McEvoy, N.; O'Brien, S.; Nicolosi, V.; Duesberg, G. S., Nitrogen-doped reduced graphene oxide electrodes for electrochemical supercapacitors. *Physical Chemistry Chemical Physics* **2014,** *16* (6), 2280-2284.
145. McEvoy, N.; Nolan, H.; Ashok Kumar, N.; Hallam, T.; Duesberg, G. S., Functionalisation of graphene surfaces with downstream plasma treatments. *Carbon* **2013,** *54*, 283-290.
146. Wood, K. N.; O'Hayre, R.; Pylypenko, S., Recent progress on nitrogen/carbon structures designed for use in energy and sustainability applications. *Energy & Environmental Science* **2014,** *7* (4), 1212-1249.
147. Podyacheva, O. Y.; Ismagilov, Z. R., Nitrogen-doped carbon nanomaterials: To the mechanism of growth, electrical conductivity and application in catalysis. *Catalysis Today* **2015,** *249*, 12-22.
148. Deng, J.; Ren, P.; Deng, D.; Yu, L.; Yang, F.; Bao, X., Highly active and durable non-precious-metal catalysts encapsulated in carbon nanotubes for hydrogen evolution reaction. *Energy & Environmental Science* **2014,** *7* (6), 1919-1923.
149. Zhang, J.; Zhao, C.; Liu, N.; Zhang, H.; Liu, J.; Fu, Y. Q.; Guo, B.; Wang, Z.; Lei, S.; Hu, P., Tunable electronic properties of graphene through controlling bonding configurations of doped nitrogen atoms. *Scientific Reports* **2016,** *6* (1), 28330.
150. Ma, C.; Liao, Q.; Sun, H.; Lei, S.; Zheng, Y.; Yin, R.; Zhao, A.; Li, Q.; Wang, B., Tuning the Doping Types in Graphene Sheets by N Monoelement. *Nano Letters* **2018,** *18* (1), 386-394.
151. Schiros, T.; Nordlund, D.; Pálová, L.; Prezzi, D.; Zhao, L.; Kim, K. S.; Wurstbauer, U.; Gutiérrez, C.; Delongchamp, D.; Jaye, C.; Fischer, D.; Ogasawara, H.; Pettersson, L. G. M.; Reichman, D. R.; Kim, P.; Hybertsen, M. S.; Pasupathy, A. N., Connecting Dopant Bond Type with Electronic Structure in N-Doped Graphene. *Nano Letters* **2012,** *12* (8), 4025-4031.

152. Shibuya, R.; Takeyasu, K.; Guo, D.; Kondo, T.; Nakamura, J., Chemisorption of CO2 on Nitrogen-Doped Graphitic Carbons. *Langmuir* **2022,** *38* (47), 14430-14438.
153. Kondo, T.; Casolo, S.; Suzuki, T.; Shikano, T.; Sakurai, M.; Harada, Y.; Saito, M.; Oshima, M.; Trioni, M. I.; Tantardini, G. F.; Nakamura, J., Atomic-scale characterization of nitrogen-doped graphite: Effects of dopant nitrogen on the local electronic structure of the surrounding carbon atoms. *Physical Review B* **2012,** *86* (3), 035436.
154. Maldonado, S.; Morin, S.; Stevenson, K. J., Structure, composition, and chemical reactivity of carbon nanotubes by selective nitrogen doping. *Carbon* **2006,** *44* (8), 1429-1437.
155. Meier, J. C.; Galeano, C.; Katsounaros, I.; Witte, J.; Bongard, H. J.; Topalov, A. A.; Baldizzone, C.; Mezzavilla, S.; Schüth, F.; Mayrhofer, K. J. J., Design criteria for stable Pt/C fuel cell catalysts. *Beilstein Journal of Nanotechnology* **2014,** *5*, 44-67.
156. Jarju, J. J.; Figueiredo, M. C.; Kolen'ko, Y. V., Chapter 8 - Electrocatalysis using nanomaterials. In *Frontiers of Nanoscience*, Wain, A. J.; Dickinson, E. J. F., Eds. Elsevier: 2021; Vol. 18, pp 343-420.
157. Sanyal, U.; Koh, K.; Meyer, L. C.; Karkamkar, A.; Gutiérrez, O. Y., Simultaneous electrocatalytic hydrogenation of aldehydes and phenol over carbon-supported metals. *Journal of Applied Electrochemistry* **2021,** *51* (1), 27-36.
158. Speder, J.; Zana, A.; Spanos, I.; Kirkensgaard, J. J. K.; Mortensen, K.; Hanzlik, M.; Arenz, M., Comparative degradation study of carbon supported proton exchange membrane fuel cell electrocatalysts – The influence of the platinum to carbon ratio on the degradation rate. *Journal of Power Sources* **2014,** *261*, 14-22.
159. Zhou, Y.; Pasquarelli, R.; Holme, T.; Berry, J.; Ginley, D.; O'Hayre, R., Improving PEM fuel cell catalyst activity and durability using nitrogen-doped carbon supports: observations from model Pt/HOPG systems. *Journal of Materials Chemistry* **2009,** *19* (42), 7830-7838.
160. Olson, T. S.; Dameron, A. A.; Wood, K.; Pylpenko, S.; Hurst, K. E.; Christensen, S.; Bult, J. B.; Ginley, D. S.; O'Hayre, R.; Dinh, H.; Gennett, T., Enhanced Fuel Cell Catalyst Durability with Nitrogen Modified Carbon Supports. *Journal of The Electrochemical Society* **2013,** *160* (4), F389.
161. Corpuz, A. R.; Olson, T. S.; Joghee, P.; Pylypenko, S.; Dameron, A. A.; Dinh, H. N.; O'Neill, K. J.; Hurst, K. E.; Bender, G.; Gennett, T.; Pivovar, B. S.; Richards, R. M.; O'Hayre, R. P., Effect of a nitrogen-doped PtRu/carbon anode catalyst on the durability of a direct methanol fuel cell. *Journal of Power Sources* **2012,** *217*, 142-151.
162. Wood, K. N.; Christensen, S. T.; Pylypenko, S.; Olson, T. S.; Dameron, A. A.; Hurst, K. E.; Dinh, H. N.; Gennett, T.; O'Hayre, R., In situ small-angle x-ray scattering analysis of improved catalyst—support interactions through nitrogen modification. *MRS Communications* **2012,** *2* (3), 85-89.
163. Cao, J.; Zhou, J.; Zhang, Y.; Liu, X., A Clean and Facile Synthesis Strategy of MoS2 Nanosheets Grown on Multi-Wall CNTs for Enhanced Hydrogen Evolution Reaction Performance. *Scientific Reports* **2017,** *7* (1), 8825.
164. Xia, X.; Zheng, Z.; Zhang, Y.; Zhao, X.; Wang, C., Synthesis of MoS2-carbon composites with different morphologies and their application in hydrogen evolution reaction. *International Journal of Hydrogen Energy* **2014,** *39* (18), 9638-9650.
165. Murthy, A. P.; Theerthagiri, J.; Madhavan, J.; Murugan, K., Highly active MoS2/carbon electrocatalysts for the hydrogen evolution reaction – insight into the effect of the internal resistance and roughness factor on the Tafel slope. *Physical Chemistry Chemical Physics* **2017,** *19* (3), 1988-1998.

166. Xiang, Z.; Zhang, Z.; Xu, X.; Zhang, Q.; Yuan, C., MoS2 nanosheets array on carbon cloth as a 3D electrode for highly efficient electrochemical hydrogen evolution. *Carbon* **2016,** *98*, 84-89.
167. Li, D. J.; Maiti, U. N.; Lim, J.; Choi, D. S.; Lee, W. J.; Oh, Y.; Lee, G. Y.; Kim, S. O., Molybdenum Sulfide/N-Doped CNT Forest Hybrid Catalysts for High-Performance Hydrogen Evolution Reaction. *Nano Letters* **2014,** *14* (3), 1228-1233.
168. Chen, C.; Li, G.; Lu, Y.; Zhu, J.; Jiang, M.; Hu, Y.; Cao, L.; Zhang, X., Chemical vapor deposited MoS2/electrospun carbon nanofiber composite as anode material for high-performance sodium-ion batteries. *Electrochimica Acta* **2016,** *222*, 1751-1760.
169. Gnanasekar, P.; Periyanagounder, D.; Kulandaivel, J., Vertically aligned MoS2 nanosheets on graphene for highly stable electrocatalytic hydrogen evolution reactions. *Nanoscale* **2019,** *11* (5), 2439-2446.
170. Li, S.; Wang, S.; Salamone, M. M.; Robertson, A. W.; Nayak, S.; Kim, H.; Tsang, S. C. E.; Pasta, M.; Warner, J. H., Edge-Enriched 2D MoS2 Thin Films Grown by Chemical Vapor Deposition for Enhanced Catalytic Performance. *ACS Catalysis* **2017,** *7* (1), 877-886.
171. He, M.; Lei, J.; Zhou, C.; Shi, H.; Sun, X.; Gao, B., Growth of vertical MoS2 nanosheets on carbon materials by chemical vapor deposition: influence of substrates. *Materials Research Express* **2019,** *6* (11), 1150c1.
172. O'Brien, M.; McEvoy, N.; Hallam, T.; Kim, H.-Y.; Berner, N. C.; Hanlon, D.; Lee, K.; Coleman, J. N.; Duesberg, G. S., Transition Metal Dichalcogenide Growth via Close Proximity Precursor Supply. *Scientific Reports* **2014,** *4* (1), 7374.
173. Wen, Z.; Liu, J.; Li, J., Core/Shell Pt/C Nanoparticles Embedded in Mesoporous Carbon as a Methanol-Tolerant Cathode Catalyst in Direct Methanol Fuel Cells. *Advanced Materials* **2008,** *20* (4), 743-747.
174. Tavakkoli, M.; Kallio, T.; Reynaud, O.; Nasibulin, A. G.; Johans, C.; Sainio, J.; Jiang, H.; Kauppinen, E. I.; Laasonen, K., Single-Shell Carbon-Encapsulated Iron Nanoparticles: Synthesis and High Electrocatalytic Activity for Hydrogen Evolution Reaction. *Angewandte Chemie International Edition* **2015,** *54* (15), 4535-4538.
175. Deng, D.; Yu, L.; Chen, X.; Wang, G.; Jin, L.; Pan, X.; Deng, J.; Sun, G.; Bao, X., Iron Encapsulated within Pod-like Carbon Nanotubes for Oxygen Reduction Reaction. *Angewandte Chemie International Edition* **2013,** *52* (1), 371-375.
176. Fronczak, M.; Łabędź, O.; Kaszuwara, W.; Bystrzejewski, M., Corrosion resistance studies of carbon-encapsulated iron nanoparticles. *Journal of Materials Science* **2018,** *53* (5), 3805-3816.
177. Ai, L.; Tian, T.; Jiang, J., Ultrathin Graphene Layers Encapsulating Nickel Nanoparticles Derived Metal–Organic Frameworks for Highly Efficient Electrocatalytic Hydrogen and Oxygen Evolution Reactions. *ACS Sustainable Chemistry & Engineering* **2017,** *5* (6), 4771-4777.
178. Deng, J.; Yu, L.; Deng, D.; Chen, X.; Yang, F.; Bao, X., Highly active reduction of oxygen on a FeCo alloy catalyst encapsulated in pod-like carbon nanotubes with fewer walls. *Journal of Materials Chemistry A* **2013,** *1* (47), 14868-14873.
179. Cui, X.; Ren, P.; Deng, D.; Deng, J.; Bao, X., Single layer graphene encapsulating non-precious metals as high-performance electrocatalysts for water oxidation. *Energy & Environmental Science* **2016,** *9* (1), 123-129.
180. Lu, J.; Yin, S.; Shen, P. K., Carbon-Encapsulated Electrocatalysts for the Hydrogen Evolution Reaction. *Electrochemical Energy Reviews* **2019,** *2* (1), 105-127.
181. Deng, J.; Ren, P.; Deng, D.; Bao, X., Enhanced Electron Penetration through an Ultrathin Graphene Layer for Highly Efficient Catalysis of the Hydrogen Evolution Reaction. *Angewandte Chemie International Edition* **2015,** *54* (7), 2100-2104.

182. Fei, H.; Yang, Y.; Peng, Z.; Ruan, G.; Zhong, Q.; Li, L.; Samuel, E. L. G.; Tour, J. M., Cobalt Nanoparticles Embedded in Nitrogen-Doped Carbon for the Hydrogen Evolution Reaction. *ACS Applied Materials & Interfaces* **2015,** *7* (15), 8083-8087.
183. Ma, Y.-Y.; Wu, C.-X.; Feng, X.-J.; Tan, H.-Q.; Yan, L.-K.; Liu, Y.; Kang, Z.-H.; Wang, E.-B.; Li, Y.-G., Highly efficient hydrogen evolution from seawater by a low-cost and stable CoMoP@C electrocatalyst superior to Pt/C. *Energy & Environmental Science* **2017,** *10* (3), 788-798.
184. Yoo, J. M.; Shin, H.; Chung, D. Y.; Sung, Y.-E., Carbon Shell on Active Nanocatalyst for Stable Electrocatalysis. *Accounts of Chemical Research* **2022,** *55* (9), 1278-1289.
185. Meyyappan, M.; Lance, D.; Alan, C.; David, H., Carbon nanotube growth by PECVD: a review. *Plasma Sources Science and Technology* **2003,** *12* (2), 205.
186. Domínguez, C.; Behan, J. A.; Colavita, P. E., Electrocatalysis at Nanocarbons: Model Systems and Applications in Energy Conversion. In *Nanocarbon Electrochemistry*, 2020; pp 201-249.
187. Guo, D.; Shibuya, R.; Akiba, C.; Saji, S.; Kondo, T.; Nakamura, J., Active sites of nitrogen-doped carbon materials for oxygen reduction reaction clarified using model catalysts. *Science* **2016,** *351* (6271), 361-365.
188. Favaro, M.; Perini, L.; Agnoli, S.; Durante, C.; Granozzi, G.; Gennaro, A., Electrochemical behavior of N and Ar implanted highly oriented pyrolytic graphite substrates and activity toward oxygen reduction reaction. *Electrochimica Acta* **2013,** *88*, 477-487.
189. Pylypenko, S.; Queen, A.; Olson, T. S.; Dameron, A.; O'Neill, K.; Neyerlin, K. C.; Pivovar, B.; Dinh, H. N.; Ginley, D. S.; Gennett, T.; O'Hayre, R., Tuning Carbon-Based Fuel Cell Catalyst Support Structures via Nitrogen Functionalization. I. Investigation of Structural and Compositional Modification of Highly Oriented Pyrolytic Graphite Model Catalyst Supports as a Function of Nitrogen Implantation Dose. *The Journal of Physical Chemistry C* **2011,** *115* (28), 13667-13675.
190. Pylypenko, S.; Queen, A.; Olson, T. S.; Dameron, A.; O'Neill, K.; Neyerlin, K. C.; Pivovar, B.; Dinh, H. N.; Ginley, D. S.; Gennett, T.; O'Hayre, R., Tuning Carbon-Based Fuel Cell Catalyst Support Structures via Nitrogen Functionalization. II. Investigation of Durability of Pt–Ru Nanoparticles Supported on Highly Oriented Pyrolytic Graphite Model Catalyst Supports As a Function of Nitrogen Implantation Dose. *The Journal of Physical Chemistry C* **2011,** *115* (28), 13676-13684.
191. Lasia, A., Impedance of porous electrodes. *Journal of Electroanalytical Chemistry* **1995,** *397* (1), 27-33.

Chapter II

2. Experimental methods and background

This chapter will introduce the materials and methods as well as the theory behind the main techniques used in this work. Three methods were used for the synthesis of thin film materials and samples in this thesis: sputter deposition, evaporation and chemical vapour deposition (CVD). The following section provides an introduction to the basic principles underpinning these methods as a background to the specific experimental approaches used in the chapters devoted to experimental results. The majority of the results were obtained using a combination of surface spectroscopic characterization via XPS and Raman methods with results correlated then with the electrochemical performance of fabricated thin films. Therefore, section 2.3 will discuss fundamentals of XPS and Raman spectroscopy whereas section 2.4 will be devoted to key elements of electrochemical characterisation of relevance to this work.

2.1. Materials

Glassy Carbon (Sigradur) plates (2 × 1 cm) and discs (ø = 0.5 cm) were purchased from Hochtemperatur Werkstoffe GmbH. Silicon wafers and silicon dioxide wafers were purchased from MicroChemicals GmbH. Nitrogen (Oxygen Free, 99.998%) and Argon (Pureshield, 99.998%) were purchased from BOC. Ammonia was purchased from Air Products. Carbon (99.999%), titanium (Grade 2) and copper (99.99%) sputter targets were purchased from Kurt J. Lesker. All aqueous solutions were made using Millipore water. Sulphuric acid (Sigma Aldrich, 99.999%), sodium sulphate (Sigma, > 99 %), potassium hydroxide (Acros, 99.98%) benzaldehyde (Sigma Aldrich, Reagent Plus, ≥99%), ethyl acetate (Sigma Aldrich, HPLC Plus, 99.9 %) and acetophenone (Sigma Aldrich, Reagent Plus 99%) were obtained commercially and used without further purification.

2.2. Thin film deposition

2.2.1. Sample preparation

Glassy carbon (GC) was polished in a multiple step process with decreasing grades of alumina slurry (Ted Pella Inc.). This procedure has previously been published.[1] In a first step, the substrate surface was removed on sandpaper (1200 grid, 3M) with 1 µm alumina slurry. In a second step the substrates were polished to a shiny surface on nylon cloth (Buehler) with 0.3 µm slurry. After that the electrodes were polished to a mirror finish on micro cloth (Buehler) with 0.3 µm slurry and finally 0.05 µm slurry. The final polishing step was carried out just before loading the substrates into the deposition chamber or using them as bare glassy carbon substrate, to ensure a clean surface immediately before use/testing. In between the steps, the substrates were rinsed and sonicated in deionized water.

Silicon and SiO_2 wafers were cut to the required size, depending on the intended use, sonicated in methanol (Fisher, HPLC Grade) and rinsed with water. The wafers were subsequently cleaned in piranha solution (3:1 H_2SO_4:H_2O_2 CAUTION: *Piranha solution is a strong oxidant which may react explosively with organic solvents and must always be used in a fumehood*). After the piranha solution the wafers were thoroughly rinsed with deionized water and dried under nitrogen prior to loading into the deposition system.

2.2.2. Physical vapour deposition

Physical vapour deposition (PVD) is used for thin film deposition in many different fields.[2] During PVD the source material is brought into the vapour phase from a solid or liquid state. The material vapor is transported through a vacuum and deposits as a thin film on a surface.[3] Vaporization of a material can be achieved through different means, of which physical sputtering and thermal evaporation are two common techniques.[4]

2.2.2.1. Sputter deposition

Sputtering is the removing of atoms from a target surface following collision with an incident particle of the process gas.[5] The dislodged particles can deposit onto a different surface, forming a sputtered film. The impact of an incident particle can displace atoms at the target surface. This displaced atom is 'pushed' into the target, dislodging further atoms, and subsequently initiating a cascade of collisions. In this cascade, surface atoms can be dislodged with sufficient energy to overcome the surface biding energy, which will result in ejection of the atom as a sputtered atom.[4] The sputter yield (emitted atoms per incident particles) is dependent on the energy of the incident particle. If the energy is too low, there is not enough energy to dislodge any atoms. This so-called threshold is usually around 10 eV. If the energy of the incident particle is too high, > 50 keV, the incident particle moves into the target, dissipating the energy away from the surface. For thin film deposition usually incident energies in the range of 50 – 2000 eV are used, as these lead to the described sputter process.[6]

In many cases, the incident particles for sputter deposition are generated in a plasma of the inert process gas. In DC sputtering, a DC voltage is applied between the target, acting as the cathode and the grounded chamber acting as the anode. This ionizes the process gas and the positive ions are accelerated to the negatively charged target, where they initiate the sputter emission of atoms. This ion bombardment also causes the emission of secondary electrons away from the cathode, which can cause ionization of the process gas, thus maintaining the plasma.[7] If the deposition pressure is low, the ionization by secondary electrons is also low, resulting in a high electron flux to the substrate (anode) which can cause heating. If the pressure is higher, the ionization increases, but the sputtered atoms are scattered by collisions with gas molecules, lowering the deposition rate.[4] These drawbacks can be overcome by using magnetrons. The created magnetic field manipulates

the trajectories of the secondary electrons, increasing their ionization utilization even at low pressures.[4] In a circular planar magnetron, a central and a ring-shaped magnetic pole are placed behind the target. The magnetic field induces Lorentz force, leading to an electron drift in a closed loop around the circular target. This leads to a nonuniform usage of the target, with a coaxial shape around the target. A schematic of a typical DC-magnetron sputter setup is shown in Figure 2.1.

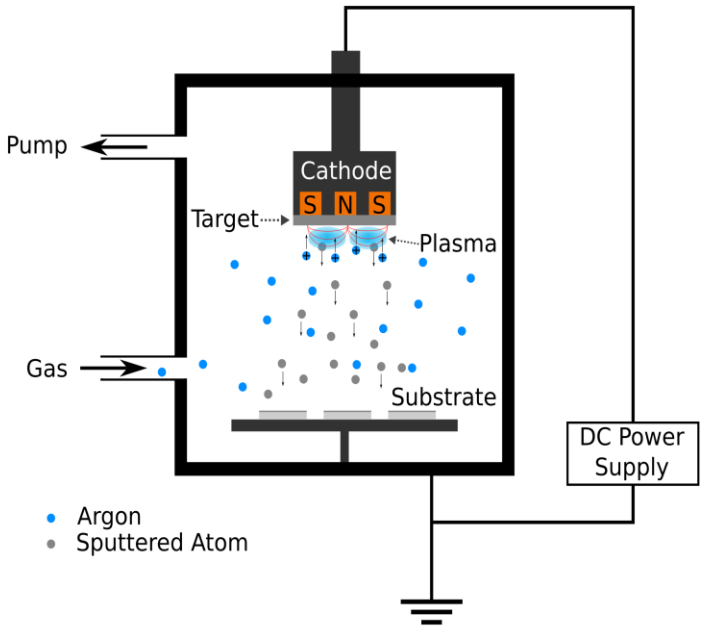

Figure 2.1 Schematic of a DC magnetron sputter chamber.

Sputtered atoms arriving at the substrate, and any other surface can condense and form a film. Sputter deposition occurs in 'line of sight', introducing shadowing effects during deposition. The influence of operation parameters on the structure and morphology of the deposited film have been summarised by Thornton in the so called structure zone model, taking into account deposition pressure and substrate temperature during the sputter deposition of metal films.[8] This model has been extended by Mahieu et al. considering also the film growth.[9]

Incident energy of the sputtered atoms can be considered in place of substrate temperature, as this energy will determine the mobility of the atom on the surface. If this incident energy is low, there is little surface mobility, and the atoms will stick where it lands. This leads to rough films, with the presence of voids due to self-shadowing effects. If deposition under these conditions is continued, it can lead to knock-on effects induced by the incoming sputtered atoms. This will lead to rough films, with less voids. Increase in the energy leads

to an increase in surface mobility of the atoms. The resulting microstructure is columnar, with grain boundaries between faceted crystallites. This occurs, as atoms can diffuse on one grain, but not from one grain to another. Further increase in the energy allows the diffusion of atoms from one grain to the other, but not yet restructuring of grain boundaries. The preferential orientation is determined by the fastest growth direction. This restructuring only occurs at even higher energies, where the preferential orientation is determined by the lowest surface energy.[4, 5, 8, 9]

The sputtering of carbon and metals used in this work was carried out in a dc-magnetron sputter deposition system (Torr international Inc.). The deposition chamber, shown in Figure 2.2, was pumped to a pressure < 2×10^{-6} mbar before deposition. For all depositions the current was set to 200 mA, allowing the system to adjust the voltage accordingly.

Figure 2.2 Sputter chamber used for deposition of carbon and metal films.

The gas flow during deposition was controlled using mass flow controllers (MFC; Brooks Instruments). For deposition of metals a gas flow of 25 sccm of Ar was used. The deposition of carbon was carried out using a total flow of 50 sccm of either pure argon, or a mixture of argon and nitrogen. The pressure during deposition was in the range of 1-2 × 10^{-2} mbar. A pre-sputter step was carried out to ensure a stable deposition rate and a fresh surface, prior to the deposition. After the deposition, the chamber was allowed to cool down before venting and unloading.

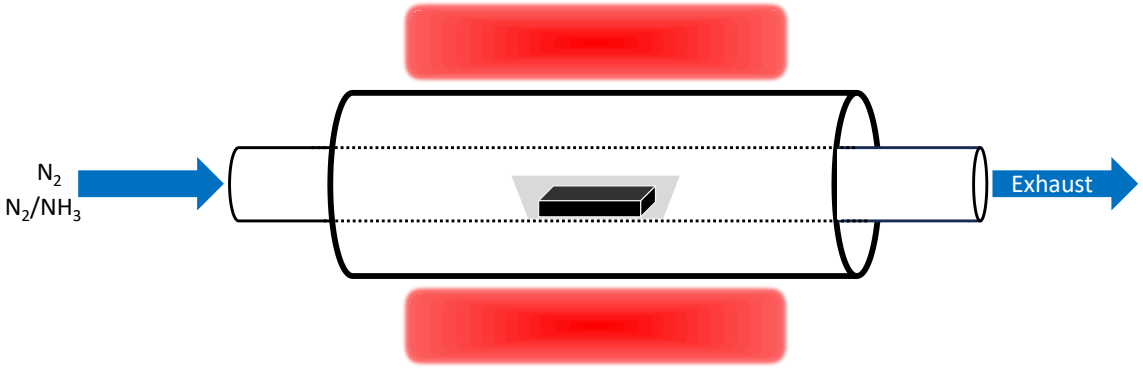

Figure 2.3 Schematic of the annealing furnace used for graphitisation of amorphous carbon films.

Amorphous carbon films were subsequently graphitised at elevated temperatures. The substrates with the deposited carbon films were placed in alumina crucibles (Almath) and placed in a quartz tube (GVB GmbH) in a furnace (Carbolite Gero). A typical setup of the annealing is shown in Figure 2.3. The annealing procedure was optimised as part of this project and is described in greater detail in chapter III. The samples were loaded and unloaded only at temperatures below 230 °C.

2.2.2.2. Electron beam evaporation

Electron-beam evaporation is a PVD technique, often used for deposition of films. The source material is heated by an electron beam . This melts and subsequently evaporates the material, which is subsequently transported away from the source, covering all surfaces in its path,[10] this is also shown in Figure **2.**2.4. As the e-beam only melts and evaporates a small portion of the material source, contaminations by interaction with the crucible can be limited.[4] The electron beam is generated using a hot filament, which is placed out of sight of the source material. This avoids any contamination from the filament. The electron beam is manipulated by the Lorentz force, induced by a magnetic field, onto the material. The process occurs in vacuum, to avoid scattering of the evaporated atoms or any reactions, as oxidation, with atmospheric gas molecules.

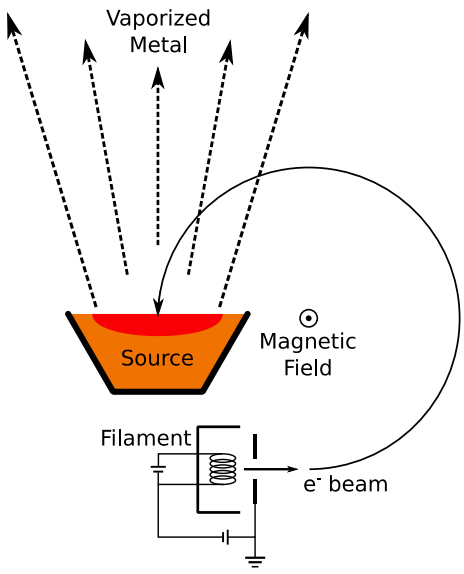

Figure 2.4 Setup for E-beam evaporation.

The deposition rate of evaporation is generally higher compared to sputter processes, with rates up to 100 nm/min.[11] Deposition of heavy and high melting point materials can be slow with sputter deposition, whereas e-beam evaporation still allows high rates of evaporation and deposition. E-beam evaporation allows good control over the deposition rate by regulating the electron beam. As evaporation occurs using a e-beam in above setup, the evaporation does not introduce any contamination into the metal, resulting in pure films.[7]

2.2.3. Chemical vapour deposition

During chemical vapour deposition (CVD) one or more precursor gases are introduced into a reactor, where they undergo a chemical reaction at elevated temperatures. This can be a reaction between two precursor materials, or the decomposition of a precursor.[12] The reaction deposits a solid material on the heated substrate surface, whereby the entire surface is covered, without any shadowing effects as in PVD.[13] In general, the growth rate is determined by the temperature of the substrate and the gas flow, which determines the residence time of the precursor. There will be a boundary layer of gas at the surface of the substrate with zero velocity according to fluid dynamics. The precursor and the reaction products are transported into this boundary layer, where the deposition will occur. This is shown in Figure 2.5. There are different ways in which CVD processes can lead to growth of films. One way is through the reaction of the precursor in the gas phase. The

intermediate products of this will diffuse into the boundary layer and onto the surface of the substrate, where the growth will occur. Another way is the transport of the precursor into the boundary layer. From there it can adsorb onto the substrate, where it reacts and deposit.[14]

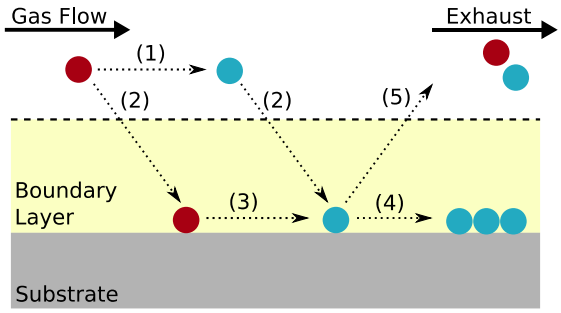

Figure 2.5 Typical reaction steps during CVD (1) gas phase reaction of the precursor (red) to the intermediate (blue), (2) Transport into the boundary layer and adsorption on the substrate, (3) surface reaction (4) surface diffusion and nucleation (film growth) and (5) desorption from the surface.

CVD processes are used for many applications and growth of many different films. CVD processes can be used to grow single crystals, polycrystals or amorphous films and even atomic single layers. CVD processes generally require high temperatures, which needs to be considered when setting up a CVD system, as it limits the choice of substrates and reactor materials.

2.3. Spectroscopic characterization

2.3.1. X-ray photoelectron spectroscopy

In X-ray photoelectron spectroscopy (XPS) the photoelectric effect is exploited to gain information about a probed sample.[15] The photoelectric effect describes the emission of electrons from a material, irradiated by photons of sufficient energy. This effect has been known since the end of the 19th century, when Hertz reported its observation[16] and Einstein gave a detailed explanation based on photons[17], although the term photon was only introduced later. The work of Hertz was based on UV radiation, but it was quickly discovered that the photoelectric effect is also present with X-rays, discovered in 1895 by Roentgen.[18] After the 2nd world war, Kai Siegbahn and others obtained the first high resolution spectra and developed the first commercial XPS system.[19-21] Today, XPS is a crucial analysis technique in physics, chemistry and material science. UV radiation can

only emit electrons from the valence band of a material and X-rays can emit electrons from the core levels of an atom. A typical XPS setup is shown in Figure 2.6.

The emitted electrons of a material are analysed by their kinetic energy (KE) in an analyser and detector. A schematic drawing of this is shown in Figure . The analyser scans over a range of KEs and only lets electrons of this defined KE pass, yielding a spectrum. The measured KE and the binding energy (BE) of an electron are related as follows:

$$\mathrm{KE} = h\nu - \mathrm{BE} - \Phi \qquad (2.1)$$

With hν being the photon energy and Φ being the spectrometer work function, which in general is constant. The binding energies of core level electrons are characteristic for an element and for the elements used in this work are typically below 1500 eV.[22] For this reason, the characteristic Al K_α radiation at 1486.7 eV ($\lambda = 0.83$ nm) is usually suited to analyse a wide range of elements. Electrons in a typical XPS energy range up to 1300 eV have an varying inelastic mean free path (IMFP) up to 20 Å, with the exact value depending on the material. This IMFP is the range from which electrons can escape without energy loss, contributing to the characteristic peak signals. Because of this, XPS is a surface sensitive technique. For a mixture of elements, the resulting spectra is approximately the sum of the individual spectra, allowing for quantification of the elements.[23] Here it is important to take the relative sensitivity factor (RSF) into account. The RSF is a value combining the IMFP, the photoemission cross section of an atom as well as the transmission function of the spectrometer,[24] thus giving a measurement of the probability of a element to eject an electron.

The elemental core binding energies are unique to an element, thus allowing the quantification of the elements in the surface of a sample.[23] Another important feature of XPS is the so called chemical shift. This is the variation of the binding energy of an element depending on the chemical environment.[25] From this shift chemical information can be extracted, for example the oxidation state or the chemical bonds of an atom. The full derivation of this is out of the scope of this work, but in general binding resulting in a partial positive charge on the emitting atom, leads to a shift to higher binding energies, as expected from an increase in the potential well depth for the ionization. The opposite effect is observed when bonding involves an increase in electron density around the emitting atomic species. Similar trends can be observed for the oxidation state, where a higher oxidation state shifts the BE to higher values.

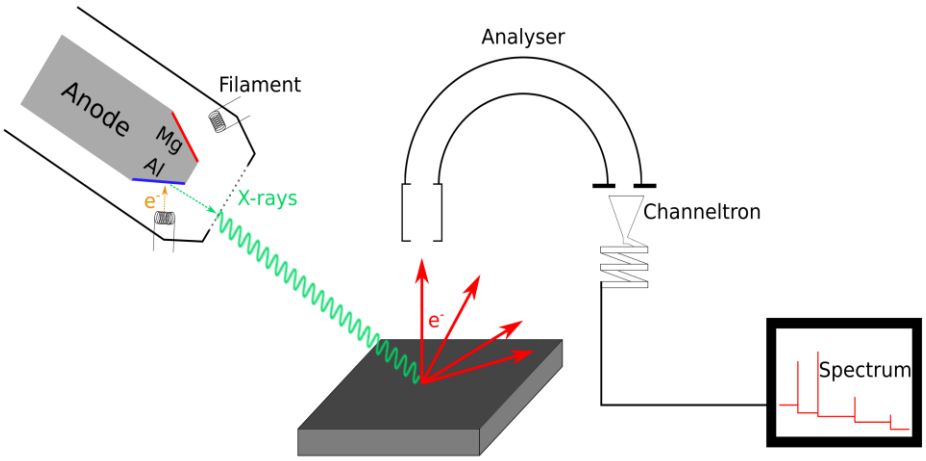

Figure 2.6 Schematic of XPS setup with X-ray source, photoelectron emission, analyser and a channeltron detector.

Elemental core level spectra of a sample are a combination of the signals of all components of an element. To get information from the measured spectra, it is necessary to deconvolute the signal into the individual contributions. When fitting the peaks, care needs to be taken in the selection of the background subtraction procedure and the line shapes and full width half maxima used. When fitting core levels with $l \geq 1$ (*p, d* etc.), spin-orbital splitting is can be observed. This splitting is approximately independent of the chemical shift, so when a doublet is observed the fitted components will be observed in both peaks. The two peaks in a doublet will exhibit defined area ratios according to the orbital splitting.[23]

In addition to the core level peaks, Auger peaks are observed in XPS spectra as well. Auger electron peaks occur, when an electron vacancy of an inner shell is filled with an electron of an outer shell. The released energy can cause the emission of another electron.[26] The Auger electron energy is independent of the incident photon and does therefore remain at a constant binding energy in a measured spectrum, as BE is calculated according to above equation.

XPS data was recorded using an Omicron ESCA system with an EA 125 analyser and XM1000MK II monochromated Al Kα X-ray source (1486.7 eV). The irradiation spot size is roughly 2 mm, which means, that all XPS data is representative of the sample surface. The spectral resolution for the core level spectra resulted to around 0.55 eV. For survey scans the pass energy of the analyser was set to 50 eV. For core level spectra the pass energy was set to 15 eV. Data analysis was done using CasaXPS software. Fitting of core levels was done using Gaussian-Lorentzian peaks and subtraction of a Shirley background.

Quantification was done using the area of the core level spectra, normalised for the relative sensitivity factor and the number of scans.

2.3.2. Raman spectroscopy

Raman spectroscopy is a spectroscopic technique used to investigate the vibrational modes of molecules and solids. This phenomenon was discovered by Sir Chandrasekhara Venkata Raman and Sir Kariamanikkam Srinivasa Krishnan in 1928.[27] Illumination of a sample with a laser, usually in the visible or near infrared region, leads to scattering of photons. An incoming photon excites the sample into a virtual energy state. Upon relaxation a photon is emitted. If the vibrational state before and after excitation and relaxation is the same, the emitted photon will have the same energy as the incident photons. This elastic scattering is called Rayleigh scattering and is the most probably process observed.[28] If the molecule relaxes into a vibrational state with higher energy, than the initial state, the emitted photon will have a lower energy, that differs from the incident one by a vibrational quantum. This inelastic scattering is called Stokes-scattering. At room temperature the majority of molecules will be in the lowest vibrational state, with only a small number in exited states. If these molecules are excited and relax to a vibrational state with lower energy, the emitted photon will have a higher energy and the process is called anti-Stokes scattering.[29] A schematic of this is shown below.

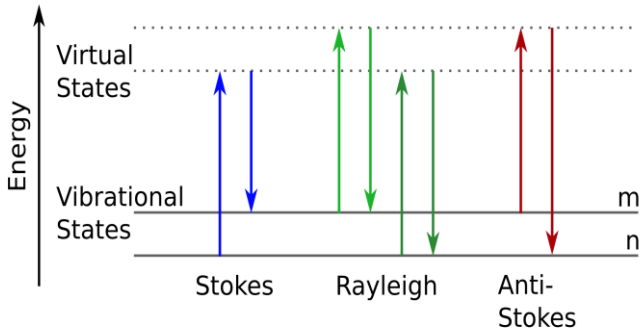

Figure 2.7 Diagram of scattering modes observed in Raman spectroscopy. Bottom vibrational state has the lowest energy, and energy increases upwards.[29]

For an excitation to be active in Raman spectroscopy, there needs to be a change in the polarizability of the molecule.[30] For a polarized electromagnetic wave the electric field (E) is fluctuating perpendicular to the direction of wave propagation. This electric field induces an electric dipole moment (P) according to the following equation.[28]

$$P = \alpha E = \alpha E_0 \cos 2\pi \nu_0 t \qquad (2.2)$$

Where α is the polarizability, E_0 the vibrational amplitude and ν_0 the frequency of the laser. When a molecule is vibrating with a frequency ν_m, the nuclear displacement q can be written as:

$$q = q_0 \cos 2\pi \nu_m t \qquad (2.3)$$

With q_0 being the vibrational amplitude. If the vibration has a small amplitude, α can be approximated as a linear function of q, using a Taylor series:

$$\alpha = \alpha_0 + \left(\frac{\partial \alpha}{\partial q}\right)_0 q_0 \ldots \qquad (2.4)$$

With α_0 being the polarizability at the equilibrium state and q being the displacement of the atoms from equilibrium positions. It needs to be mentioned, that the electric field and the dipole moment are vectors and the polarizability is a tensor, which will not be shown here for simplification. Combining (2.2), (2.3) and (2.2.4) gives:

$$P = \alpha E_0 \cos 2\pi \nu_0 t + \left(\frac{\partial \alpha}{\partial q}\right)_0 q_0 E_0 \cos 2\pi \nu_0 t \cos 2\pi \nu_m t \qquad (2.5)$$

The first part is the fluctuating dipole emitting photons with a frequency ν_0 which is the Rayleigh scattering. The second term can be rewritten, resulting in:

$$P = \alpha E_0 \cos 2\pi \nu_0 t + \frac{1}{2}\left(\frac{\partial \alpha}{\partial q}\right)_0 q_0 E_0 [\cos 2\pi(\nu_0 + \nu_m) + \cos 2\pi(\nu_0 - \nu_m)t] \qquad (2.6)$$

Here the term with (ν_0 + ν_m) is the anti-Stokes scattering and (ν_0 - ν_m) is the Stokes scattering. From this equation it can be seen, that if the change in polarizability $\left(\frac{\partial \alpha}{\partial q}\right)_0$ is zero, only Rayleigh scattering will be observed; however, for a non-zero derivative, a fraction of the scattered light will display a frequency shift relative to the incident radiation that is equivalent to the characteristic frequency of the normal vibrational mode q.

The intensity of a scattered Raman signal is generally dependent on the wavelength/frequency of the excitation wave (ν_0) and the frequency of the vibrational transition (ν_k):[31]

$$I \approx (\nu_0 \pm \nu_k)^4 \qquad (2.7)$$

As the latter is a constant for a given vibration, the intensity can only be increased by choice of the wavelength of the incident wave. Another way to increase the intensity of the Raman scattering is to tune the incident beam to be close to resonance of a vibration. Resonance occurs when the energy of the incoming or the scattered photon matches the transition energy of an allowed electronic transition.[32] This excitation to an electronic state, instead of just a virtual state, leads to intensity enhancements around 10^3 to 10^5 for a Raman band. [28, 31]

Raman spectroscopy is often used for the characterisation of graphitic carbon materials, as it can give valuable insights into the microstructure of the material.[33] The primary feature of graphitic carbon materials are the so called D and G bands, at ~ 1340 cm^{-1} and ~ 1580 cm^{-1}, respectively.[34, 35] A schematic of these vibrations is shown in Figure 2.8.

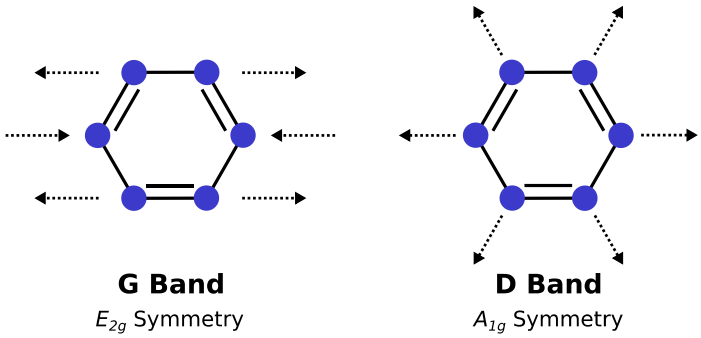

Figure 2.8 Characteristic vibration modes of graphitic carbon.

Raman scattering of carbon will always be a resonant process, as all mixtures of sp^3, sp^2 and sp^1 carbons will have a band gap between 0 and 5.5 eV.[36] This makes Raman spectroscopy a powerful tool in the characterisation of carbon materials. Carbon materials can have varying compositions of sp^2-carbon, sp^3-carbon, hydrogen and heteroatoms as discussed in chapter 1. Raman spectroscopy can be used, to obtain structural information about the investigated carbon material.[37] Figure 2.9 gives an overview of this for amorphous carbon materials.

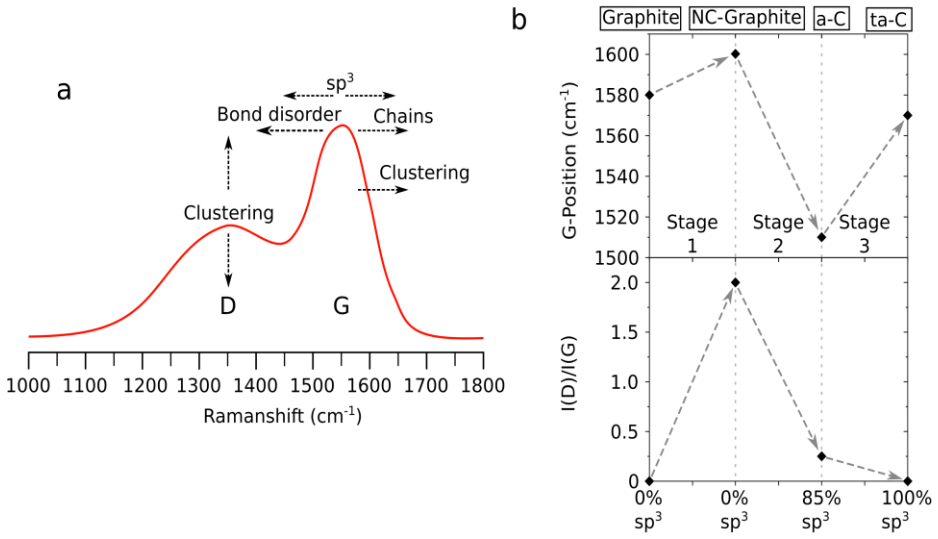

Figure 2.9 (a) Causes and effects of the main factors on the Raman spectra of amorphous carbon materials. Reproduced from Ferrari and Robertson (b) Amorphization Trajectory showing the position of the G band and the I(D)/I(G) Ratio from graphite to tetrahedral amorphous carbon.[38]

It can be seen from Figure 2.9(b), that depending on the amount of sp^3-carbon in the material, changes in the Raman spectra will be observed. The fist change is the position of the G band. The other change is the ratio of the intensity of D and G band. The amorphization trajectory states an increase in I(D)/I(G) going from graphite to nano crystalline (NC) graphite. As the D band is not observable in perfect graphite and only appears with the presence of disorder. This increase in the intensity of the D band stems from the increase on edge sites in nano crystalline graphite. With increasing sp^3-carbon content, the ratio lowers again, as there will be less presence of six membered rings. In the case of amorphous and nanocrystalline graphitic materials, the effects leading to this have been described by Ferrari and Robertson[39, 40] and are shown in Figure (a).

If the ratio of I(D)/I(G) and the sp^3 content is also known, the average crystallite size of the carbon material can be determined. The equation needed for this determination depends on the investigated carbon and where on the amorphization trajectory it lands.[41] For the region from graphite to NC-graphite, the equation needed is:

$$\frac{I(D)}{I(G)} = \frac{C(\lambda)}{L_a} \qquad (2.8)$$

And for nano crystalline graphite to amorphous carbon, the equation is:

$$\frac{I(D)}{I(G)} = C'(\lambda)L_a^2 \qquad (2.9)$$

The exact intensities for the D and G band can be obtained by deconvoluting the measured spectra. For a correct fit, the number of peaks needs to be considered. According to Ferrari, for disordered and amorphous carbon materials, four contributions are present,[36] In addition to the D and G band, two modulations around 1100 - 1200 cm^{-1} and 1400 – 1500 cm^{-1}.[38]

When investigating carbon materials, the wavelength of the laser needs to be considered, as changes in the wavelength will shift the peaks, as reported by Ferrari and Robertson.[36] The reason for the wavelength dependent shift is different for the D- and the G-band. The shift in the G-band is due to disordering in the carbon, with no shift observed for graphite. Disorder in a carbon lattice leads to different local band gaps, with clusters of wider π band gaps, and higher vibration frequencies, being selected. For the D band, the dispersion increases with increasing order in the carbon. Larger clusters in more ordered carbons will lower the band gaps, thus lowering the frequency of the breathing mode.[38, 42]

Two Raman systems were used in this work. First, a Witec alpha 300R confocal Raman spectroscopy microscope, with a 532 nm laser was used for characterisation of MoS_2/an-C:N (Chapter 5) and Cu@C (Chapter 6). This system allows scanning Raman spectroscopy with a piezoelectric sample stage. Scanning Raman allowed to measure Raman maps over areas up to 100 × 100 μm^2. The obtained Raman spectra were analysed using Witec Project 5.1. Raman spectra of carbon films in Chapter 3 were obtained with a second system, a Renishaw 1000 Microraman, with a 633 nm Helium-Neon laser excitation. Spectra were analysed using CasaXPS

2.3.3. Additional techniques

2.3.3.1. Scanning electron microscopy

Scanning electron microscopy (SEM) was carried out using a Zeiss Ultra FE SEM at 5 kV acceleration voltage. Both in-lens and secondary electron detectors were used. The relevant details accompany any SEM images presented.

2.3.3.2. Optical microscopy

Optical microscopy was performed on an Olympus DSX1000 digital microscope. A 10× objective was used for imaging. The system allowed imaging in bright field and dark field, among others.

2.3.3.3. Atomic force microscopy

Atomic force microscopy of carbon films was carried out using a Park Systems AFM to characterise the carbon topography and film thickness. Images were obtained in non-contact mode with a NCHR (Non-Contact/Tapping Mode-High Resonance Frequency-Reflex Coating) tip. Thickness determinations were carried out by preparing Si wafers that were partly masked with polymethyl methacrylate (PMMA) before deposition; after carbon sputtering, the polymer was removed in acetone leaving a step edge that allowed measurement of the sputtered layer thickness. Images were analysed using the Park Systems software XEI.

AFM of Cu@C films was performed using an Asylum Research AFM MFP-3D Stand Alone, using gold tips (NSG01/AU; NT-MDT) in non-contact mode; roughness analysis was carried out over 2×2 μm^2 regions using open software (Gwyddion).

2.3.3.4. Transmission electron microscopy

TEM was carried out using a JEOL 2100 LaB TEM with an accelerating voltage of 200 kV. Samples for TEM were prepared by delaminating the MoS_2/anC:N films from a Si wafer using a razor blade; film sections were transferred onto a gold grid (Ted Pella Inc., 200 mesh carbon film).

2.3.3.5. X-ray reflectivity

X ray reflectometry (XRR) was carried out in a PANalytical theta theta diffractometer; best-fits of XRR curves were carried out using commercial software (X'Pert Reflectivity).

2.4. Electrochemical techniques

Electrochemistry is the branch of physical chemistry concerned with the correlation between chemical and electrical effects. Electrochemical reactions involve the separation of electron- and ion transfer. The electron is transported through a (electronic) conducting phase, while the ions move through the ion-conducting electrolyte. This results in separation of oxidation and reduction of electrochemical redox reactions. Electrochemical reactions involve the charge transfer across a phase boundary, e.g. electrode and electrolyte. The theory explained in this section follows the outline of Allen J. Bard and Larry R. Faulkner in Electrochemical Methods – Fundamentals and Applications.[43]

2.4.1. Electron transfer at the electrode-electrolyte interface

According to thermodynamics, the maximum amount of non-expansion work, a reaction can perform under constant pressure and temperature, is equivalent to the Gibbs free energy of the reaction, $\Delta_R G$. Given that the potential difference is the work carried out per unit charge, the two quantities are related according to:

$$\Delta_R G = -nF \cdot \Delta E \qquad (2.10)$$

$\Delta_R G$ of a reaction is related to the change in free energy under standard conditions, $\Delta_R G^0$ according to:

$$\Delta_R G = \Delta_R G^0 + RT \cdot \ln \prod_i a_i^{\nu_i} \qquad (2.11)$$

Where R is the gas constant, T the temperature, and a_i and ν_i are the activity and stochiometric coefficients of reactants and products. The stochiometric coefficient is positive for products and negative for reactants. If the reaction is in equilibrium and all reactant and product activities are in equilibrium, $\prod_i a_i^{\nu_i} = K$, the equilibrium constant. This defines $\Delta_R G^0$ as:

$$\Delta_R G^0 = -RT\ln K \qquad (2.12)$$

With a combination of these equations, ΔE can be defined according to following equation.

$$\Delta E = -\frac{\Delta_R G}{nF} = -\frac{\Delta_R G^0}{nF} - \frac{RT}{nF} \cdot \ln \prod_i a_i^{\nu_i} = \frac{RT}{nF} \ln K - \frac{RT}{nF} \cdot \ln \prod_i a_i^{\nu_i} \qquad (2.13)$$

The above equation can be re-written in terms of the standard potential E^0 , replacing the first term in the sum and yielding the Nernst equation:

$$\Delta E = E^0 - \frac{RT}{zF} \cdot \ln \prod_i a_i^{\nu_i} \qquad (2.14)$$

In electrochemistry, the potential of the standard hydrogen electrode (SHE) is used as the universal reference. The SHE is defined as the redox potential of the half-cell reaction of protons in acid, and hydrogen gas, both with an activity of one, at a platinum electrode.

In the above description, the structure of the phase boundary has been neglected. This structure does however play a crucial role in electrochemical processes. Applying an external potential to the electrode will attract/repel charged species from the electrolyte. Different models have been developed over the years to describe the electrochemical double layer. The Helmholtz model is the simplest model, assuming a rigid double layer. This model predicts a surface capacitance independent of the applied potential, which is not in agreement with experimental values. Building on the Helmholtz model, Gouy and Chapman predicted a diffuse double layer, with a Boltzmann distribution. As this model assumes ions to be point charges, an unlimited rise in double layer capacitance would be expected for increasing electrode potentials. Otto Stern combined the two models of the electrochemical double layer. Instead of point charges, ions were given a defined extension and a solvation shell. The solvation shell determines how close and how tightly packed the counter ions can get to the interface. After that first Helmholtz layer, a diffuse double layer, according to the Gouy-Chapman model, appears. The differences in the three models, together with the change of the potential across the interface are shown below. Improved understanding and modifications on the models of the double layer continue to this day.

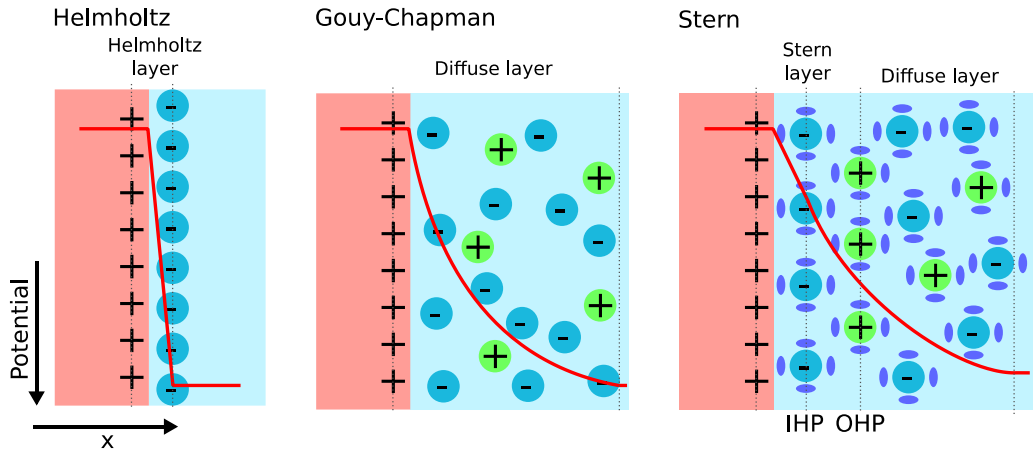

Figure 2.2 Representation of the Helmholtz, Gouy-Chapman and Stern model of the electrochemical double layer with their potential curves across the interface. (IHP: Inner Helmholtz Plane; OHP: Outer Helmholtz Plane).

When redox-active species are present in the electrolyte, electron transfer to and from the electrode and the species can take place. In an electrochemical system, the charge transfer can be controlled by the potential between the electrode and the solution, e.g. by applying an external potential. When the system is in equilibrium, there is no net-transfer of charge. Therefore $\Delta_R G = 0$ and no driving force for a chemical reaction is present. If a potential is applied to the system, the Fermi level of the electrode changes. The redox active species in the electrolyte possess gaussian distributions of donor and acceptor levels. If the Fermi level is above an acceptor level, an electron can transfer from the electrode to the redox-species. Similar when the Fermi level falls below a filled state, an electron can be transferred from solution to the electrode.[44] This is shown in Figure 2.11.

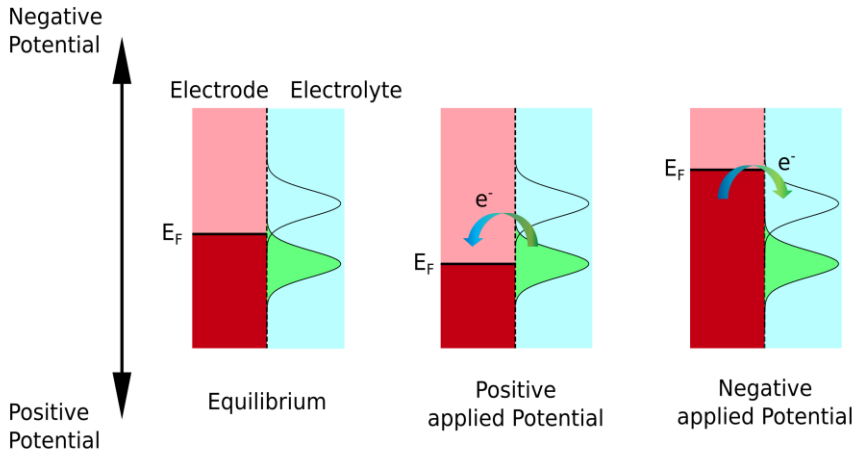

Figure 2.11 Effect of applied potential on the Fermi Level of an electrode and the resulting electron transfer process.

Assuming a one electron reaction, the equation can be written as:

$$A + e^- \rightleftharpoons B \qquad (2.15)$$

With rate constants k_c and k_a for the cathodic and the anodic reaction, respectively. Then the total current of the reaction is the sum of anodic and cathodic current:

$$j = j_a + j_c = F \cdot \left(k_a c_B(0,t) - k_c c_A(0,t)\right) \qquad (2.16)$$

Here j is the current density, c the concentration and k the rate constants for the cathodic and anodic reaction. The rate constants are dependent on the activation energy, $\Delta G^{\ddagger}$, following the Arrhenius equation and therefore on the applied potential. This can be written as:

$$\Delta G(E) = \Delta G(E_0) - \alpha_i F(E - E_0) \qquad (2.17)$$

With $\Delta G(E_0)$ being the enthalpy in equilibrium. In equilibrium the activation energy for cathodic and anodic reaction are equal, thus the rate constants will be equal too. This equilibrium constant is k_0. This results in the rate constants k_c and k_a being:

$$k_c = k_0 \exp\left(-\alpha_c \frac{F(E - E_0)}{RT}\right) \qquad (2.18)$$

$$k_a = k_0 \exp\left(\alpha_a \frac{F(E - E_0)}{RT}\right)$$

With $\alpha_c + \alpha_a = 1$. Combining this with (2.16) gives:

$$j(E) = k_0 F\left(c_B(0,t) \exp\left(\alpha_a \frac{F(E - E_0)}{RT}\right) - c_A(0,t) \exp\left(-\alpha_c \frac{F(E - E_0)}{RT}\right)\right) \qquad (2.19)$$

In equilibrium, the net current is zero, which means the anodic current is equal to the cathodic current, which is defined as the exchange current density, j_0. The exchange current densities can be written as:

$$j_a^* = F k_0 c_B^* \exp\left(\alpha_a \frac{F(E_{eq} - E_0)}{RT}\right) = j_0 \qquad (2.20)$$

An analogous expression can be derived for the cathodic current. Replacing $E - E_0 = \eta$,, i.e. the overpotential, equation 2.19 can be re-written as:

$$j(\eta) = j_0 \left(\frac{c_B(0,t)}{c_B^*} \exp\left(\alpha_a \frac{F\eta}{RT}\right) - \frac{c_A(0,t)}{c_A^*} \exp\left(-\alpha_c \frac{F\eta}{RT}\right)\right) \qquad (2.21)$$

which is known as the Butler-Volmer equation.

For high overpotentials, either the anodic or the cathodic current will be dominating. In this case $c_i^* \gg c_i(x = 0)$, which, for the cathodic case will give for equation (2.21)

$$j = j_0 \exp\left(-\alpha_c \frac{zF\eta}{RT}\right) \qquad (2.22)$$

This allows the determination of j_0 and α according to the Tafel equation:

$$\ln j = \ln j_0 + \alpha_a \frac{zF\eta}{RT} \qquad (2.23)$$

Many electrochemical techniques have been developed over the years, to derive information about the investigated system. In general, for all techniques, a potential or a

current is applied, and the resulting current or potential is measured, respectively. Here potential sweep and potential step techniques will be explained, as these are the main techniques used in this work.

2.4.2. Chrono amperometry

In potential step techniques, a potential is applied to the system, and the current response over time is recorded. This is called chrono amperometry. If a potential is chosen where a reduction occurs rapidly, no oxidised species can be present in proximity to the electrode. This leads to a high current as soon as the potential is applied. As the concentration of the oxidised species drops to almost zero in front of the electrode, a concentration gradient builds up, which leads to diffusion of species to the electrode. This leads to a diffusion front, which will grow deeper into the bulk of the electrolyte, if only diffusion is present. As the diffusion front grows, the current declines, as the mass transport to the electrode determines the current response, if the potential of the electrode is chosen cathodic enough. As the current in this case is only dependent on the diffusion of species, one can derive a quantitative formula for this. This gives the so called Cottrell equation:

$$i(t) = \frac{zFAc_0\sqrt{D}}{\sqrt{\pi t}} \qquad (2.24)$$

Where i(t) is the current, A the electrode area, D the diffusion coefficient of the redox species and t the time. A graphic representation of this is given in Figure 2.12. As the potential switches to a reductive potential, a huge current is measured, as all species in close proximity of the electrode are reduced. As the concentration gradient builds up over time, the current decreases further.

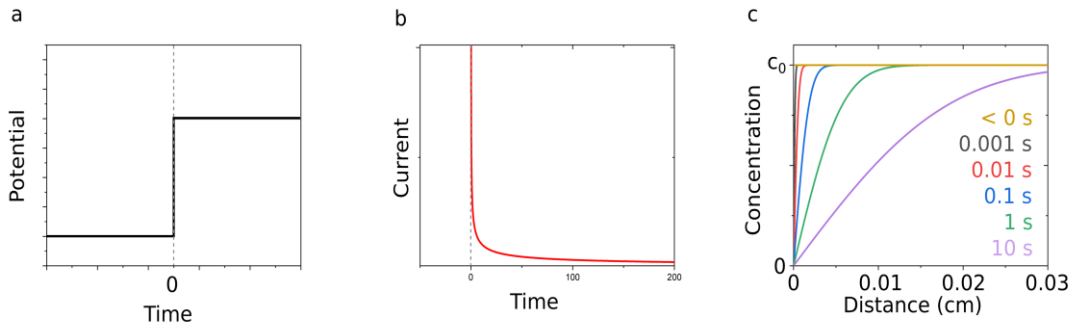

Figure 2.12(a) Potential during a chrono amperometry experiment with (b) the resulting current response and (c) the concentration profiles in front of the electrode, for a diffusion coefficient of 1×10^{-5} cm^2/s.

This effect of diffusion is important for electrodes with microscopic roughness and for electrodes active over a subsection of the area. For short times, the diffusion front will be shorter than the length scale of microroughness or the distance between active sites. As the diffusion zone grows, the length of diffusion is large compared to the length scale of electrode features. Thus, the geometric area can be used in the Cottrell equation.

2.4.3. Potential Sweep Methods

More information about an electrochemical system can be obtained by sweeping the potential with time and recording the current response. This gives a cross section through the three dimensional current-time-potential space. There are two sweep techniques which will be used in this work, linear sweep voltammetry (LSV) and cyclic voltammetry (CV). In an LSV, the potential is swept from a starting potential to an end potential. In a CV the potential is swept from a start potential to an end potential and back again. The rate with which the potential is changed is called the scan rate, ν.

If a faradaic process occurs within the potential window, a peak will be seen. The presence of peaks has multiple origins. As the potential reaches a value where a reduction or oxidation can occur, the current increases. As the potential is increased further, the surface concentration will drop to near zero, similar as was the case in chrono amperometry. Further potential increase will lead to a decreasing current and eventually a diffusion controlled current. In a CV, the sweep direction is reversed and in proximity of the electrode are now either oxidised or reduced species, depending on the direction of the first scan. So as the potential sweeps back to the starting potential, the generated species from the first scan will be reduced or oxidised. As before, at a certain point the surface concentration will be close to zero and the current is determined not by potential, but by the diffusion of the species to the electrode. Based on the peak currents and the separation of the peaks, information about reversibility can be made.

Electrochemical measurements were performed using a Metrohm Autolab potentiostat in a three-electrode setup. A jacketed cell was used to allow for temperature control using a circulator. Disc electrodes were mounted in a Teflon disc holder (Pine instruments) and plate electrodes were contacted using tantalum clips and copper tape. Graphite rods were used as counter electrode. Reference electrode in acidic and neutral conditions was an Ag/AgCl electrode (1 M KCl, CHInstruments, 0.235 V vs. NHE) and in alkaline a Hg/HgO electrode (1 M NaOH, CHInstruments, 0.14 V vs. NHE) was used. Electrolytes were

purged with N_2 for 15 min prior to electrochemical measurements. Electrolyte compositions are specified in the result section. Analysis of electrochemical data was done using OriginLab software.

2.5. Gas chromatography

Gas chromatography is widely used for separation and quantification of organic molecules. Chromatography in general is the separation of compounds between a stationary and a mobile phase. The theory explained here in this section is adapted from 'Basic Gas Chromatography' by McNair and Miller.[45] In gas chromatography the mobile phase is a carrier gas, which transports the vaporized solutes through the column, which contains the stationary phase. Based on the interactions between the solutes and the stationary phase, the time it takes to move a compound through the column will be determined. Then the solutes are brought into the detector, which analyses the gas mixture and gives quantitative results. A scheme of this is shown in Figure 2.12.

Upon injection of the compound in the inlet, the sample is vaporized and transported into the column by the carrier gas. In the column, the solute will partition between the stationary phase and the mobile phase. This distribution between two phases can be described by the partition coefficient K_P.

$$K_P = \frac{[A]_S}{[A]_M} \qquad (2.25)$$

In cases where K_P is large, the interaction between solute and the stationary phase is stronger, and the retention time of the solute will be increased. This is the basis for separation of compounds in gas chromatography. The retention times of a compound can be varied by a change in gas flow, which keeps K_P the same, but increases the volume of carrier gas. Another way is to increase the temperature, which lowers the strength of interaction between the compounds and the stationary phase.

Different ways to detect and analyse samples in gas chromatography have been developed. Here only the flame ionization detector (FID) will be explained, as this is what is used in this work. FIDs are widely used in gas chromatography systems, as they are relatively affordable and require little maintenance. They have a good detection range with good linearity. The sample with the carrier gas enter the FID body, where it is heated up, to make sure the sample remains in a gaseous state. It is mixed with hydrogen and air, to create a flammable mixture, that is combusted at a jet nozzle. If organic samples are combusted in

the flame, they are ionized. A voltage is applied between the nozzle and a collector electrode to repel and attract ionized carbon, respectively. The impact of the ions gives an electric signal, which is then amplified and turned into a signal output. FIDs can only detect organic carbon compounds. The obtained signal is approximately proportional to the amount of carbon in a molecule. Holm reported the formation of methane out of the carbons in the organic compounds in the hydrogen flame. The methane is then reduced to the methylidyne radical (HC ·) which reacts with oxygen to give CHO^+ and an electron.[46] For heteroatom bound carbons there are competing reactions, as for the alcohols, where methane can form but also CO, which would not be detected.[47] Thus, the so called effective carbon number is lower in the presence of heteroatoms.

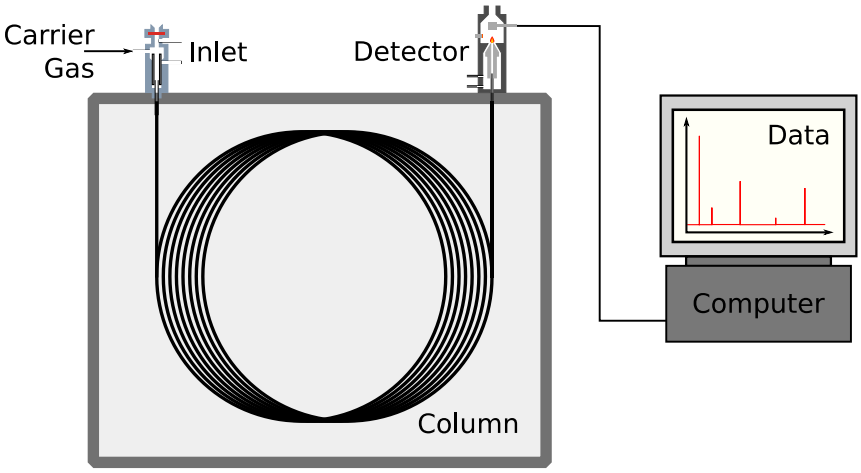

Figure 2.13 Schematic of a gas chromatography system with an FID detector.

Analysis and quantification of the electrolyte was carried out using a gas chromatography system with flame ionization detector (GC-FID, Agilent GC8860). For analysis 2 mL of the electrolyte were taken and an internal standard of acetophenone was added. The organics were extracted with 2 mL of ethyl acetate. To separate the compounds, a 2 mL/min flow of hydrogen, from a H_2 generator (VICI DBS) as carrier gas was used through the column (DB Wax, Agilent, 30 m length, 0.25 mm diameter, 0.5 µm film thickness). The FID detector was fed with hydrogen, zero air (Vici DBS) and N_2 as make-up gas. 1 µL of the organic phase was injected, using a split injection with a ratio of 10:1. The procedure consisted of three temperature regimes, starting at 150 °C after 10 min increasing to 180 °C and finally to 220 °C. Analysis was carried out using the ratio of peak areas in relation to the internal standard. From this the reactions could be quantified according to the equations given in chapter 1.

References

1. Nolan, H.; Schröder, C.; Brunet-Cabré, M.; Pota, F.; McEvoy, N.; McKelvey, K.; Perova, T. S.; Colavita, P. E., MoS2/carbon heterostructured catalysts for the hydrogen evolution reaction: N-doping modulation of substrate effects in acid and alkaline electrolytes. *Carbon* **2023,** *202*, 70-80.
2. Helmersson, U.; Lattemann, M.; Bohlmark, J.; Ehiasarian, A. P.; Gudmundsson, J. T., Ionized physical vapor deposition (IPVD): A review of technology and applications. *Thin Solid Films* **2006,** *513* (1), 1-24.
3. Mattox, D. M., *Handbook of physical vapor deposition (PVD) processing*. William Andrew: 2010.
4. Rossnagel, S. M., Thin film deposition with physical vapor deposition and related technologies. *Journal of Vacuum Science & Technology A* **2003,** *21* (5), S74-S87.
5. Depla, D.; Mahieu, S.; Greene, J. E., Chapter 5 - Sputter Deposition Processes. In *Handbook of Deposition Technologies for Films and Coatings (Third Edition)*, Martin, P. M., Ed. William Andrew Publishing: Boston, 2010; pp 253-296.
6. Mahan, J. E.; Vantomme, A., A simplified collisional model of sputtering in the linear cascade regime. *Journal of Vacuum Science & Technology A* **1997,** *15* (4), 1976-1989.
7. Mattox, D. M., Physical vapor deposition (PVD) processes. *Metal Finishing* **1999,** *97* (1, Supplement 1), 417-430.
8. Thornton, J. A., Influence of apparatus geometry and deposition conditions on the structure and topography of thick sputtered coatings. *Journal of Vacuum Science and Technology* **1974,** *11* (4), 666-670.
9. Mahieu, S.; Ghekiere, P.; Depla, D.; De Gryse, R., Biaxial alignment in sputter deposited thin films. *Thin Solid Films* **2006,** *515* (4), 1229-1249.
10. Harsha, K. S., *Principles of vapor deposition of thin films*. Elsevier: 2005.
11. Wang, Z.; Zhang, Z., Electron Beam Evaporation Deposition. In *Advanced Nano Deposition Methods*, 2016; pp 33-58.
12. Creighton, J.; Ho, P., Introduction to chemical vapor deposition (CVD). *ASM International* **2001,** *407*.
13. Martin, P., *Handbook of deposition technologies for films and coatings: science, applications and technology*. Elsevier: 2009.
14. Sun, L.; Yuan, G.; Gao, L.; Yang, J.; Chhowalla, M.; Gharahcheshmeh, M. H.; Gleason, K. K.; Choi, Y. S.; Hong, B. H.; Liu, Z., Chemical vapour deposition. *Nature Reviews Methods Primers* **2021,** *1* (1), 5.
15. Hollander, J. M.; Jolly, W. L., X-ray photoelectron spectroscopy. *Accounts of chemical research* **1970,** *3* (6), 193-200.
16. Hertz, H., Ueber einen Einfluss des ultravioletten Lichtes auf die electrische Entladung. *Annalen der Physik* **1887,** *267* (8), 983-1000.
17. Einstein, A., Über einen die Erzeugung und Verwandlung des Lichtes betreffenden heuristischen Gesichtspunkt. *Annalen der Physik* **1905,** *322* (6), 132-148.
18. Röntgen, W. C., Über eine neue Art von Strahlen (Erste Mittheilung). *Ann. Phys.(Berl.)* **1898,** *300*, 1-11.
19. Nordling, C.; Sokolowski, E.; Siegbahn, K., Precision Method for Obtaining Absolute Values of Atomic Binding Energies. *Physical Review* **1957,** *105* (5), 1676-1677.
20. Siegbahn, K., Electron spectroscopy for atoms, molecules, and condensed matter. *Reviews of Modern Physics* **1982,** *54* (3), 709-728.
21. Siegbahn, K.; Edvarson, K., β-Ray spectroscopy in the precision range of 1 : 105. *Nuclear Physics* **1956,** *1* (8), 137-159.

22. DeVault, D., A method of teaching the electronic structure of the atom. I. Elementary presentation. *Journal of Chemical Education* **1944,** *21* (11), 526.
23. Chastain, J.; King Jr, R. C., Handbook of X-ray photoelectron spectroscopy. *Perkin-Elmer Corporation* **1992,** *40*, 221.
24. Shallenberger, J. R.; Smith, N. J.; Banerjee, J., Derivation of empirical XPS relative sensitivity factors from silicate glasses. *Surface and Interface Analysis* **2021,** *53* (6), 569-579.
25. Watts, J. F., X-ray photoelectron spectroscopy. *Surface science techniques* **1994,** *45* (5).
26. Bruin, M. d., Glossary of terms used in nuclear analytical chemistry (Provisional). *Pure and Applied Chemistry* **1982,** *54* (8), 1533-1554.
27. Raman, C. V.; Krishnan, K. S., A New Type of Secondary Radiation. *Nature* **1928,** *121* (3048), 501-502.
28. Ferraro, J. R.; Nakamptp, K.; Brown, C. W., *Introductory Raman Spectroscopy*. 2003.
29. Smith, E.; Dent, G., *Modern Raman Spectroscopy – A Practical Approach*. Wiley: 2004.
30. Keresztury, G.; Chalmers, J.; Griffith, P., Raman spectroscopy: theory. *Handbook of vibrational spectroscopy* **2002,** *1*, 71-87.
31. Strommen, D. P.; Nakamoto, K., Resonance raman spectroscopy. *Journal of Chemical Education* **1977,** *54* (8), 474.
32. Thomsen, C.; Reich, S., Double Resonant Raman Scattering in Graphite. *Physical Review Letters* **2000,** *85* (24), 5214-5217.
33. Ferrari, A. C.; Robertson, J., Raman spectroscopy in carbons: from nanotubes to diamond-preface. ROYAL SOC LONDON 6 CARLTON HOUSE TERRACE, LONDON SW1Y 5AG, ENGLAND: 2004; Vol. 362, pp 2269-2270.
34. Schuepfer, D. B.; Badaczewski, F.; Guerra-Castro, J. M.; Hofmann, D. M.; Heiliger, C.; Smarsly, B.; Klar, P. J., Assessing the structural properties of graphitic and non-graphitic carbons by Raman spectroscopy. *Carbon* **2020,** *161*, 359-372.
35. Ferrari, A. C.; Robertson, J., Raman Signature of Bonding and Disorder in Carbons. *MRS Online Proceedings Library* **1999,** *593* (1), 299-304.
36. Ferrari, A. C.; Robertson, J., Resonant Raman spectroscopy of disordered, amorphous, and diamondlike carbon. *Physical Review B* **2001,** *64* (7), 075414.
37. Ferrari, A. C., Determination of bonding in diamond-like carbon by Raman spectroscopy. *Diamond and Related Materials* **2002,** *11* (3), 1053-1061.
38. Ferrari, A. C.; Robertson, J., Interpretation of Raman spectra of disordered and amorphous carbon. *Physical Review B* **2000,** *61* (20), 14095-14107.
39. Ferrari, A. C.; Robertson, J., Raman spectroscopy of amorphous, nanostructured, diamond–like carbon, and nanodiamond. *Philosophical Transactions of the Royal Society of London. Series A: Mathematical, Physical and Engineering Sciences* **2004,** *362* (1824), 2477-2512.
40. Ferrari, A. C.; Rodil, S. E.; Robertson, J., Interpretation of infrared and Raman spectra of amorphous carbon nitrides. *Physical Review B* **2003,** *67* (15), 155306.
41. Ferrari, A. C., Raman spectroscopy of graphene and graphite: Disorder, electron–phonon coupling, doping and nonadiabatic effects. *Solid State Communications* **2007,** *143* (1), 47-57.
42. Matthews, M. J.; Pimenta, M. A.; Dresselhaus, G.; Dresselhaus, M. S.; Endo, M., Origin of dispersive effects of the Raman D band in carbon materials. *Physical Review B* **1999,** *59* (10), R6585-R6588.
43. Bard, A. J.; Faulkner, L. R., *Electrochemical Methods: Fundamentals and Applications*. 2nd ed.; John Wiley & Sons: New York, 2001.

44. Memming, R., Electron Transfer Theories. In *Semiconductor Electrochemistry*, 2015; pp 127-168.
45. McNair, H. M.; Millner, J. M., *Basic Gas Chromatography*. Wiley -VCH: New York, 1997.
46. Holm, T.; Madsen, J. Ø., Methane Formation by Flame-Generated Hydrogen Atoms in the Flame Ionization Detector. *Analytical Chemistry* **1996,** *68* (20), 3607-3611.
47. Holm, T., Mechanism of the flame ionization detector II. Isotope effects and heteroatom effects. *Journal of Chromatography A* **1997,** *782* (1), 81-86.

Chapter III

3. Nitrogenated carbon thin films

The results presented in this chapter have in part been published in peer-reviewed journals in the following articles:

Hugo Nolan, **Christian Schröder**, Marc Brunet Cabré, Filippo Pota, Neill McEvoy, Kim McKelvey, Tatiana S. Perova, Paula E. Colavita: "MoS_2/carbon heterostructured catalysts for the hydrogen evolution reaction: N-doping modulation of substrate effects in acid and alkaline electrolytes", Carbon, **2023**, 202, 70-80.

Marc Brunet Cabré, **Christian Schröder**, Filippo Pota, Maida A. Costa de Oliveira, Hugo Nolan, Lua Henderson, Laurence Brazel, Dahnan Spurling, Valeria Nicolosi, Pietro Martinuz, Mariangela Longhi, Faidra Amargianou, Peer Bärmann, Tristan Petit, Kim McKelvey, Paula E. Colavita: "Carbon Thin-Film Electrodes as High-Performing Substrates for Correlative Single Entity Electrochemistry", Small Methods, **2024**, 2400639.

For both papers I led the development and the synthesis of the annealed carbon films and collaborated closely with the first authors.

3.1. Introduction

Metal-free carbon materials are gaining increased attention as electrocatalytic materials for different reactions.[1] These reactions include the ORR, the OER, the HER and hydrogenation reactions, like the CO_2RR. The growing interest in metal-free carbon is due to the importance of discovering sustainable and cost-effective alternatives to precious metal catalysts. Carbon-based materials, such as graphene, carbon nanotubes, and porous carbon, offer several advantages, including high electrical conductivity, good (electro)chemical stability, and abundant availability. Their tuneable electronic properties, for example through the incorporation of nitrogen into the carbon lattice plays a crucial role in enhancing the catalytic performance, as it introduces new active sites and modifies the electronic structure of the carbon material.

In Chapter 1 the role of nitrogenated carbon materials in electrocatalysis was discussed and different synthetic routes were outlined. The introduction of nitrogen into carbon structures has been shown to improve their activity and performance. As the demand for sustainable hydrogenation processes grows, nitrogenated carbons present an exciting avenue for reducing reliance on precious metals, providing an environmentally friendly and cost-effective alternative.

For applications in the HER, nitrogen doping of graphitic carbon materials has yielded promising results. Computational data has shown that N-doping modulates ΔG_{H*}, allowing for better performance.[2] This activity in the HER suggests that nitrogenation might also open routes to impart activity in the ECH, as a supply of adsorbed hydrogen at the electrode surface needs to be ensured for this reaction to be sustained. Indeed, electrocatalytic hydrogenation should be possible at potentials for which the HER occurs; this was supported by the work of Koper et al.,[3] who showed a correlation between the onset potential of the HER with potentials for which ECH products were observed. This activity towards the generation of H_{ads}, has also been employed in the reduction of CO_2 using N-doped carbon materials.[1, 4-7] However, there are only limited studies on the ECH of complex organic molecules at N-doped metal-free carbon electrodes. In many of these studies, graphitic nanostructures like CNTs or graphene are used, which makes it difficult to separate the intrinsic activity of the material from structural and mass transport effects, such as those arising from increased specific surface areas. A further issue is the reported

presence of metal impurities in many carbon nanostructures[8-11] due to their synthetic route, and that can lead to a wrong assessment of the electrocatalytic activity of the material.

In this chapter, a truly metal-free synthesis of nitrogenated carbons will be used to generate model thin film electrodes with well-defined area and geometry. The synthesis route enables the control of the graphitisation and the nitrogenation of the carbon materials, which in turn allows for investigation of the effect of different nitrogen functionalities on the ECH. As there are limited studies on this reaction on metal-free carbons, this chapter can give a base for future research in this field.

3.2. Synthesis and characterisation

3.2.1. Carbon thin film deposition and characterisation

Amorphous carbon thin films were synthesised using dc-magnetron sputtering, according to previously reported procedures.[12] Briefly, carbon thin films were deposited in a dc-magnetron sputtering chamber (Torr international, Inc.). The base pressure before sputtering was $< 2 \times 10^{-6}$ mbar. The sputtering was done using either pure Ar or a mixture of N_2/Ar (by flow) to deposit amorphous carbon (a-C) and nitrogenated amorphous carbon (a-C:N), respectively. The content of nitrogen in the gas flow was varied from 2% to 10%, resulting in a-C:N-X, where X indicates the percentage of nitrogen in the gas flow. The total gas flow was set to 50 sccm in both cases, using mass flow controllers (Brook Instruments). The resulting pressure during the deposition was in the range $1\text{-}2 \times 10^{-2}$ mbar; the deposition protocol consisted of a pre-sputtering step of 20 min to ensure a stable deposition rate, followed by a 40 min deposition step onto the desired substrate. The sputter chamber was cooled down before venting and unloading.

The roughness and thickness of the two films was analysed using AFM. The height profile of a 1×1 μm^2 area of the a-C and the a-C:N-2 are shown in Figure 3.1. A thickness of 73 ± 3 nm was measured after 40 min deposition of a-C, whereas a thickness 88 ± 2 nm was measured for a-C:N-2. The RMS roughness was measured at 1.6 nm for both a-C and a-C:N-2.

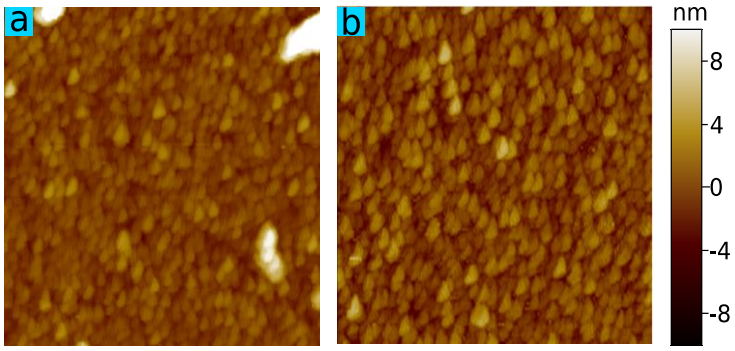

Figure 3.1 AFM images over a 1×1 μm^2 area for (a) a-C (b) a-C:N-2. (z scale valid for all images).

The chemical composition of the as-deposited carbon films was investigated using XPS. Survey spectra for as deposited amorphous carbon films, Figure a, show the presence of C 1s (≈ 285 eV), N 1s (≈ 400 eV) and O 1s (≈ 530 eV) core excitations. In the a-C film no signal for nitrogen was detected. Quantification of the atomic composition was done using the high-resolution spectra of the core levels and results are summarised in Table 3.1. Both films show a similar oxygen content. This oxygen is most likely a result of air exposure of reactive sites after deposition as well as of water adsorption, as shown for other sputtered carbons.[13] The 2% nitrogen in the process gas yields 10% of nitrogen in the sputtered film. For the C 1s peak six components were used to obtain the best fit. The main components are sp^2 and sp^3 carbon at *ca.* 284.4 eV and 285 eV, respectively. As nitrogen-bound carbon overlaps with oxygen bound carbons,[14] the deconvolution only considered the resolution of C-O (*ca.* 286.7 eV), C=O (*ca.* 288 eV) and COOH (*ca.* 289.2 eV) species. The final high binding energy component is assigned to the π-π* interaction (*ca.* 290.5 eV).[15] This is summarised in Table 3.1. The relative proportion of sp^2 carbon provides information on the graphitisation. It can be seen that the presence of nitrogen in the carbon structure lowers the amount of sp^2 carbon from 54.4 % to 42.2 %. This comes with an increase of sp^3 carbon from 25.1 % to 29.2 %, suggesting that the incorporation of nitrogen in the carbon lowers the level of graphitisation of the carbon.

For the deconvolution of the N 1s spectrum, three contributions were considered, graphitic, pyrrolic and pyridinic nitrogen at 400.8 eV, 400 eV and 398.5 eV, respectively.[12] The nitrogen in the sputtered carbon film mainly occupies edge sites, with only 19.4 % of the nitrogen being graphitic; 48.4 % of the nitrogen is present at pyridinic sites and 32.2 % at pyrrolic sites. The low amount of graphitic nitrogen does again indicate a lower level of graphitisation and high defect concentration due to nitrogen incorporation.

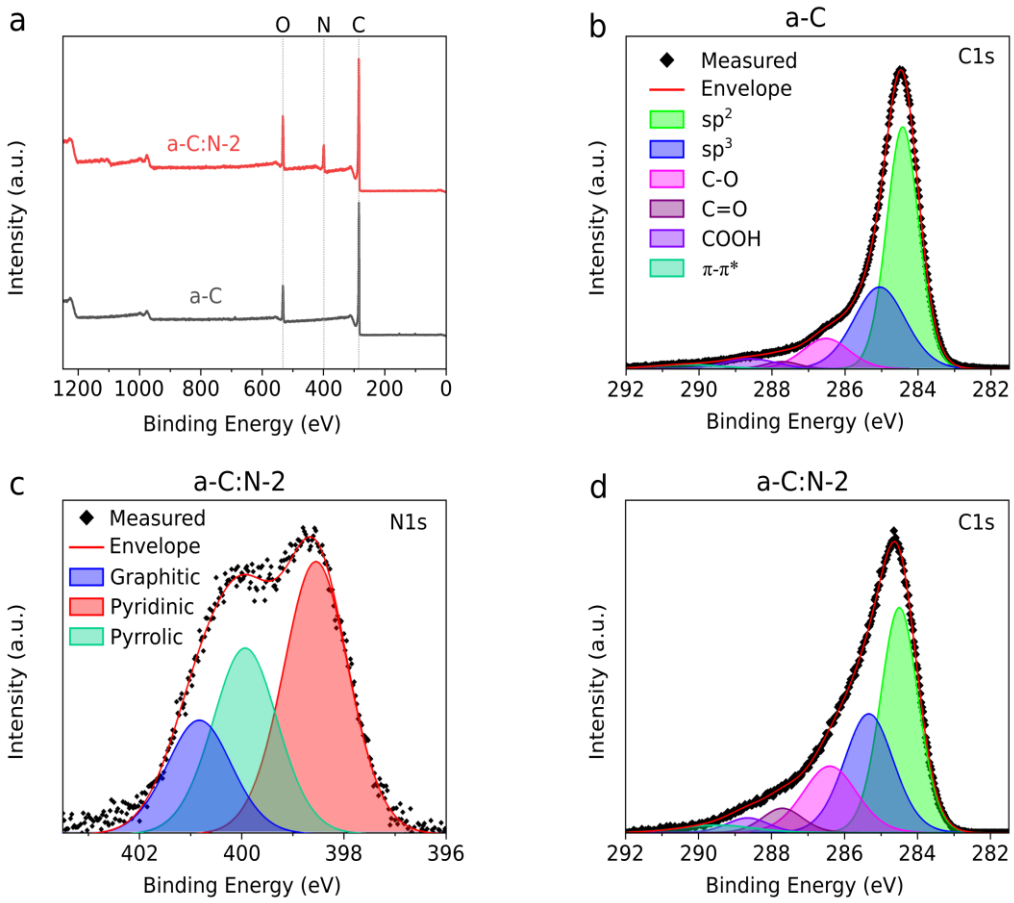

Figure 3.2 (a) XPS survey spectra, normalised to the intensity of the C 1s peak, of a-C and a-C:N-2. High resolution core level spectra with best fits of (b) C 1s of a-C film, (c) N 1s and (d) C 1s of a-C:N-2 film.

Table 3.1 Atomic composition of the as deposited films obtained from core level spectra.

	C					**N**	**O**
	%	**sp^2**	**sp^3**	**COs**	**π-π***	**%**	**%**
a-C	88.9					-	11.1
		53.5	29.2	15.2	2.1		
a-C:N-2	78.9					10	11.1
		42.2	29.2	28.6	2.8		

The electrocatalytic activity of the amorphous carbon films in the HER is poor. There is no control over the nitrogen distribution in the film, as even higher proportions of nitrogen in the deposition process would only change the N content but not the distribution of functionalities. For this reason, the amorphous films were graphitised using an annealing setup.

3.2.2. Annealing and Characterisation of nitrogenated carbon films

The pre-existing setup for the annealing led to partial edging of the carbon films. Therefore, a new annealing procedure was developed for the work in this thesis. This new setup and protocol improved reproducibility, homogeneity and partial etching of annealed films compared with the prior protocols. The upgraded annealing furnace is shown in Figure 3.3; the setup consisted of a 25 mm O.D. quartz tube connected to gas inlet/outlets via compression fittings, so that all couplings were stainless steel KF or Swagelok type. Gas tubing was upgraded to high purity copper and an inline gas filter (Restek, Triple Filter) was installed to remove moisture and oxygen residues from the annealing gas, yielding nominal gas purity > N6.

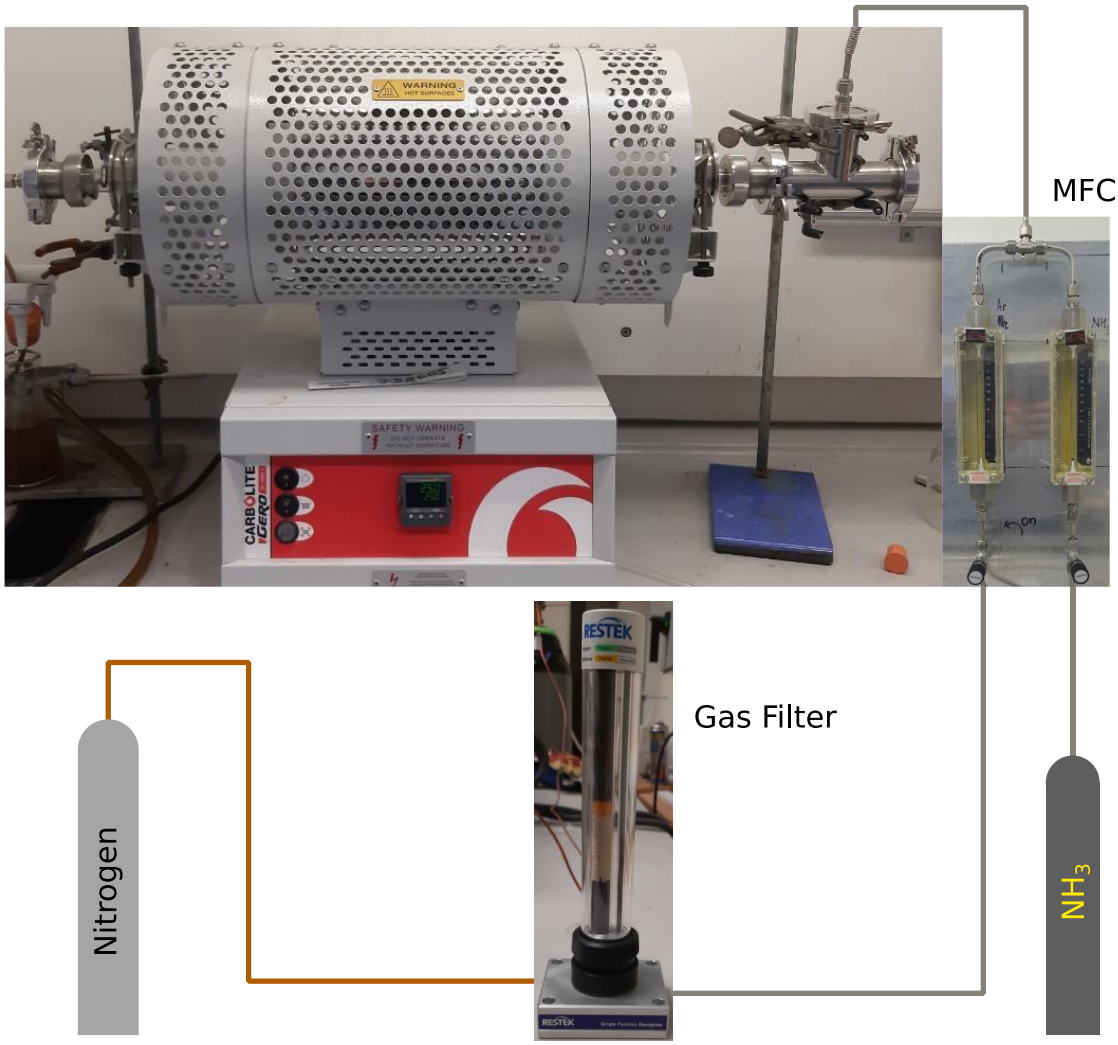

Figure 3.3 Annealing setup used in this work. Updated with Gas Filter, stainless steel KF and Swagelok fitting.

In addition to the upgrade of the setup, a new annealing protocol was developed. A key step in the optimised procedure consisted of a high temperature pre-bake of the furnace under high purity gas flow conditions. Briefly, prior to any annealing experiments the tube was heated to 900°C under inert gas flow (≈ 200 mL/min N_2); this allowed moisture/oxygen and other impurities dissolved in the quartz solid matrix to thoroughly degas from the tube prior to sample introduction. After the "pre-anneal" the furnace was cooled down to 230°C under high purity gas flow for loading of samples. If the furnace was not used for longer period of times, or a fresh tube was used, the "pre-anneal" was repeated twice before annealing, as this was found to ensure reliability.

After loading of the sample, the furnace was kept at 230°C for at least 15 min before ramping up to the annealing temperature of 900°C, unless otherwise mentioned. The temperature ramp was set to be 10°C/min. The temperature was kept for 1 h when annealing nitrogenated carbon films or if carbon without any nitrogen was wanted. Amorphous carbon was also annealed for one hour at 900°C under the flow of nitrogen (≈ 200 mL/min) followed by 30 min in NH_3/N_2 mixture (≈ 100 mL/min each). After 30 min, pure nitrogen was allowed to flush the system for 10 min before letting the system cool down to 230°C before unloading the samples. The temperature profiles and gas flows are graphically shown in the Appendix. The nomenclature for the carbon films used in this work is summarised in Table 3.2.

Table 3.2 Nomenclature used for the carbon films in this work, together with their deposition and annealing conditions.

	Sputter Conditions	**Annealing Conditions**
a-C	50 sccm Ar	n.a.
a-C:N-2	49 sccm Ar + 1 sccm N_2	n.a.
an-C	50 sccm Ar	1 h @ 900°C with 200 mL/min N_2
an-C:N$_{Graphitic}$	49 sccm Ar + 1 sccm N_2	1 h @ 900°C with 200 mL/min N_2
an-C:N$_{Pyridinic}$	50 sccm Ar	1 h @ 900°C with 200 mL/min N_2 0.5 h @ 900°C with N_2/NH_3 (100 mL/min each) 10 min @ 900°C with 200 mL/min N_2
an-C:N$_{Mixed}$	49 sccm Ar + 1 sccm N_2	1 h @ 700°C with 200 mL/min N_2

Atomic force microscopy was used to obtain roughness and thickness information of the carbon films. Figure 3.4 shows AFM images for the annealed carbon thin films on a Si wafer. After annealing, film roughness was found to decrease to <1.5 nm. Table 3.3 summarises the roughness and thickness values for the annealed films.

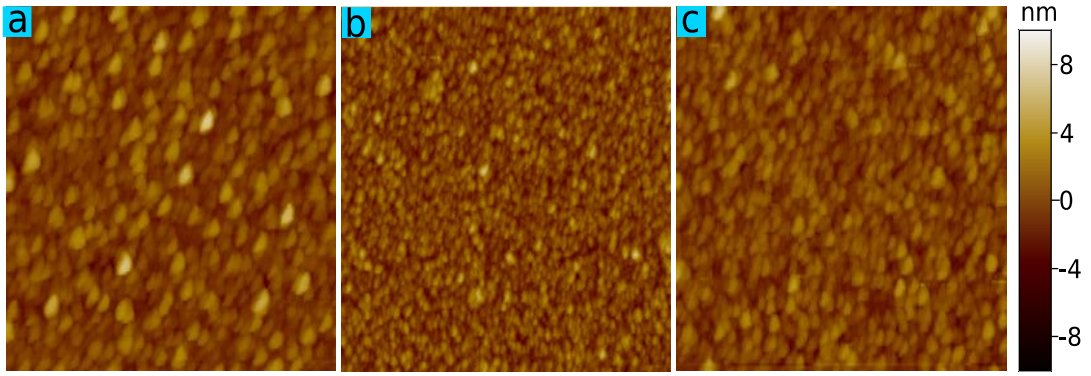

Figure 3.4 AFM images over a 1×1 μm^2 area for (a) an-C:$N_{Pyridinic}$ (b) an-C:$N_{Graphitic}$ and (c) an-C:N_{Mixed}. (z scale valid for all images).

The thickness of the annealed films was found to be in the range of 60-80 nm. The lowest %-contraction was observed for an-C:N_{Mixed} with only 8% followed by an-C:$N_{Pyridinic}$ and an-C:$N_{Graphitic}$ with 11% and 26%, respectively. The smaller shrinkage of the an-C:N_{Mixed} compared to the two films annealed at 900°C suggests a less graphitised film resulting from the lower annealing temperature. Both of the nitrogenated films annealed at 900°C were found to have a similar thickness of 65 ± 1 nm after the annealing suggesting similar degrees of graphitisation. The shrinking for all three films is minor relative to the sputtered precursor film while the roughness does not increase, thus showing that the sputtering-annealing synthesis procedure yields continuous and smooth carbon films.

Table 3.3 Thickness and Roughness values obtained from AFM of the carbon films after different annealing procedures.

	Thickness **nm**	**Shrinkage** [a] **%**	**RMS Roughness** **nm**
an-C	83 ± 1	-	0.7
an-C:$N_{Pyridinic}$	65 ± 1	11	1.4
an-C:$N_{Graphitic}$	65 ± 1	26	1.3
an-C:N_{Mixed}	81 ± 1	8	1.3

[a] Shrinkage in relation to the as-deposited film

The a-C film was annealed at 900°C using the N_2/NH_3 mixture. The nitrogenated sputtered film was annealed under nitrogen atmosphere at 900°C and 700°C. The XPS survey spectra of these films are shown in Figure 3.5. As before, the presence of carbon and oxygen is shown while nitrogen is evident in all three films. The XPS spectra for an-C can be found in the Appendix, as this film is mostly shown for completeness.

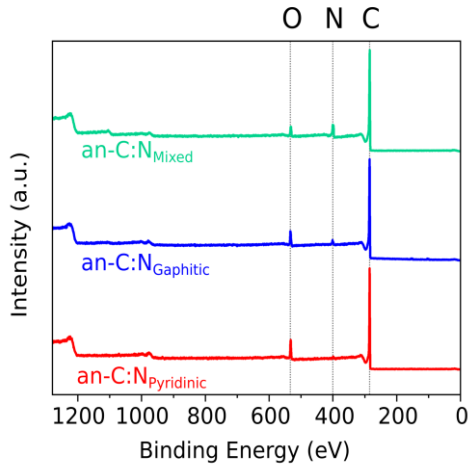

Figure 3.5 XPS survey spectra, normalised to the intensity of the C 1s peak, of annealed nitrogenated carbon films.

The chemical composition was determined using the core level spectra and the summarised data are shown in Table 3.4. It can be seen that in all three nitrogenated films a similar carbon atomic content was found while oxygen content was lower than for the as deposited films. The nitrogen amount in the an-C:N_{Mixed} is >5% higher than in the an-C:$N_{Graphitic}$. The lowest amount of nitrogen was found in the an-C:$N_{Pyridinic}$. The lower oxygen content in the annealed films compared to the as deposited films indicates that oxidized groups are burnt off, with oxygen remaining after annealing due to exposure of air/water vapour during sample handling.

Table 3.4 Atomic composition (in atomic %) obtained from core level spectra for nitrogenated carbon films.

	C %	**O %**	**N %**
an-C	97.8	2.2	-
an-C:$N_{Pyridinic}$	90.3	8.3	1.4
an-C:$N_{Graphitic}$	92.1	4.9	3
an-C:N_{Mixed}	87.1	4.1	8.8

The nitrogen content found for an-C:N_{Mixed} and an-C:$N_{Graphitic}$ were found to be lower compared to a-C:N-2. This indicates that during the annealing some of the nitrogen in the film burns off. This is supported by the fact that an-C:N_{Mixed} contains almost three times the amount of nitrogen compared to an-C:$N_{Graphitic}$. Best fits of the core levels were obtained the same way as for the as-deposited carbon films. This is shown in Figure 3.6 and the obtained data is summarised in Table 3.5.

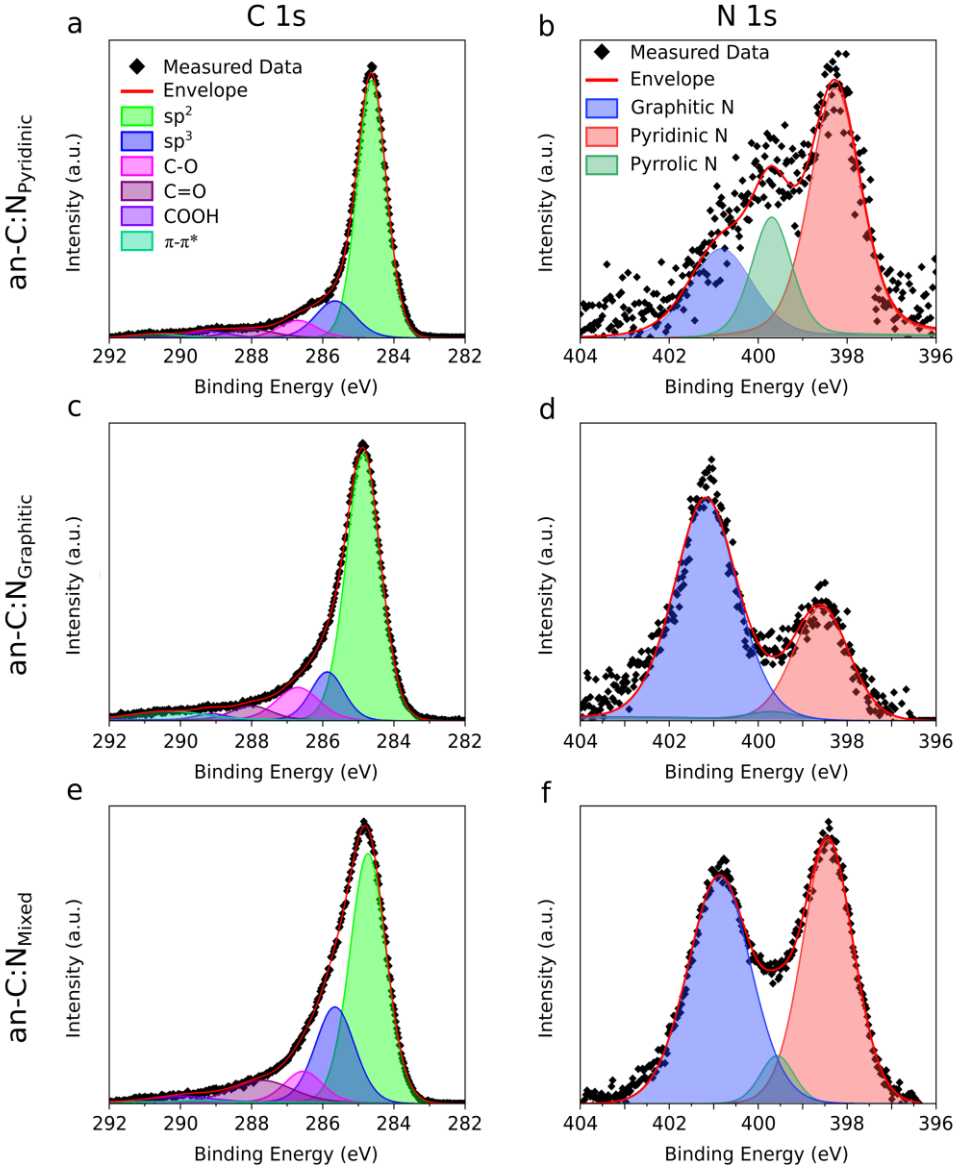

Figure 3.6 Best fits obtained for the C 1s core level spectra of (a) an-C:$N_{Pyridinic}$, (c) an-C:$N_{Graphitic}$, (e) an-C:N_{Mixed} and the N 1s core level spectra for (b) an-C:$N_{Pyridinic}$, (d) an-C:$N_{Graphitic}$, (f) an-C:N_{Mixed}. Data amended from Nolan et al.[16]

The relative content of sp^2 carbon in the two films annealed at 900°C is similar at around 70%. The an-C:N_{Mixed} film shows less graphitic carbon with only 57.4%, which is consistent with a higher temperature leading to a higher degree of graphitisation. Similar

to this is the ratio of sp^3 carbon which is at 13.8 % and 11.7 % for an-C:$N_{Pyridinic}$ and an-C:$N_{Graphitic}$, respectively. The ratio of sp^3 carbon for an-C:N_{Mixed} is approximately double at 24.2 %.

Table 3.5 Obtained information from best fits of XPS core level spectra, for the annealed nitrogenated carbon films.

	sp^2/C_{total} %	sp^3/C_{total} %	$N_{Graphitc}$ %	$N_{Pyridinic}$ %	$N_{Pyrrolic}$ %
an-C	74.1	6.9		n.a.	
an-C:$N_{Pyridinic}$	72	13.8	24.7	54.2	21.1
an-C:$N_{Graphitic}$	68.1	11.7	67.6	30.5	1.9
an-C:N_{Mixed}	57.4	24.1	48.7	45.7	5.5

The nitrogen distribution, obtained from the best fits of the three films varies greatly. The an-C:$N_{Pyridinic}$ shows a high proportion of pyridinic and pyrrolic nitrogen functionalities. As the a-C film is annealed for one hour before ammonia is introduced, the graphitic lattice is mainly formed, which allows for the ammonia to only react at edge sites. The annealing of the a-C:N-2 film at 900°C results in a mainly graphitic nitrogen content, while the annealing at 700°C gives an almost equal content of pyridinic and graphitic nitrogen. The annealing of the nitrogenated carbon film lowers the overall content of nitrogen compared to the as deposited a-C:N film, and especially the content of the pyridinic and pyrrolic nitrogen sites. A similar trend was observed by Hellgren et al.[13]

Further understanding of the chemical structure of the carbon films was obtained with Raman spectroscopy. Raman spectra of the annealed carbon films in comparison to the as deposited films are shown in Figure 3.7. Two distinctive peaks can be seen at around 1350 cm^{-1} and 1600 cm^{-1} which are assigned to the D and G band.[17] In the as deposited films the two peaks are not fully resolved but after annealing the resolution of the two peaks becomes more pronounced. For an-C:N_{Mixed} the resolution of the two peaks is poorer compared to an-C:$N_{Graphitic}$.

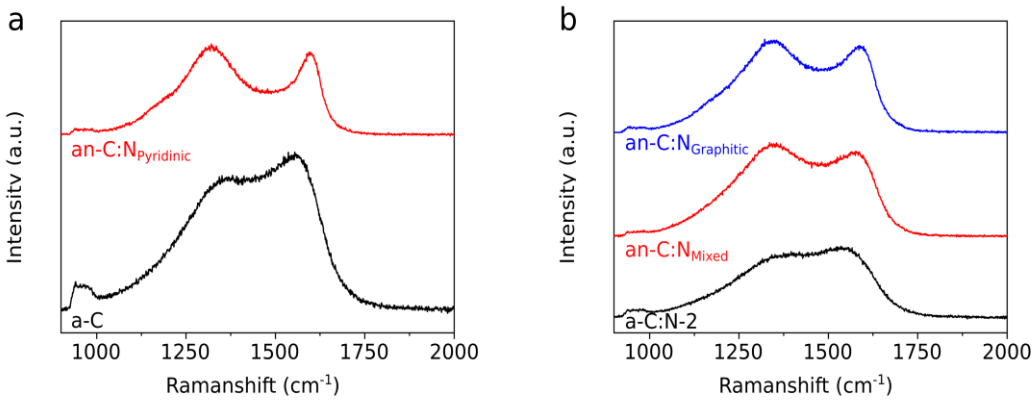

Figure 3.7 Raman spectra for (a) a-C as deposited and annealed and (b) a-C:N-2 as deposited and annealed 700°C and 900°C. Data amended from Nolan et al.[16]

To be able to determine the exact ratio between the G and D band, Raman spectra were deconvoluted. Best fits were obtained using four components: G and D bands and two minor components around 1100 cm^{-1} and 1500 cm^{-1} following Ferrari and Robertson.[17] The peak around 1500 cm^{-1} can be attributed to the presence of amorphous carbon.[18, 19] The contribution around 1100 cm^{-1} can be linked to the presence of sp^3-like bonds.[20] These best fits are shown in Figure 3.8 (Fitted Raman spectra for as deposited films in appendix) and summarised in Table 3.6. The obtained results follow the amorphization trajectory as outlined by Ferrari and Robertson.[21, 22] On the as-deposited films, the D/G ratio is below one, indicating amorphous carbon films. Annealing at 700°C leads to some graphitisation with an increased D/G ratio. The films annealed at 900°C show the highest D/G ratio, indicating a higher level of graphitisation.

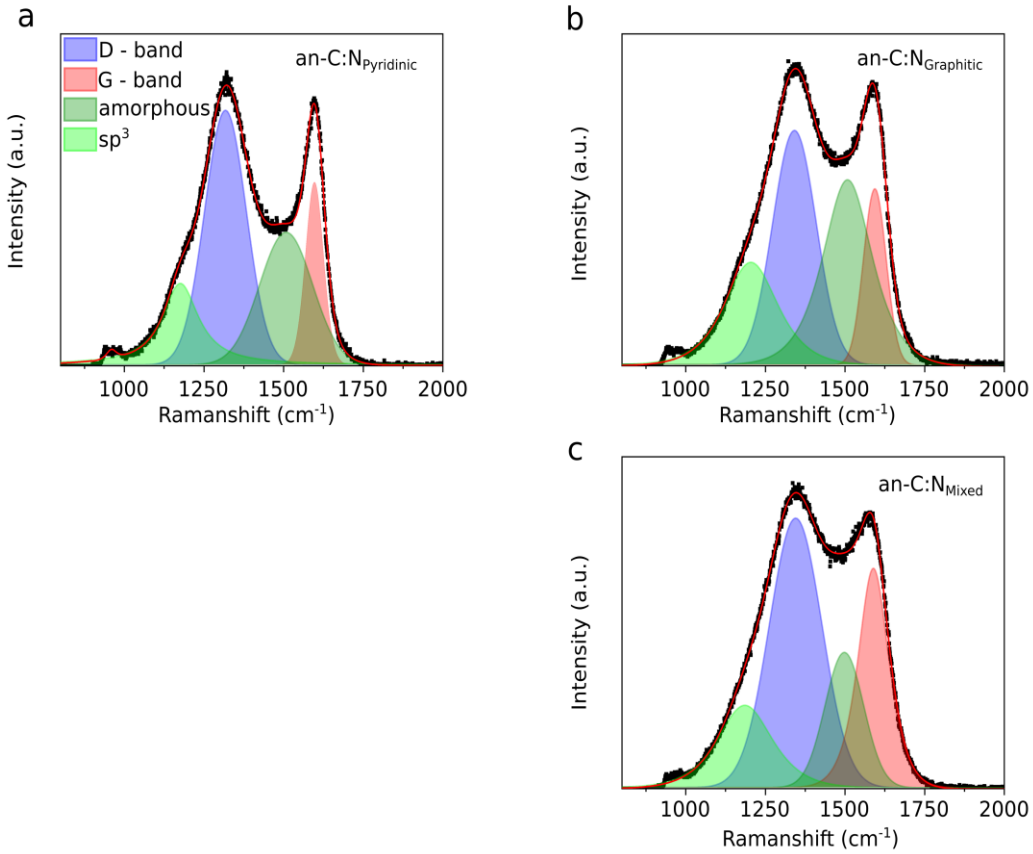

Figure 3.8 Best fit obtained for Raman spectra for (a) an-C:$N_{Pyridinic}$, (b) an-C:$N_{Graphitic}$ and (c) an-C:N_{Mixed}. Data amended from Nolan et al.[16]

This increase in D/G ratio follows the decrease in the %-contribution of sp^3 carbon found via XPS analysis. As the carbon graphitises the concentration of six-membered rings, which are required for observing D bands, increases; however, as the carbon is still defective and polycrystalline the presence of edge sites/vacancies allows for the D-band transitions via optical excitation.

Table 3.6 I(D)/I(G) ratios obtained from the best fits of the Raman spectra of the (nitrogenated) carbon films.

Sample	I(D)/I(G) ratio
a-C	0.82
a-C:N-2	0.91
an-C	1.4
an-C:$N_{Pyridinic}$	1.39
an-C:$N_{Graphitic}$	1.33
an-C:N_{Mixed}	1.23

In summary the sputtering-annealing synthesis procedure allowed reliable synthesis of graphitised nitrogenated carbon thin films. Combining the AFM, XPS and Raman results, it can be seen, that the increased level of graphitisation from an-C:N_{Mixed} to an-C:$N_{Graphitic}$ results in greater thickness shrinkage, while the thickness of both films annealed at 900°C was found to be similar. By using the two-step synthesis process it is possible to tailor the chemical composition and the distribution of the Nitrogen functionalities in the amorphous carbon films. The XPS data of the three films shows further, that the nitrogenated carbons used in this study consist of one with mainly graphitic-nitrogen, one with mainly pyridinic-nitrogen and one with an almost 50:50 ratio. This allows the investigation of the influence of different nitrogen distributions on the electrocatalytic behaviour of the nitrogenated carbon films.

3.3. Hydrogen evolution reaction at N-carbons

Electrochemical studies of the HER were first carried out to evaluate the performance of the films in a reaction that requires activation of hydrogen at the surface. LSV experiments at a scan rate of 2 mV/s were carried out in a three-electrode cell in aqueous electrolyte at pH 1, pH 7 and pH 13, to investigate the pH-dependence of the HER activity. The electrolytes were 0.1 M solutions of H_2SO_4, Na_2SO_4 and KOH, respectively. The obtained voltammograms for acidic media and the derived activity descriptors are shown in Figure 3.9.

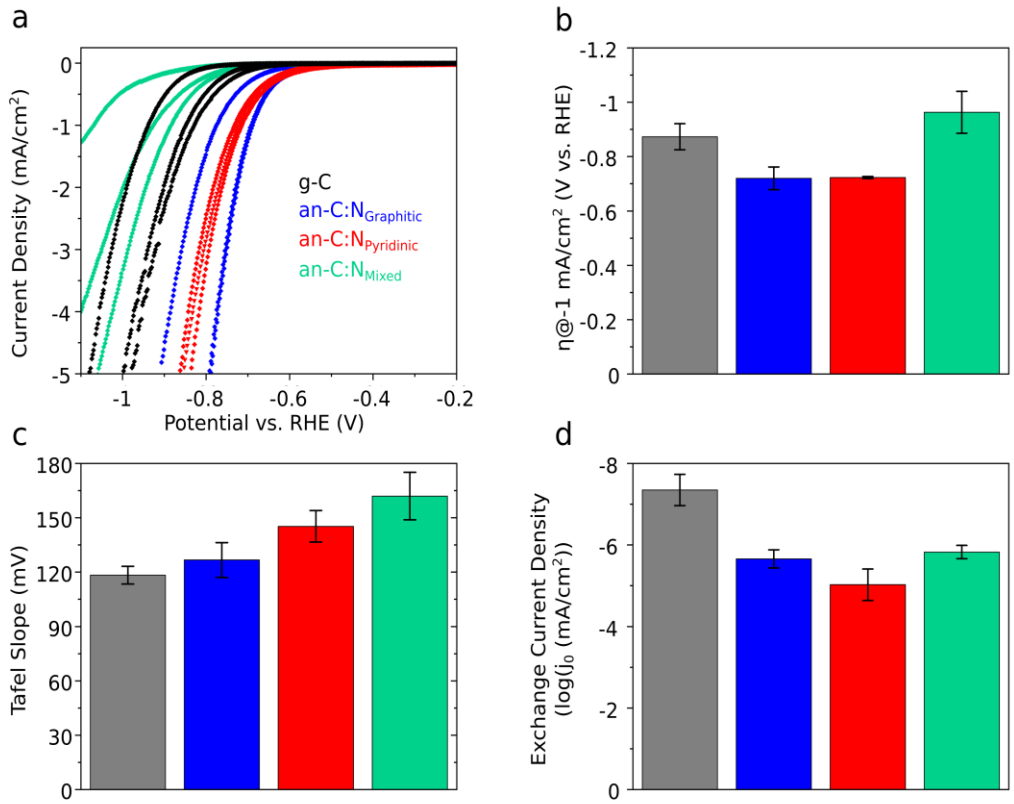

Figure 3.9 (a) Linear sweep voltammetry at 2 mV/s on nitrogenated carbon discs in 0.1 M H_2SO_4 and extracted (b) overpotential at 1 mA/cm^2, (c) Tafel slope and (d) exchange current density. Error bars indicate standard deviations; results for polished GC discs are also shown for comparison.

The onset potentials, defined in this work as the overpotentials (η) at 1 mA/cm^2, for an-C:$N_{Graphitic}$ and an-C:$N_{Pyridinic}$ are almost the same, at *ca.* -0.72 V vs. RHE. All carbon materials show cathodic currents that start at more negative potentials than the thermodynamic value of 0 V vs RHE thus indicating that all the Carbon films are relatively poor HER electrocatalysts. However, the presence of N-functionalities in the most graphitised Carbon films leads to an enhancement of the HER activity relative to that observed for GC electrodes. The Tafel slope obtained from voltammetry can give insights into the mechanism of a reaction, with the r.d.s. being Volmer, Heyrovsky and Tafel step leading to Tafel slopes of approximately 120, 40 and 30 mV, respectively.[23, 24] The Tafel slopes for all carbon thin films were in the 118-162 mV range, which is consistent with the Volmer step being rate determining.[23] The exchange current densities are similar for all three nitrogenated carbons with log j_0 (mA/cm^2) values between -5 to -6. These results are in agreement with descriptors for the HER on carbon materials reported in literature.[25, 26]

In 0.1 M KOH the general trend for the HER on the nitrogenated carbons is similar as shown in Figure 3.10. an-C:$N_{Graphitic}$ and an-C:$N_{Pyridinic}$ show an earlier onset compared to

the GC support and the an-C:N_{Mixed}. The onset on the nitrogenated carbons is *ca.* -0.9 V vs. RHE, which is ~150 mV more cathodic compared to the HER in acidic conditions. The Tafel slopes found for the HER in alkaline conditions were higher compared to the ones found in acidic conditions. The carbons exhibit higher slopes, with the an-C:N_{Mixed} showing a slope above 350 mV. The Tafel slope of 149 mV found for an-C:$N_{Graphitic}$ is similar to the 143 mV reported by Shinagawa et al. for nitrogen doped graphene in 0.1 M KOH.[23] The higher Tafel slopes of the other carbons could arise from the kinetic barrier for water dissociation, consistent with expected high values for a chemical rds.[27, 28]

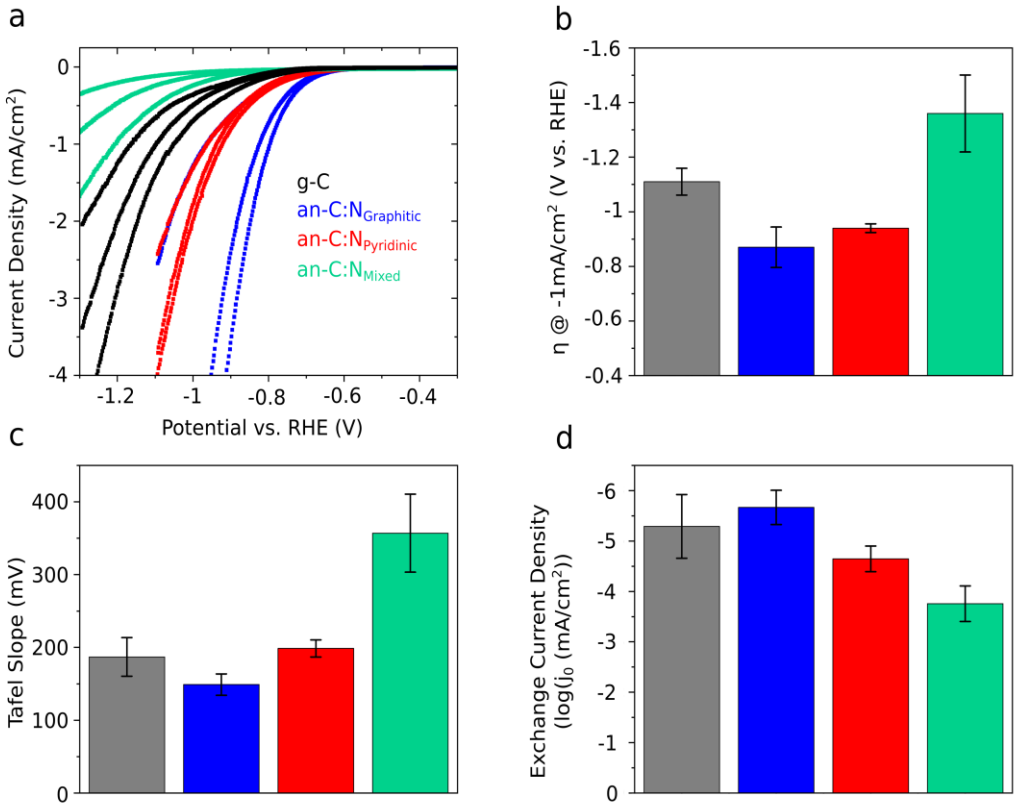

Figure 3.10 (a) Linear sweep voltammetry (2 mV/s) on nitrogenated carbon discs in 0.1 M KOH and extracted (b) onset potential (η at 1 mA/cm^2), (c) Tafel slope and (d) exchange current density. Error bars indicate standard deviations; results for polished GC discs are also shown for comparison.

In neutral conditions all tested carbons performed relatively poorly as shown in Figure 3.11. For the an-C:N_{Mixed} only one of the samples reached the desired current density. The exchange current densities follow a similar trend as for the alkaline conditions. The Tafel slopes are *ca.* 250 mV for an-C:$N_{Graphitic}$ and an-C:$N_{Pyridinic}$ and even > 400 mV for an-C:N_{Mixed}, suggesting that the barrier to water dissociation leads to the higher Tafel slope.

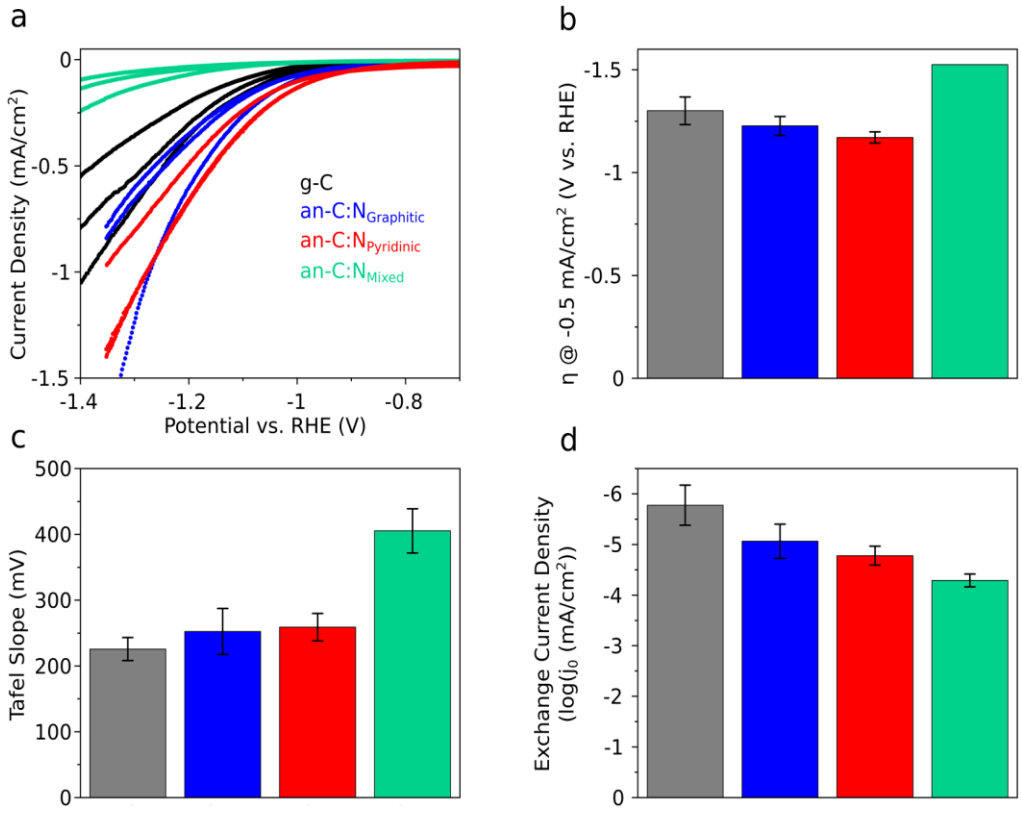

Figure 3.11 (a) Linear sweep voltammetry at 2 mV/s on nitrogenated carbon discs in 0.1 M Na_2SO_4 and extracted (b) onset potential (η at -0.5 mA/cm^2), (c) Tafel slope and (d) exchange current density. Error bars indicate standard deviations; results for polished GC discs are also shown for comparison.

The results of HER studies on the nitrogenated carbons show an improved performance of the HER on the nitrogenated and graphitised carbon films relative to the bare glassy carbon electrode. The poor performance of the an-C:N_{Mixed}, which also showed a lower level of graphitisation, indicates that in addition to the nitrogenation, the graphitisation plays an important part in the performance in the HER. The HER activity in acidic conditions is the highest, followed by alkaline conditions. In neutral conditions the HER was least active for all tested carbons.

To show that the nitrogenation does have an effect on the HER activity and the improvement is not just an effect of graphitisation, the HER was tested in acidic conditions with on an-C film. On this film the HER had an onset potential of -0.75 V vs. RHE, which is more cathodic compared to the nitrogenated carbon films. This will further be discussed in Chapter 6. In addition to this, a Tafel slope of around 160 mV was found, which is in the range of the an-C:N_{Mixed}. This shows that while the graphitisation does play an important role on the electrocatalytic activity, the nitrogenation improves performance

further. Especially, as the an-C has a higher degree of sp^2 carbon compared to the nitrogenated films, indicating a higher degree of graphitisation.

3.4. ECH on N-carbon

Voltammetry in the presence of benzaldehyde was carried out in acidic and in neutral conditions to test the effect of an organic on the HER performance. The resulting voltammograms are shown in Figure 3.12. In acidic conditions a suppression of the HER currents was found. The currents found for glassy carbon and the nitrogenated carbons were in a similar range. The current on the an-C:N_{Mixed} was most suppressed. At pH 1 there is no discernible peak and any ECH appears to be suppressed or masked by the onset of HER currents. A shoulder in the cathodic current can be seen, especially at the GC electrode.

In neutral conditions a cathodic peak can be seen around -0.85 V vs RHE. As this peak is only visible in the presence of benzaldehyde. The cathodic peak is in a similar potential range as a reduction peak for benzaldehyde reported by Cantu et al.[29] at graphene electrodes. Compared to the observed HER currents in bare supporting electrolyte, the cathodic currents are smaller in the presence of benzaldehyde. This can be attributed to benzaldehyde adsorption onto the carbon resulting in suppression of the HER current background.

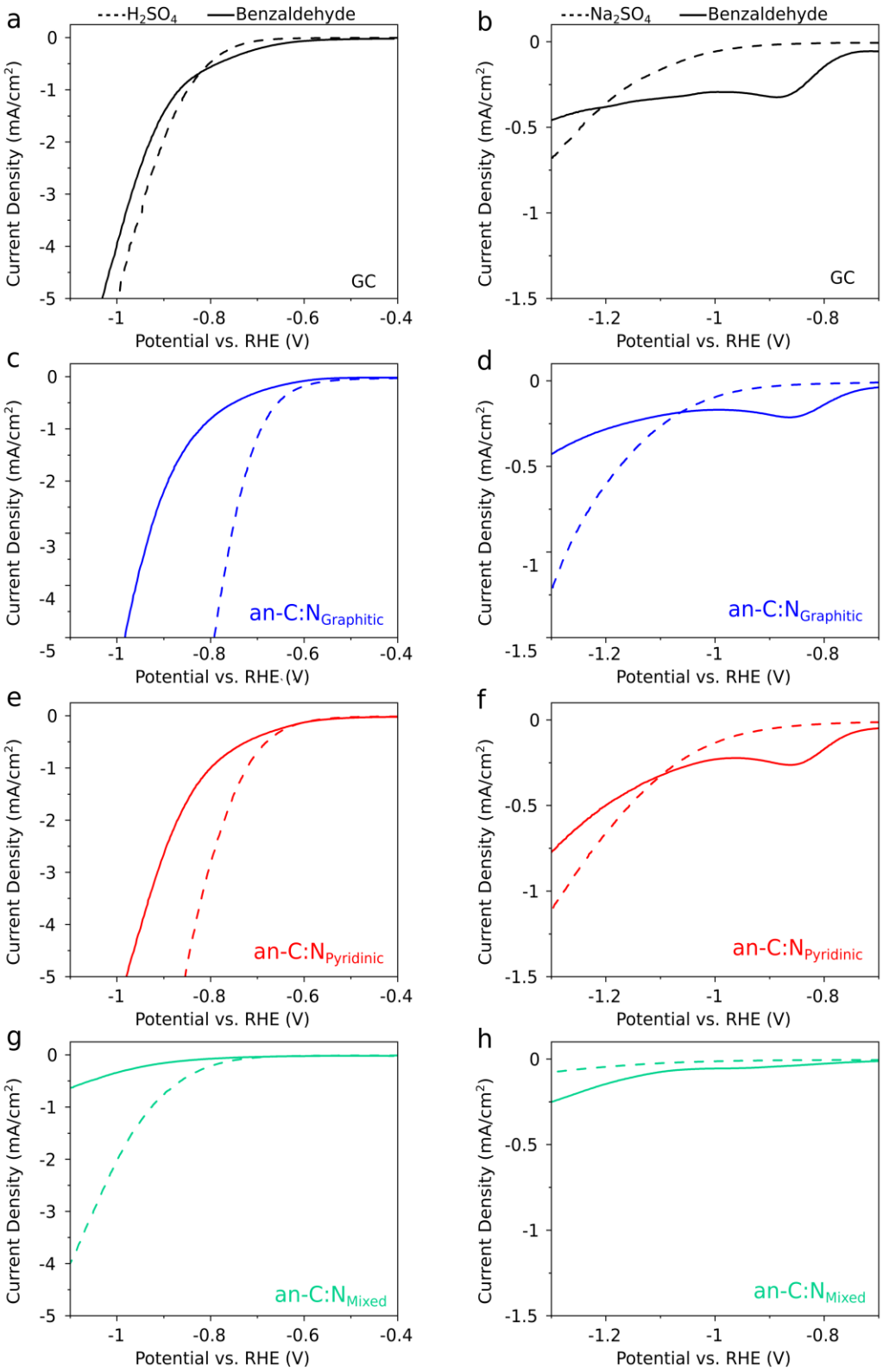

Figure 3.12 Linear sweep voltammetry at 2 mV/s in (a, c, e and g) 0.1 M H_2SO_4 and (b, d, f and h) 0.1 M Na_2SO_4 with (solid lines) and without (dashed lines) 10 mM benzaldehyde on (a, b) GC, (c, d) an-C:$N_{Graphitic}$ (e, f) an-C:$N_{Pyridinic}$ and (g, h) an-C:N_{Mixed}. Deposited on GC disc electrodes.

For electrolysis experiments an electrochemical cell was designed and custom made by a glassblower. The materials used in the cell needed to be chemically stable in the conditions of the electrolysis experiments. Also, separating the two compartments with a membrane was needed to avoid crossover of reaction products during the experiment. The design consisted of a half-cell adapted from a 25 mL glass bottle, with a glass flange attached at a defined height. With the flange, two half cells could be connected with a Teflon centering ring and sealed with a Viton O-ring using a tensioning chain. The electrical connection was done through silicon septa, allowing to run experiments under controlled atmosphere in the headspace. The setup of the electrolysis cell is shown in Figure 3.13.

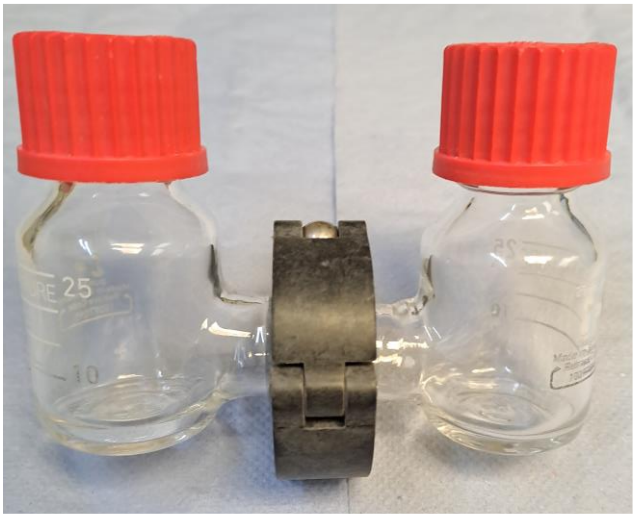

Figure 3.13 Custom made electrolysis cell used in this work.

3.4.1. Electrolysis under static conditions

Electrolysis experiments were carried out to study the electrochemical reduction of benzaldehyde. Cathodic potentials of *ca.* -0.8 and -0.95 V vs. RHE (-1.1 and -1.6 V vs. Ag/AgCl) were applied in 0.1 M H_2SO_4 and Na_2SO_4, respectively, with addition of benzaldehyde at 10 mM concentration. Chronoamperograms of 4 h were then obtained, with Gas Chromatography and FID analysis of the electrolyte carried out before and after the electrolysis. A representative current response with the charge as well as the resulting gas chromatograms are shown in Figure 3.14. It can be seen that the current increases significantly over time. Towards the end of the chronoamperogram the current becomes noisy due to bubble formation during the HER. The chromatogram displays multiple peaks; the first one due to ethyl acetate solvent, the second one ($t_R \approx 3$ min) corresponding to benzaldehyde and a third one ($t_R \approx 4$ min) due to acetophenone used as internal standard.

A fourth peak at *ca.* 17 min is due to benzoic acid, which is present as an impurity. After electrolysis, peaks for benzyl alcohol ($t_R \approx 8$ min) and hydrobenzoin ($t_R \approx 50$ min) can also be seen.

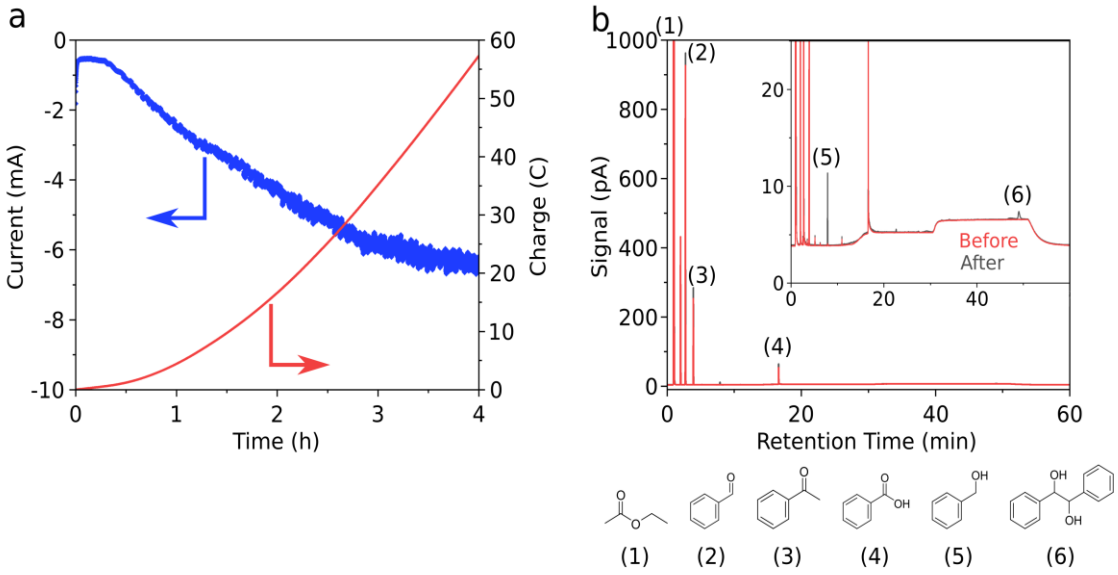

Figure 3.14 (a) Representative chrono amperogram on a an-C:$N_{Graphitic}$ deposited on a glassy carbon plate electrode (Area = 1cm^2) on of a 4 h electrolysis experiment in 0.1 M H_2SO_4 with 10 mM benzaldehyde at -0.8 V vs. RHE in static electrolyte and (b) the resulting gas chromatogram before and after electrolysis. Inset shows a zoomed in version.

Finally, an additional peak at ca. 2 min is observed, which is a hydrolysis product of ethyl acetate in presence of acid and results from storage prior to analysis.[30] From peak area ratios relative to the internal standard, the key performance indicators of the different reactions can be calculated as discussed in section 1.3.4. It is interesting to note that the data shown in Figure 3.14 is the result of an electrolysis experiment with a quiescent solution; therefore, it is likely that the current trend observed in the chronoamperogram is the result of benzaldehyde depletion in the diffusion layer, which would result in the HER becoming favoured and less suppressed over time.

The resulting selectivity towards benzyl alcohol and the faradaic efficiencies of organic reductions derived for the nitrogenated carbon electrodes and the glassy carbon electrode are shown in Figure 3.15.

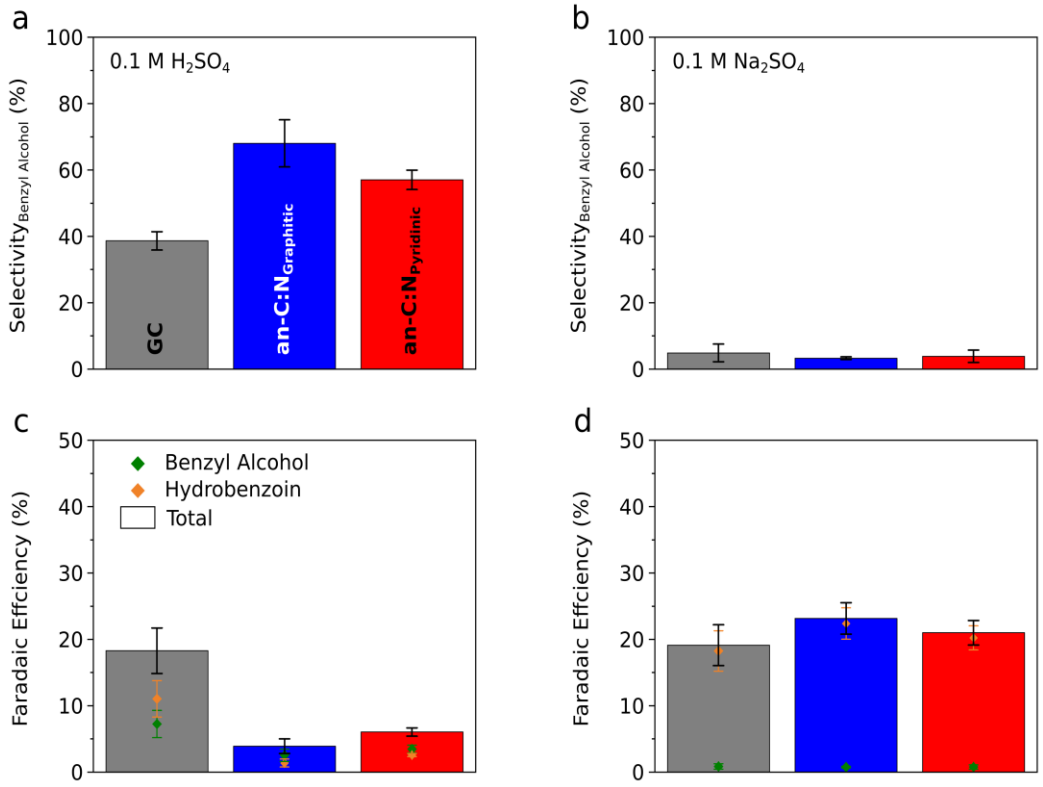

Figure 3.15 (a) Selectivity towards benzyl alcohol obtained for the glassy carbon electrode and the nitrogenated carbons in 0.1 M H_2SO_4 at -0.8 V vs RHE and (b) in 0.1 M Na_2SO_4 at -0.95 V vs RHE (c) The resulting faradaic efficiencies of organic reductions for the two products and the total organic reduction in 0.1 M H_2SO_4 and (d) 0.1 M Na_2SO_4. With 10 mM benzaldehyde without stirring. Error bars indicate standard errors.

In neutral conditions there is almost no selectivity towards benzyl alcohol. In acidic conditions there is a clear difference between the nitrogenated carbons, yielding over 60% benzyl alcohol and glassy carbon giving less than 40% of benzyl alcohol. This follows the trend observed in the HER on the different carbons.

The faradaic efficiencies are poor, with less than 10% for the nitrogenated carbons in acid electrolyte, thus indicating that the HER is the dominant reaction. On GC the faradaic efficiency is higher, as it is less active in the HER at the tested potential. In neutral conditions the faradaic efficiencies are higher and almost independent of the carbon used. Together with the low selectivity towards benzyl alcohol, this is most likely due to the low HER activity at the applied potential. It needs to be noted, that the faradaic efficiencies are averaged over the four hours of electrolysis. The current response over the four hours does indicate a depletion of benzaldehyde at the electrode and an increased HER activity. The trends in production rates, Figure 3.16, further support that benzaldehyde depletion limits the performance under these electrolysis conditions. Although there are differences in

selectivity and faradaic efficiency, in acidic conditions there is almost no difference in the amount of benzaldehyde reduced at the different carbon electrodes. In neutral electrolyte there is even more benzaldehyde reduced, on the GC compared to the nitrogenated carbons, with a decrease in production of hydrobenzoin on them.

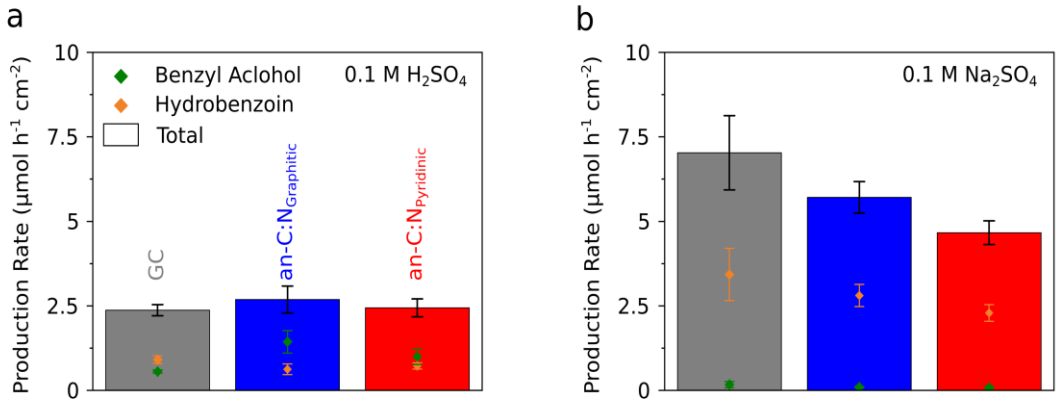

Figure 3.16 Production rate for benzyl alcohol, hydrobenzoin and the total amount of reduced benzaldehyde after 4 h on glassy carbon and the nitrogenated carbons with 10 mM benzaldehyde without stirring in (a) 0.1 M H_2SO_4 at -0.8 V vs. RHE and (b) 0.1 M Na_2SO_4 at -0.95 V vs. RHE. Error bars indicate standard errors.

3.4.2. Electrolysis under forced convection

The previous results show that the electrolysis without forced convection is mass transport limited likely resulting in greater selectivity towards the HER over time and negligible differences among the performances at the different carbon electrodes. For this reason, the electrolysis setup was changed and the cell was equipped with a stirring bar and placed on a magnetic stirring plate. In addition, temperature fluctuations in the lab were avoided by placing the cell in a water bath set at 25°C. A stirring rate of 500 rpm was chosen, as this was a speed at which the convection in the cell could be maintained without damaging the electrodes. In contrast to the current response of the chrono amperometry without stirring, the forced convection inhibits the increase in current over time. This is shown in Figure 3.17 for an-C:$N_{Graphitic}$ using 20 mM benzaldehyde.

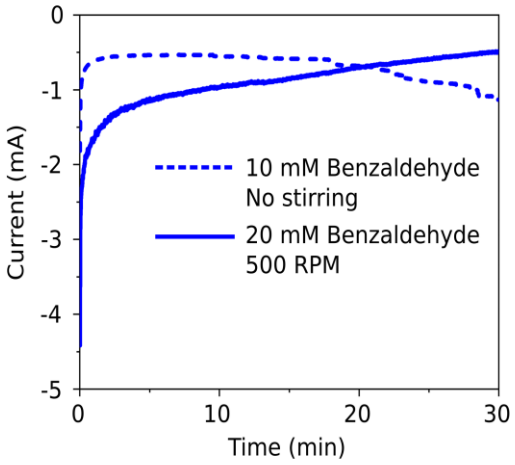

Figure 3.17 Chrono amperometry on an-C:$N_{Graphitic}$ in 0.1 M H_2SO_4 with 20 mM benzaldehyde with 500 rpm stirring (solid line) and with 10 mM benzaldehyde without stirring (dashed line).

Selectivity, production rates and faradaic efficiencies were then studied using the same conditions via 30 min potentiostatic experiments at varying potentials, and results are shown in Figure . The shorter time was used as due to the stirring higher rates were observed, allowing for a shorter time of electrolysis. Compared to electrolysis in quiescent solutions, the rate at which benzaldehyde is reduced is significantly higher on GC and on the nitrogenated carbon electrode. The amount of reduced benzaldehyde for an-C:$N_{Graphitic}$ at -1.1 V vs. Ag/AgCl is almost double compared to that of GC. At -1 V vs. Ag/AgCl the reduction rates found for both carbons were similar. The production rate for both products increases with more cathodic potentials. The production of hydrobenzoin increases significantly at more cathodic potentials, while only a slight increase was found for the production of benzyl alcohol. The selectivity towards benzyl alcohol is high at less cathodic potentials, with 100% benzyl alcohol on GC at -0.5 V vs RHE. With more cathodic potentials the selectivity drops down to 12% at -0.8 V vs RHE. On an-C:$N_{Graphitic}$ the selectivity at -0.5 V vs RHE is around 90% but decreases to ca. 30% for more cathodic potentials. At -0.8 V vs RHE the selectivity was found to be 26%, which is significantly higher compared to the selectivity found for GC at the same potential (12%). Without stirring a selectivity of about 70% was found for an-C:$N_{Graphitic}$ at -0.8 V vs RHE. This indicates that the limited mass transport of benzaldehyde that was found in static conditions leads to increased selectivity. Another reason for the lower selectivity between the two data sets could be the increased concentration of benzaldehyde. A higher concentration of benzaldehyde was used to increase the production rate and allow shorter electrolysis times. With more benzaldehyde in the electrolyte, and stirring, more benzaldehyde is supplied to

the electrode, leading to more ketyl radicals forming and in turn to more hydrobenzoin being produced. The faradaic efficiency of organic reduction increases for both carbons going to more cathodic potentials. However, the faradaic efficiency for the ECH to benzyl alcohol on glassy carbon drops when the potential is decreased from -0.7 V to -0.8 V vs RHE.

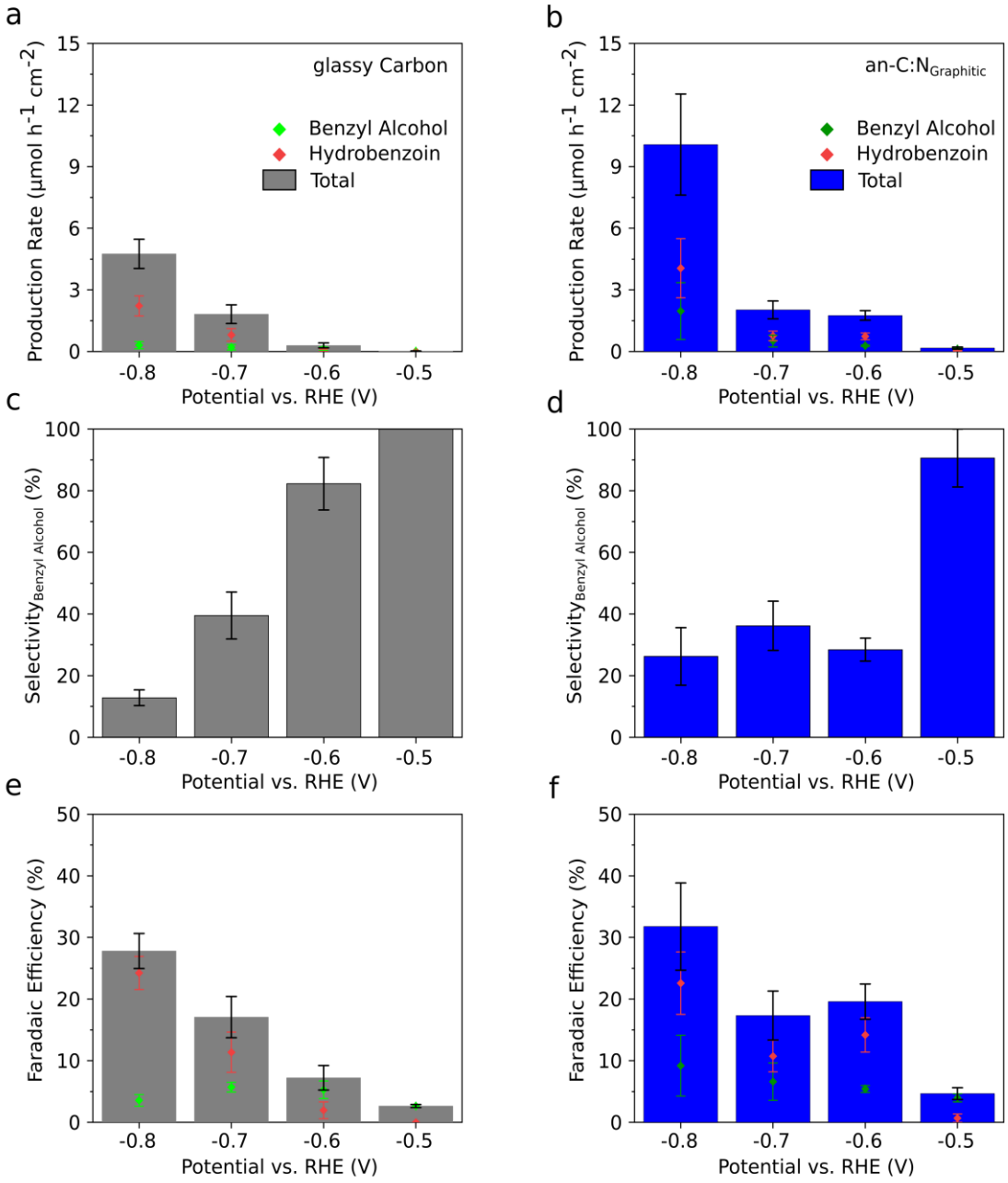

Figure 3.18 Production rate for benzyl alcohol, hydrobenzoin and the total reduction rate of benzaldehyde after 0.5 h for electrolysis in 0.1 M H_2SO_4 with 20 mM benzaldehyde at 500 rpm on (a) glassy carbon and (b) an-C:$N_{Graphitic}$. Selectivity towards benzyl alcohol obtained at (c) GC and (d) an-C:$N_{Graphitic}$ electrodes. Faradaic efficiencies of organic reductions for each of the two products and for the total organic reduction at (e) GC and (f) an-C:$N_{Graphitic}$. Error bars indicate standard errors.

Stirring of the electrolyte during electrolysis minimises mass transport limitations, as shown by increased production rates, particularly for an-C:$N_{Graphitic}$. Forced convection resulted in the faradaic efficiency on the nitrogenated carbon electrode increasing to over 30%, with the efficiency for ECH to benzyl alcohol increasing to about 10%. The drop in selectivity could have multiple sources. One explanation could be that at more cathodic potentials more benzaldehyde is reduced to the ketyl radical. If in addition to this, the hydrogen coverage is not increasing to the same extent, then more hydrobenzoin formation can be expected. An alternative explanation could be a change in the reaction mechanism, as described by Cantu et al.[29] The authors found that at low cathodic potentials the most favourable reaction mechanism is the so called concerted proton-electron reduction, i.e. the addition of an adsorbed hydrogen. At more cathodic potentials the step wise addition of an electron and then a proton becomes more favourable. From this reaction pathway a higher coverage of ketyl radical would follow, which again leads to more dimerization. The selectivity on the nitrogenated carbon at high cathodic potentials is higher compared to the glassy carbon. This indicates that the higher activity in the HER translates to a higher selectivity, even at highly cathodic potentials.

3.5. Conclusion

Through the improved annealing protocol, the reliable synthesis of nitrogenated carbon films was possible. Characterisation via microscopy and spectroscopic methods indicated that the films are smooth and have a controlled degree of nitrogenation and graphitisation. Three carbons, one with mainly graphitic nitrogen, one with mainly pyridinic nitrogen and one with a mixed nitrogen distribution were chosen to study the effects of nitrogenation on the HER and ECH reactions. The nitrogenated carbon films show an improved activity in the HER. The data suggests that a carbon with good electrocatalytic activity needs to have a certain level of graphitisation in addition to the nitrogenation. This was seen by the poor performance of the an-C:N_{Mixed} film in contrast to the materials graphitized at higher temperatures.

In the presence of benzaldehyde the HER currents are suppressed, indicating some activity in the ECH, which was shown through electrolysis experiments in a custom-made electrolysis cell. Without stirring of the electrolyte, the ECH was found to be mass transport limited, resulting in poor faradaic efficiencies and poor production rates. Through the introduction of stirring, production rates and the faradaic efficiencies were increased,

however the selectivity towards benzyl alcohol was decreased. This is consistent with a higher concentration of benzaldehyde at the electrode surface, which is maintained by the forced convection process, and facile formation of ketyl radicals. The selectivity at low cathodic potentials is instead higher. Interestingly, the nitrogenated carbon electrode tested does show a higher selectivity towards the alcohol compared to GC, thus suggesting that nitrogen functionalities might play a role in imparting ECH activity. The nitrogen doping does lead to an improved electrocatalytic activity, but the nitrogenated carbons are overall still poor electrocatalysts for the HER and the ECH. The work presented in this chapter did give insights into the ECH and how to investigate it. The effect of mass transport on the different KPIs is important.

The poor electrocatalytic activity of the nitrogenated carbon film makes them less applicable as an electrocatalyst by themselves. They can however be used as a support for other electrocatalysts as will be explored in the next chapter.

References

1. Zhai, Q.; Pan, Y.; Dai, L., Carbon-Based Metal-Free Electrocatalysts: Past, Present, and Future. *Accounts of Materials Research* **2021,** *2* (12), 1239-1250.
2. Dai, L., *Carbon-based metal-free catalysts: design and applications*. John Wiley & Sons: 2018.
3. Kwon, Y.; Birdja, Y. Y.; Raoufmoghaddam, S.; Koper, M. T. M., Electrocatalytic Hydrogenation of 5-Hydroxymethylfurfural in Acidic Solution. *ChemSusChem* **2015,** *8* (10), 1745-1751.
4. Fan, Q.; Zhang, M.; Jia, M.; Liu, S.; Qiu, J.; Sun, Z., Electrochemical CO2 reduction to C2+ species: Heterogeneous electrocatalysts, reaction pathways, and optimization strategies. *Materials Today Energy* **2018,** *10*, 280-301.
5. Ma, T.; Fan, Q.; Li, X.; Qiu, J.; Wu, T.; Sun, Z., Graphene-based materials for electrochemical CO2 reduction. *Journal of CO2 Utilization* **2019,** *30*, 168-182.
6. Duan, X.; Xu, J.; Wei, Z.; Ma, J.; Guo, S.; Wang, S.; Liu, H.; Dou, S., Metal-Free Carbon Materials for CO2 Electrochemical Reduction. *Advanced Materials* **2017,** *29* (41), 1701784.
7. Liu, S.; Yang, H.; Su, X.; Ding, J.; Mao, Q.; Huang, Y.; Zhang, T.; Liu, B., Rational design of carbon-based metal-free catalysts for electrochemical carbon dioxide reduction: A review. *Journal of Energy Chemistry* **2019,** *36*, 95-105.
8. Ge, C.; Lao, F.; Li, W.; Li, Y.; Chen, C.; Qiu, Y.; Mao, X.; Li, B.; Chai, Z.; Zhao, Y., Quantitative Analysis of Metal Impurities in Carbon Nanotubes: Efficacy of Different Pretreatment Protocols for ICPMS Spectroscopy. *Analytical Chemistry* **2008,** *80* (24), 9426-9434.
9. Heras, A.; Colina, A.; López-Palacios, J.; Ayala, P.; Sainio, J.; Ruiz, V.; Kauppinen, E. I., Electrochemical purification of carbon nanotube electrodes. *Electrochemistry Communications* **2009,** *11* (7), 1535-1538.
10. Kruusma, J.; Mould, N.; Jurkschat, K.; Crossley, A.; Banks, C. E., Single walled carbon nanotubes contain residual iron oxide impurities which can dominate their electrochemical activity. *Electrochemistry Communications* **2007,** *9* (9), 2330-2333.
11. Šljukić, B.; Banks, C. E.; Compton, R. G., Iron Oxide Particles Are the Active Sites for Hydrogen Peroxide Sensing at Multiwalled Carbon Nanotube Modified Electrodes. *Nano Letters* **2006,** *6* (7), 1556-1558.
12. Behan, J. A.; Stamatin, S. N.; Hoque, M. K.; Ciapetti, G.; Zen, F.; Esteban-Tejeda, L.; Colavita, P. E., Combined Optoelectronic and Electrochemical Study of Nitrogenated Carbon Electrodes. *The Journal of Physical Chemistry C* **2017,** *121* (12), 6596-6604.
13. Hellgren, N.; Haasch, R. T.; Schmidt, S.; Hultman, L.; Petrov, I., Interpretation of X-ray photoelectron spectra of carbon-nitride thin films: New insights from in situ XPS. *Carbon* **2016,** *108*, 242-252.
14. Chastain, J.; King Jr, R. C., Handbook of X-ray photoelectron spectroscopy. *Perkin-Elmer Corporation* **1992,** *40*, 221.
15. Blyth, R. I. R.; Buqa, H.; Netzer, F. P.; Ramsey, M. G.; Besenhard, J. O.; Golob, P.; Winter, M., XPS studies of graphite electrode materials for lithium ion batteries. *Applied Surface Science* **2000,** *167* (1), 99-106.
16. Nolan, H.; Schröder, C.; Brunet-Cabré, M.; Pota, F.; McEvoy, N.; McKelvey, K.; Perova, T. S.; Colavita, P. E., MoS2/carbon heterostructured catalysts for the hydrogen evolution reaction: N-doping modulation of substrate effects in acid and alkaline electrolytes. *Carbon* **2023,** *202*, 70-80.

17. Ferrari, A. C.; Robertson, J., Interpretation of Raman spectra of disordered and amorphous carbon. *Physical review B* **2000,** *61* (20), 14095.
18. Yamaguchi, T.; Bandow, S.; Iijima, S., Synthesis of carbon nanohorn particles by simple pulsed arc discharge ignited between pre-heated carbon rods. *Chemical Physics Letters* **2004,** *389* (1), 181-185.
19. Peña-Álvarez, M.; Corro, E. d.; Langa, F.; Baonza, V. G.; Taravillo, M., Morphological changes in carbon nanohorns under stress: a combined Raman spectroscopy and TEM study. *RSC Advances* **2016,** *6* (55), 49543-49550.
20. Paillard, V., On the origin of the 1100 cm−1 Raman band in amorphous and nanocrystalline sp3 carbon. *Europhysics Letters* **2001,** *54* (2), 194.
21. Ferrari, A. C.; Robertson, J., Raman Signature of Bonding and Disorder in Carbons. *MRS Online Proceedings Library* **1999,** *593* (1), 299-304.
22. Ferrari, A. C.; Robertson, J., Raman spectroscopy of amorphous, nanostructured, diamond–like carbon, and nanodiamond. *Philosophical Transactions of the Royal Society of London. Series A: Mathematical, Physical and Engineering Sciences* **2004,** *362* (1824), 2477-2512.
23. Shinagawa, T.; Garcia-Esparza, A. T.; Takanabe, K., Insight on Tafel slopes from a microkinetic analysis of aqueous electrocatalysis for energy conversion. *Scientific Reports* **2015,** *5* (1), 13801.
24. Fletcher, S., Tafel slopes from first principles. *Journal of Solid State Electrochemistry* **2009,** *13* (4), 537-549.
25. Brennan, M. P. J.; Brown, O. R., Carbon electrodes: Part 1. Hydrogen evolution in acidic solution. *Journal of Applied Electrochemistry* **1972,** *2* (1), 43-49.
26. Drossbach, P.; Schulz, J., Elektrochemische untersuchungen an kohleelektroden—I: Die überspannung des wasserstoffs. *Electrochimica Acta* **1964,** *9* (11), 1391-1404.
27. Zheng, Y.; Jiao, Y.; Vasileff, A.; Qiao, S.-Z., The Hydrogen Evolution Reaction in Alkaline Solution: From Theory, Single Crystal Models, to Practical Electrocatalysts. *Angewandte Chemie International Edition* **2018,** *57* (26), 7568-7579.
28. Lamoureux, P. S.; Singh, A. R.; Chan, K., pH Effects on Hydrogen Evolution and Oxidation over Pt(111): Insights from First-Principles. *ACS Catalysis* **2019,** *9* (7), 6194-6201.
29. Cantu, D. C.; Padmaperuma, A. B.; Nguyen, M.-T.; Akhade, S. A.; Yoon, Y.; Wang, Y.-G.; Lee, M.-S.; Glezakou, V.-A.; Rousseau, R.; Lilga, M. A., A Combined Experimental and Theoretical Study on the Activity and Selectivity of the Electrocatalytic Hydrogenation of Aldehydes. *ACS Catalysis* **2018,** *8* (8), 7645-7658.
30. Otero-López, M.; González-Brambila, M.; Dutta, A.; Castillo-Araiza, C., Elucidating Kinetic, Adsorption and Partitioning Phenomena from a Single Well Tracer Method: Laboratory and Bench Scale Studies. 2016.

Chapter IV

4. MoS_2 supported on N-carbon

The results presented in this chapter have in part been published in peer-reviewed journals in the following articles:

Hugo Nolan, **Christian Schröder**, Marc Brunet Cabré, Filippo Pota, Neill McEvoy, Kim McKelvey, Tatiana S. Perova, Paula E. Colavita: "MoS_2/carbon heterostructured catalysts for the hydrogen evolution reaction: N-doping modulation of substrate effects in acid and alkaline electrolytes", Carbon, **2023**, 202, 70-80.

Datasets presented in this chapter were the result of close collaboration with Dr. Hugo Nolan. The development and characterisation of the nitrogenated carbon films used as substrates were carried out by myself. The concept of the heterostructures was introduced by HN, who led the investigation of the HER. I expanded on the characterisation and used them for the investigation of their activity in the ECH.

4.1. Introduction

Molybdenum disulfide (MoS_2) supported by nitrogen-doped carbon has emerged as a promising electrocatalyst for the HER,[1] which makes it also a potentially promising candidate for applications in the ECH of organic molecules. The graphitic carbon support has been argued to enhance the conductivity allowing the use of MoS_2 which is a semiconducting material. By choosing a graphitic carbon support with a 3D structure, the specific surface area of heterostructured catalysts can also be increased to obtain high performing electrodes in the HER. Nitrogen doping of the carbon support has also been argued to further tune the intrinsic activity of MoS_2, increase its stability, while proving beneficial for the growth of MoS_2.[2] This makes MoS_2/N-carbon heterostructures materials of interest also for the ECH of organic molecules.

Many studies investigated MoS_2/N-carbon materials in the HER[3-7] and similar heterostructures have gained attention for electrocatalytic CO_2 reduction (CO2RR) applications.[8, 9] However, as most of the work has been carried out using nanostructured electrode materials with complex 3D architectures it is difficult to understand and deconvolute the activity of these materials. Nanostructure and porosity often make it difficult to distinguish improvements in performance that arise from changes in intrinsic activity of the material and nitrogen functionalities, from those arising from mass transport and specific surface area effects. Furthermore, studies on the electrochemical hydrogenation of organic molecules using MoS_2 on nitrogenated carbon are scarce indicating this as a knowledge gap and a potential area of application for these interesting materials.

To gain a deeper insight in the activity of MoS_2/N-carbon materials in the HER and the ECH, model electrodes were synthesised and employed in this work. The goal was to generate heterostructures with controlled morphology and a high contact area between the carbon film and the MoS_2. As a route for synthesis of MoS_2 a close proximity precursor method, previously reported by O'Brien et al.[10] This method yields monolayers of MoS_2, when growing onto silicon wafers. In this chapter, the synthesis route got adapted and expanded to grow the MoS_2 onto the nitrogenated carbon films presented in chapter 3. As substrate an-C:$N_{Graphitic}$ and an-C:$N_{Pyridinic}$ will be chosen. For one these films showed beneficial results in the HER and ECH, and secondly, the CVD of MoS_2 occurs at temperatures of 750°C, making only films annealed at higher temperatures applicable.

Using the two different films will allow to investigate the effect of different nitrogen functionalities on the electrochemical activity of the materials. Further, different potentials and varying concentrations will be examined to better understand the behaviour of the heterostructures. First, the synthesis and characterization of thin film MoS_2/C heterostructured electrodes will be discussed. Then their activity in the HER will be investigated and, finally, the ECH of benzaldehyde will be tested to experimentally assess their potential.

4.2. Synthesis and characterisation

Electrochemical synergies between nitrogenated carbon substrates and molybdenum disulfide were investigated by synthesising MoS_2/N-carbon heterostructures. The nitrogenated carbon films from the previous chapter were used as support, and a CVD process was used to grow the MoS_2 directly onto the carbon. Through this, good electrical contact between the support and the MoS_2 could be achieved. The method used was first reported by O'Brien et al.[10] and had been developed to allow growth of mono/few layer MoS_2 onto Si wafers. This approach was extended to grow MoS_2 on nitrogenated carbon thin films. Exfoliated MoO_3 is first drop-cast as a precursor onto a Si wafer to serve as a seed layer. The seed wafer was placed in close contact against the carbon thin film substrate and the precursor was then vaporized in close proximity, within the microreactor setup shown in Figure 4.. The sulfur vapour was generated in a second hot zone upstream from the substrate position and reacted to form MoS_2 at the carbon surface.

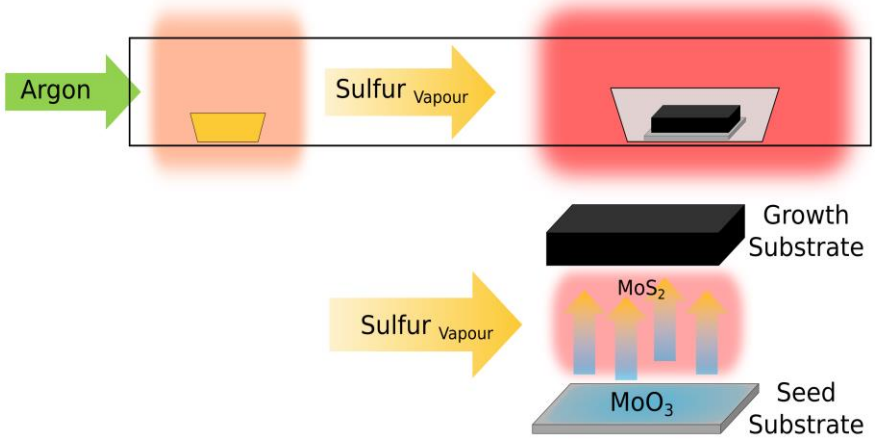

Figure 4.1 Schematic of the close proximity setup used to grow MoS_2.

An image of the MoS_2 grown onto nitrogenated carbon on a glassy carbon plate is shown in Figure 4.. It can be seen that the growth occurs over the entire surface but is non homogenous in thickness/coverage.

Figure 4.2 Image of MoS_2 grown on an-C:$N_{Graphitic}$ on a GC plate (2×1 cm^2) used for electrolysis.

The heterogeneity can also be seen in the optical microscopy images in Figure 4.. The growth of the film occurs as small islands, which can be observed more clearly in Figure 4.3b. The darkfield image in Figure 4.3c shows a microstructure present across the surface, indicating a polycrystalline nature of the MoS_2.

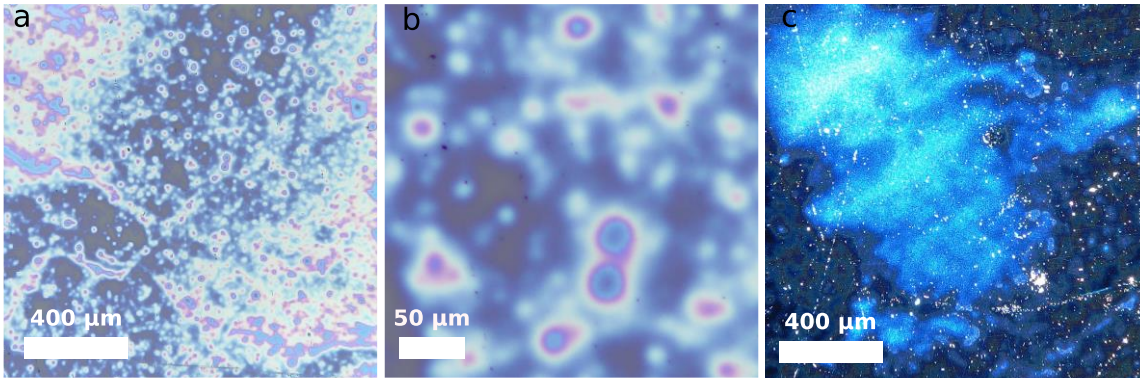

Figure 4.3 Optical microscopy of MoS_2/an-C:$N_{Graphitic}$ in (a, b) bright field and (c) dark field.

The presence of MoS_2 was investigated using Raman spectroscopy. Figure 4.4 shows the average Raman spectrum obtained from a scanning Raman experiment across a 40×40 μm^2 area. The spectrum shows the characteristic D- and G-band of graphitic carbon around 1200 and 1600 cm^{-1}, respectively.[11] In addition to this a doublet can be seen between 350 and 400 cm^{-1}. This doublet is assigned to the presence of MoS_2.[12]

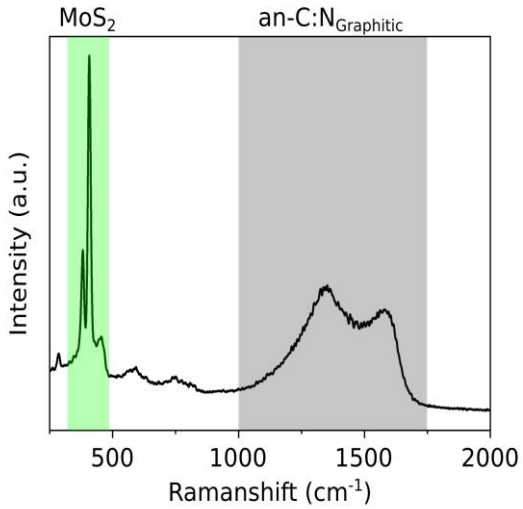

Figure 4.4 Average Raman spectra of a 40 × 40 μm area with 40 × 40 spectra obtained over this area of a MoS_2/an-C:$N_{Graphitic}$ on a GC plate, with the characteristic signals for MoS_2 (green) and carbon (grey) shown.

The spectrum suggests that the nitrogenated carbon is still intact after the CVD process and the MoS_2 was successfully grown onto it, as the signal is consistent with that of N-carbon films. This fact is supported by the fact that the Raman spectra of GC looks very different to the signal seen here (shown in the Appendix). Indicating that the graphitized film remains present after MoS_2 growth. The Raman spectrum indicates growth of MoS_2 in the 2H morphology, as the 1T' phase would lead to Raman peaks around 150, 220 and 335 cm^{-1}.[13] A heat map of the intensity of the MoS_2 peak, together with an optical image of the probed area are shown in Figure 4.. The intensity map shows the presence of MoS_2 signals across the entire probed surface, which indicates that the whole surface is covered by MoS_2, as far as the resolution of the Raman microscopy image allows (~ 1 μm) to probe. The heat map shows that the edge of the 'islands' is brighter, suggesting a higher density of MoS_2 at their edges.

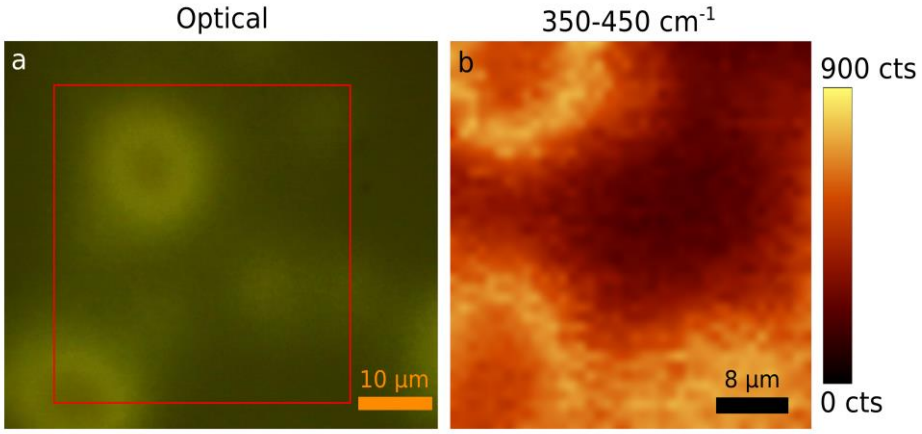

Figure 4.5 (a) Optical image of MoS_2/an-C:$N_{Graphitic}$ with the 40 × 40 µm area of the Raman scan shown in red. (b) Heat map of intensity maximum between 350 and 450 cm^{-1} of the 40 × 40 spectra scanned over the area.

The composition of the heterostructured films was investigated using XPS. Survey spectra of MoS_2 grown on an-C:$N_{Graphitic}$ and an-C:$N_{Pyridinic}$ are shown in Figure 4.. Both survey spectra show peaks at binding energies corresponding to O 1s (532 eV), Mo 3p/N 1s (400 eV), C 1s (285 eV), Mo 3d (230 eV) and S 2p (164 eV).[14] The XPS was carried out on heterostructures deposited on Si wafers, but no Si signal was observed in the XPS, further supporting that the heterostructure provides full coverage of the Si surface, even after CVD of MoS_2. Quantification of the samples was done from high resolution spectra. The obtained results are summarized in Table 4.1. Analysis of the nitrogen composition was not possible, as the N 1s core level overlaps with the Mo 3p core level.

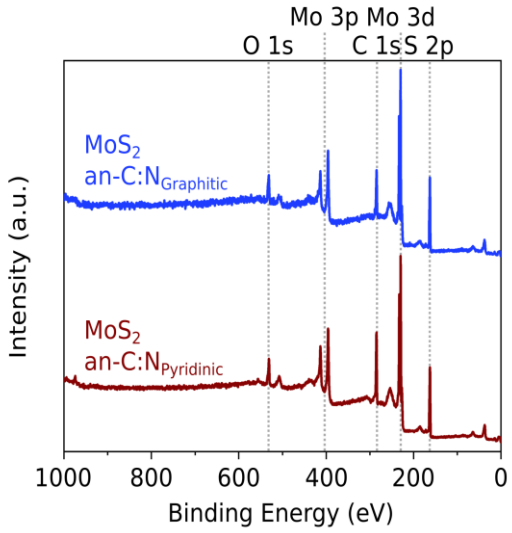

Figure 4.6 XPS spectra for MoS_2 supported by an-C:$N_{Graphitic}$ and an-C:$N_{Pyridinic}$ on a silicon wafer.

Table 4.1 Atomic composition of MoS_2 grown on an-C:$N_{Graphitic}$ and an-C:$N_{Pyridinic}$.

	MoS_2 an-C:$N_{Graphitic}$	**MoS_2 an-C:$N_{Pyridinic}$**
Mo (%)	18.4	15.1
S (%)	30.9	25.7
O (%)	13.3	9.2
C (%)	37.4	50

Best fits were obtained for the S 2p and the Mo 3d core level, shown in Figure 4.. The best fits for the Mo 3d peak were obtained by fitting one doublet corresponding to Mo^{+4} and one doublet corresponding to Mo^{+6}, with the $3d_{5/2}$ peaks at 229.5 eV and 233 eV, respectively.[15, 16] In addition to the two doublets a peak to account for the S 2s core level was fitted at 226.5 eV. The S 2p peak was fitted using a doublet with the $2p_{3/2}$ peak at *ca.* 164.5 eV.[17]

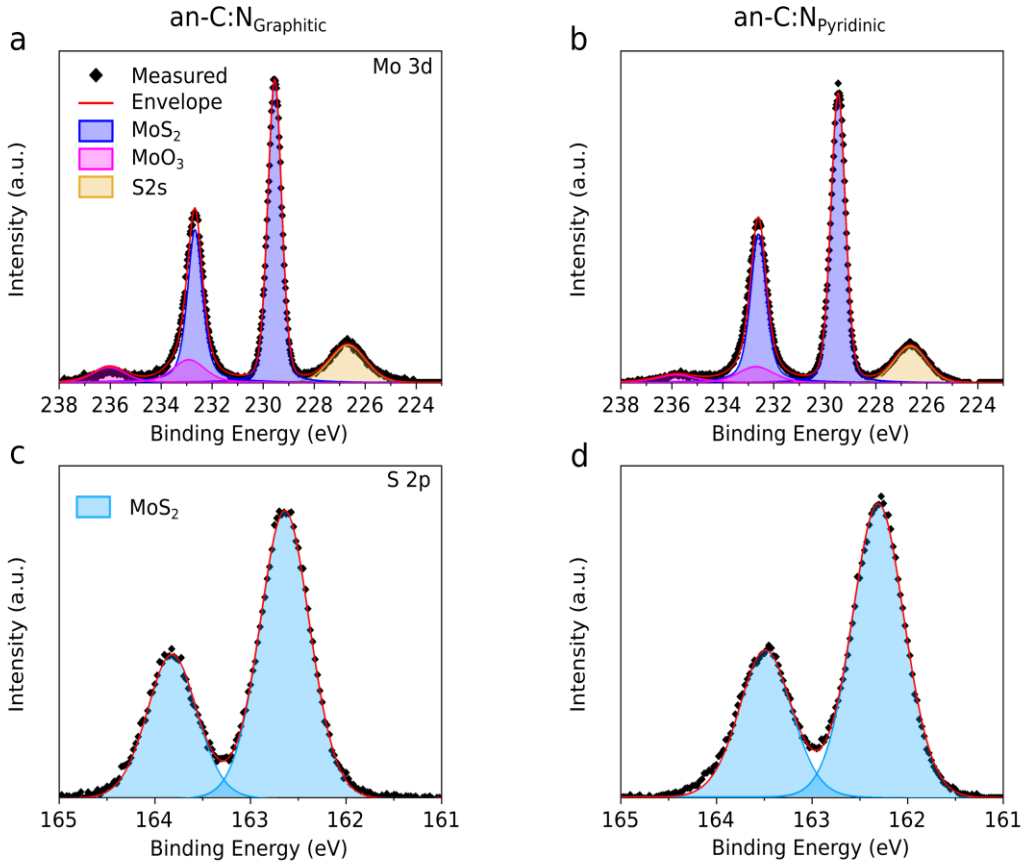

Figure 4.7 Best fits for the XPS spectra of the (a)(b) Mo 3d and (c)(d) S 2p core level for (a)(c) MoS_2 on an-C:$N_{Graphitic}$ and (b)(d) MoS_2 on an-C:$N_{Pyridinic}$.

Best fits were used for determination of the stoichiometry of the Mo S_2, by correlating the contribution of the Mo^{+4} peak to the S 2p peak area. Results summarised in

Table 4.2 4.2 show that the CVD process yielded a slightly sub stoichiometric molybdenum disulfide, with $MoS_{1.93}$ and $MoS_{1.96}$ stoichiometries for CVD growth onto an-C:$N_{Graphitic}$ and an-C:$N_{Pyridinic}$. The %-contributions of Mo^{+4} to the total Mo signal were also found to be similar on both carbon substrates. The negligible differences observed suggest that the growth of MoS_2 occurs independently of the degree or type of nitrogenation of the carbon.

Table 4.2 Percentage of MoS_2 and ratio of S:Mo obtained for MoS2 grown on the two nitrogenated carbons.

	MoS_2 in Mo	**S:Mo**
MoS_2 an-C:$N_{Graphitic}$	86.9%	1.93
MoS_2 an-C:$N_{Pyridinic}$	87.3%	1.96

SEM imaging gave insights on the morphology of the MoS_2/an-C:N heterostructures. Figure 4.a shows the SEM image of MoS_2/an-C:$N_{Graphitic}$; the heterogeneity can be seen, as well as a structured surface. Figure 4.8b shows the SEM image of the heterostructured film peeled off a Si wafer with a razor blade. It can be seen that a polycrystalline film is grown over large parts of the surface of the underlying film. A more detailed picture was obtained via TEM imaging of the peeled film, as shown in Figure 4.8c and 4.8d. Figure 4.8c evidences the polycrystalline nature of the film and the presence of carbon underlayer. The average crystallite size in this region was found to be 53 ± 8 nm. On the edges of some crystals the layered structure of the MoS_2 can be seen, as highlighted in Figure 4.8d. The spacing was found to be 0.74 ± 0.1 nm, which is in the range of the spacing of 0.65 nm reported for MoS_2.[18]

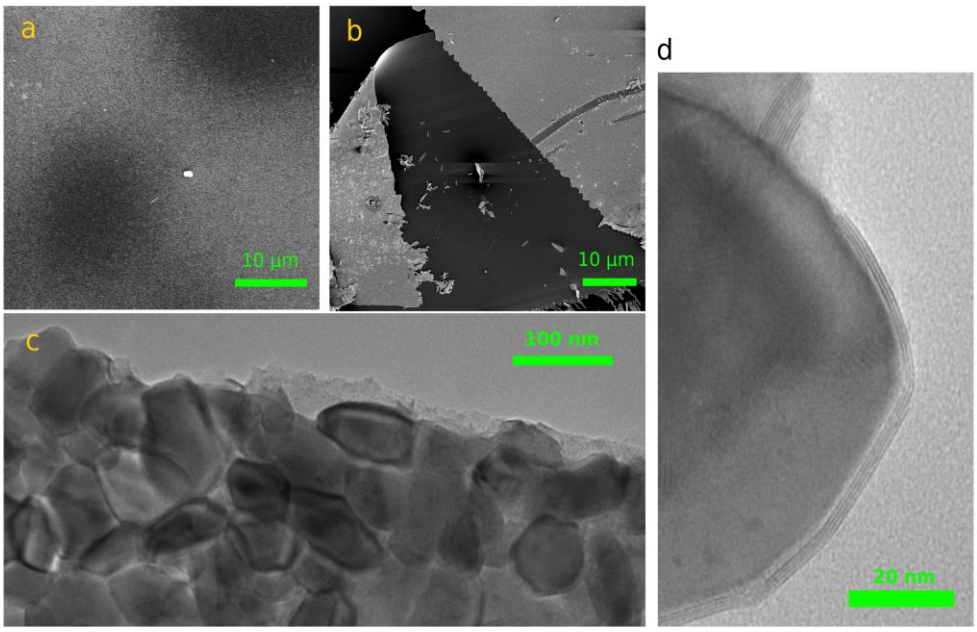

Figure 4.8 (a) SEM image of MoS_2/an-C:$N_{Graphitic}$ with InLens detector. (b) SEM image of the heterostructure peeled of a Si wafer. (c)(d) TEM images of the peeled of MoS_2/an-C:$N_{Graphitic}$.

Overall, these results suggest that MoS_2 was successfully grown on the nitrogenated carbon substrate. A polycrystalline film that covers the majority of the carbon substrate was grown. The conductive carbon support is still present after the CVD process and there seems to be close contact between the MoS_2 and the nitrogenated carbon. No significant difference between the growth on an-C:$N_{Graphitic}$ and anC:$N_{Pyridinic}$ was found.

4.3. MoS_2/N-carbon as electrocatalyst

4.3.1. Hydrogen evolution reaction

The electrochemical response of the synthesised MoS_2/N-carbon films was first investigated in the HER. Linear sweep voltammetry in 0.1 M H_2SO_4 as well as the obtained descriptors for the HER are shown in Figure 4.. The voltammograms show that the current response for the MoS_2 grown on the two nitrogenated carbons does not differ significantly. For both films a clear improvement of the HER response was found compared to the N-carbon films. An overpotential at 1 mA/cm^2 of *ca.* 0.3 V vs RHE was found for the heterostructured films, which is a notable improvement compared to the bare metal-free carbon films, where the onset was found to be around -0.7 V as discussed in chapter 3.

Finally, the overpotential of the heterostructured electrodes is in good agreement with values observed in the literature for MoS_2 on other carbon supports.[19, 20]

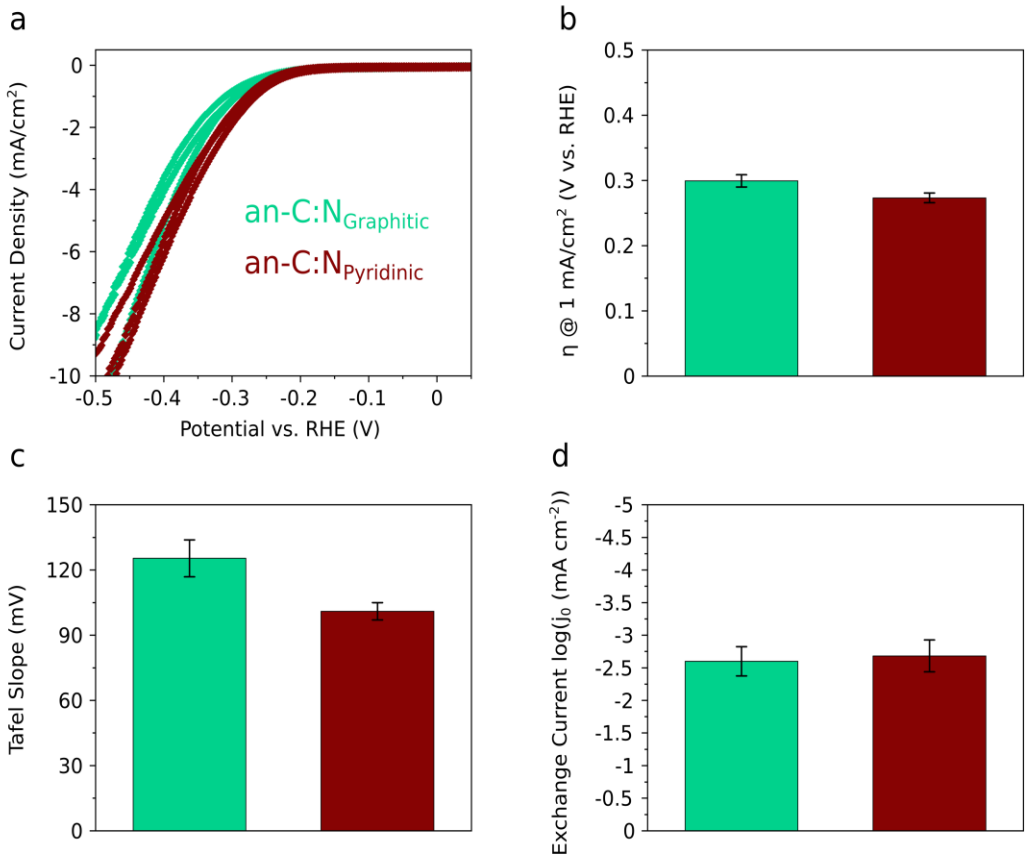

Figure 4.9 (a) Linear sweep voltammograms at 2 mV/s of MoS_2 grown on an-C:$N_{Graphitic}$ and an-C:$N_{Pyridinic}$ in 0.1 M H_2SO_4, and the obtained (b) overpotentials at 1 mA/cm^2, (c) Tafel slopes and (d) exchange current densities. Adapted from Nolan et al.[21]

A further comparison of the observed HER activity descriptors and values reported in literature for MoS_2 on different support materials is shown in Table 4.3. The Tafel slope of *ca.* 120 mV indicates that for the films the Volmer step is rate determining.[22] An exchange current density between -2.5 and -3 log(mA/cm^2) was found for both films, indicating good activity in the HER; these values are in good agreement with those reported for other MoS_2 electrodes, as summarised in Table 4.3. This indicates that the synthesis route effectively "wires" the MoS_2 to the nitrogenated carbons.

Table 4.3 Comparison of onset potential, Tafel slope and exchange current density for the HER in acidic conditions on MoS_2 materials reported in literature.

	η@1mA/cm^2 (V vs RHE)	**Tafel Slope (mV)**	**log(j_0) (mA/cm^2)**	**Reference**
MoS_2/an-C:$N_{Graphitic}$ 0.1 M H_2SO_4	-0.299 ± 0.008	117 ± 12	-2.47 ± 0.1	This Work
MoS_2/an-C:$N_{Pyridinic}$ 0.1 M H_2SO_4	-0.294 ± 0.035	100 ± 5	-3 ± 0.5	This Work
MoS_2 on Au 0.5 M H_2SO_4	ca. -0.16	92	-2.8	23
MoS_2 on GC* 0.5 M H_2SO_4	ca. -0.32	105-120	-5.65	24
MoS_2 on Toray 0.5 M H_2SO_4	ca. -0.29	120	-5.3	20
MoS_2 on GC** 0.5 M H_2SO_4	ca. -0.13	64	-1.65	19
MoS_2^{***} 0.5 M H_2SO_4	ca. -0.21	104	-4.85	25

*Vertically aligned; **monolayer;***mechanically activated

The current response of the linear sweep voltammetry in alkaline conditions (0.1 M KOH) is shown in Figure 4.. The Tafel slopes for both of the nitrogenated carbon supports were found to be greater than 180 mV, suggesting a difference in the nature of the rate limiting step under alkaline conditions as the most probable explanation.[26] In alkaline conditions a difference between the MoS_2 supported on the two nitrogenated carbons is visible. The MoS_2 grown on an-C:$N_{Graphitic}$ performed well in alkaline conditions. The onset potential was found to be slightly more cathodic compared to that in acid electrolytes. The HER on MoS_2/an-C:$N_{Pyridinic}$ thin film electrodes seems to be significantly suppressed, resulting in a more cathodic onset potential. This increase is less significant when comparing η@1mA/cm^2 values but is clearly visible from a comparison between the LSV waveforms.

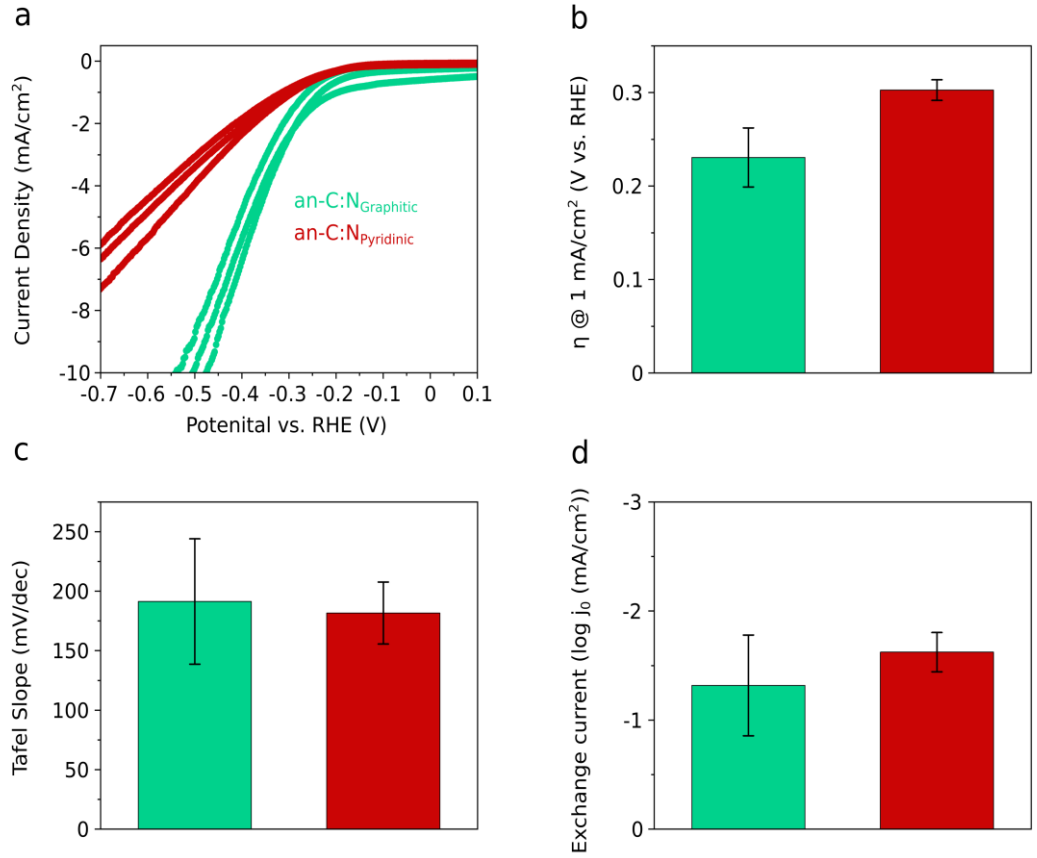

Figure 4.10 (a) Linear sweep voltammograms (2mV/s) of MoS_2 grown on an-C:$N_{Graphitic}$ and an-C:$N_{Pyridinic}$ in 0.1 M KOH, and the obtained (b) Overpotentials for 1 mA/cm^2, (c) Tafel slopes and (d) Exchange current densities. Adapted from Nolan et al.[21]

Overall, results indicate that for MoS_2 in acid there is no evidence that N-functionalities at the carbon support have an impact on the HER activity or its rate limiting step. Given that LSVs obtained via normalization by geometric area yield the same trends, we conclude that the total density of active sites at pH 1 is similar independent of the distribution of N-functionalities displayed at the carbon thin film supports. On the other hand, clear differences emerge at pH 13, and the significant loss of activity observed for MoS_2 at an-C:$N_{Pyridinic}$ relative to an-C:$N_{Graphitic}$ supports indicates that the chemistry of the N-functionalities plays an important role in promoting/inhibiting HER activity under alkaline conditions.

The difference in the HER activity in alkaline electrolyte could be due to differences in the basicity of the N-functionalities present in the carbons. If a pK_a for pyridinic groups is assumed to be similar to the one of pyridine (pK_a = 5.2), a change in pH from 1 to 13 would lead to almost no pyridinic groups being protonated (> 99% at pH 1; < 1 ppm at pH 13). This would result in the lone pair of the deprotonated pyridinic group to be involved in

coordination with Lewis-acids, which is known to take place for example for CO_2 chemisorption.[27, 28] If pyridinic sites are present at the MoS_2-carbon interface, a change in pH is expected to change the electrostatic interactions between the two phases. The basicity of graphitic nitrogen is known to be negligible compared to pyridinic nitrogen sites,[28-30] which is consistent with the lack of pH dependence on the HER activity for MoS_2/an-C:$N_{Graphitic}$. To further investigate this, a deeper study of the pH dependence would be needed.

The known chemistry of pyridinic nitrogen could explain the observed behaviour in the HER in alkaline conditions. We suggest that deprotonation and the resulting availability of the lone-pair leads to suppression of the HER by deactivation of some of the active sites. A similar behaviour was reported by the group for metal-free carbon electrodes in the ORR, where the observed overpotentials changed significantly at pH values close to the expected equivalence point of pyridinium cations.[31]

The MoS_2 activity in electrocatalysis in alkaline conditions is not yet well understood. There is evidence that undercoordinated Mo sites are critical for HER activity. Lewis et al. reported sensitivity of overpotentials against the degree of crystallinity in acidic conditions,[32] while in alkaline conditions an insensitivity to edge/boundary exposure was reported. The authors concluded that in acidic conditions edge sites are the dominating active sites in the HER, while in alkaline solution the basal plane sites become dominant. Li et al.[33] further examined the interplay between S-vacancies, MoS_2 crystallinity and pH conditions, and showed that undercoordinated Mo sites are active at both pH 0 and pH 13. Detailed computational studies of the kinetic barriers involved in the HER at sulfur vacancies reported by Huang et al.[34, 35] further support the role of Mo-centres in the HER; their most recent work confirms that S-vacancies at basal planes are active at both pH 0 and pH 14, with the mono-hydride species MoS-H being the key active site and dihydride formation being the limiting step.

The above results suggest that the extent of TMDC-substrate coupling to Mo-centres at or near S-vacancies should have significant effects on activity, as a good coupling is needed for electrocatalytic activity. The interactions that modulate coupling at Mo-centres in the basal plane might be particularly important to explain activity changes in alkaline electrolytes. Pyridinic N-functionalities offer an attractive and rather unique route to achieving pH-switching of TMDC-carbon coupling to Mo-centres. At low pH, sulfide-pyridinium interactions across the MoS_2 plane are electrostatically favourable and can

facilitate a close approach of Mo-centres to the conductive carbon support. At high pH, on the other hand, sulfide-lone pair interactions are repulsive, and should therefore decrease the TMDC-support coupling. Interestingly, the switching behaviour should affect isolated Mo-centres at basal plane S-vacancies to a greater extent, as these are surrounded by sulphide neighbours, while undercoordinated Mo at edges would be less affected by repulsive interactions between the carbon and the sulfide plane and might even be stabilized by the Mo–N Lewis acid-base interactions, as proposed in computational studies.[36]

It is interesting to note that the recent work by Qin et al.[36] on few-layer MoS_2 supported on N-doped graphene shows that pyridinic-N is positively correlated with HER activity in both acid and base. The apparent contradiction between their findings and ours is however resolved when noting that the TMDC/N-graphene electrocatalysts used in their work consist of vertically aligned MoS_2 layers relative to the N-graphene planes. In fact, their computational results confirm that attractive interactions between undercoordinated Mo-centres at edges and pyridinic-N stabilize edge-on assembly of the two 2D nanomaterials, while stable parallel geometries were not observed. In the case of our work, the use of a thin film carbon electrode as substrate for the CVD growth forces the formation of large areas of basal plane MoS_2-carbon contacts, leading to average TMDC-carbon contact distances that will strongly depend on the presence of protons for screening sulfide-lone pair repulsions.

4.3.2. ECH of benzaldehyde on MoS_2 on N-carbon

The LSV curves in the presence of benzaldehyde are shown in Figure 4.. It can be seen that the presence of benzaldehyde leads only to a slight suppression of the HER and the measured currents. No cathodic peaks were observed in either H_2SO_4 or Na_2SO_4 supporting electrolyte. The suppression of the HER current, observed on the MoS_2/an-C:$N_{Graphitic}$ is less pronounced compared to the suppression found in bare carbons. The suppression of the HER in the presence of benzaldehyde can potentially indicate to adsorption and competition over the catalytic sites.[37]

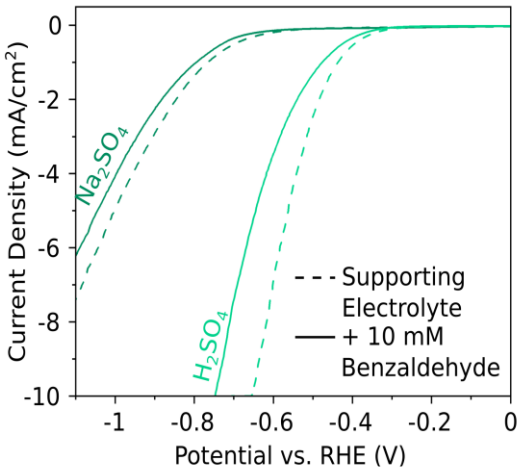

Figure 4.11 Current response of linear sweep voltammetry (2 mV/s) om 0.1 M H_2SO_4 and Na_2SO_4 with (solid lines) and without (dashed lines) 10 mM benzaldehyde on MoS_2/an-C:$N_{Graphitic}$ heterostructures.

On the heterostructured electrodes, the suppression observed in the cathodic current is less prominent compared to the ones observed on the bare carbons in Chapter 3. This could indicate that the relatively high activity in the HER, results from preferred adsorption of the hydrogen. This is supported by looking at the adsorption strength of benzaldehyde on the materials. Patil and Caffrey have reported similar adsorption energies for benzaldehyde on MoS_2 and on graphene.[38] If similar binding is assumed, the lower suppression is likely due to differences in activity towards hydrogen activation and adsorption.

To investigate differences between the electrocatalytic response of MoS_2 grown on the two different nitrogenated carbons, electrolysis in acidic conditions was carried out for 4 h under static conditions at -0.8 V vs Ag/AgCl and with 10 or 20 mM concentration of benzaldehyde. The reduction rate and the faradaic efficiencies are shown in Figure 4.. While no difference was observed for the reduction rate with 10 mM benzaldehyde, MoS_2/an-C:$N_{Graphitic}$ shows a slightly better faradaic efficiency. A similar observation was made for electrolysis with a 20 mM concentration. For both types of heterostructures an increase in reduction rate and faradaic efficiency was observed. As was the case for the lower concentration of benzaldehyde, a better faradaic efficiency for organic reductions was observed for the MoS_2 grown on the carbon with more graphitic nitrogen. The slightly better faradaic efficiency on an-C:$N_{Graphitic}$ supported MoS_2 is the reason while only this type of electrode is used in the rest of this work.

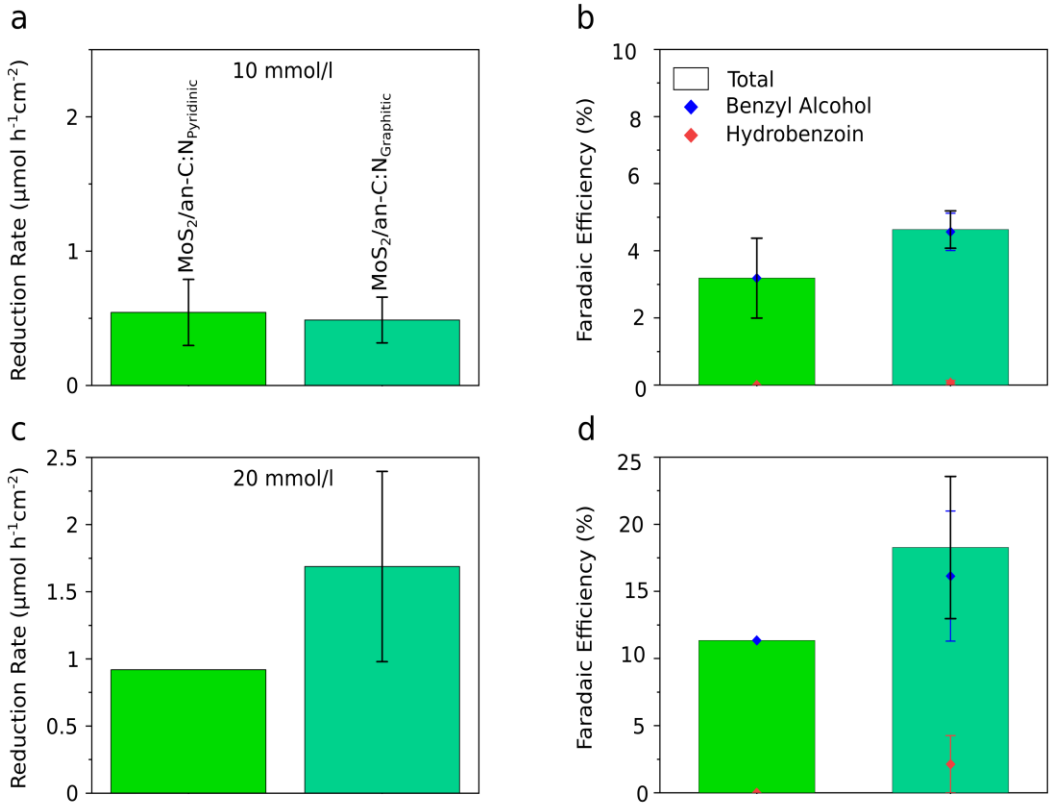

Figure 4.12 (a, c) Reduction rates of benzaldehyde and (b, d) faradaic efficiencies after 4 h electrolysis experiments at MoS_2 grown on the nitrogenated carbon support with a concentration of (a, b) 10 mM and (c, d) 20 mM benzaldehyde in 0.1 M H_2SO_4 at -0.5 V vs RHE without stirring. Error bars indicate standard errors.

The potential dependence under static conditions was tested in a first step, to gain more insights into the ECH response of the MoS_2/N-carbon heterostructures. A benzaldehyde concentration of 10 mM was used and the potential was applied for 4 h. The obtained descriptors are shown in Figure 4.. It can be seen that with increasing cathodic potential the reduction rate of benzaldehyde increases. A similar trend was observed for the production rates of benzyl alcohol and hydrobenzoin. Generation of the dimerization product starts only at an applied potentials of -0.5 V vs RHE. This can also be seen in the selectivity, where only benzyl alcohol is produced at potentials less cathodic than -0.5 V. The faradaic efficiency of organic reduction increases from -0.3 V to -0.6 V, before decreasing again. The relatively low faradaic efficiency could be due to the lack of stirring, which over the course of four hours leads to benzaldehyde depletion of the electrolyte in proximity of the electrode.

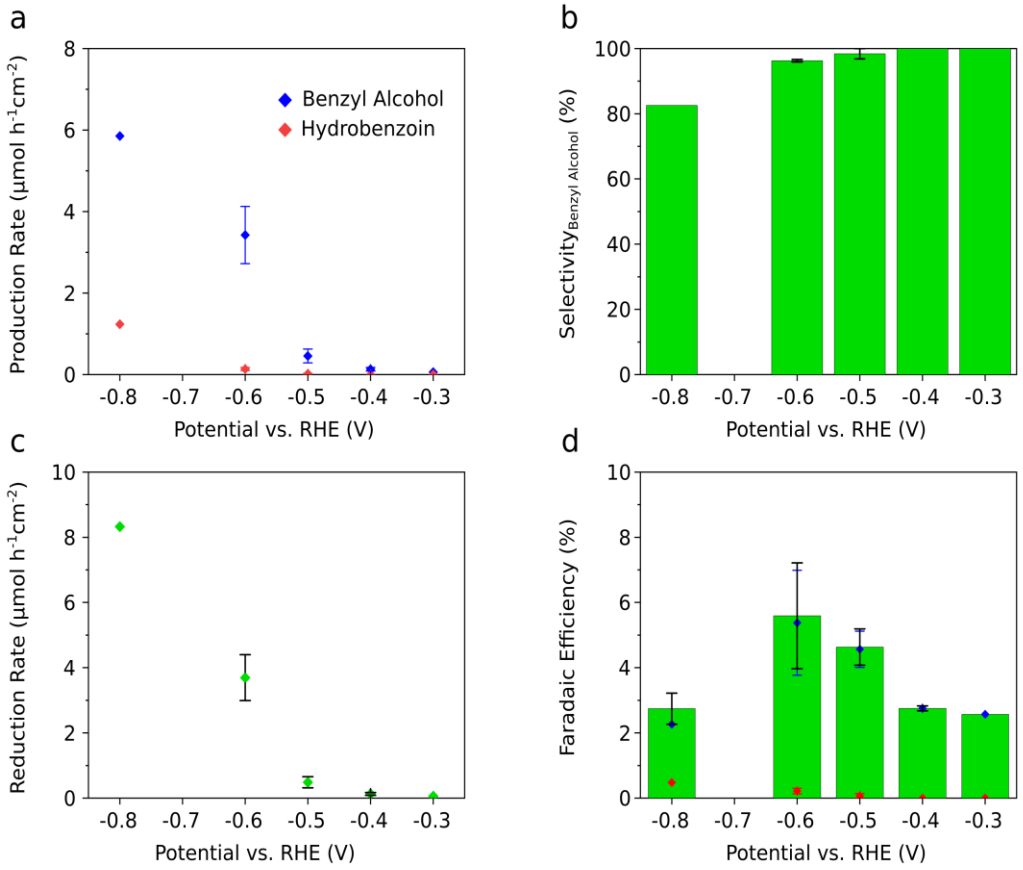

Figure 4.13 Results of electrolysis experiments using MoS_2/an-C:$N_{Graphitic}$. (a) Production rate for benzyl alcohol and hydrobenzoin, (b) selectivity towards benzyl alcohol, (c) reduction rate of benzaldehyde and (d) the faradaic efficiency in 0.1 M H_2SO_4 with 10 mM benzaldehyde without stirring.

Figure 4. shows a comparison of electrolysis in 10 and 20 mM benzaldehyde solutions. The reduction rate and faradaic efficiency increase significantly by increasing the concentration of organic substrate. The mean selectivity towards benzyl alcohol appears to decrease slightly when more benzaldehyde is present, although the change is not statistically significant.

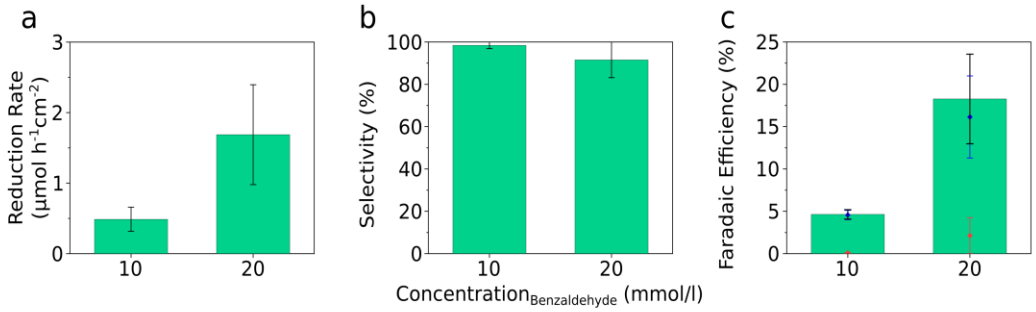

Figure 4.14 Comparison of (a) reduction rate (b) selectivity towards benzyl alcohol and (c) faradaic efficiency obtained for electrolysis on MoS2/an-C:NGraphitic with 10 and 20 mM benzaldehyde in 0.1 M H_2SO_4 at -0.5 V vs RHE without stirring.

These results show that the heterostructured electrodes have a higher production in the ECH of benzaldehyde compared to the bare nitrogenated carbons. The appearance of hydrobenzoin at more cathodic potentials was observed for the nitrogenated carbons as well and could be due to a change in reaction mechanism. The overall production, and reduction rates are still low, indicating that the mass transport might be limiting the reaction, which brings the need for forced convection and stirring of the electrolyte. In the following, electrolysis was carried out for 30 minutes with 20 mM benzaldehyde in 0.1 M H_2SO_4 with a stirring speed of 500 rpm.

The production and reduction rates as well as the selectivity for benzyl alcohol are shown in Figure 4. for the heterostructures. The production rate increases with more cathodic potentials and as observed for electrolysis under static conditions, the production of hydrobenzoin occurs only at potentials more cathodic than -0.5 V vs. RHE. At a cathodic potential of -0.7 V vs. RHE the production rate for the dimerization is superior that of benzyl alcohol. This trend is clearer in the selectivity, which decreases to less than 50% for electrolysis at -0.7 V. Comparing the rates under stirring with the ones without stirring a significant difference is observed at lower potentials, and less for high cathodic potentials. The reason for this could be in the high degree of dimerization at more cathodic potentials or in higher HER activity, which leads to the formation of bubbles and thereby to convection of the electrolyte even in the absence of mechanical agitation.

The faradaic efficiency of the benzaldehyde reduction (Figure 4.15d) was found to increase from <5% at -0.8 V to *ca.* 12% at -0.7 V vs. RHE, with the majority of current contributing to the HER. The FE for the production of benzyl alcohol slightly increases with increasing cathodic potential until -0.6 V vs. RHE. At more cathodic potentials the FE seems to drop down, similar to the selectivity, resulting in more production of hydrobenzoin and similarly higher FE for the hydrobenzoin production. There is, as was observed for the production rates, not much difference between results obtained under quiescent or stirred conditions.

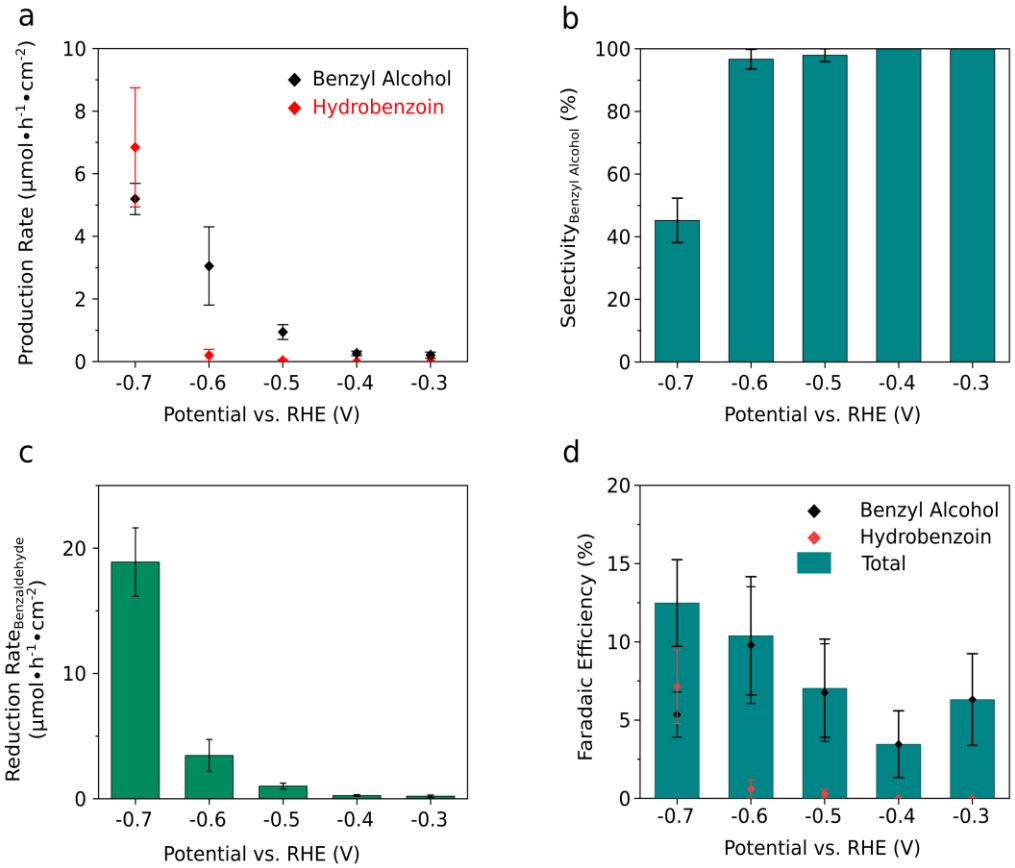

Figure 4.15 (a) Production rate (b) selectivity and (c) reduction rate and (d) faradaic efficiency for electrolysis on MoS_2/an-C:$N_{Graphitic}$ with 500 rpm with 20 mM benzaldehyde in 0.1 M H_2SO_4.

The production rates show that the trends for benzyl alcohol and hydrobenzoin differ. While it appears that the alcohol production rate increases gradually with more cathodic potentials, the production rate for hydrobenzoin shows a drastic jump between -0.6 and -0.7 V vs. RHE. This increase in dimerization rate, which goes hand in hand with the decreased selectivity towards benzyl alcohol, suggests that there could be a potential-dependent change in the mechanism of the ECH.

To classify the performance of the MoS_2/an-C:$N_{Graphitic}$ heterostructured electrocatalyst and to make it comparable with other catalyst materials reported in literature, the loading of MoS_2 was quantified. This was done by electrooxidizing the MoS_2 as previously reported by Bonde et al.[20] A representative cyclic voltammetry for this is shown in Figure 4.16. On the first scan, a cathodic current, representative of the HER is seen. On the first anodic scan, around 0.5 V vs. Ag/AgCl a peak is visible. On the second scan, the HER current on the cathodic end is negligible and the oxidation peak is no longer visible. This peak can be

attributed to the oxidation of MoS_2, with the, by Bonde et al. proposed reaction shown below. From the charge of the peak, the loading of MoS_2 can thus be determined.

$$MoS_2 + 7\,H_2O \rightarrow MoO_3 + SO_4^{2-} + {}^1/_2\,S_2^{2-} + 14\,H^+ + 11\,e^- \qquad (4.3)$$

For the electrodes used in this work an average loading of 6.4 ± 3 nmol/cm^2 was found. This loading translates to a mass loading of about 1 µg/cm^2. This is significantly smaller compared to values used in literature. A comparison is shown in Table 4.4.

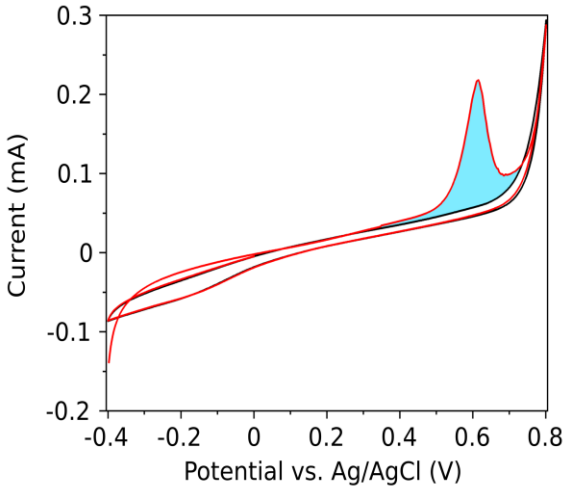

Figure 4.16 Representative cyclic voltammogram (2 mV/s) for the oxidation of MoS_2 in 0.1 M H_2SO_4.

Table 4.4 Comparison of MoS_2 mass loading reported in literature with this work.

	Mass Loading	**Reference**
CVD MoS2	1 µg/cm^2	This Work
MoS_2 on carbon black	0.14 – 1 mg/cm^2	39
MoS_2 / Carbon	0.07 - 0.28 mg/cm^2	1
MoS_2 on GC	0.28 mg/cm^2	40

With the loading of MoS_2, the production rates can be normalised to the loading of MoS_2 and a turnover frequency (TOF) can be obtained (Figure 4.17) assuming that at lower potentials the activity of the N-carbon is negligible. The TOFs of the catalyst follow the same trend. The TOF for the ECH at -0.5 and -0.6 V vs. RHE changes only slightly from 0.13 s^{-1} to 0.17 s^{-1} respectively. ECH at -0.7 V vs. RHE leads to a tenfold increase in the TOF, again supporting the idea that there is a change in the reaction pathway.

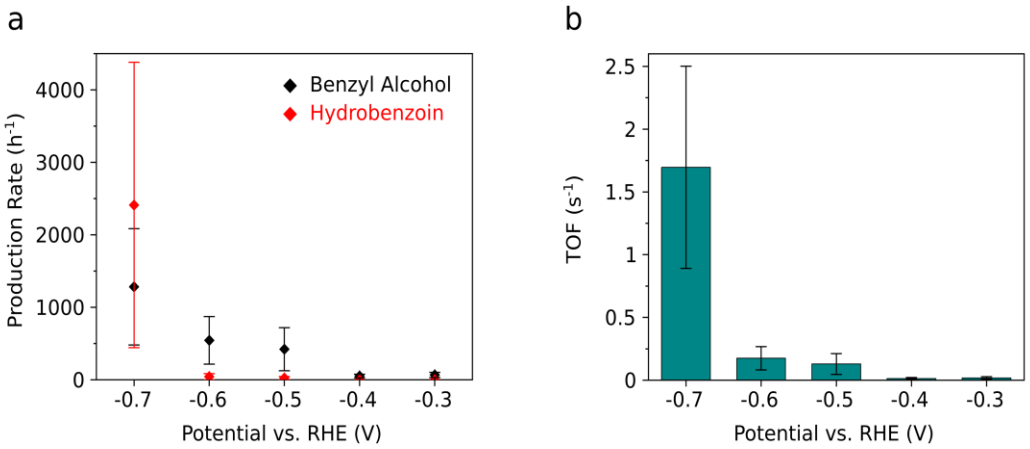

Figure 4.17 (a) Production rate and (b) turn over frequency, normalised by the loading of MoS_2.

The normalisation for MoS_2 loading considers any homogeneities during the synthesis of the films and makes it possible to compare the material with literature. Lopez-Ruiz et al.[41] investigated the ECH of different organic compounds on different metals. The authors report a TOF for Pd, the 'gold' standard of ECH for benzaldehyde, of around 500 h^{-1} at -1.2 V vs Ag/AgCl in an electrolyte composed of 47.5 wt % isopropanol, 47.5 wt % H_2O, and 5 wt % acetic acid. The reported TOF of around 500 h^{-1} is similar compared to the performance of the MoS_2/an-C:$N_{Graphitic}$ heterostructure presented in this work, which translates to reduction rates of 468 h^{-1} and 612 h^{-1} for ECH at -0.5 and -0.6 V vs RHE respectively. While Lopez-Ruiz et al. report higher faradaic efficiencies, it needs to be mentioned, that the reaction conditions are not the same, with a different electrolyte and higher benzaldehyde concentration in the cited work.

Song et al.[42] also investigated the ECH of benzaldehyde on different carbon supported metals and found TOFs from below 500 h^{-1} up to around 4000 h^{-1} in a potential range between -0.5 and -0.9 V vs. Ag/AgCl (*ca.* 0 to -0.4 V vs. RHE) on Rh/C, Pt/C and Pd/C. These materials show a higher activity in the ECH and achieve similar TOFs to the ones presented in this chapter, at lower potentials. By optimising the electrolyte and reaction conditions an improved activity on the MoS_2/N-carbon heterostructures should be achieved. The comparison of the performance of the MoS_2/an-C:$N_{Graphitic}$ to the performance on the metals reported in literature, shows that the approach of our heterostructured catalyst material is promising, especially considering the significant lower price of MoS_2 compared to the precious metals.

Even with a relatively low loading of MoS_2 compared to other reports in literature, it was possible to obtain promising electrocatalytic activity. The effect of an increased mass loading should be investigated in future works.

The significant increase in organic reduction at -1 V suggests a change in the reaction pathway of the hydrogenation. Cantu et al.[43] reported the potential dependent free energies for different reaction pathways for the reduction of benzaldehyde. According to the authors, at less cathodic potentials a concerted reaction mechanism is more favourable, which is the addition of an adsorbed hydrogen. At more cathodic potentials, a sequential electron and proton transfer will have lower free energies, resulting in a higher rate of ketyl radical formation, which will lead to more dimerization. The report found that the potential at which the change of most favourable pathway occurs is dependent on the catalyst material. The group of Lessard have previously reported the difference between electrocatalytic hydrogenation and a reaction pathway they call electronation-protonation.[44] The electronation-protonation pathway will lead to an increased production of ketyl radicals, which will lead to more hydrobenzoin produced.

The investigated MoS_2/an-C:$N_{Graphitic}$ heterostructures show good performance, e.g. high selectivity towards benzyl alcohol with promising production rates/TOFs. The relatively low faradaic efficiencies compared to some of the metal catalysts reported in literature indicate that the catalyst's performance in the HER still remain dominant under the tested conditions. Future work should focus on changing the reaction conditions, namely pH and organic concentration to supress the HER and try to maintain the ECH activity.

4.4. Conclusion

The MoS_2 did not grow in a mono- or few-layer form. Instead, the CVD process using N-carbon as a growth substrate resulted in a polycrystalline film of MoS_2. Characterisation indicated coverage with MoS_2 over the entirety of the film. The growth of the MoS_2 seems independent of the nitrogenation of the carbon.

The heterostructures showed good activity in the HER, with a suppression of the HER in alkaline conditions for the MoS_2 grown on an-C:$N_{Pyridinic}$. This indicates an effect of a deprotonation/protonation equilibrium of the pyridinic nitrogen groups and resulting attraction or repulsion between the N-sites and the MoS_2. This indicates that the obtained

MoS_2 layer is not fully covering the carbon film, resulting in interactions of the carbon with the electrolyte. Further investigation of this mechanism would be needed.

The high activity in the HER in acidic conditions, resulted in a low faradaic efficiency of the heterostructures in the ECH of benzaldehyde. In contrast to the bare nitrogenated carbon, did the HER activity result in enough convection, so that stirring did not seem to add any benefit. While these results do not seem to be promising, the obtained production rates and TOFs were in a range comparable to metal electrocatalysts.

Future studies on these heterostructures will look at the effect of reaction conditions on the electrocatalytic hydrogenation. Choosing higher pH values and higher concentrations, which has been shown to lower HER currents on electrocatalysts, could potentially lead to an improved ECH activity, especially an improved faradaic efficiency. Increasing the pH will potentially bring a difference between an-C:$N_{Graphitic}$ and an-C:$N_{Pyridinic}$, as was observed for the HER.

References

1. Murthy, A. P.; Theerthagiri, J.; Madhavan, J.; Murugan, K., Highly active MoS2/carbon electrocatalysts for the hydrogen evolution reaction – insight into the effect of the internal resistance and roughness factor on the Tafel slope. *Physical Chemistry Chemical Physics* **2017,** *19* (3), 1988-1998.
2. Li, D. J.; Maiti, U. N.; Lim, J.; Choi, D. S.; Lee, W. J.; Oh, Y.; Lee, G. Y.; Kim, S. O., Molybdenum Sulfide/N-Doped CNT Forest Hybrid Catalysts for High-Performance Hydrogen Evolution Reaction. *Nano Letters* **2014,** *14* (3), 1228-1233.
3. Bian, X.; Zhu, J.; Liao, L.; Scanlon, M. D.; Ge, P.; Ji, C.; Girault, H. H.; Liu, B., Nanocomposite of MoS_2 on ordered mesoporous carbon nanospheres: A highly active catalyst for electrochemical hydrogen evolution. *Electrochemistry Communications* **2012,** *22*, 128-132.
4. Cao, J.; Zhou, J.; Zhang, Y.; Liu, X., A Clean and Facile Synthesis Strategy of MoS2 Nanosheets Grown on Multi-Wall CNTs for Enhanced Hydrogen Evolution Reaction Performance. *Scientific Reports* **2017,** *7* (1), 8825.
5. Chen, X.; Zhang, K.; An, Z.; Wang, L.; Wang, Y.; Sun, S.; Guo, T.; Zhang, D.; Xue, Z.; Zhou, X., Facile synthesis of MoS_2/N-doped macro-mesoporous carbon hybrid as efficient electrocatalyst for hydrogen evolution reaction. *International Journal of Hydrogen Energy* **2018,** *43* (15), 7326-7337.
6. Gnanasekar, P.; Periyanagounder, D.; Kulandaivel, J., Vertically aligned MoS_2 nanosheets on graphene for highly stable electrocatalytic hydrogen evolution reactions. *Nanoscale* **2019,** *11* (5), 2439-2446.
7. He, M.; Kong, F.; Yin, G.; Lv, Z.; Sun, X.; Shi, H.; Gao, B., Enhanced hydrogen evolution reaction activity of hydrogen-annealed vertical MoS_2 nanosheets. *RSC Advances* **2018,** *8* (26), 14369-14376.
8. Li, H.; Liu, X.; Chen, S.; Yang, D.; Zhang, Q.; Song, L.; Xiao, H.; Zhang, Q.; Gu, L.; Wang, X., Edge-Exposed Molybdenum Disulfide with N-Doped Carbon Hybridization: A Hierarchical Hollow Electrocatalyst for Carbon Dioxide Reduction. *Advanced Energy Materials* **2019,** *9* (18), 1900072.
9. Lv, K.; Suo, W.; Shao, M.; Zhu, Y.; Wang, X.; Feng, J.; Fang, M.; Zhu, Y., Nitrogen doped MoS2 and nitrogen doped carbon dots composite catalyst for electroreduction CO2 to CO with high Faradaic efficiency. *Nano Energy* **2019,** *63*, 103834.
10. O'Brien, M.; McEvoy, N.; Hallam, T.; Kim, H.-Y.; Berner, N. C.; Hanlon, D.; Lee, K.; Coleman, J. N.; Duesberg, G. S., Transition Metal Dichalcogenide Growth via Close Proximity Precursor Supply. *Scientific Reports* **2014,** *4* (1), 7374.
11. Ferrari, A. C.; Robertson, J., Raman spectroscopy of amorphous, nanostructured, diamond–like carbon, and nanodiamond. *Philosophical Transactions of the Royal Society of London A: Mathematical, Physical and Engineering Sciences* **2004,** *362* (1824), 2477-2512.
12. Zhang, X.; Han, W. P.; Wu, J. B.; Milana, S.; Lu, Y.; Li, Q. Q.; Ferrari, A. C.; Tan, P. H., Raman spectroscopy of shear and layer breathing modes in multilayer MoS_2. *Physical Review B* **2013,** *87* (11), 115413.
13. Yu, Y.; Nam, G.-H.; He, Q.; Wu, X.-J.; Zhang, K.; Yang, Z.; Chen, J.; Ma, Q.; Zhao, M.; Liu, Z.; Ran, F.-R.; Wang, X.; Li, H.; Huang, X.; Li, B.; Xiong, Q.; Zhang, Q.; Liu, Z.; Gu, L.; Du, Y.; Huang, W.; Zhang, H., High phase-purity 1T′-MoS2- and 1T′-MoSe2-layered crystals. *Nature Chemistry* **2018,** *10* (6), 638-643.
14. Laursen, A. B.; Pedersen, T.; Malacrida, P.; Seger, B.; Hansen, O.; Vesborg, P. C. K.; Chorkendorff, I., MoS2—an integrated protective and active layer on n+p-Si for solar H2 evolution. *Physical Chemistry Chemical Physics* **2013,** *15* (46), 20000-20004.

15. Baker, M. A.; Gilmore, R.; Lenardi, C.; Gissler, W., XPS investigation of preferential sputtering of S from MoS_2 and determination of MoSx stoichiometry from Mo and S peak positions. *Applied Surface Science* **1999,** *150* (1), 255-262.
16. Nielsen, J. H.; Bech, L.; Nielsen, K.; Tison, Y.; Jørgensen, K. P.; Bonde, J. L.; Horch, S.; Jaramillo, T. F.; Chorkendorff, I., Combined spectroscopy and microscopy of supported MoS_2 nanoparticles. *Surface Science* **2009,** *603* (9), 1182-1189.
17. Rumble Jr, J.; Bickham, D.; Powell, C., The NIST x-ray photoelectron spectroscopy database. *Surface and interface analysis* **1992,** *19* (1-12), 241-246.
18. Radisavljevic, B.; Radenovic, A.; Brivio, J.; Giacometti, V.; Kis, A., Single-layer MoS2 transistors. *Nature Nanotechnology* **2011,** *6* (3), 147-150.
19. Li, G.; Chen, Z.; Li, Y.; Zhang, D.; Yang, W.; Liu, Y.; Cao, L., Engineering Substrate Interaction To Improve Hydrogen Evolution Catalysis of Monolayer MoS_2 Films beyond Pt. *ACS Nano* **2020,** *14* (2), 1707-1714.
20. Bonde, J.; Moses, P. G.; Jaramillo, T. F.; Nørskov, J. K.; Chorkendorff, I., Hydrogen evolution on nano-particulate transition metal sulfides. *Faraday Discussions* **2009,** *140* (0), 219-231.
21. Nolan, H.; Schröder, C.; Brunet-Cabré, M.; Pota, F.; McEvoy, N.; McKelvey, K.; Perova, T. S.; Colavita, P. E., MoS_2/carbon heterostructured catalysts for the hydrogen evolution reaction: N-doping modulation of substrate effects in acid and alkaline electrolytes. *Carbon* **2023,** *202*, 70-80.
22. Shinagawa, T.; Garcia-Esparza, A. T.; Takanabe, K., Insight on Tafel slopes from a microkinetic analysis of aqueous electrocatalysis for energy conversion. *Scientific Reports* **2015,** *5* (1), 13801.
23. Li, H.; Wu, H.; Yuan, S.; Qian, H., Synthesis and characterization of vertically standing MoS2 nanosheets. *Scientific Reports* **2016,** *6* (1), 21171.
24. Kong, D.; Wang, H.; Cha, J. J.; Pasta, M.; Koski, K. J.; Yao, J.; Cui, Y., Synthesis of MoS2 and MoSe2 Films with Vertically Aligned Layers. *Nano Letters* **2013,** *13* (3), 1341-1347.
25. Wang, D.; Wang, Z.; Wang, C.; Zhou, P.; Wu, Z.; Liu, Z., Distorted MoS2 nanostructures: An efficient catalyst for the electrochemical hydrogen evolution reaction. *Electrochemistry Communications* **2013,** *34*, 219-222.
26. Fletcher, S., Tafel slopes from first principles. *Journal of Solid State Electrochemistry* **2009,** *13* (4), 537-549.
27. Kiuchi, H.; Shibuya, R.; Kondo, T.; Nakamura, J.; Niwa, H.; Miyawaki, J.; Kawai, M.; Oshima, M.; Harada, Y., Lewis Basicity of Nitrogen-Doped Graphite Observed by CO_2 Chemisorption. *Nanoscale Research Letters* **2016,** *11* (1), 127.
28. Lim, G.; Lee, K. B.; Ham, H. C., Effect of N-Containing Functional Groups on CO_2 Adsorption of Carbonaceous Materials: A Density Functional Theory Approach. *Journal of Physical Chemistry C* **2016,** *120* (15), 8087-8095.
29. Bitter, J. H.; van Dommele, S.; de Jong, K. P., On the virtue of acid–base titrations for the determination of basic sites in nitrogen doped carbon nanotubes. *Catalysis Today* **2010,** *150* (1), 61-66.
30. Shimoyama, I.; Wu, G.; Sekiguchi, T.; Baba, Y., Study of electronic structure of graphite-like carbon nitride. *Journal of Electron Spectroscopy and Related Phenomena* **2001,** *114-116*, 841-848.
31. Behan, J. A.; Iannaci, A.; Domínguez, C.; Stamatin, S. N.; Hoque, M. K.; Vasconcelos, J. M.; Perova, T. S.; Colavita, P. E., Electrocatalysis of N-doped carbons in the oxygen reduction reaction as a function of pH: N-sites and scaffold effects. *Carbon* **2019,** *148*, 224-230.
32. Wiensch, J.; John, J.; Velazquez, J.; Torelli, D.; Pieterick, A.; McDowell, M.; Sun, K.; Zhao, X.; Brunschwig, B.; Lewis, N., Comparative Study in Acidic and Alkaline

Media of the Effects of pH and Crystallinity on the Hydrogen-Evolution Reaction on MoS_2 and $MoSe_2$. *ACS Energy Letters* **2017,** *2*, 2234-2238.
33. Li, L.; Qin, Z.; Ries, L.; Hong, S.; Michel, T.; yang, J.; Salameh, C.; Bechelany, M.; Miele, P.; Kaplan, D.; Chhowalla, M.; Voiry, D., Role of Sulfur Vacancies and Undercoordinated Mo Regions in MoS_2 Nanosheets toward the Evolution of Hydrogen. *ACS Nano* **2019,** *13* (6), 6824-6834.
34. Huang, Y.; Nielsen, R. J.; Goddard, W. A., Reaction Mechanism for the Hydrogen Evolution Reaction on the Basal Plane Sulfur Vacancy Site of MoS_2 Using Grand Canonical Potential Kinetics. *Journal of the American Chemical Society* **2018,** *140* (48), 16773-16782.
35. Huang, Y.; Nielsen, R. J.; Goddard, W. A.; Soriaga, M. P., The Reaction Mechanism with Free Energy Barriers for Electrochemical Dihydrogen Evolution on MoS_2. *Journal of the American Chemical Society* **2015,** *137* (20), 6692-6698.
36. Qin, J.; Xi, C.; Zhang, R.; Liu, T.; Zou, P.; Wu, D.; Guo, Q.; Mao, J.; Xin, H.; Yang, J., Activating Edge-Mo of 2H-MoS_2 via Coordination with Pyridinic N–C for pH-Universal Hydrogen Evolution Electrocatalysis. *ACS Catalysis* **2021,** *11* (8), 4486-4497.
37. Pota, F.; Costa de Oliveira, M. A.; Schröder, C.; Brunet Cabré, M.; Nolan, H.; Rafferty, A.; Jeannin, O.; Camerel, F.; Behan, J. A.; Barrière, F.; Colavita, P. E., Porous N-Doped Carbon-encapsulated Iron as Novel Catalyst Architecture for the Electrocatalytic Hydrogenation of Benzaldehyde. *ChemSusChem n/a* (n/a), e202400546.
38. Patil, U.; Caffrey, N. M., Adsorption of common solvent molecules on graphene and MoS2 from first-principles. *The Journal of Chemical Physics* **2018,** *149* (9).
39. Xue, N.; Diao, P., Composite of Few-Layered MoS2 Grown on Carbon Black: Tuning the Ratio of Terminal to Total Sulfur in MoS2 for Hydrogen Evolution Reaction. *The Journal of Physical Chemistry C* **2017,** *121* (27), 14413-14425.
40. Benson, J.; Li, M.; Wang, S.; Wang, P.; Papakonstantinou, P., Electrocatalytic Hydrogen Evolution Reaction on Edges of a Few Layer Molybdenum Disulfide Nanodots. *ACS Applied Materials & Interfaces* **2015,** *7* (25), 14113-14122.
41. Lopez-Ruiz, J. A.; Andrews, E.; Akhade, S. A.; Lee, M.-S.; Koh, K.; Sanyal, U.; Yuk, S. F.; Karkamkar, A. J.; Derewinski, M. A.; Holladay, J.; Glezakou, V.-A.; Rousseau, R.; Gutiérrez, O. Y.; Holladay, J. D., Understanding the Role of Metal and Molecular Structure on the Electrocatalytic Hydrogenation of Oxygenated Organic Compounds. *ACS Catalysis* **2019,** *9* (11), 9964-9972.
42. Song, Y.; Sanyal, U.; Pangotra, D.; Holladay, J. D.; Camaioni, D. M.; Gutiérrez, O. Y.; Lercher, J. A., Hydrogenation of benzaldehyde via electrocatalysis and thermal catalysis on carbon-supported metals. *Journal of Catalysis* **2018,** *359*, 68-75.
43. Cantu, D. C.; Padmaperuma, A. B.; Nguyen, M.-T.; Akhade, S. A.; Yoon, Y.; Wang, Y.-G.; Lee, M.-S.; Glezakou, V.-A.; Rousseau, R.; Lilga, M. A., A Combined Experimental and Theoretical Study on the Activity and Selectivity of the Electrocatalytic Hydrogenation of Aldehydes. *ACS Catalysis* **2018,** *8* (8), 7645-7658.
44. Chan-Shing, E. S.; Boucher, D.; Lessard, J., The electrochemical reduction of α-nitrocumene in a protic and basic medium on large surface area (porous) electrodes: electronation-protonation or electrocatalytic hydrogenation? *Canadian Journal of Chemistry* **1999,** *77* (5-6), 687-694.

Chapter V

5. Carbon encapsulated copper

The results presented in this chapter have in part been published in peer-reviewed journals in the following articles:

Christian Schröder, Lua Henderson, Filippo Pota, Kiaya Doyle, Paula E. Colavita: ”Modulating the Electrocatalytic Hydrogenation of Benzaldehyde on Cu@ C Electrode Materials”, The Journal of Physical Chemistry C, **2025**, 129(15), 7217-7224.

5.1. Introduction

While precious metals like platinum remain highly effective electrocatalysts, transition metals provide a more accessible and cost-effective alternative without too much compromise on the electrocatalytic activity. This can be seen in Figure 5.1. showing linear sweep voltammetry measured on polished disc electrodes of Pt, Au, Cu and GC disk electrodes in acidic conditions. While copper has a higher overpotential for the HER, the lower price and availability compared to precious metals makes it a sought after material in electrocatalysis. For this reason, copper has been intensively studied as an electrocatalyst in the ECH.[1-8]

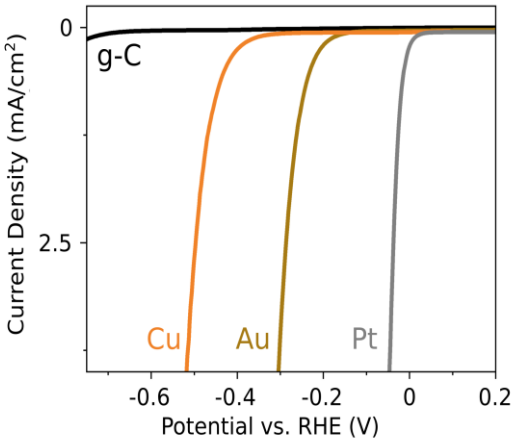

Figure 5.1 Linear sweep voltammetry at 2 mV/s in 0.1 M H_2SO_4 on platinum, gold, copper and glassy carbon disc electrodes.

Copper is widely used in electrocatalytic applications. In the reduction of CO_2, Cu is often used to produce multi carbon molecules.[9] This tendency of the copper to be able to catalyse carbon-carbon coupling reactions has also been shown in the ECH.[10, 11] While C-C coupled products are often desired, a high selectivity for the full hydrogenation or the dimer product is still desired.

Carbon encapsulation is a promising strategy to improve the stability and modulate the activity of metals in electrocatalysis. In this chapter it will be shown that carbon-copper heterostructured electrodes offer an interesting alternative strategy for modulating activity and selectivity in ECH processes relative to the performance at bare metal electrodes. Metal-carbon heterostructures in which the metal is encapsulated or partially encapsulated (M@C) have been exploited successfully for electrocatalysis of other cathodic processes[12, 13] but have received limited attention in the ECH of organics.[14, 15]

The results of this chapter report on the investigation of the effect of encapsulating sputtered Cu films using amorphous carbon layers. While many transition metals would corrode in the conditions of the ECH, Cu offers a decent stability, allowing to investigate the effect of carbon layers. The goal of this was to maintain the electrocatalytic activity, while protecting the copper from the outside environment. For this, varying thicknesses of carbon was sputtered on Cu films and after spectroscopic and microscopic characterisation, the electrocatalytic activity of these materials was tested.

5.2. Deposition of CuXC films

Synthesis of the copper carbon heterostructures was done by sequential sputtering of a Cu layer followed by an amorphous carbon layer onto a Si wafer.[16-18] For electrochemical studies a titanium adhesion layer was deposited first. The subsequent sputtering of copper and carbon was done without breaking vacuum, maintaining a pristine interface. The thickness of the copper was kept constant at around 35 nm and the deposition time of the carbon shell was varied. The obtained samples will be labelled CuXC, where X identifies the time of carbon deposition (4, 8, 16, 24 and 32 min).

The samples were investigated using scanning electron microscopy. SEM images for bare Cu, Cu8C and Cu24C are shown in Figure 5.. The cross section of the bare Cu (Fig. 2b) shows a uniform average thickness of the Cu film. A columnar growth in the sputtered metal film can be seen. This microstructure is in agreement with the zone model of sputtering introduced before.[19, 20] In top view (Fig 2a) the microstructure can also be discerned, with darker areas in the SEM contrast, indicating valleys or troughs. With sputtering of carbon, the structure of the film becomes less clear in top view (Figure 2b and 2c). For Cu8C the carbon deposition leads to reduced resolution of the darker areas due to the carbon coverage, which become almost indistinguishable in Cu24C. In the cross sections of the CuXC films an underlayer can be seen, which seems to be rich in voids, which is covered by an amorphous carbon layer of relative uniform density.

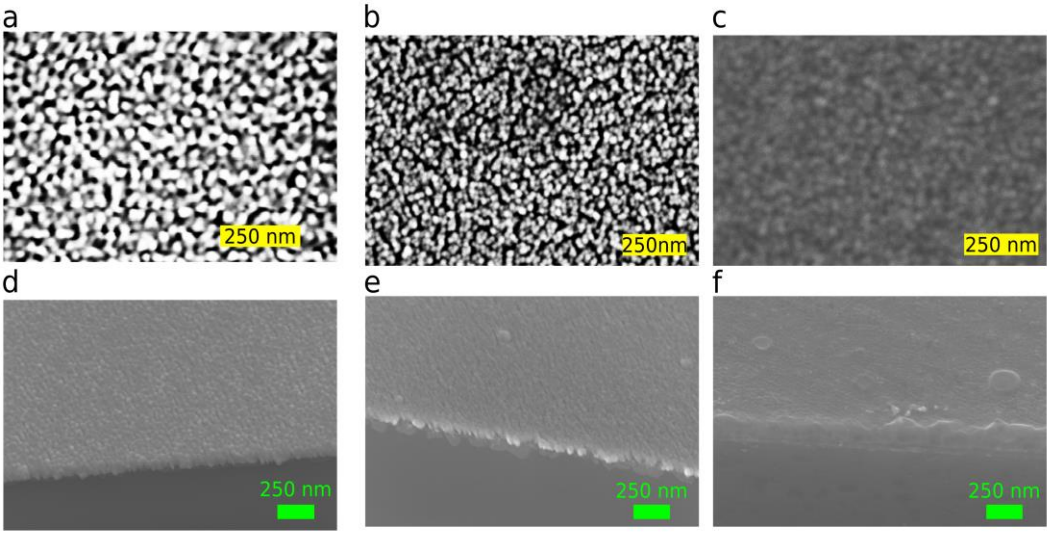

Figure 5.2 SEM images of (a)(d) a sputtered Cu film, (b)(e) a sputtered Cu with 8min carbon deposition and (c)(f) a sputtered Cu with 24min carbon deposition.

These results were supported by AFM images (Figure 5.) that show a decrease in RMS roughness for the Cu8C film, and an increase in RMS roughness with increasing carbon deposition. The roughness seems to level off for high carbon depositions. This could be suggestive of an incomplete filling of valleys/troughs in the Cu underlayer due to self-shadowing effects.[21]

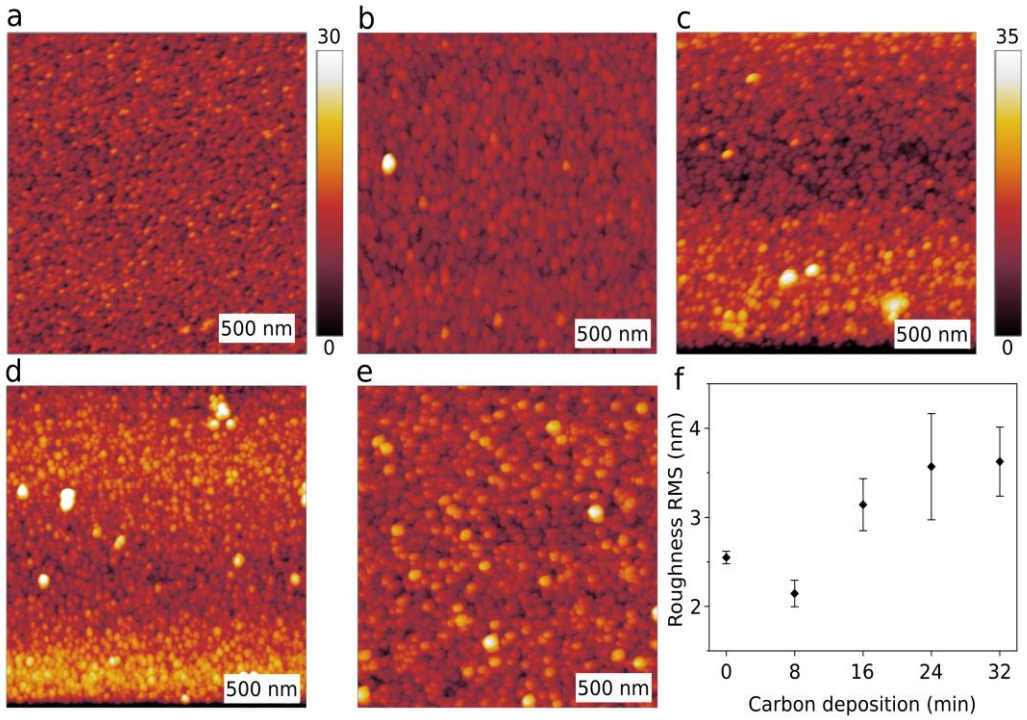

Figure 5.3 AFM images obtained for (a) bare copper, (b) Cu8C, (c) Cu16C, (d) Cu24C and (e) Cu32C. (f) The obtained RMS roughness for each sample (error bar for deviation within film).

The average mass coverage of carbon was determined using X-ray reflectivity measurements. An amorphous carbon film was sputtered for 40 minutes onto a Si wafer and probed with XRR. The resulting curve is shown in Figure 5.. The best fit was obtained by modelling the response of a Si substrate with an SiO_2 passive oxide and a carbon layer. The thickness of SiO_2 and carbon, and the roughness and density of the carbon film were used as fit parameters.

Results yielded a best fit with carbon thickness of 56.7 nm and a density of 1.52 g/cm3. The sputtered carbon density is in satisfactory agreement with density values reported for dc magnetron sputtered a-C films.[22] The obtained values for thickness and density were used to obtain a mass loading per minute, which was then used to calculate carbon mass coverage at CuXC electrodes reported in Table 5.1.

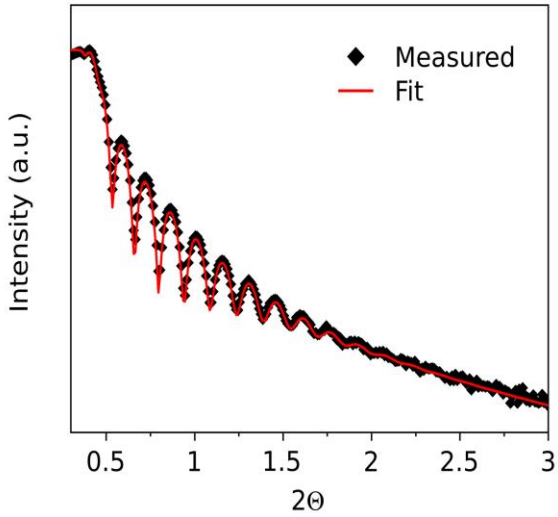

Figure 5.4 X-ray reflectivity data and best fit obtained for an amorphous carbon film deposited for 40 min on a Si wafer.

Table 5.1 Mass coverage and RMS obtained from XRR and AFM

Sample	Mass coverage (ng/cm^2)	RMS roughness (nm)
Cu	-	2.6 ± 0.1
Cu4C	85	
Cu8C	170	2.1 ± 0.1
Cu16C	340	3.1 ± 0.3
Cu24C	510	3.6 ± 0.6
Cu32C	680	3.6 ± 0.4

Scanning Raman spectroscopy was done to investigate the carbon coverage over macroscopic areas. Figure 5.5 shows the obtained Raman spectra at all pixel points and the corresponding intensity maps for the maximum peak from 1200 to 1700 cm^{-1}. The spectra and the intensity maps show only minor variation, thus indicating uniform coverage over relatively large regions, with at least 40×40 μm^2. Raman chemical maps indicate the C-shell coverage is evenly distributed over the Cu support within the spatial resolution of the Raman map (~ 1 μm).

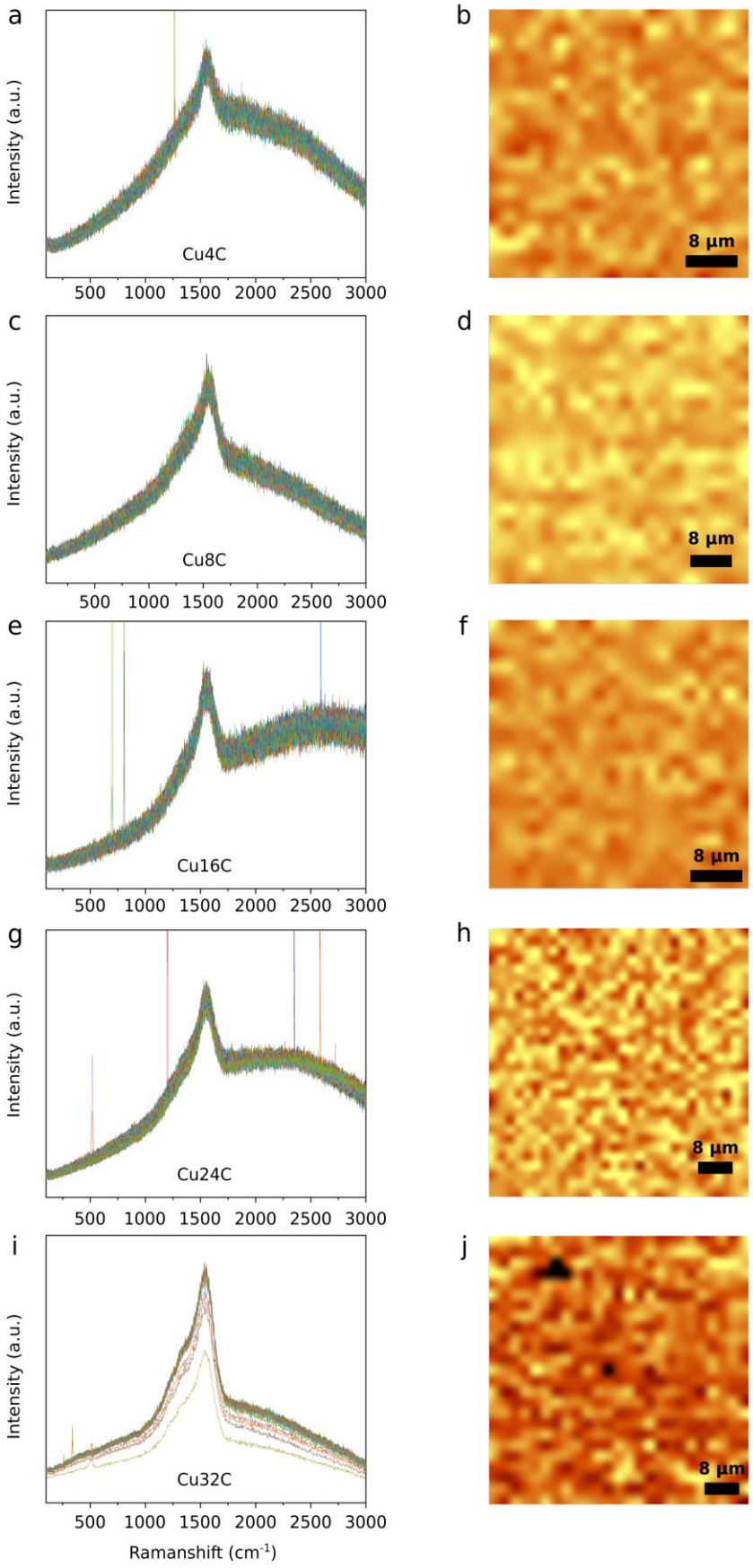

Figure 5.5 Raman spectra obtained for each point of a scanning Raman map with intensity maps of the G-band of (a, b) Cu4C, (c, d) Cu8C, (e, f) Cu16C, (g, h) Cu24C and (i, j) Cu32C

From the scanning Raman spectra as well as from the average spectra shown in figure 5.6 the characteristics of the Raman spectrum of amorphous carbon can be seen. In contrast to the spectrum of amorphous carbon deposited on a silicon wafer, the obtained spectra for the CuXC heterostructures show a higher intensity of the G band (around 1600 cm^{-1}) compared to the D band (around 1200 cm^{-1}). The overall intensity of the D and G bands grows and become better resolved as the mass coverage increases. These results suggest that for each mass coverage a relatively uniform carbon layer over macroscopic areas was achieved.

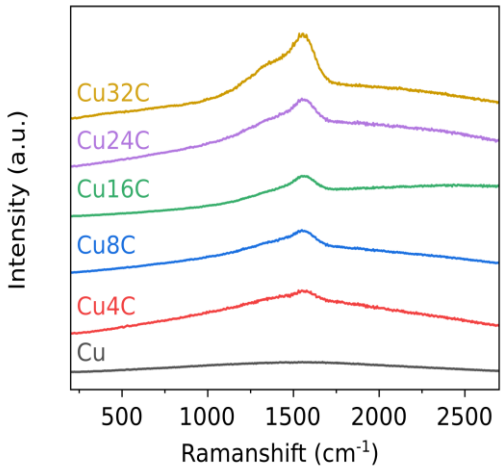

Figure 5.6 Raman spectra of sputtered Cu and CuXC samples normalised to maxima of G band.

The survey spectrum of the XPS of a bare copper sample is shown in figure 5.7. Peaks associated with Cu 2p (932 eV), O 1s (532 eV) and C 1s (284 eV)[23, 24] are identifiable in the spectrum. The characteristic peaks for the Cu 2s (1196 eV), Cu LMM (570 eV), Cu 3s (122 eV) and Cu 3p (76 eV) can also be seen.[25]

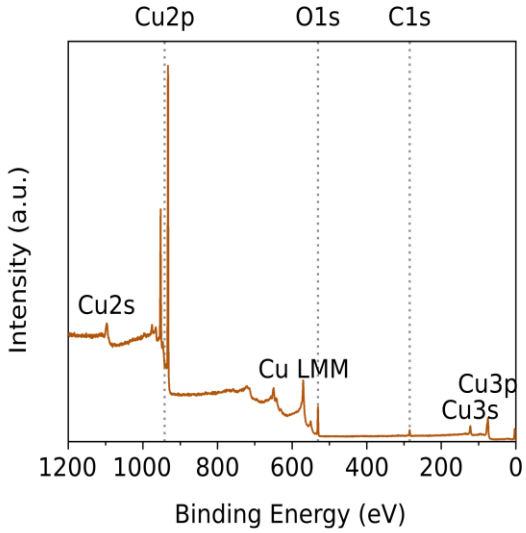

Figure 5.7 XPS survey spectrum of bare sputtered Cu.

High resolution spectra of the O 1s and the Cu 2p core levels are shown in Figure 5.8. Best fits of the doublet corresponding to the Cu 2p core level were carried out using a single component, associated with Cu^0 or Cu^{+1}, as their binding energies cannot be resolved. The presence of an oxide can be seen from the best fit obtained for the O 1s spectrum, where two components are required, one at 530.5 eV and one at 53.2 eV, assigned to a metal oxide[24] and adsorbed water and advantageous carbonaceous oxides,[18] respectively. The absence of a peak around 534 eV arising from Cu^{2+} in the Cu 2p spectrum indicates that the oxide is mainly Cu_2O.[23, 24] Comparing the amount of copper with the amount of copper oxide a ratio of O:Cu of about 2 was found, indicating that mostly Cu_2O is present at the surface, which follows from exposure of the samples to the atmosphere.

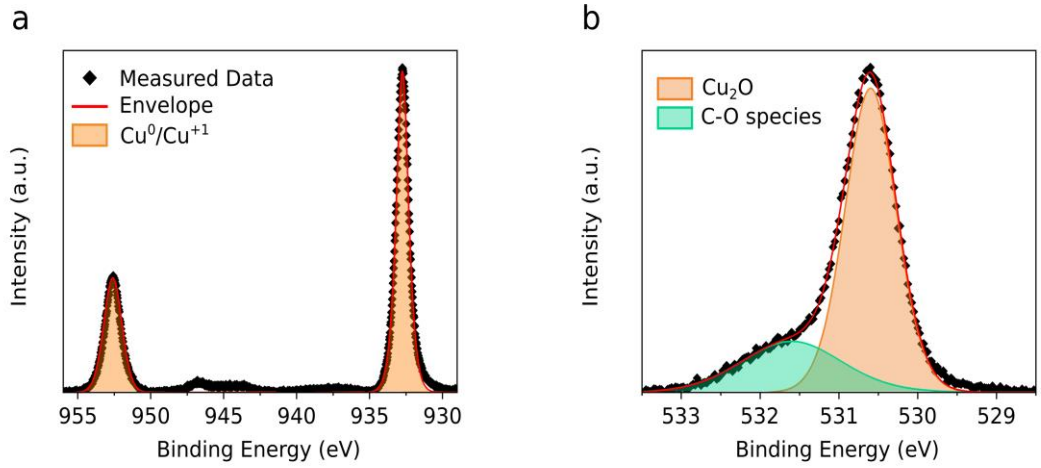

Figure 5.8 XPS core level of (a) Cu 2p and (b) O 1s of a bare sputtered Cu film.

Survey spectra for the CuXC (Figure 5.9) samples show an attenuation of the Cu peaks with increasing carbon deposition. The spectra show again the characteristic signals of the Cu 2p, the O 1s and the C 1s.

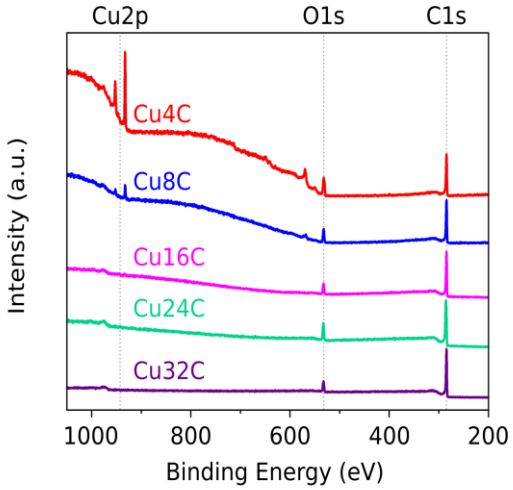

Figure 5.9 XPS surveys of CuXC samples normalised to the intensity of the C 1s peak.

Quantification of the components was done through the high-resolution scans of the core levels, and the results are summarised in table 5.2. It can be seen that the signal of the copper becomes attenuated with increasing carbon coverage. This indicates that increased carbon coverages lead to progressive encapsulation of Cu nanostructures. The relative amount of oxygen and carbon for the films with higher carbon coverage is relatively similar around 10% and 90%, respectively. This suggests, that the O1s peaks arise exclusively from the O-content of the film. This is consistent with an increased carbon coverage with chemical composition of the carbon layer being independent of the total mass loading. As summarised in Table 5.3.

Table 5.2 Atomic composition obtained from XPS high resolution core level spectra.

	Cu at%	**O at%**	**C at%**
Bare Cu	49	29	22
Cu4C	5.9	17.4	76.8
Cu8C	1	11.8	87.2
Cu16C	0.1	10.1	89.8
Cu24C	-	11	89
Cu32C	-	9.1	90.9

Best fits for the Cu 2p spectra were obtained with a single doublet assigned to Cu^{0}/Cu^{+1} as was done for the bare Cu. For the Cu16C and higher carbon coverages no sensible fit could be done of the Cu 2p peak. The O 1s spectra and the best fit are consistent with the presence of a passive oxide, based on analysis of Cu4C and Cu8C, whereas for higher carbon depositions it was not possible to detect a copper oxide peak/component. Best fits of the O 1s region were obtained using two components at 530 and 532.5 eV corresponding to the metal oxide and the O-containing groups in the carbon shell, respectively. The presence of a metal oxide peak in the O 1s spectrum indicates that the signal of the Cu 2p is most likely due to Cu_2O. As there is no exposure to atmosphere between deposition of Cu and C, this suggests that the carbon shell on these samples does not avoid oxidation of the copper interface. Best fit of the C 1s peaks is shown in Figure 5.10. As previously discussed, the best fits were obtained using six components, assigned to sp^2 (284.4 eV) and sp^3 (284.9 eV) centres, C-O (286.1 eV) and C=O (287.4 eV) species, COOH (288.8 eV) and the π-π* satellite (289.5 eV).

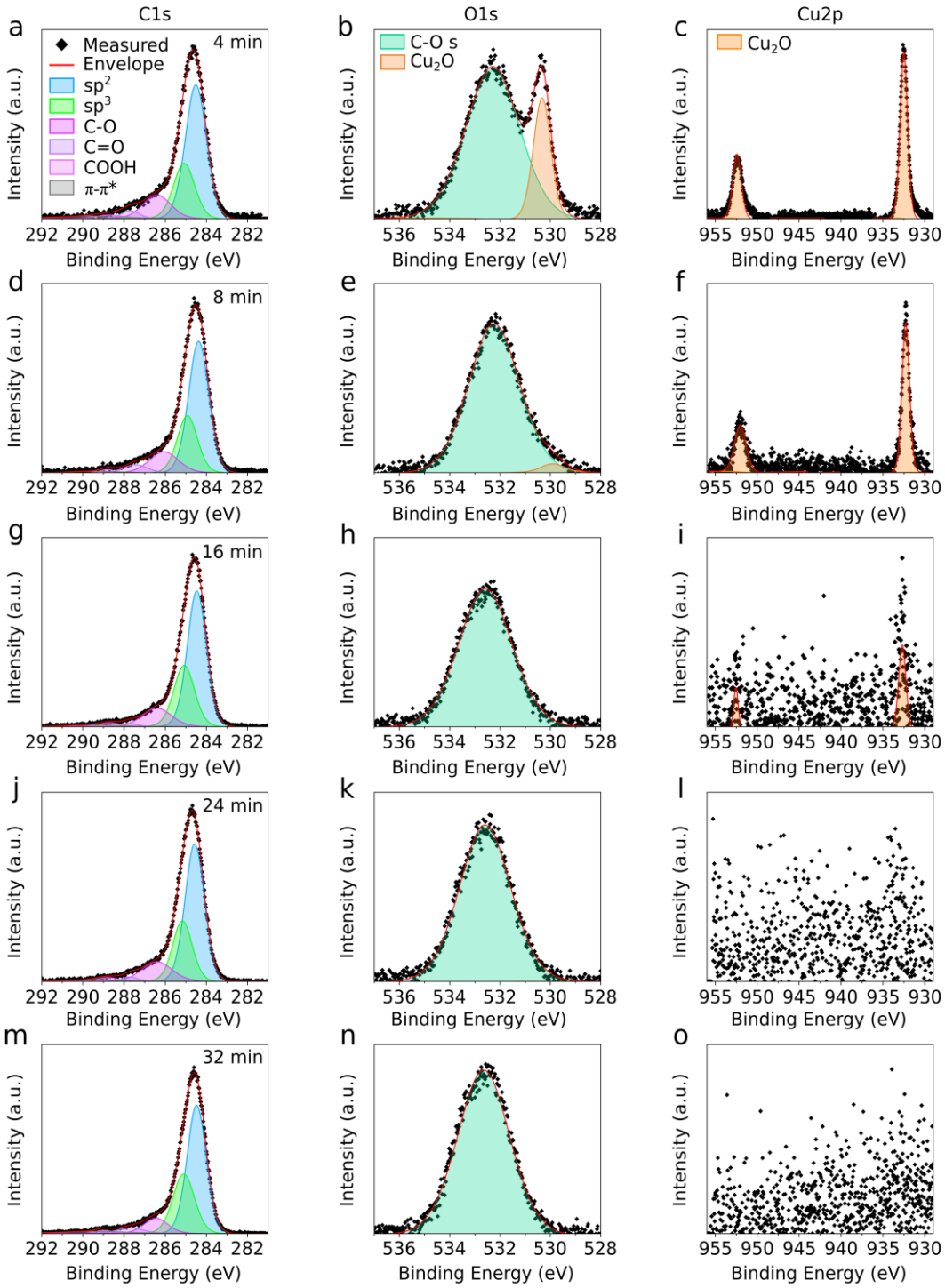

Figure 5.10 High resolution spectra and best fits in the C 1s, O 1s and Cu 2p regions for (a, b, c) Cu4C, (d, e, f) Cu8C, (g, h, i) Cu16C, (j, k, l) Cu24C and (m, n, o) Cu32C.

Table 5.3 Contribution of sp^2 carbon and ratio of O:Cu derived from XPS analysis.

	sp^2 in C %	**Cu / O (Cu_xO)**
Bare Cu	-	2.0
Cu4C	56	1.5
Cu8C	56.2	1.8
Cu16C	56.6	-
Cu24C	56.9	-
Cu32C	55.9	-

5.3. Electrocatalytic activity

Linear sweep voltammograms of a polished Cu disk electrode and of sputtered copper in 0.1 M H_2SO_4 are shown in Figure 5.. Compared to polished Cu, sputtered Cu films show a lower overpotential and higher current density, likely due to a higher microscopic area of the sputtered Cu film.

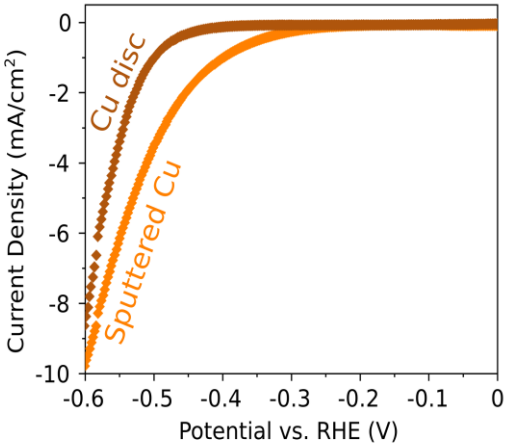

Figure 5.11 LSV at 2 mV/s in 0.1 M H_2SO_4 on a polished Cu disc and a sputtered Cu electrode.

LSVs of the CuXC electrodes in acidic conditions without any benzaldehyde are shown in Figure 5.. It can be seen that the carbon deposition on the copper has no visible effect on the HER performance of the material. The voltammogram of the CuXC electrodes show that the electrodes remain HER-active after fabrication of Cu@C heterostructures.

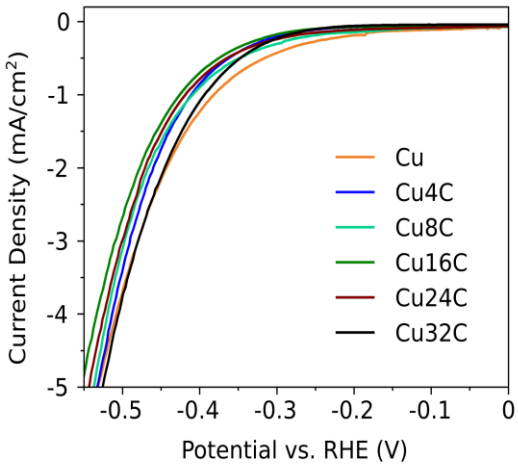

Figure 5.12 LSV at 2 mV/s in 0.1 M H_2SO_4 on sputtered CuXC electrodes.

As amorphous carbon has no HER activity in this current range, as can be seen from the CV in the Appendix, the results suggest that the HER response of these Cu@C heterostructured electrodes remains dominated by Cu sites in the underlayer. This is supported by Tafel slopes remaining nearly constant for all CuXC electrodes which is consistent with kinetic currents being controlled by the same type of active sites.

This can be seen more clearly in Figure 5.. The onset potential, the Tafel slopes and the exchange current densities that were found for the CuXC heterostructures seem independent of the carbon coverage. The Tafel slope, for the bare sputtered Cu and the CuXC films is in the range of 200 mV/s, which is significantly higher than values reported for copper electrodes. This is most likely the effect of the high degree of roughness and microscopic area.[26] The obtained exchange current density for the CuXC materials is higher compared to literature values on Cu. Which can also be associated with the high degree of roughness.

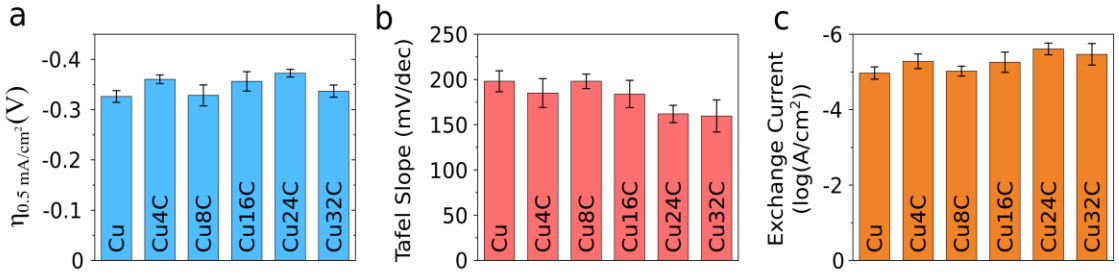

Figure 5.13 (a) Potential for 0.5 mA/cm^2, (b) Tafel slope and (c) exchange current densities obtained for the HER on CuXC samples.

The lack of negative effects arising from carbon coverage on the HER performance was also investigated by using an evaporated copper electrode. Metal films obtained by electron beam evaporation are known to be smoother compared to sputtered films. A comparison between the evaporated copper, the sputtered copper and the copper disc in the HER are shown in Figure 5., together with the capacitance obtained by CVs of a different scan rate. It can be seen that the evaporated Cu has a similar onset potential compared to the Cu disc. At more cathodic potentials it seems that the evaporated Cu yields less current compared to the disc electrode.

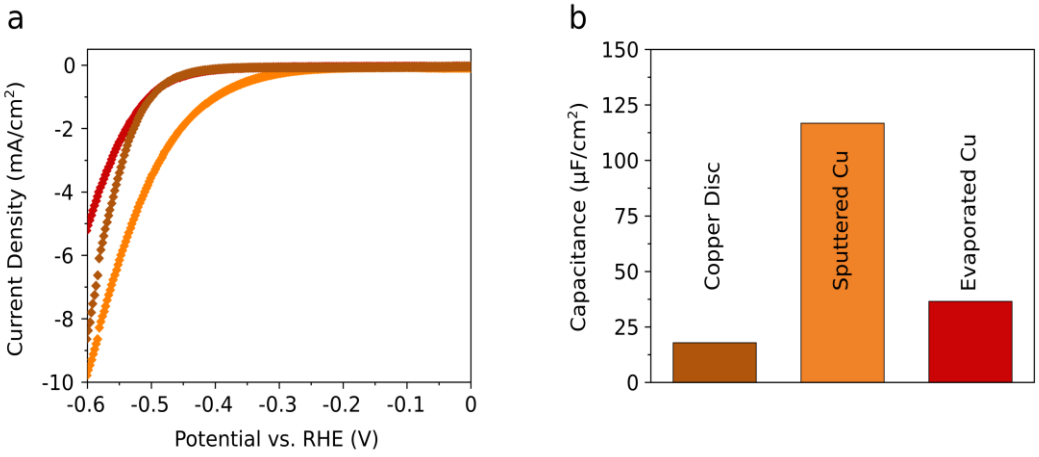

Figure 5.14 (a) LSVs (2 mV/s) in 0.1 M H_2SO_4 on a polished copper disc electrode, a sputter copper film and an evaporated copper film and (b) the capacitance obtained for the films through CVs in the non-faradaic region.

The double layer capacitance of the three Cu electrodes is shown in Figure 5.14b; the bar chart indicates that the capacitance of the sputtered copper film is >4 times that of the copper disc. The evaporated copper in contrast exhibited a smaller increase in capacitance to the polished copper disc, indicating a lower microroughness. The Tafel slope, overpotential and exchange current density of the three copper electrodes is summarised in Table 5.4.

Table 5.4 Comparison of overpotential, Tafel slope and exchange current density obtained on sputtered Cu, evaporated Cu and a Cu disc electrode.

	η @ 1mA/cm² (V vs. RHE)	**Tafel slope (mV)**	**Exchange Current Log (A/cm²)**
Cu disc	-0.501	99	-8
Evaporated Cu	-0.504	114	-7
Sputtered Cu	-0.387 ± 0.01	198 ± 11	-5 ± 0.2

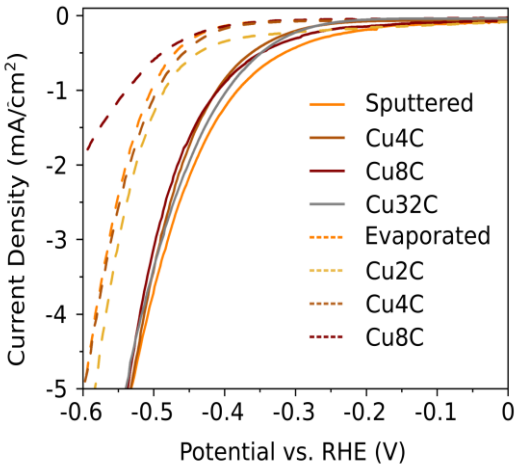

Figure 5.15 LSVs at 2 mV/s in 0.1 M H_2SO_4 on Sputtered CuXC (solid) and evaporated CuXC (dashed) films.

The effect of carbon coverage on the HER was further tested on the evaporated copper film and the results in comparison to the sputtered CuXC are shown in Figure 5.. It can be seen that for a carbon deposition of eight minutes on the evaporated films the HER performance drops significantly. For depositions of carbon for two and four minutes the same trend was found as was the case for the sputtered films, where no effect of the carbon on the HER was found. This suggests that the amount of carbon coverage needed for suppression of the HER is dependent on the roughness of the copper underlayer, as the carbon seems to not form a closed layer on the Cu.

The sputtered carbon copper heterostructures were tested in LSV experiments in acidic conditions in the presence of benzaldehyde, the obtained current responses are shown in Figure 5.. As for the LSV response in just sulphuric acid no effect of the carbon coverage can be observed. For all of the films a cathodic peak appears around -0.4 V vs. RHE, which is not observed in pure supporting electrolyte.

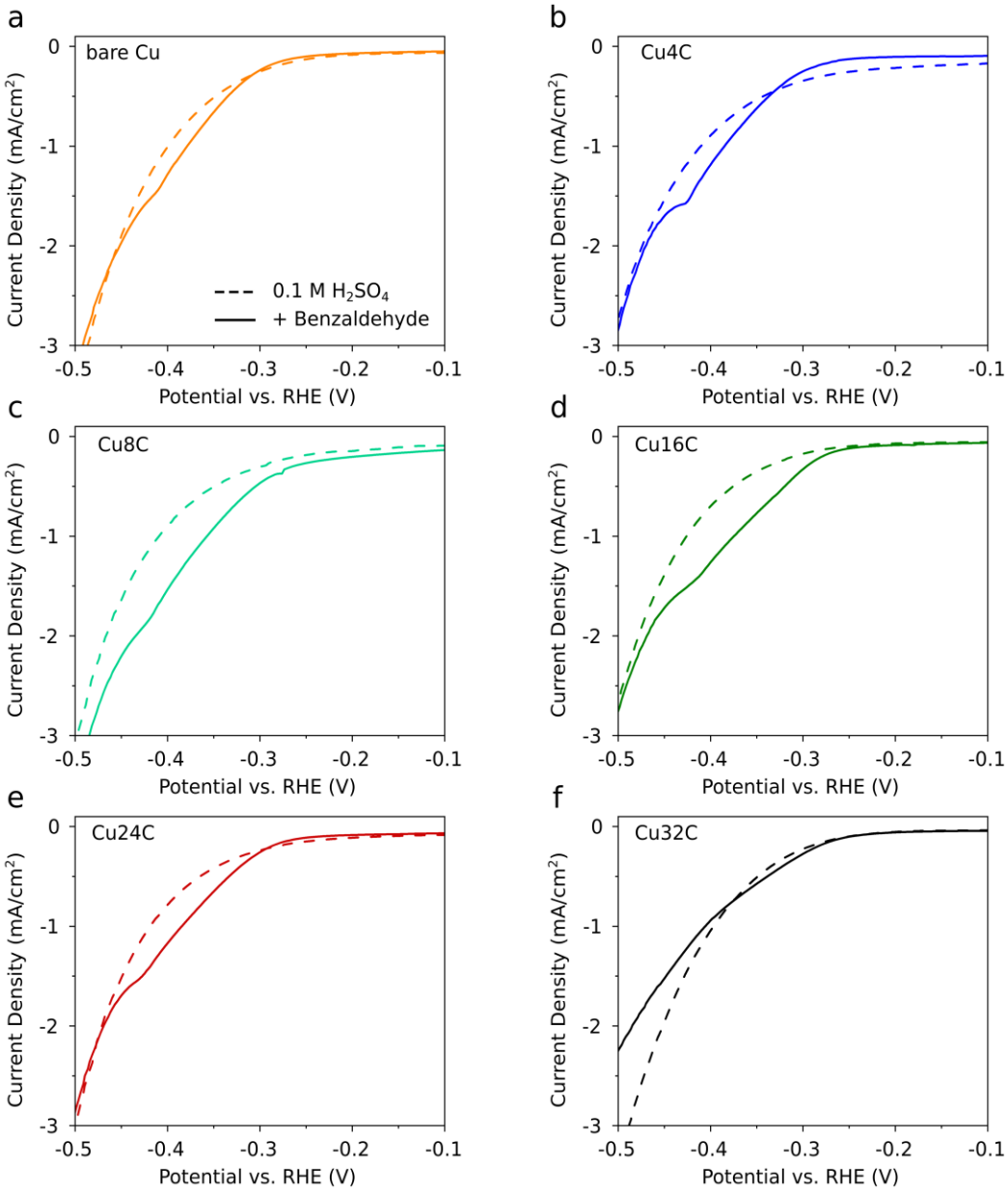

Figure 5.16 LSVs at 2 mV/s in 0.1 M H_2SO_4 with 20 mM benzaldehyde on (a) sputtered copper, (b) Cu4C, (c) Cu8C, (d) Cu16C, (e) Cu24C and (f) Cu32C.

To investigate the performance of the CuXC electrodes, electrolysis experiments were carried out at the peak potential (-0.4 V vs RHE). Conditions were chosen as presented in the previous chapters, with an electrolysis time of 30 min, stirring at 500 rpm, and concentration of 20 mM benzaldehyde in 0.1 M H_2SO_4 supporting electrolyte. Figure 5. shows the reduction rate of benzaldehyde as well as the total faradaic efficiency of organic reductions. It can be seen that, similar to the results obtained for voltammetry, there seems to be no significant effect arising from the presence of carbon on the rate of benzaldehyde reduction or on the total faradaic efficiency; indeed, values remain relatively high with

approximately 70% of the charge contributing to the reduction of benzaldehyde rather that to the HER.

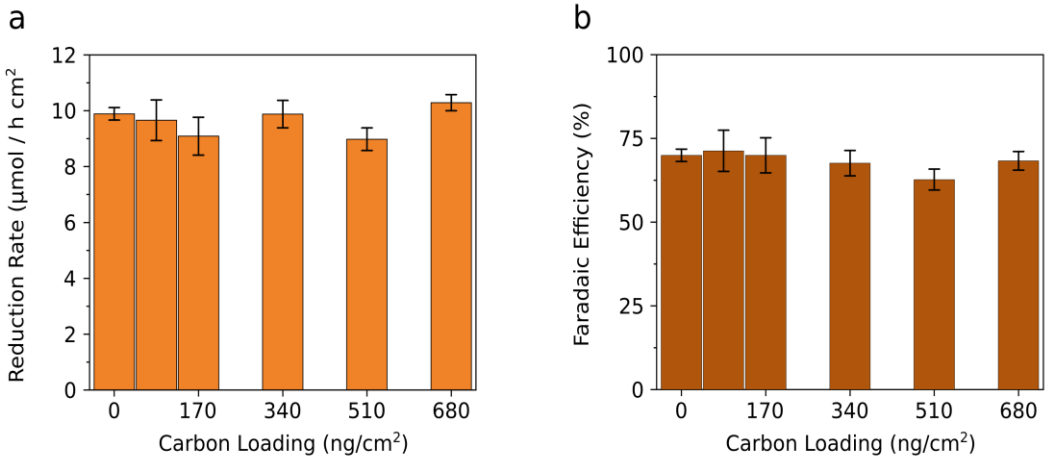

Figure 5.17 (a) Total reduction Rate of benzaldehyde and (b) total faradaic efficiency obtained for the electrolysis of CuXC samples.

A different trend is observed when examining the production rates and faradaic efficiencies of the two possible products of benzaldehyde reduction, as shown in Figure 5.. The rate of benzyl alcohol production increases for carbon coverages in the 85-170 ng/cm^2 range (Cu4C and Cu8C) and decreases back to lower levels for higher carbon coverages. This suggests that the presence of a C-shell in the Cu@C heterostructures can modulate product selectivity.

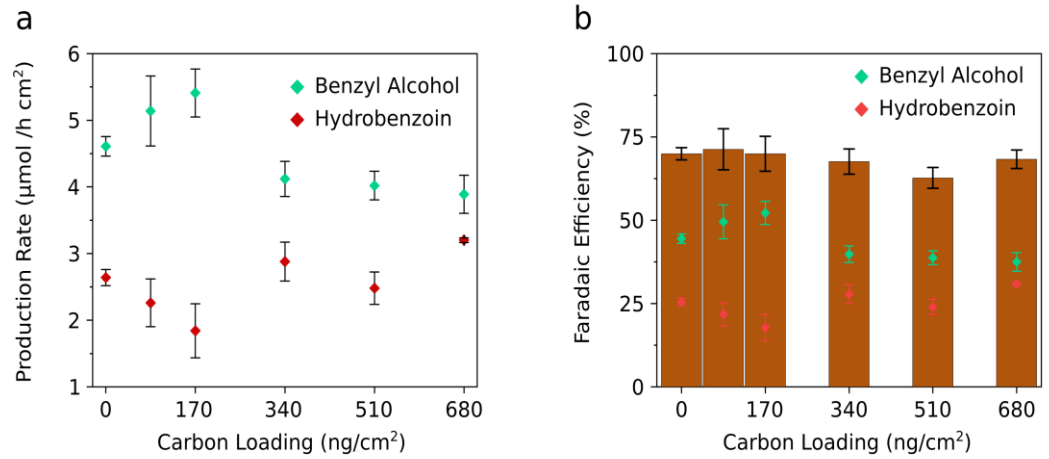

Figure 5.18 (a) Production rate of benzyl alcohol and hydrobenzoin and (b) the faradaic efficiency for the two products obtained for electrolysis on CuXC samples.

Figure 5.19 shows a plot of the ECH selectivity towards the alcohol as a function of carbon coverage for all CuXC electrodes in the dataset. The figure indicates that the mean selectivity of bare Cu (black line) is ca. 60%; this is comparable with results by Anibal et

al. obtained using metal foils, that show that Cu catalyses dimerization efficiently yielding mixed products. As the carbon coverage is increased up to 170 ng/cm^2, the majority of Cu@C electrodes yield significant enhancements in selectivity towards the alcohol product, as shown by their position outside the 95% confidence interval (blue dashed lines). Three regions with distinctive selectivity can thus be clearly identified in the plot: region I (orange) corresponds to the response of bare Cu, region II (green) corresponding to moderate carbon coverage leading to enhanced alcohol selectivity or, conversely, suppressed selectivity towards hydrobenzoin; and, finally, region III in which the selectivity reverts to lower values. It is copper electrodes in region II whose selectivity represents an interesting departure from the conventional behaviour observed at bare copper.

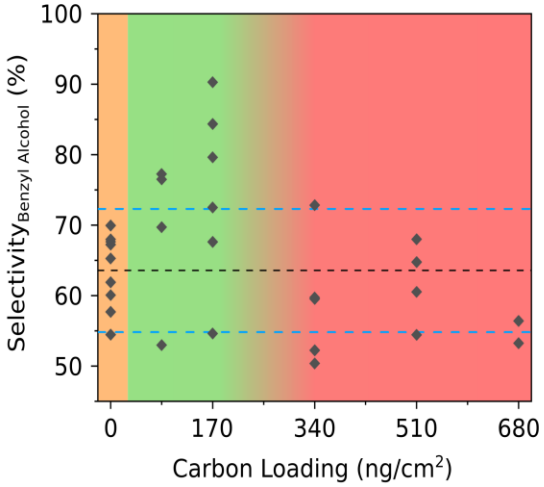

Figure 5.19 Selectivity for all individual CuXC samples, with the mean (grey dashed line) and 95% confidence interval (blue dashed lines) for the bare copper response.

Previous works have studied the ECH of benzaldehyde on a range of metals and on glassy carbon.[10, 27, 28] The tendency of copper towards dimerization to hydrobenzoin has been reported.[10] The ability of Cu to catalyse C-C coupling reactions has further been reported for other organic reductions as well as for the CO_2 reduction to C_2H_4.[1, 5, 6, 29, 30] Anibal et al.[27] investigated the electrochemical coupling of benzaldehyde on Cu, Au, Pt and Pd and argued that the C-C coupling activity of Cu stems from a balance between the ability to catalyse hydrogenation to ketyl radicals, and the relatively low binding energy of these species. Low binding energy was proposed to translate into good stability of this species at the Cu surface and facile surface-diffusion. In contrast, at Pd or Pt, strong adsorption leads to ketyl decomposition and decreased surface coverages, which together with high activity towards the HER results into benzyl alcohol as the preferred product. Recent work

by Chen et al. indicates that formation of ketyl radicals is fast relative to either the second hydrogenation to form benzyl alcohol, or relative to C-C coupling to form hydrobenzoin.[30] They concluded that the Cu surface is readily covered by benzaldehyde adsorbates, which might suppress H_{ads} coverages, but facilitates reduction to ketyl radicals: benzyl alcohol forms then from the ketyl species through both proton coupled reduction and H_{ads} addition, whereas hydrobenzoin results from coupling of surface ketyl species to physisorbed benzaldehyde followed by a further proton coupled reduction. In light of this, any strategies that lead to reduced surface coverage of benzaldehyde/ketyl radicals or to increased concentration of H_{ads} can be expected to lead to increased selectivity for the alcohol product. Both a lowering of benzaldehyde concentration, as in previous work,[30, 31] and an increase in the decomposition rate of surface ketyl radicals, e.g. by alloying Cu with Pd,[32] offer routes to this end. Conversely, any strategies that suppress H_{ads} activation without significantly affecting surface benzaldehyde coverage, e.g. use of self-assembled organic monolayers,[33] could be expected to increase hydrobenzoin selectivity at copper.

Our results suggest that heterostructured M@C electrodes offer an alternative approach to modulating selectivity. The carbon shell does not display faradaic activity at the applied potentials; indeed, both HER and organic reduction currents at the amorphous carbon shell alone were found to be negligible at -0.7 V. Hence, the carbon overlayer can be considered electrochemically inert under this operating condition and any HER/ECH activity at CuXC electrodes is expected to arise from reactions at the Cu surface. Notably, the electrode fabrication process is mild and does not lead to changes in copper surface chemistry due to Cu-C interlayer reactions, as evidenced by XPS. Therefore, we propose that the presence of the carbon overlayer is most likely to affect selectivity by altering the relative coverages of H_{ads} vs benzaldehyde/ketyl radicals at the pristine electroactive Cu sites in the metal underlayer.

Carbons are in general excellent organic adsorbents, and we speculate that this property might provide a first possible explanation of its effect on selectivity. The carbon shell should be effective at physisorbing benzaldehyde from solution; this is supported by the suppression of HER currents at high overpotentials on carbon electrodes shown in Chapter 3, which is characteristic of the presence of a passive organic adlayer. The binding strength of benzaldehyde has been estimated to be similar for copper (0.5 eV)[32] and graphene (0.52 eV)[34] therefore the two surfaces should display similar benzaldehyde coverages at open circuit. However, no ketyl radicals are expected to form at the carbon surface;

therefore, at cathodic potentials, a gradient in ketyl coverage should form at Cu-C boundaries that could deplete Cu sites of the radical species via spillover. This appears plausible given that the barrier to surface diffusion of a phenyl ring is low and similar in magnitude at both copper and graphite surfaces (< 20 meV).[35, 36] Assuming the carbon to also be inert towards the second proton-coupled electron transfer, a spillover would result in lower surface concentrations of ketyl radicals at Cu sites and, in turn, higher selectivity towards the alcohol.

An alternative hypothesis is that the carbon shell negatively affects the mass transport of organic species to the electroactive Cu while having lower or negligible effect on proton transport. The approximately constant capacitance values and HER Tafel slopes observed for CuXC in acid electrolyte over the range of carbon mass coverages explored do support the conclusion that proton/H_2 mass transports are not significantly hindered due to the presence of the C-shell. If the mass transport of benzaldehyde through the C layer or holes in the carbon is on the other hand hindered, the effective concentration of benzaldehyde/ketyl radicals is lowered at the Cu surface and a higher H_{ads} surface density becomes possible, thus enhancing selectivity towards benzyl alcohol. In this scenario, the C-shell would function as a proton permeable layer with significant mass transport impedance for the larger organics. Sputtered amorphous carbon is not as rich in ionizable groups as a commercial proton conductive membrane, however it does possess protonable groups (O-sites) that could facilitate transport. Also, it is known that amorphous carbons prepared via physical deposition can display intra-film porosity,[37] hydrogen permeability and molecular sieving properties.[30] Therefore, it appears plausible that the C-shell in CuXC electrodes could impart a degree of mass transport selectivity.

Experimental trends show that peak alcohol selectivity is observed only for a moderate range of C-shell coverages, thus suggesting that if the carbon were to act as a proton permeable layer, its thickness must impact H_{ads} coverages at Cu sites in a complex manner. Intriguingly, Gao et al. have recently reported that HER currents at Pt electrodes coated with a proton conducting Nafion layer can display a complex trend as a function of layer thickness.[38] HER currents were enhanced when Nafion layers of ~200 nm were used, while currents were instead much lower at bare Pt (i.e. zero Nafion thickness) and at Pt coated with >200 nm Nafion layers. They proposed anomalous enhancement at intermediate thickness to result from a complex balance between increased proton concentrations at the Pt-membrane interface and a lower proton mobility relative to the aqueous solution.

Selectivity increases at Cu4C and Cu8C could similarly be the result of the C-shell thickness being thin enough to maintain relatively fast proton transport and sustain high Hads coverages. We are currently investigating this hypothesis using a wider range of metal electrodes to further probe proton transport in the amorphous carbon shell.

5.4. Conclusion

We used sputtered copper electrodes with varying mass loading of carbon to investigate the performance of Cu@C heterostructures in the electrocatalytic hydrogenation of benzaldehyde. A detailed structural characterization of the morphology and chemical composition of Cu@C electrodes shows that the carbon overcoats the sputtered copper overlayer without leading to significant alterations in the surface chemistry of either the carbon layer or the copper. Voltammetry studies indicate that sputtered copper layers display channels/pores, so that after C-shell deposition the majority of Cu-sites in the underlayer remain active towards H_{ads} activation and the HER. Electrolysis studies carried out via chronoamperometry followed by product analysis revealed that bare sputtered Cu yields benzyl alcohol and the dimerization product hydrobenzoin. Interestingly, the C-shell of Cu@C heterostructured electrodes does not suppress the electrocatalytic activity of copper, but instead leads to changes in selectivity over the range explored and, notably, to improved alcohol selective at low/moderate carbon coverages (85-170 ng/cm^2).

Given that carbon has negligible electrocatalytic activity at the applied cathodic potential, ketyl radicals and adsorbed hydrogen can only be electrogenerated at the copper surface. Therefore, our results indicate that coating of ECH active materials with an amorphous carbon shell is a viable route to modulate selectivity. We propose two possible mechanisms by which the presence of a C-shell might modulate selectivity but, in both hypotheses, put forward we suggest that the carbon layer affects the relative concentrations of Hads and ketyl radicals at the copper. The reported Cu@C architectures, which maintain the electrocatalytic activity of the metal and modulate the selectivity through the carbon layer offer an original alternative strategy for electrocatalyst design that departs from approaches involving metal alloying. The advantages of carbon encapsulation/heterostructuring are the use of low-cost materials, as no precious metals are required. Additionally, the process is scalable to large surface areas and could so be implemented in industrial applications. The principles behind M@C strategies for selectivity could potentially be extended to different catalyst architectures and metal underlayers.

References

1. Jung, S.; Karaiskakis, A. N.; Biddinger, E. J., Enhanced activity for electrochemical hydrogenation and hydrogenolysis of furfural to biofuel using electrodeposited Cu catalysts. *Catalysis Today* **2019,** *323*, 26-34.
2. Karaiskakis, A. N.; Biddinger, E. J., Evaluation of the Impact of Surface Reconstruction on Rough Electrodeposited Copper-Based Catalysts for Carbon Dioxide Electroreduction. *Energy Technology* **2016,** *5* (6), 901-910.
3. Mallapragada, D. S.; Dvorkin, Y.; Modestino, M. A.; Esposito, D. V.; Smith, W. A.; Hodge, B.-M.; Harold, M. P.; Donnelly, V. M.; Nuz, A.; Bloomquist, C.; Baker, K.; Grabow, L. C.; Yan, Y.; Rajput, N. N.; Hartman, R. L.; Biddinger, E. J.; Aydil, E. S.; Taylor, A. D., Decarbonization of the chemical industry through electrification: Barriers and opportunities. *Joule* **2023,** *7* (1), 23-41.
4. May, A. S.; Biddinger, E. J., Strategies to Control Electrochemical Hydrogenation and Hydrogenolysis of Furfural and Minimize Undesired Side Reactions. *ACS Catalysis* **2020,** *10* (5), 3212-3221.
5. May, A. S.; Biddinger, E. J., Speciation of potential-dependent fouling on copper foil electrodes during electrochemical hydrogenation and hydrogenolysis of furfural in strong acid. *Green Chemistry* **2023,** *25* (21), 8687-8697.
6. Sharifi Golru, S.; May, A. S.; Biddinger, E. J., Modifying Copper Local Environment with Electrolyte Additives to Alter CO_2 Electroreduction vs Hydrogen Evolution. *ACS Catalysis* **2023,** *13* (12), 7831-7843.
7. Kwon, Y.; Birdja, Y. Y.; Raoufmoghaddam, S.; Koper, M. T., Electrocatalytic hydrogenation of 5-hydroxymethylfurfural in acidic solution. *ChemSusChem* **2015,** *8* (10), 1745-51.
8. Kwon, Y.; de Jong, E.; Raoufmoghaddam, S.; Koper, M. T., Electrocatalytic hydrogenation of 5-hydroxymethylfurfural in the absence and presence of glucose. *ChemSusChem* **2013,** *6* (9), 1659-67.
9. Woldu, A. R.; Huang, Z.; Zhao, P.; Hu, L.; Astruc, D., Electrochemical CO_2 reduction (CO2RR) to multi-carbon products over copper-based catalysts. *Coordination Chemistry Reviews* **2022,** *454*.
10. Andrews, E.; Lopez-Ruiz, J. A.; Egbert, J. D.; Koh, K.; Sanyal, U.; Song, M.; Li, D.; Karkamkar, A. J.; Derewinski, M. A.; Holladay, J.; Gutiérrez, O. Y.; Holladay, J. D., Performance of Base and Noble Metals for Electrocatalytic Hydrogenation of Bio-Oil-Derived Oxygenated Compounds. *ACS Sustainable Chemistry & Engineering* **2020,** *8* (11), 4407-4418.
11. Carroll, K. J.; Burger, T.; Langenegger, L.; Chavez, S.; Hunt, S. T.; Roman-Leshkov, Y.; Brushett, F. R., Electrocatalytic Hydrogenation of Oxygenates using Earth-Abundant Transition-Metal Nanoparticles under Mild Conditions. *ChemSusChem* **2016,** *9* (15), 1904-10.
12. Peng, Y.; Chen, S., Electrocatalysts based on metal@carbon core@shell nanocomposites: An overview. *Green Energy & Environment* **2018,** *3* (4), 335-351.
13. Yoo, J. M.; Shin, H.; Chung, D. Y.; Sung, Y. E., Carbon Shell on Active Nanocatalyst for Stable Electrocatalysis. *Acc Chem Res* **2022,** *55* (9), 1278-1289.
14. Zheng, M.; Zhang, J.; Wang, P.; Jin, H.; Zheng, Y.; Qiao, S. Z., Recent Advances in Electrocatalytic Hydrogenation Reactions on Copper-Based Catalysts. *Adv Mater* **2024,** *36* (14), e2307913.
15. Pota, F.; Costa de Oliveira, M.; Schröder, C.; Brunet Cabré, M.; Nolan, H.; Rafferty, A.; Jeannin, O.; Camerel, F.; Behan, J.; Barrière, F.; Colavita, P. E., Porous N-doped carbon-encapsulated iron as a novel catalyst architecture for the electrocatalytic hydrogenation of benzaldehyde. *ChemSusChem* **2024,** *n/a* (n/a), e202400546.

16. Behan, J. A.; Hoque, M. K.; Stamatin, S. N.; Perova, T. S.; Vilella-Arribas, L.; García-Melchor, M.; Colavita, P. E., Experimental and Computational Study of Dopamine as an Electrochemical Probe of the Surface Nanostructure of Graphitized N-Doped Carbon. *The Journal of Physical Chemistry C* **2018,** *122* (36), 20763-20773.
17. Hoque, M. K.; Behan, J. A.; Stamatin, S. N.; Zen, F.; Perova, T. S.; Colavita, P. E., Capacitive storage at nitrogen doped amorphous carbon electrodes: structural and chemical effects of nitrogen incorporation. *RSC Adv* **2019,** *9* (7), 4063-4071.
18. Behan, J. A.; Stamatin, S. N.; Hoque, M. K.; Ciapetti, G.; Zen, F.; Esteban-Tejeda, L.; Colavita, P. E., Combined Optoelectronic and Electrochemical Study of Nitrogenated Carbon Electrodes. *The Journal of Physical Chemistry C* **2017,** *121* (12), 6596-6604.
19. Kusano, E., Revisitation of the structure zone model based on the investigation of the structure and properties of Ti, Zr, and Hf thin films deposited at 70–600 °C using DC magnetron sputtering. *Journal of Vacuum Science & Technology, A: Vacuum, Surfaces, and Films* **2018,** *36* (4).
20. Thornton, J. A., The microstructure of sputter-deposited coatings. *Journal of Vacuum Science & Technology, A: Vacuum, Surfaces, and Films* **1986,** *4* (6), 3059-3065.
21. Karabacak, T.; Lu, T.-M., Enhanced step coverage by oblique angle physical vapor deposition. *Journal of Applied Physics* **2005,** *97* (12).
22. Ferrari, A. C.; Libassi, A.; Tanner, B. K.; Stolojan, V.; Yuan, J.; Brown, L. M.; Rodil, S. E.; Kleinsorge, B.; Robertson, J., Density, ${\mathrm{sp}}^{3}$ fraction, and cross-sectional structure of amorphous carbon films determined by x-ray reflectivity and electron energy-loss spectroscopy. *Physical Review B* **2000,** *62* (16), 11089-11103.
23. Fleisch, T. H.; Mains, G. J., Reduction of copper oxides by UV radiation and atomic hydrogen studied by XPS. *Applications of Surface Science* **1982,** *10* (1), 51-62.
24. Platzman, I.; Brener, R.; Haick, H.; Tannenbaum, R., Oxidation of Polycrystalline Copper Thin Films at Ambient Conditions. *The Journal of Physical Chemistry C* **2008,** *112* (4), 1101-1108.
25. Chastain, J.; King Jr, R. C., Handbook of X-ray photoelectron spectroscopy. *Perkin-Elmer Corporation* **1992,** *40*, 221.
26. Lasia, A., Impedance of porous electrodes. *Journal of Electroanalytical Chemistry* **1995,** *397* (1), 27-33.
27. Anibal, J.; Xu, B., Electroreductive C–C Coupling of Furfural and Benzaldehyde on Cu and Pb Surfaces. *ACS Catalysis* **2020,** *10* (19), 11643-11653.
28. Lopez-Ruiz, J. A.; Andrews, E.; Akhade, S. A.; Lee, M.-S.; Koh, K.; Sanyal, U.; Yuk, S. F.; Karkamkar, A. J.; Derewinski, M. A.; Holladay, J.; Glezakou, V.-A.; Rousseau, R.; Gutiérrez, O. Y.; Holladay, J. D., Understanding the Role of Metal and Molecular Structure on the Electrocatalytic Hydrogenation of Oxygenated Organic Compounds. *ACS Catalysis* **2019,** *9* (11), 9964-9972.
29. Asperti, S.; Hendrikx, R.; Gonzalez-Garcia, Y.; Kortlever, R., Benchmarking the Electrochemical CO_2 Reduction on Polycrystalline Copper Foils: The Importance of Microstructure Versus Applied Potential. *ChemCatChem* **2022,** *14* (21).
30. Chen, H.; Iyer, J.; Liu, Y.; Krebs, S.; Deng, F.; Jentys, A.; Searles, D. J.; Haider, M. A.; Khare, R.; Lercher, J. A., Mechanism of Electrocatalytic H_2 Evolution, Carbonyl Hydrogenation, and Carbon-Carbon Coupling on Cu. *Journal of the American Chemical Society* **2024,** *146* (20), 13949-13961.
31. Mairanovskii, S. G.; Rubinskaya, T. Y.; Gul'tyai, V. P.; Proskurovskaya, I. V., Electrochemical reduction of benzaldehyde to benzyl alcohol at a mercury cathode. *Bulletin of the Academy of Sciences of the USSR, Division of chemical science* **1976,** *25* (10), 2203-2205.

32. Yu, J.; Zhang, P.; Li, L.; Li, K.; Zhang, G.; Liu, J.; Wang, T.; Zhao, Z. J.; Gong, J., Electroreductive coupling of benzaldehyde by balancing the formation and dimerization of the ketyl intermediate. *Nat Commun* **2022,** *13* (1), 7909.
33. Gong, L.; Zhao, S.; Yu, J.; Li, J.; Arbiol, J.; Kallio, T.; Calcabrini, M.; Martínez-Alanis, P. R.; Ibáñez, M.; Cabot, A., Influence of the catalyst surface chemistry on the electrochemical self-coupling of biomass-derived benzaldehyde into hydrobenzoin. *Energy Advances* **2024,** *3* (9), 2287-2294.
34. Liu, C.; Li, R.; Zhou, W.; Liang, Y.; Shi, Y.; Li, R.-L.; Ling, Y.; Yu, Y.; Li, J.; Zhang, B., Selectivity Origin of Organic Electrosynthesis Controlled by Electrode Materials: A Case Study on Pinacols. *ACS Catalysis* **2021,** *11* (14), 8958-8967.
35. Fouquet, P.; Johnson, M. R.; Hedgeland, H.; Jardine, A. P.; Ellis, J.; Allison, W., Molecular dynamics simulations of the diffusion of benzene sub-monolayer films on graphite basal plane surfaces. *Carbon* **2009,** *47* (11), 2627-2639.
36. Sacchi, M.; Singh, P.; Chisnall, D. M.; Ward, D. J.; Jardine, A. P.; Allison, W.; Ellis, J.; Hedgeland, H., The dynamics of benzene on Cu(111): a combined helium spin echo and dispersion-corrected DFT study into the diffusion of physisorbed aromatics on metal surfaces. *Faraday Discussions* **2017,** *204* (0), 471-485.
37. Broitman, E.; Lindquist, O. P. A.; Hellgren, N.; Hultman, L.; Holloway, B. C., Structural, electrical, and optical properties of diamondlike carbon films deposited by dc magnetron sputtering. *Journal of Vacuum Science & Technology, A: Vacuum, Surfaces, and Films* **2003,** *21* (6), L23-L27.
38. Gao, R.; Edwards, M. A.; Qiu, Y.; Barman, K.; White, H. S., Visualization of Hydrogen Evolution at Individual Platinum Nanoparticles at a Buried Interface. *Journal of the American Chemical Society* **2020,** *142* (19), 8890-8896.

Chapter VI

6. Carbon thin films for correlative nano-electrochemistry

Part of the results presented in this chapter have been included in the following publications:

M. B. Cabré, **C. Schröder**, F. Pota, M. A. C. de Oliveira, H. Nolan, L. Henderson, L. Brazel, D. Spurling, V. Nicolosi, P. Martinuz, M. Longhi, F. Amargianou, P. Bärmann, T. Petit, K. McKelvey, P. E. Colavita, Carbon Thin-Film Electrodes as High-Performing Substrates for Correlative Single Entity Electrochemistry. Small Methods 2025, 9, 2400639.

M. B. Cabré , D. Spurling , P. Martinuz , M. Longhi , **C. Schröder** , H. Nolan , V. Nicolosi, P. E. Colavita, K. McKelvey: Isolation of pseudocapacitive surface processes at monolayer MXene flakes reveals delocalized charging mechanism. *Nat Commun* **14**, 374 (2023).

M. A. C. de Oliveira, M. Brunet Cabré, **C. Schröder**, H. Nolan, F. Pota, J. A. Behan, F. Barrière, K. McKelvey, P. E. Colavita, Single-Entity Electrochemistry of N-Doped Graphene Oxide Nanostructures for Improved Kinetics of Vanadyl Oxidation. Small 2025, 21, 2405220.

Datasets presented in this chapter were the result of close collaboration with Dr. Maida Costa de Oliveira and Dr. Marc Brunet-Cabré. Carbon substrates were synthesized and characterized via XPS, Raman, optical microscopy and, where applicable via SXM, by myself while the SECCM data shown is courtesy of MBC and MCDO.

The work presented in the chapter was the result of close collaboration with Dr. Marc Brunet-Cabré and Dr. Maida Costa de Oliveira, which resulted in different publications. The majority of conceptualization, investigation and analysis of these was carried out by my collaborators using the annealed carbon films described in chapter 3 as substrate for their investigations, and details of these can be found elsewhere. The work shown in this chapter is used to highlight the beneficial properties of the annealed carbon films for these nano-electrochemical and correlative measurements. The development of the synthesis, as well as the growth and characterisation of the films were carried out by myself, or under my supervision.

In the case of the bare carbon films (6.2.) the synthesis and the spectroscopic characterisation were done by myself. For the nitrogenated graphene oxide (6.3.) I carried out scanning Raman spectroscopy and supported the analysis and interpretation of the results. For the studies of the MXenes (6.4.) I transferred the carbon synthesis onto the SiN membranes and carried out optical microscopy. In addition to this, I contributed to the beamtime at the BESSY II synchrotron for the results of scanning X-Ray microscopy.

6.1. Introduction

In the work presented in Chapters 3-5 model electrodes were used to investigate the intrinsic activities of carbon and carbon-based heterostructures in the electrocatalytic hydrogenation. However, for future applications of electrochemical devices there is great interest in developing nanomaterial-based electrodes to achieve improved performance. Nanomaterials offer several advantages over bulk materials due to their high proportion of surface atoms and large specific surface area. These characteristics are particularly beneficial for surface processes such as electrocatalysis, sensing and energy storage (e.g., capacitance). With a greater number of surface atoms relative to bulk materials, nanomaterials require less material overall, which helps reduce both the cost and weight of devices. Furthermore, semiconducting materials, like MoS_2 can be used for electrochemical applications more effectively when in combination with nanomaterials to e.g. improve conductivity.[1]

Electrochemical studies on nanomaterials are typically conducted by depositing the material onto a bulk electrode. The electrochemical response from these bulk systems is

the ensemble response from the active sites present in the electrode. This can make a proper interpretation of the electrochemical response difficult, as the behaviour of specific domains might be concealed. To gain a better understanding of the behaviour of nanomaterials and differentiate the behaviour of different sites, single entity measurements can be used. A variety of these techniques have been developed over recent years, but this section will focus on the application of scanning electrochemical cell microscopy (SECCM).

A typical SECCM setup is shown in Figure 6.1 and a detailed description of the technique can be found elsewhere.[2, 3] Briefly, a nanopipette filled with electrolyte is brought in close proximity to a conductive substrate, acting as the working electrode. A quasi counter reference electrode, e.g. a Pd hydride wire, is also inserted in the nanopipette. As the electrolyte droplet comes into contact with the working electrode it forms a nanoscale electrochemical cell that probes the local response of the contacted area, e.g. via voltammetry. The nanopipette can then be detached and repositioned in hopping mode, taking multiple measurements in a grid pattern, thus enabling to electrochemically map the sample. This technique has been used in our group for example to investigate the charge transfer kinetics of TMDCs, depending on the thickness[4] and defects.[5] Other reports compared the edge and plane sites of MoS_2, or the activity of step edges on HOPG.[6] The radius of the nanopipette probe can be varied from few tens of nm to few microns in size, therefore allowing to map single nano entities and even subdomains within the nanomaterials.

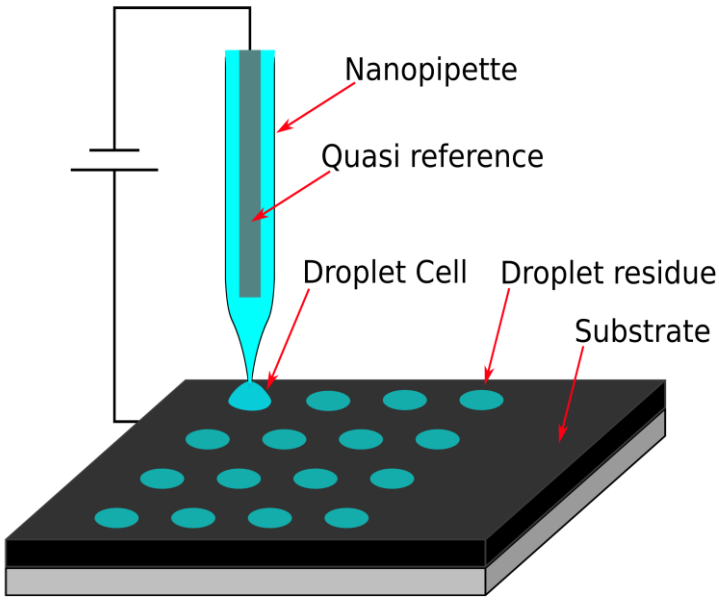

Figure 6.1 Scheme of a scanning electrochemical cell microscopy (SECCM) measurement.

The full potential of SECCM can be exploited when the electrochemical data is complemented by microscopic and/or spectroscopic techniques, to correlate electrochemical response with morphological and chemical properties of the investigated nanomaterials. This correlation is possible due to residue left by the droplet cell and the electrolyte, which can be used to localize and quantify the electrochemical probed area for each grid point. The role of the substrate is fundamental in SECCM of nanomaterials in general, and even more so in correlative measurements. In the recent advancements of SECCM, the substrate has often been overlooked, despite its critical role. Substrates employed in SECCM included HOPG, ITO or transition metals. These materials work for a wide range of applications but are not ideal. HOPG for example is not fully flat and has a significant surface roughness, with increased electrochemical activity on step edges. Transition metals tend to have good electrocatalytic activity, which will exclude some electrochemical measurements, if the response of the substrate overlaps with the region of interest of the probed material.

In this chapter the annealed carbon films presented in Chapter 3 will be applied as substrate for correlative SECCM measurements. Two projects carried out in close collaboration with Dr. Maida Costa de Oliveira and Dr. Marc Brunet-Cabré will be discussed, that exemplify the potential of the carbon thin films synthesized in this thesis for nanoscale electrochemical characterization. Applications to the advanced characterization of 2D nanomaterials are discussed with an emphasis on what properties of the carbon thin films have an impact in their performance as substrates for SECCM. The first section shows data on chemical, structural an electrochemical homogeneity of the carbon thin films. The second section discusses an example of Raman-SECCM correlative analysis of graphene oxide nanostructures and their performance in an anodic reaction that is enabled by the properties of the thin film electrodes. The final section discusses applications to the characterization of the capacitive properties of MXene monolayers, as MXenes are proposed as a good candidate for supercapacitors, and more recent ongoing work using scanning X-ray microscopy (SXM) to achieve SXM-SECCM correlation at these 2D materials.

6.2. Experimental section

The annealed carbon films were prepared as substrates for SECCM as discussed in Chapter 3 and using SiO_2/Si wafers as substrate. Graphene flakes were prepared via

electrochemical exfoliation using graphite targets as precursor materials. The full procedure can be found in de Oliveira et al.[7] Samples for SECCM were prepared by drop-casting 2 µL of a 5 µg mL^{-1} stock graphene flake dispersion onto the graphitized carbon thin-film substrates; samples were dried in air for 1 h prior to measurement.

The synthesis of $Ti_3C_2T_x$ MXenes for the pseudocapacitive measurements was carried out in the Nicolosi group as previously reported,[8] via etching of the MAX phase in a mixture of 9 M HCl and LiF powder.[9] After dilution of the MXene dispersion, 2 µl of the ink were drop-cast onto annealed carbon substrates, within 24 h of obtaining the stock dispersion. The samples were left to dry overnight in air, obtaining regions within the drop-cast area with single MXene flakes onto the carbon substrate, which established the bottom-contact connection to the carbon thin film substrate. Electrochemical measurements were carried out within 1 day.

MXenes for STXM measurement were synthesized in the Petit group, following a procedure proposed by Mathis et al.[10] involving HF etching, that leads to MXene delamination as reported in prior work.[11] The stock dispersion was diluted in water and drop-cast on SiN_x windows (Norcada) coated with the thin-film carbon electrode substrate.[12]

Single-barrelled nanopipettes were used as SECCM probes. The nanopipettes were fabricated using borosilicate capillaries (1.5 mm O.D and 0.86 mm I.D., BF150-86-7.5, Sutter Instrument, USA) using a laser puller (P-2000, Sutter Instrument, USA). The obtained pipettes were filled with electrolyte using a pipette filler(MicroFil MF34G-5, World Precision Instruments, USA). Two types of quasi reference counter electrodes (QRCE) were used. Either a leak-free Ag/AgCl electrode (LF-1-45, Innovative Instruments, Inc., USA) or a Pd-H electrode, as noted in each case. For the latter, a Pd wire (0.25 mm OD, PD005130, Goodfellow, UK) was biased at -3 V vs, a Pt counter electrode for 15 minutes in a solution of a strong acid (H_2SO_4 or $HClO_4$).

Two systems were used to perform SECCM measurements. SECCM of the N-GO flakes was done using a Park NX10 (Park Systems, South Korea). SECCM on the MXene flakes was performed on a custom-built system as previously described.[13] The SECCM measurements were performed across a predefined grid of points using hopping mode to map the electrochemical response. After the approach of the pipette voltammetry was carried out. After the measurement the pipette was retracted and repositioned to the next point of the grid.

SEM and Raman measurements were carried out as described in the previous chapters. The STXM measurements were carried out at the "MAXYMUS" microscope at the UE46-PGM2 undulator beamline at Helmholtz Zentrum Berlin/BESSY II. The measurements were done using ultra-high vacuum scanning X-ray microscopy. Transmission measurements and surface sensitive total electron yield (TEY) measurements were carried out simultaneously.

6.3. Electrochemical and spectroscopic dispersion of carbon thin films

An essential requirement for SECCM applications is for carbon thin films to be continuous and homogeneous. This was made possible via optimization of the annealing process with the protocol described in Chapter 3. The improvement in annealing is illustrated in Figure 6.2a. The figure shows the an-C films on a Si wafer using the annealing procedure prior (top) and following (bottom) optimization, which involved the introduction of pre-annealing steps described in chapter 3. It is possible to see that despite the a-C film being continuous, only a small amount of carbon remains in an-C samples in the absence of pre-annealing steps. The survey spectrum of samples prepared with the non-optimized procedure in Figure 6.2b further confirms this, as it is possible to see that the Si 2p peak (100 eV) of the underlying wafer support dominates the spectrum, whereas the contribution from the C 1s emission (285 eV) is small, indicating that the film is etched during the annealing process. The optimized procedure yields a film whose survey XPS spectrum displays only peaks assigned to C 1s and O 1s (532 eV), as expected of a continuous graphitised carbon film, as the thickness of the film remains sufficiently high at all points to attenuate any emission from the SiO_2 substrate.

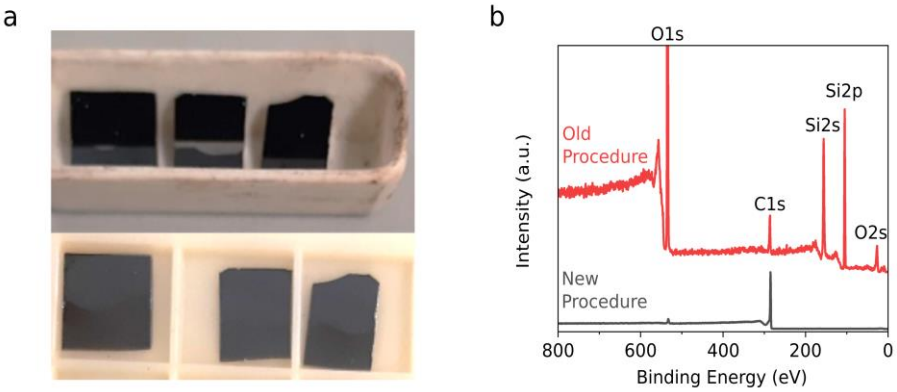

Figure 6.2 (a) a-C films deposited on wafers before annealing (top) and after annealing with the non-optimized procedure (bottom), showing clear evidence of etching. (b) XPS survey scans of an-C prepared with the non-optimized (red) and optimized (black) annealing procedures.

The chemical homogeneity was probed using mapping Raman spectroscopy. Figure 6.3a shows all spectra obtained for a 33×33 points grid on a an-C:$N_{Graphitic}$ film over an area of 100×100 μm^2. It can be seen that spectra are narrowly distributed with only a small dispersion in the intensity. The D/G intensity ratio was obtained for all 1089 spectra and a scatter plot of the results is shown in Figure 6.3b; the D/G ratio was found to be 1.01 ± 0.01, 1.06 ± 0.02 and 1.02 ± 0.01 for an-C, an-C:$N_{Graphitic}$ and an-C:$N_{Pyridinic}$, respectively. This is a variance of less than 2% across the probed area. Intensity maps of I(D)/I(G) are shown in Figures 6.3c, 6.3d and 6.3e for an-C, an-C:$N_{Graphitic}$ an-C:$N_{Pyridinic}$. The small dispersions on the D/G ratio indicates a homogeneous structure of the carbon thin films.

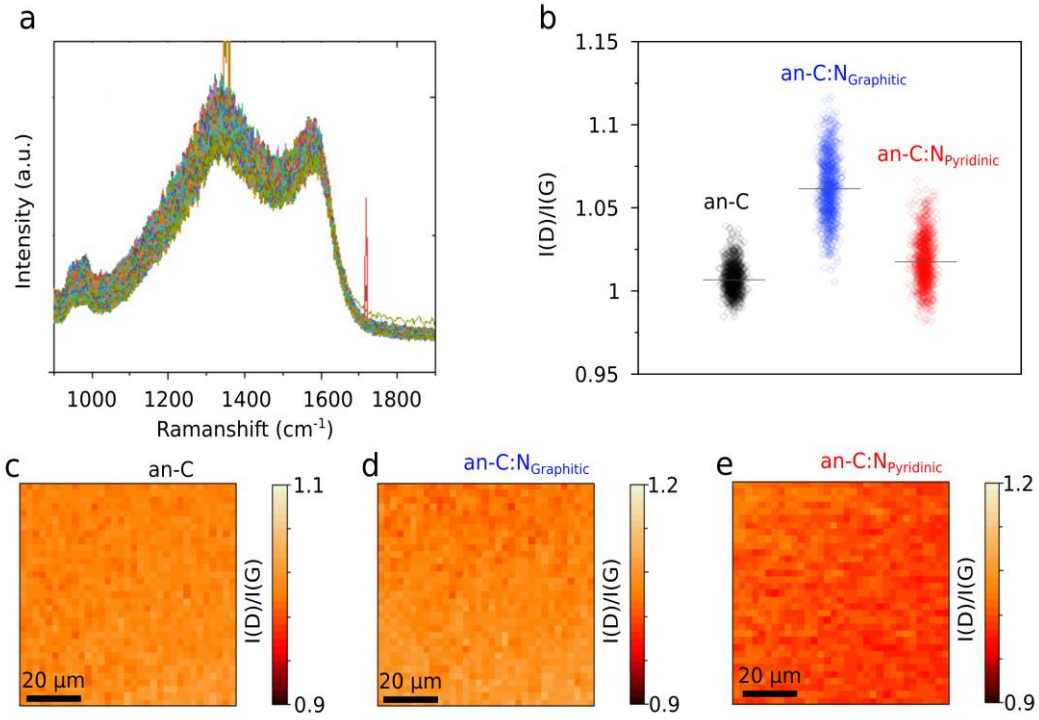

Figure 6.3 (a) Overlay of Raman spectra obtained over a 33×33 point grid on an an-C:$N_{Graphitic}$ film. (b) Scatter plot of I(D)/I(G) of annealed carbon films and intensity maps for the I(D)/I(G) ratio for (c) an-C, (d) an-C:$N_{Graphitic}$ and (e) an-C:$N_{Pyridinic}$. Adapted from Brunet Cabré et al.[12]

Beyond the chemical homogeneity, the electrochemical homogeneity of the carbon films is also relevant for SECCM applications. To probe this, SECCM measurements were carried out on the C films in the cathodic region. Current responses obtained in 20 mM H_2SO_4 at 0.5 V/s are shown in Figure 6.4a. Each of the single lines is representative of one point in a 5×5 grid where points are spaced by 20 μm so that the entire probed area is approximately 80×80 μm^2. The figure shows that the 25 CVs exhibit only small deviations from each other, thus supporting that the an-C film is electrochemically

homogeneous in the HER region. To further probe the homogeneity and the applicability of the annealed carbon films as substrate for SECCM, an outer sphere ($Ru(NH_3)_6^{2+/3+}$) and a surface sensitive redox species ($Fe(CN)_6^{3-/4-}$) were investigated using the three annealed carbon thin films as working electrodes. The current responses obtained in 4.0 mM $Ru(NH_3)_6^{3+}$ in 20 mM KCl, and 1.0 mM $Fe(CN)_6^{3-}$ in 10 mM KCl electrolyte at 0.5 V/s are shown in Figure 6.4b and 6.4c, respectively. The current response for each film is narrowly dispersed; the variances within each type of film are most likely due to differences in the size of the droplet cell, for example through local morphological features. This will be discussed later in this Chapter. The results indicate that the annealed carbon films offer good (electro)chemical homogeneity and sufficient conductivity which can allow their use as substrates in SECCM measurements. The homogeneity of the electron transfer in outer sphere reactions suggests that the annealed carbon films have a sufficient electron transfer resistance for the use in SECCM. The CV curves obtained with the surface sensitive $Fe(CN)_6^{3-/4-}$ supports this further. These results therefore indicate that an-C, an-C:$N_{Graphitic}$ and an-C:$N_{Pyridinic}$ can effectively provide a consistent and homogeneous electrochemical response across their surface for surface-sensitive and outer-sphere redox probes, making them suitable candidates for undertaking single entity electrochemistry measurements.

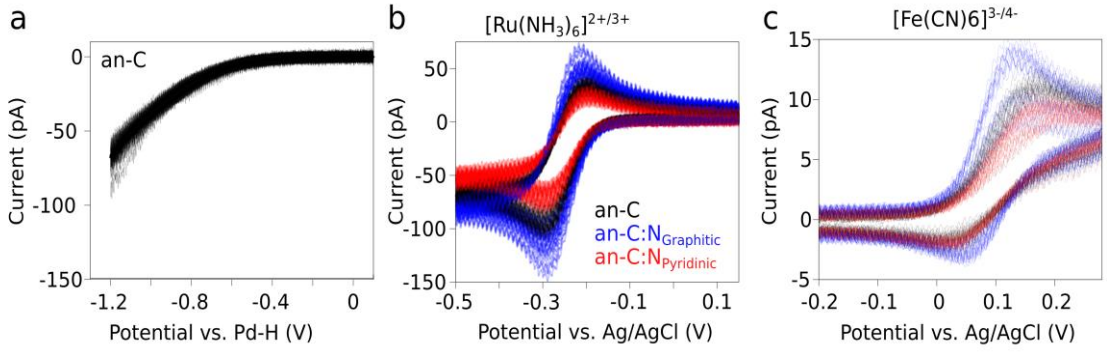

Figure 6.4 (a) Current response of an-C films obtained for CVs on each of the points in the 5×5 grid at 0.5 V/s on an-C film with 20 mM H_2SO_4. (b) Voltammograms of outer-sphere, $Ru(NH_3)_6^{3+/2+}$, and (c) $Fe(CN)_6^{3-/4-}$ redox probes on bare an-C, an-C:$N_{Graphitic}$, and an-C:$N_{Pyridinic}$. Thin lines correspond to the CV for each of the 25 points probed in a grid; thick lines represent the mean response calculated for each substrate. All voltammograms were collected at 0.5 V/s with electrolyte of 4.0 mM $Ru(NH_3)_6^{3+}$ in 20 mM KCl, and 1.0 mM $Fe(CN)_6^{3-}$ in 10 mM KCl, for A and B respectively. Data courtesy of Marc Brunet-Cabré. Adapted from Brunet Cabré et al.[12]

Previous chapters discussed the response of the annealed carbon film macroelectrodes prepared by deposition onto GC disk inserts. It is therefore interesting to further verify that trends observed via bulk electrochemistry are also observed via SECCM. A comparison of the current trends in the HER of an-C, an-C:$N_{Graphitic}$ and an-C:$N_{Pyridinic}$ is shown in Figure 6.5. For the SECCM the current response of all 25 points is shown and the an-C film is shown too. An exact comparison of potential and current ranges obtained with macroelectrodes and nanopipette probes is difficult and it is often not possible to exactly replicate the voltammetry conditions (e.g. electrolyte concentration, scan rates) with SECCM due to droplet stability and solvent evaporation during measurements. However it is possible to compare the general trends observed across the three types of carbon film, which are the same for the HER response in bulk and in nano-electrochemistry. In the case of SECCM, the an-C:$N_{Graphitic}$ film has larger HER currents and an earlier onset.

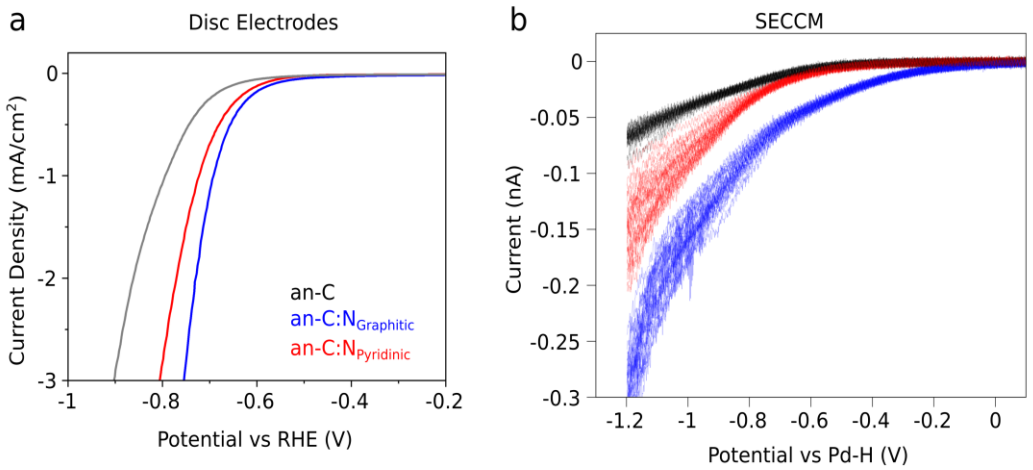

Figure 6.5 HER response on nitrogenated films (a) on disc electrodes in 0.1 M H_2SO_4 at 2 mV/s and (b) on SECCM in 20 mM H_2SO_4 with 0.5 V/s. Panel (b) data courtesy of Marc Brunet Cabré, Adapted from Brunet Cabré et al.[12]

The positive effect of nitrogenation on the electrocatalytic activity is also shown clearly in SECCM, with the an-C exhibiting a more sluggish current response in the HER compared to the nitrogenated films. It is worth mentioning here, that the roughness of the carbon films deposited on GC is expected to be higher, as polished GC is rougher than Si wafers and the roughness of the substrate should dominate the overall morphology. This is likely to affect the LSV and also accounts for some of the observed differences between the HER waveforms observed in macroelectrodes vs SECCM.

6.4. Raman-SECCM studies of anodic processes at 2D materials

Using the carbon thin film electrodes deposited on Si wafers it was possible to investigate the activity of nitrogenated graphene oxide (N-GO) in the oxidation of vanadyl as demonstrates by a recent publication of our group.[7] The vanadyl/pervanadyl process is a reaction of importance for vanadium redox flow batteries that is sluggish on pure graphitic carbon electrodes. SECCM measurements were carried out on N-GO drop casted onto an an-C film. Figure 6.6a shows a SEM image of N-GO drop cast on an-C after a SECCM measurement with the residues shown. Figure 6.6b shows the current response obtained in 0.15 M H_2SO_4 containing 0.15 mM VO^{2+} at 50 mV/s for all points measured in the SECCM grid. When correlating the points that contacted the flake (red circles in 6.6a) to the current response can be seen that the points contacting the N-GO flake gave rise to an anodic peak around 0.95 V vs. Pd-H. This peak is not visible on the points contacting the carbon substrate. A histogram of the current at 0.95 V shown in Figure 6.6c, shows that the points contacting the carbon substrate all exhibit low currents with a narrow distribution, in agreement with the results in the previous section showing that the electrochemical response of the carbon substrates is narrowly dispersed. All points that show an increased currents can be correlated to SECCM points contacting the N-GO flake.

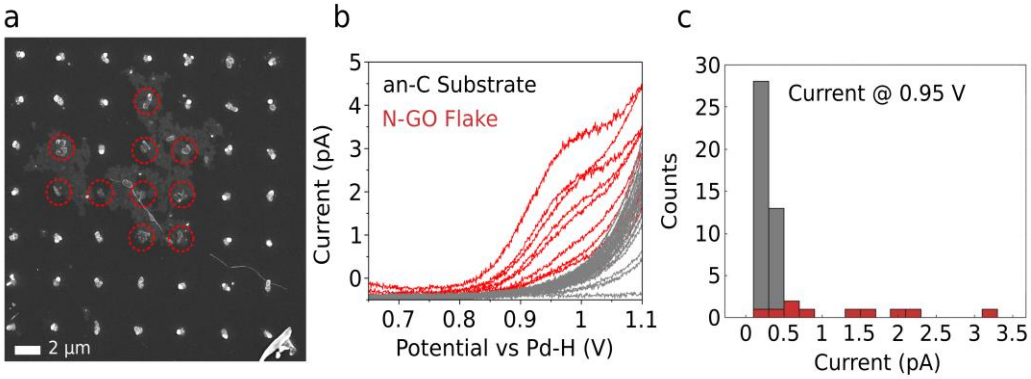

Figure 6.6 (a) SEM image of probed N-GO flake on an-C substrate with SECCM residues on the flake highlighted. (b) Current response obtained in 15 mM VO^{2+} in 0.15 M H_2SO_4 for LSVs at 50 mV/s over the SECCM grid shown in (a). (c) A histogram of current response at 0.95 V sorted by measured surface. Data courtesy of Maida Costa de Oliveira; adapted from de Oliveira et al.[7]

To get a better understanding of the chemical nature of the flakes and the grid points showing increased current response, Raman mapping was carried out on the SECCM probed areas. Raman spectra are diagnostic of the defect density at graphitic carbon materials and to the size of defect-free crystallites present. Optical images of a probed sample are shown in Figure 6.7a and 6.7b. It is important to mention, that the conditions

chosen for the Raman measurement had to be carefully tuned, as the incident laser power can lead to burning of the sample. An example of this is shown in Figure 6.7a; the black lines are the track lines resulting from the laser moving over the surface, leading to local burning shown in the black lines. The laser was therefore lowered to a level that ensured that the burning of the sample was avoided. The area shown in Figure 6.6a was then probed with the optimised incident power; the optical image is shown in Figure 6.7b: the N-GO flake slightly brighter in comparison to the substrate while the residues from the SECCM probe can also be clearly seen. The red square indicates the rough outline of the area used for Raman mapping. The average Raman spectrum of this area is shown in Figure 6.7c. The characteristic D- and G- bands of carbon can be seen, as well as the silicon signal at 520 cm^{-1} arising from the wafer substrate. The Rayleigh peak (0 cm^{-1}) is also shown. From the individual spectra an intensity map of the Rayleigh peak, the D-band and the G-band can be obtained, shown in Figure 6.7e-f. the map of the Rayleigh signal shows the exact location of the SECCM grid . This is important for assigning the Raman spectral positions relative to the SECCM grid points, as there is a slight offset between the Raman and the optical microscope. From the intensity maps of the D- and G-band the position of the GO flakes on the substrate is also clearly visible.

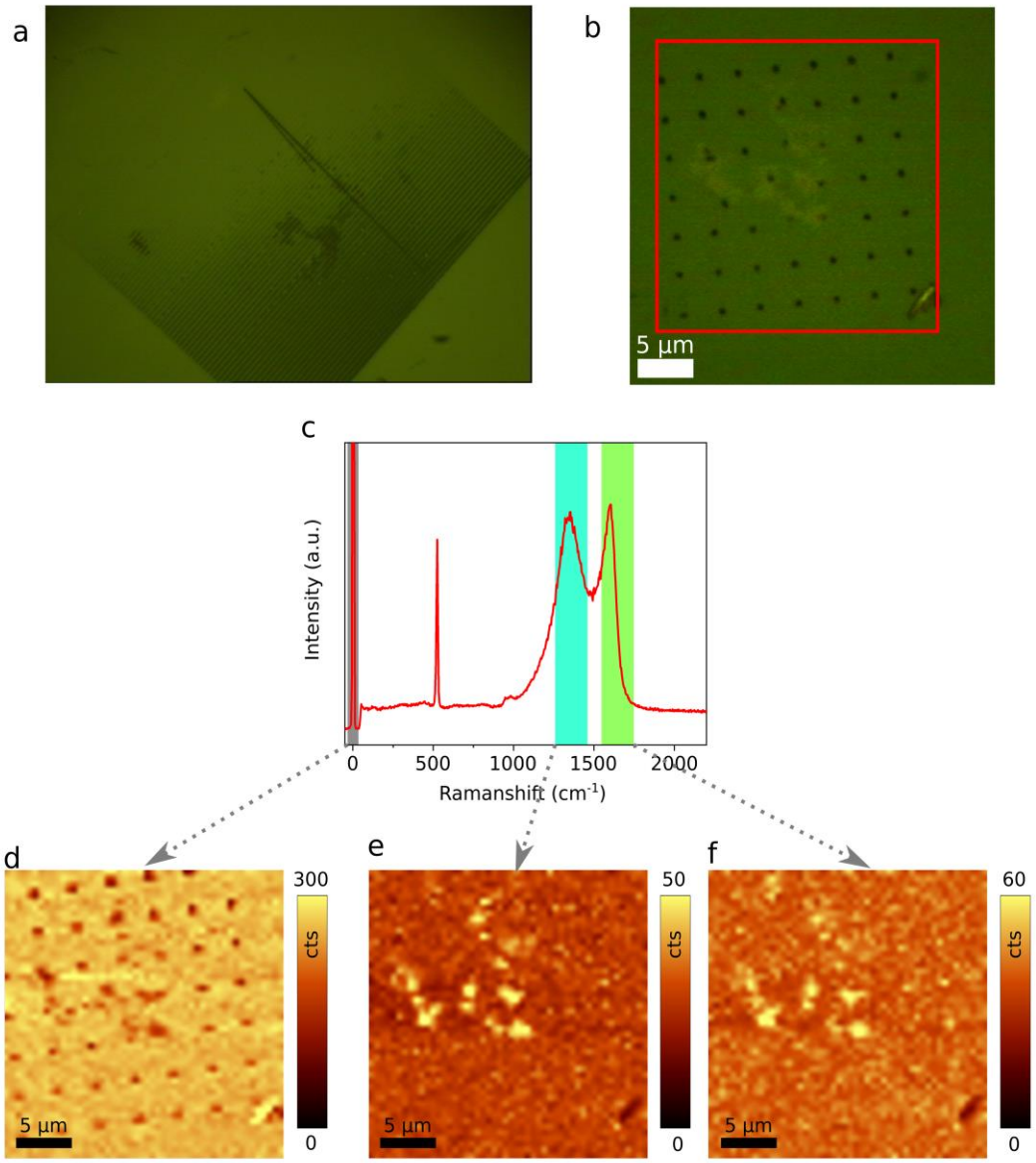

Figure 6.7 (a) Optical image of SECCM grid on drop casted N-GO after Raman mapping showing the burning of the sample, (b) Optical image of drop casted N-GO on an-C with area used for Raman mapping. (c) Average Raman spectrum obtained for area highlighted in (b). Intensity maps of (d) Rayleigh peak, (e) D-band and (f) G-band. Adapted from de Oliveira et al.[7]

Figure 6.8a shows the Raman spectra obtained by subtracting the average Raman spectrum of the substrate from the Raman spectra of points contacted on the N-GO flakes. This allowed to obtain a ratio between the D- and G-band at each of the positions probed via SECCM. From the D/G ratio, it is possible to also calculate the lateral size (L_D) of the graphene flakes.[14-16] As mentioned in Chapter 2, the relationship between I(D)/I(G) and L_D is dependent on the average crystallite size and defect density. For small defect densities (larger crystallites) the Tuinstra-Koenig relation can be used:

$$\frac{I_D}{I_G} = C(\lambda) \cdot L_D \quad (6.4)$$

Where C(λ) is a constant, which can be calculated by:

$$C(\lambda) = 2.4 \times 10^{-10} nm^{-3} \cdot \lambda^4 \quad (6.2)$$

Which for the used wavelength (532 nm) is 19.225 nm. For larger defect densities, and smaller crystallites the relation changes. According to Childres[14] the relationship changes to:

$$\frac{I_D}{I_G} = D(\lambda) \times L_D^2 \quad (6.3)$$

According to the authors the I(D)/I(G) ratio at the boundary between the two is 4, which translates to an average L_D of about 4.8 nm. With this boundary condition it is possible to calculate D(λ), by imposing continuity between the two regimes. Solving both equations for L_D the equations can be written as:

$$\sqrt{\frac{I_D/I_G}{D(\lambda)}} = L_D = \frac{C(\lambda)}{I_D/I_G} \quad (6.4)$$

Solving this equation for D(λ), the constant can be calculated as:

$$D(\lambda) = \left(\sqrt{I_D/I_G} \cdot \left(\frac{C(\lambda)}{I_D/I_G}\right)^{-1}\right)^2 = \left(\frac{\frac{\sqrt{4}}{19.225}}{2}\right)^2 = 0.173 \quad (6.5)$$

This allows to calculate L_D according to equation 6.3. Figure 6.8b shows the current at each point versus the obtained L_D.

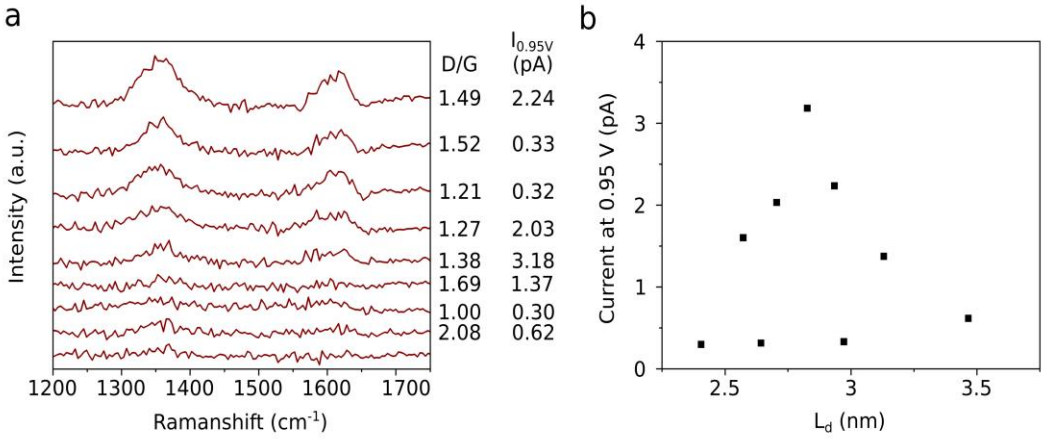

Figure 6.8 (a) Raman spectra obtained after subtraction of average substrate spectrum on spectra obtained on N-GO flakes. (b) Current at 0.95 V vs the lateral defect size calculated from the D/G ratio. Adapted from de Oliveira et al.[7]

There is no clear correlation between the L_D and the current response of the graphene flakes. This suggests that the nature of the defects is more important compared to the density of defects in determining the kinetics of the vanadyl oxidation. It does however show the potential of the annealed carbon thin films for correlative SECCM measurements, even for "carbon-on-carbon" characterisation challenges.

In summary, thanks to the (electro)chemical homogeneity of the annealed carbon film, it was possible to detect the response of sub-domains of carbon nanostructures, namely N-GO flakes, and correlate the SECCM response to Raman spectroscopy in an effort to identify relationships between defect sites and catalytic activity.

6.5. SXM-SECCM studies of capacitive processes at 2D materials

The homogeneity in the electrochemical response of carbon thin films also enabled the characterization of the capacitive response of 2D nanomaterials. This was demonstrated initially by Dr Marc Brunet-Cabré using SECCM to probe MXenes on an-C films and has recently resulted in further correlative SECCM characterization using scanning X-ray microscopy as discussed below.

MXenes are a family of transition metal carbides, nitrides or carbonitrides with a layered structure. MXenes exhibit a high electric conductivity and have gained much attention in the scientific community due to a high surface area, mechanical strength and the possibility to tune their properties.[17-20] Similar to the work in section 6.3, MXene flakes were drop cast onto annealed carbon films and probed with SECCM. An SEM image of a probed area is shown in Figure 6.9a, showing the grid of electrolyte residues left by the nanopipette probe. Figure 6.9b and c shows a histogram of the measured size of the droplet residue, which was used to estimate the contacted area of the droplet cell. It can be seen that the droplet size is narrowly dispersed with an average droplet size of 0.3 μm^2. This narrow dispersion indicates uniform wettability across the carbon surface, which in SECCM is of great importance, as variations in wettability can lead to poor resolution of the electrochemical map due to leakage of the electrolyte.

Examples of the current response of MXenes and of the carbon substrate in the capacitive region are shown in Figure 6.9d. It can be seen that the capacitance measured at MXene contacted points is significantly larger than that at the carbon substrate. A histogram of the response of the capacitance of the single points, classified by the type of contacted point

as carbon or MXene, is shown in Figure 6.9e. The capacitive response of the carbon is low and shows only small dispersion while the points exhibiting higher capacitance values are all contacted on MXene flakes.

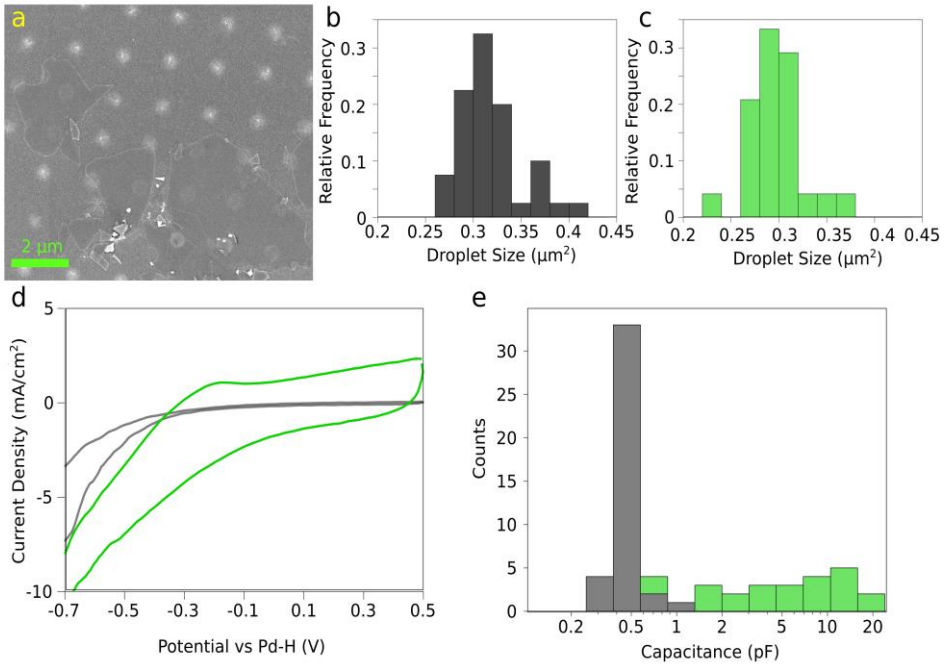

Figure 6.9 (a) SEM image of probed MXene flakes on an-C substrate with the corresponding residue size. Histogram of droplet size determined on (b) the carbon substrate and (c) MXene flakes. (d) Characteristic capacitive response of a MXene flake and the carbon substrate in 20 mM $HClO_4$ at 0.5 V/s and (e) the resulting histogram of capacitance sorted by probed point. Data courtesy of Marc Brunet-Cabré. Adapted from Brunet Cabré et al.[9]

The full explanation of this can be found in the publication by Brunet Cabré et al.[9] In short, the capacitance values measured for each droplet cell were too high to be physically sensible. On the other hand, if the capacitance is normalised by the size of the entire contacted flake, the obtained capacitance values are in agreement with values reported in literature. These results indicate a charging mechanism over the entire surface of the flake although only a small area is contacted. These results, which can have an impact on the design of devices and electrodes, were obtained, through the carbon thin films and their electrochemical homogeneity.

To further understand the behaviour of MXenes and the effect of local probing on the entire surface of contacted flakes, more recent characterization work was initiated via STXM. The detailed working principle of a synchrotron and STXM are beyond the scope of this thesis. Briefly, a tuneable beam of soft X-rays (200 eV to 1900 eV) is focused to a nanoscale spot which is scanned across the sample, probing local absorption by detecting

the intensity of the transmitted X-rays (transmission mode) or the amount of emitted secondary electrons (total electron yield, TEY). To allow for investigation of drop cast flakes the substrate needs to be transparent to X-rays. To ensure this, the an-C film was deposited on silicon nitride windows (Norcada). A scheme of this is shown in Figure 6.10a with drop cast MXene flake on the carbon film.

To allow for probing with the STXM, the location of the SECCM grid points needed to be known. To do this, optical microscopy was first used, shown in Figure 6.10b-d. Figure 6.10b shows the nitride window (1×1 mm^2) in blue in contrast against the Si support (yellow). The area of the drop cast can also be seen. Figure 6.10c and 6.10d show SECCM residues in bright-field and in dark-field, respectively. As the carbon films offer enough optical contrast with the MXene flakes and the SECCM residues, it was possible to localise the grids in relation to corners of the SiN_x window, which allowed for exact positioning of the X-ray beam and the resulting probing using STXM.

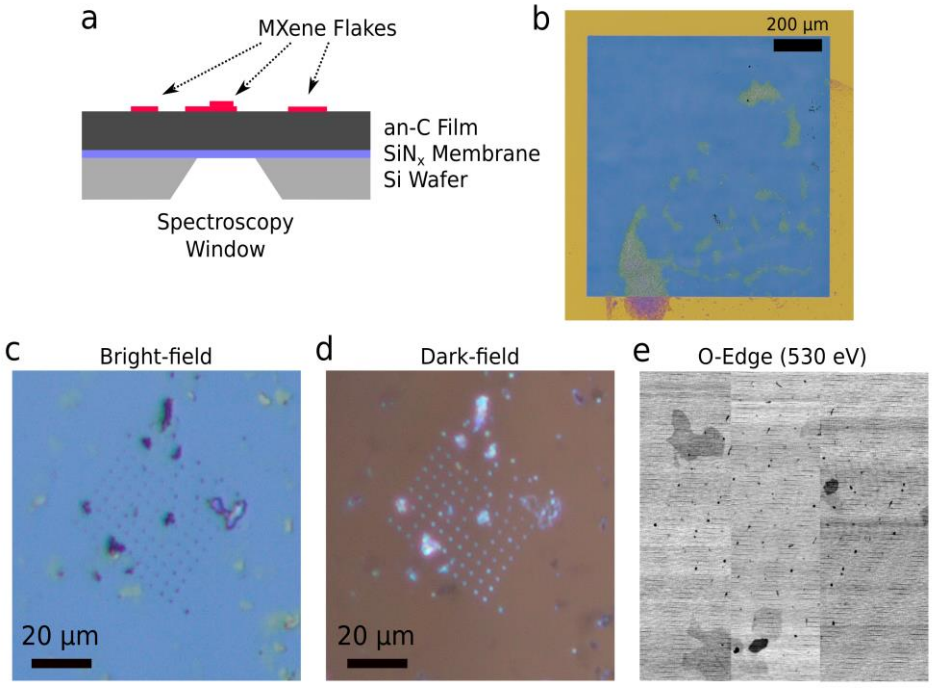

Figure 6.10 (a) Scheme of the SiN_x windows used for STXM measurements with an-C film and MXenes. (b) Optical microscopy image of the SiN_x aperture (blue) with the drop casted MXenes. (c) Bright field and (d) dark field image of the SECCM grid on the SiN_x window and (e) SECCM residue visible using STXM on the O-Edge (530 eV) of a different grid.

As mentioned above, measuring at the STXM employed both transmission mode and TEY. Transmission mode offers more bulk sensitivity and allows for distinction of monolayer and multilayer MXenes. TEY on the other hand is surface sensitive. A probed area using the two techniques is shown in Figure 6.11. In addition to the MXene flakes, the grid points

of the SECCM could be easily localized so that the electrochemical response could be correlated to chemical composition using STXM. From STXM insights on the local chemical nature and the oxidation states of the probed flakes can be gained.[12] It can be seen that TEY shows the position of the flakes, but distinction between multilayers is less clear compared to transmission mode. In addition to the imaging of defined areas, it is further possible to measure point spectra as shown in Figure 6.10c and d. The spectrum measured on the carbon substrate (green) shows no signal at the probed energy range. The points on the flake (blue, red) show spectra with clear signals correlating to the L_2 and L_3 edges of titanium. From these spectra and the ratio between the t_{2g} and the e_g peaks further information about the chemical nature, e.g. the oxidation state of the titanium can be obtained, which is currently ongoing work.[21, 22]

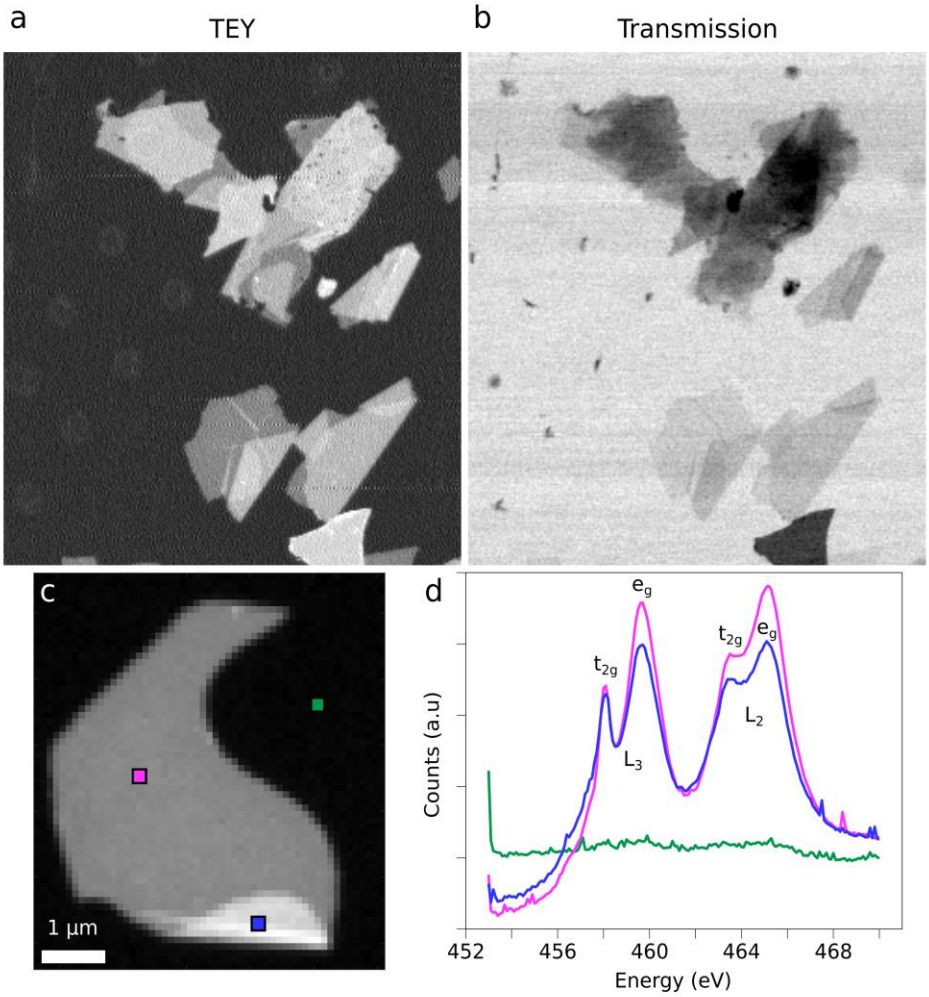

Figure 6.11 STXM image in (a) TEY and (b) Transmission mode at 463.5 eV. (c) TEY image at 463.5 eV with location of point scans and (d) the resulting spectra at the points shown in (c).

These are preliminary results obtained within a more comprehensive study carried out at BESSY II that is still ongoing. Herein, data is shown to exemplify that it is possible to use the an-C substrate for correlative STXM-SECCM.

The obtained results show that the annealed carbon thin films could be deposited on the SiN_x windows and STXM investigation was possible in transmission and TEY. With this the carbon films are a platform that can enable in depth studies of nanomaterials and correlation between their electrochemical response and their morphological and chemical nature.

6.6. Conclusion

The annealed carbon films were applied in SECCM measurements and their electrochemical homogeneity has been shown. The SECCM results confirmed the findings of Chapter 3 regarding the HER activity of nitrogenated carbon films and gave an even more detailed image. The (electro)chemical uniformity of the carbon films was shown, which allowed their use in correlative SECCM.

The use in correlative electrochemistry measurements was shown using two examples done in our group. One was the vanadyl oxidation on N-doped graphene oxide using SECCM and correlating the results with scanning Raman spectroscopy. Through the narrow distribution of the I(D)/I(G) ratio of the carbon substrate, it was possible to detect carbon nanostructures on a carbon substrate. In a second study the pseudocapacitive behaviour of MXenes was studied. As the capacitance observed on the carbon thin films is low and shows little dispersion, it was possible to detect capacitance differences and localise MXene flakes. This work was continued using synchrotron measurements, namely STXM to probe local chemical composition and oxidation states of the samples. In these measurements the carbon films allowed detection in TEY and in transmission mode, which opens the door for further research using synchrotron techniques.

The two studies all benefited and were possible because of the uniformity and homogeneity of the carbon films. These carbon films have been shown to be a promising substrate for correlative electrochemistry. Other studies that used these substrates were done on Ni nanoparticles and on carbon nanocubes together with SEM/EDS and AFM to correlate the electrochemistry with the morphology/chemistry of the sample. This can be found in the work by Brunet-Cabré et al.[12] and are reported elsewhere.

An additional advantage of the carbon films is in their synthesis. Using the sputter deposition and annealing procedure, multiple samples can be produced in one batch that will have almost identical properties. The films can further be synthesised on a variety of materials, given they can withstand the annealing temperature. In comparison to other substrates used in SECCM studies, the carbon films unify a lot of benefits needed for these studies and allow a wide variety of microscopic and spectroscopic techniques. Thereby the carbon thin films have the potential to accelerate the use of correlative studies for an in-depth understanding of the electrochemical response of nanomaterials.

References

1. Gogotsi, Y.; Penner, R. M., Energy Storage in Nanomaterials – Capacitive, Pseudocapacitive, or Battery-like? *ACS Nano* **2018,** *12* (3), 2081-2083.
2. Ebejer, N.; Güell, A. G.; Lai, S. C.; McKelvey, K.; Snowden, M. E.; Unwin, P. R., Scanning electrochemical cell microscopy: a versatile technique for nanoscale electrochemistry and functional imaging. *Annual review of analytical chemistry* **2013,** *6* (1), 329-351.
3. Ebejer, N.; Schnippering, M.; Colburn, A. W.; Edwards, M. A.; Unwin, P. R., Localized high resolution electrochemistry and multifunctional imaging: scanning electrochemical cell microscopy. *Analytical chemistry* **2010,** *82* (22), 9141-9145.
4. Brunet Cabré, M.; Paiva, A. E.; Velický, M.; Colavita, P. E.; McKelvey, K., Electrochemical kinetics as a function of transition metal dichalcogenide thickness. *Electrochimica Acta* **2021,** *393*, 139027.
5. Cabré, M. B.; Paiva, A. E.; Velický, M.; Colavita, P. E.; McKelvey, K., Electrochemical Detection of Isolated Nanoscale Defects in 2D Transition Metal Dichalcogenides. *The Journal of Physical Chemistry C* **2022,** *126* (28), 11636-11641.
6. Daviddi, E.; Gonos, K. L.; Colburn, A. W.; Bentley, C. L.; Unwin, P. R., Scanning Electrochemical Cell Microscopy (SECCM) Chronopotentiometry: Development and Applications in Electroanalysis and Electrocatalysis. *Analytical Chemistry* **2019,** *91* (14), 9229-9237.
7. de Oliveira, M. A. C.; Brunet Cabré, M.; Schröder, C.; Nolan, H.; Pota, F.; Behan, J. A.; Barrière, F.; McKelvey, K.; Colavita, P. E., Single-Entity Electrochemistry of N-Doped Graphene Oxide Nanostructures for Improved Kinetics of Vanadyl Oxidation. *Small* **2025,** *21* (3), 2405220.
8. Borghetti, M.; Serpelloni, M.; Sardini, E.; Spurling, D.; Nicolosi, V., Temperature influence on Ti3C2Tx lines printed by aerosol jet printing. *Sensors and Actuators A: Physical* **2021,** *332*, 113185.
9. Brunet Cabré, M.; Spurling, D.; Martinuz, P.; Longhi, M.; Schröder, C.; Nolan, H.; Nicolosi, V.; Colavita, P. E.; McKelvey, K., Isolation of pseudocapacitive surface processes at monolayer MXene flakes reveals delocalized charging mechanism. *Nature Communications* **2023,** *14* (1), 374.
10. Mathis, T. S.; Maleski, K.; Goad, A.; Sarycheva, A.; Anayee, M.; Foucher, A. C.; Hantanasirisakul, K.; Shuck, C. E.; Stach, E. A.; Gogotsi, Y., Modified MAX phase synthesis for environmentally stable and highly conductive Ti3C2 MXene. *ACS nano* **2021,** *15* (4), 6420-6429.
11. Shekhirev, M.; Busa, J.; Shuck, C. E.; Torres, A.; Bagheri, S.; Sinitskii, A.; Gogotsi, Y., Ultralarge flakes of Ti3C2T x MXene via soft delamination. *ACS nano* **2022,** *16* (9), 13695-13703.
12. Cabré, M. B.; Schröder, C.; Pota, F.; de Oliveira, M. A. C.; Nolan, H.; Henderson, L.; Brazel, L.; Spurling, D.; Nicolosi, V.; Martinuz, P., Carbon Thin-Film Electrodes as High-Performing Substrates for Correlative Single Entity Electrochemistry. *Small Methods* **2025,** *9* (1), 2400639.
13. Brunet Cabre, M.; Djekic, D.; Romano, T.; Hanna, N.; Anders, J.; McKelvey, K., Microscale electrochemical cell on a custom CMOS transimpedance amplifier for high temporal resolution single entity electrochemistry. *ChemElectroChem* **2020,** *7* (23), 4724-4729.

14. Childres, I.; Jauregui, L. A.; Tian, J.; Chen, Y. P., Effect of oxygen plasma etching on graphene studied using Raman spectroscopy and electronic transport measurements. *New Journal of Physics* **2011,** *13* (2), 025008.
15. Cançado, L. G.; Takai, K.; Enoki, T.; Endo, M.; Kim, Y. A.; Mizusaki, H.; Jorio, A.; Coelho, L. N.; Magalhães-Paniago, R.; Pimenta, M. A., General equation for the determination of the crystallite size La of nanographite by Raman spectroscopy. *Applied Physics Letters* **2006,** *88* (16), 163106.
16. Ferrari, A. C., Raman spectroscopy of graphene and graphite: Disorder, electron–phonon coupling, doping and nonadiabatic effects. *Solid State Communications* **2007,** *143* (1), 47-57.
17. Lim, K. R. G.; Shekhirev, M.; Wyatt, B. C.; Anasori, B.; Gogotsi, Y.; Seh, Z. W., Fundamentals of MXene synthesis. *Nature Synthesis* **2022,** *1* (8), 601-614.
18. VahidMohammadi, A.; Rosen, J.; Gogotsi, Y., The world of two-dimensional carbides and nitrides (MXenes). *Science* **2021,** *372* (6547), eabf1581.
19. Anasori, B.; Gogotsi, Y., MXenes: trends, growth, and future directions. *Graphene and 2D Materials* **2022,** *7* (3), 75-79.
20. Gogotsi, Y., The Future of MXenes. *Chemistry of Materials* **2023,** *35* (21), 8767-8770.
21. Stoyanov, E.; Langenhorst, F.; Steinle-Neumann, G., The effect of valence state and site geometry on Ti L 3, 2 and OK electron energy-loss spectra of TixOy phases. *American Mineralogist* **2007,** *92* (4), 577-586.
22. Amargianou, F.; Bärmann, P.; Shao, H.; Taberna, P.-L.; Simon, P.; Gonzalez-Julian, J.; Weigand, M.; Petit, T., Nanoscale Surface and Bulk Electronic Properties of Ti3C2Tx MXene Unraveled by Multimodal X-Ray Spectromicroscopy. *Small Methods* **2024,** *8* (12), 2400190.

Chapter VII

7. Conclusions and future work

7.1. Conclusions

The objective of this thesis was to explore the role that carbon can play in the electrocatalytic hydrogenation of oxygenated organic compounds, a reaction which could become a sustainable route to generate fuels and chemicals. Many studies on this topic use nanostructured carbon materials and 3D architectures, which makes it difficult to extract the true intrinsic activity of a material. Therefore, thin-film electrodes were investigated in this work; these thin-films were based on either (nitrogenated) carbon alone or carbon in combination with transition metals and transition metal compounds.

In Chapter 3 metal-free nitrogenated carbons were synthesised using a two-step process consisting of dc-magnetron sputtering with subsequent annealing of the carbon thin films. Nitrogen could be introduced into the structures by using nitrogen for the sputter deposition or by using ammonia gas during the annealing. These processes allowed good control over graphitisation and distribution of nitrogen functionalities at the carbon surface. The carbon films were characterised using a combination of microscopic and spectroscopic techniques, and their activity in the hydrogen evolution reaction was investigated. An improvement in the HER response was achieved through the nitrogenation, compared to bare carbon materials. For ECH experiments a custom made electrolysis cell was designed which allowed the investigation of the carbon materials in the electrocatalytic hydrogenation of benzaldehyde. A positive effect of the nitrogenation on the selectivity towards benzyl alcohol was found, similar to the improved activity in the HER. Mass transport was found to be a limiting factor, which led to changes in the electrolysis setup with the implementation of stirring. This increased the production rates, but the nitrogenated carbon thin-films were overall still poor electrocatalysts, when compared to most metal-based materials in the literature.

In Chapter 4 the nitrogenated carbon electrodes were used as a support material for molybdenum disulphide, a material which could become a low-cost HER catalyst. The CVD process used resulted in growth of a slightly sub stochiometric MoS_2 in the 2H phase, with no obvious effect of the nitrogen functionalities of the carbon film on the MoS_2 structure. However, a suppression of the HER in alkaline pH was found for the MoS_2 grown on the carbon with mainly pyridinic nitrogen. This was attributed to a protonation/deprotonation equilibrium of the pyridinic sites and resulting from that an attraction/repulsion between the carbon and the MoS_2. The ECH on the heterostructured

electrodes showed higher activity compared to the bare carbons and turn over frequencies were found to be in a comparable range to values reported for metallic catalysts in literature. There was however still a poor faradaic efficiency, with most of the current contributing to the production of hydrogen.

In Chapter 5 sputtered copper thin film electrodes were subsequently covered with amorphous carbon shells. Characterisation of these CuXC heterostructures showed that the carbon layer has the same chemical composition independently of the mass loading. In the range of the mass loadings of carbon used, no effect on the voltammetry of the heterostructures was found, neither in the HER nor in the presence of benzaldehyde. This suggests that the copper surface remains unchanged and the dominant source of the electrocatalytic activity. While the reduction rates of benzaldehyde and the faradaic efficiencies seem independent of the carbon loading, a positive trend in the selectivity was observed for a defined range of carbon loadings. While the exact mechanism of this could not yet be solved, some possible causes for this were discussed. The carbon could be introducing adsorption sites through spill-over effects, thus lowering the relative surface concentration on the copper. Alternatively, a limiting effect of the carbon on the mass transport of benzaldehyde might also be at play.

Chapter 6 expanded on the use of the annealed carbon films to scanning electrochemical cell microscopy. Here the potential of SECCM in combination with characterisation techniques for correlative electrochemistry experiments was shown. The benefits of the carbon and their applicability for SECCM and a wide range of characterisation techniques, all the way to synchrotron techniques, e.g. STXM, was highlighted. Correlative SECCM can give powerful insights in relationships between the chemical and structural nature of a material and the electrochemical behaviour of the material. The carbon thin films obtained in chapter 3 showed good homogeneity in morphological, chemical and electrochemical features, which makes them an ideal substrate for SECCM measurements to deliver good conductivity while ensuring high electrochemical contrast relative to supported nanomaterials. This has been shown exemplified by two projects carried out in collaboration within the research group. A first one, used scanning Raman spectroscopy to characterise nitrogenated graphene oxide flakes on the carbon and a second one characterising MXenes using STXM. The latter showed that the carbon films enable measurements in both, transmission and total electron yield, thus giving valuable insights on the chemical nature of the probed samples. The annealed carbon films could accelerate

the use of correlative SECCM and allowing for an in-depth understanding in the relationship between chemical and electrochemical behaviour of nanomaterials.

In this work carbon was used as nitrogenated metal-free thin films, as support for MoS_2 and as a cover layer on copper films. The ECH of benzaldehyde was studied on all these materials. The results were discussed in the context of previous results reported in literature. Effects of reaction conditions on the ECH were found and directions for future work were identified based on the results. These directions for future work will be discussed in the next section. New design principles and synthesis routes for electrocatalytic materials, especially for the ECH were found. Overall, the results show that carbon and carbon based heterostructures have the potential to play a key role in the ECH, far beyond their current use.

7.2. Future work

From this thesis promising directions for future research projects on the role of carbon in electrochemistry and electrocatalysis could be identified.

The results of Chapter 3 indicate an effect of graphitisation on the electrocatalytic activity in the HER. This would be worth exploring for nitrogen free and nitrogenated carbon films. Another approach would be the investigation of other dopants and co-dopants in the carbon. The introduction of phosphorus has been reported in literature to positively enhance the activity in the HER,[1, 2] and this should be investigated for the ECH.

The results presented in Chapter 4 on the MoS_2/an-C:$N_{Graphitic}$ heterostructures shows that these heterostructures can deliver good activity in the ECH. There is a range of applied potential, where the obtained selectivity and production rates/TOF are in a competitive range with catalyst materials reported in literature. Especially considering the significant lower cost of the MoS_2. The faradaic efficiencies observed are however far from desired values. This could be tackled for example by increasing the concentration of benzaldehyde in the electrolyte, which could lead to suppression of HER and to a higher rate (and FE) of ECH. In addition to an increased concentration a higher pH could potentially lead to higher FE. This should be investigated in future experiments. At higher pH values an effect of the different N-functionalities might arise, similar to the one observed in the HER.

Another research direction would be a variation in the growth and synthesis of MoS_2. By replacing the close proximity setup used to grow MoS_2 the growth substrate could be

placed downstream of the MoO_3 precursor, which has been reported in different publications.[3, 4]

The results obtained on the CuXC electrodes were promising, with high faradaic efficiencies and production rates. The effect of the amorphous carbon on copper on the ECH could not be finally explained. To further understand this effect, SECCM could be used. By studying different carbon thicknesses on different metals, a more complete picture of the role of the a-C could be obtained. One route is to use Pt as a substrate with a well understood electrocatalytic activity. By investigating the current response on PtXC heterostructures with and without benzaldehyde a potential effect of the a-C on the mass transport of benzaldehyde might be seen. Pt is known to be poisoned by benzaldehyde, leading to suppression of HER currents. If the a-C blocks the benzaldehyde, the HER current on the Pt should be maintained and the poisoning should be inhibited. By investigating the effect of the amorphous carbon on the electrocatalytic hydrogenation design principles on metal-carbon heterostructures can be derived. Other metal layers should also be investigated, as copper, although less critical compared to platinum, is still a highly sought after metal in electronic applications. Therefore, it will be relevant to look at the electrocatalytic activity of other transition metals.

In Chapter 6 the potential of an-C films in correlative SECCM have been shown. Here the carbon films can help to gain new and valuable insights in the working mechanisms of nanomaterials in electrochemistry.

For all the materials the stability in the ECH has not been investigated. To make materials an alternative a stable current response is needed. The ECH studies on the synthesised materials can be expanded to other organic compounds relevant in biomass upgrading, for example furfural or hydroxy methyl furfural. For all materials the reaction conditions can be varied, namely temperature, pH and concentration, to further optimise the performance.

References

1. Zheng, Y.; Jiao, Y.; Li, L. H.; Xing, T.; Chen, Y.; Jaroniec, M.; Qiao, S. Z., Toward Design of Synergistically Active Carbon-Based Catalysts for Electrocatalytic Hydrogen Evolution. *ACS Nano* **2014,** *8* (5), 5290-5296.
2. Dai, L., *Carbon-based metal-free catalysts: design and applications*. John Wiley & Sons: 2018.
3. Mouloua, D.; Rajput, N. S.; Saitzek, S.; Kaja, K.; Hoummada, K.; El Marssi, M.; El Khakani, M. A.; Jouiad, M., Broadband photodetection using one-step CVD-fabricated MoS2/MoO2 microflower/microfiber heterostructures. *Scientific Reports* **2022,** *12* (1), 22096.
4. Wang, Y.; Ma, Y.; Shi, J.; Yan, X.; Luo, J.; Zhu, H.; Jia, K.; Li, J.; Zhang, C. Y., Surface Modification of Monolayer MoS2 by Baking for Biomedical Applications. *Frontiers in Chemistry* **2020,** *8*.

Appendix I

Supplementary Information

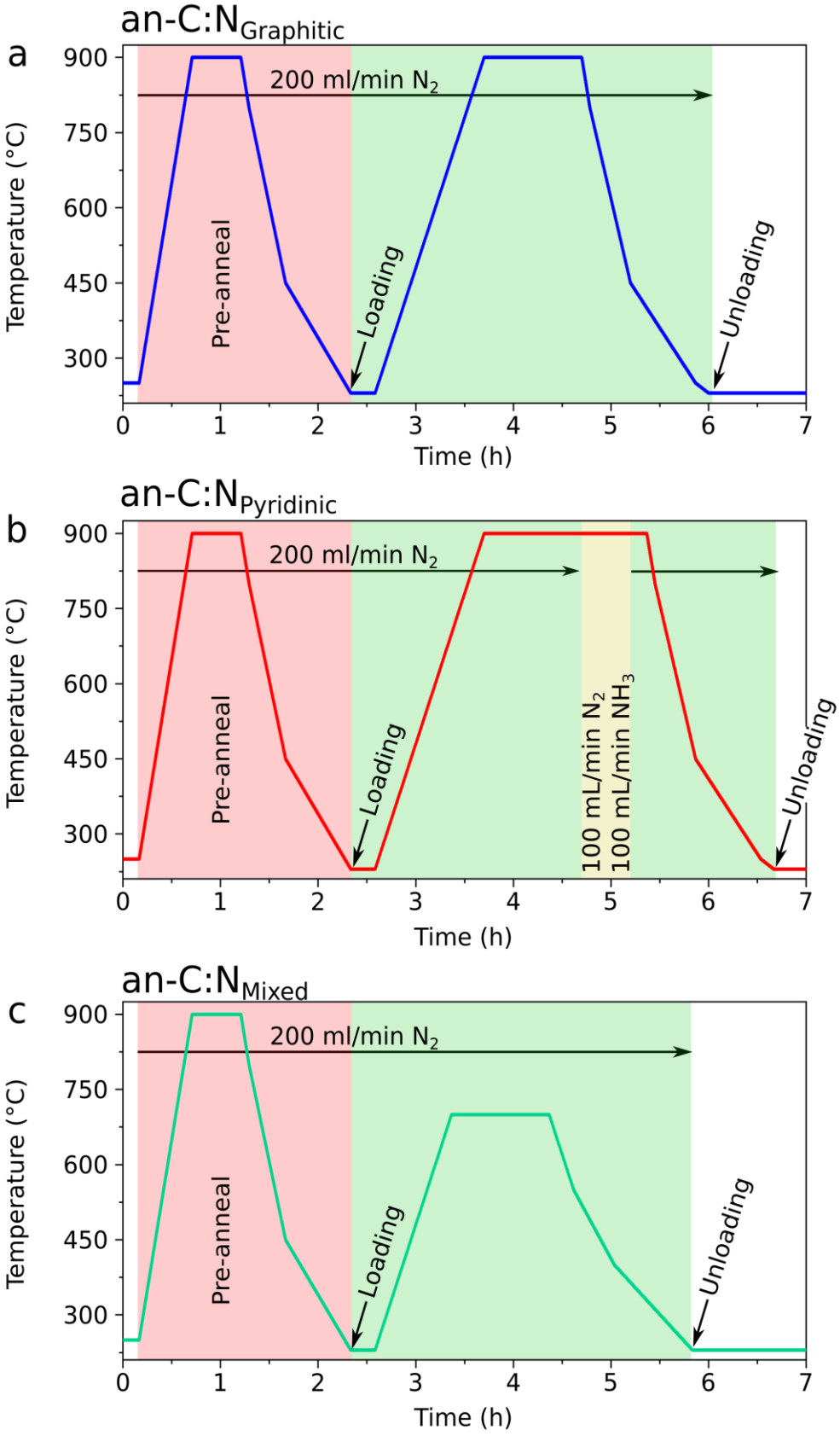

Figure A.1 Temperature profiles and gases used for the annealing of an-C:$N_{Graphitic}$, (b) an-C:$N_{Pyridinic}$ and (c) an-C:N_{Mixed}.

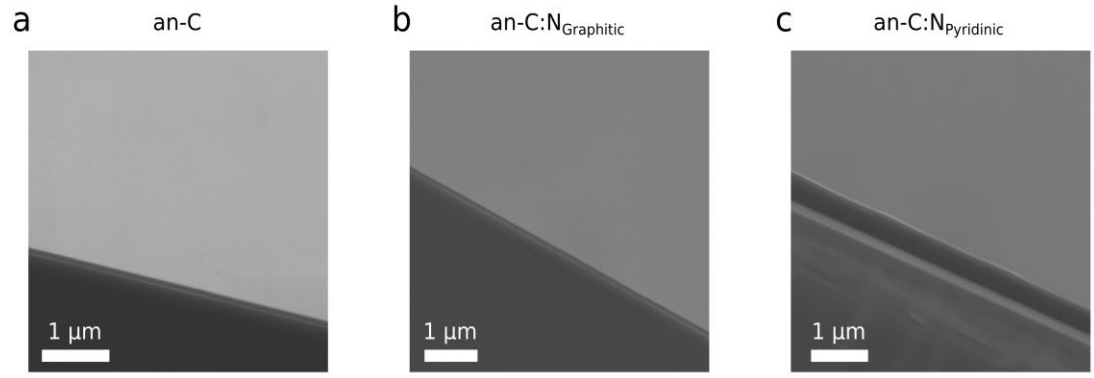

Figure A.2 SEM obtained in cross section for (a) an-C, (b) an-C:$N_{Graphitic}$ and (c) an-C:$N_{Pyridinic}$.

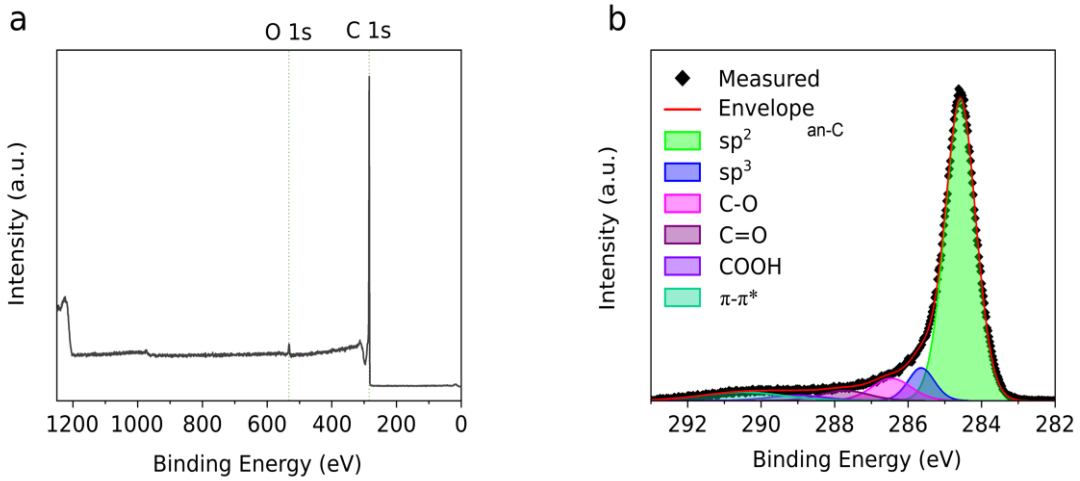

Figure A.3 (a) XPS survey spectrum and (b) C1s high resolution spectra for an-C.

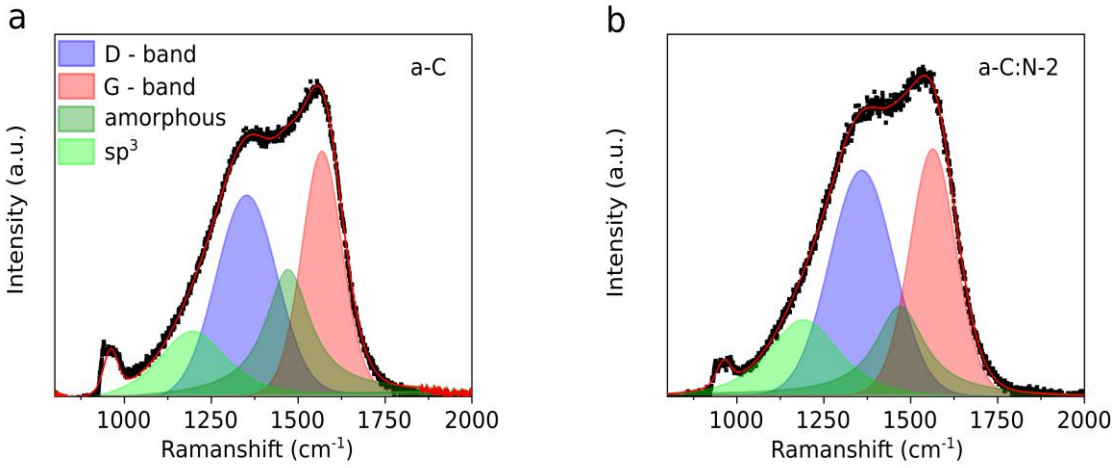

Figure A.4 Best fit obtained for Raman spectra or (a) a-C and (b) a-C:N-2

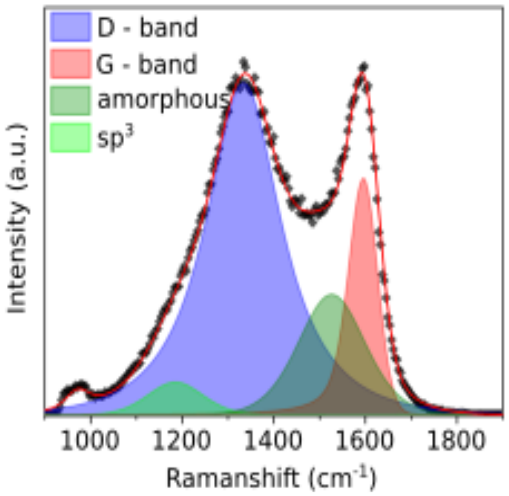

Figure A.5 Best fit obtained for Raman spectra of an-C.

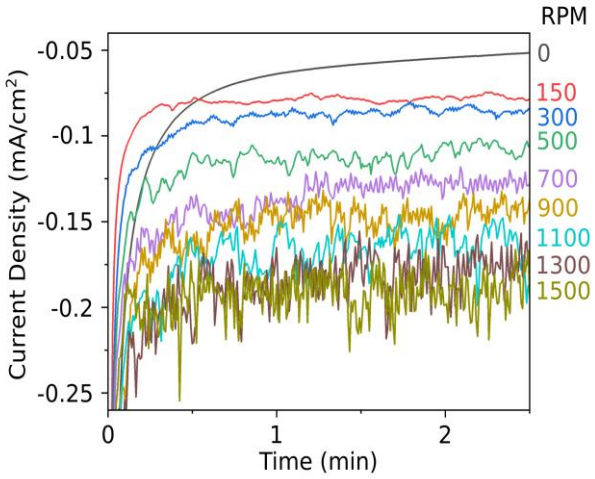

Figure A.6 Current response of chrono amperometry at -0.5 V vs Ag/AgCl in 0.1 M H_2SO_4 with 20 mM benzaldehyde on a MoS_2/an-C:$N_{Pyridinic}$ electrode at different stirring speeds.

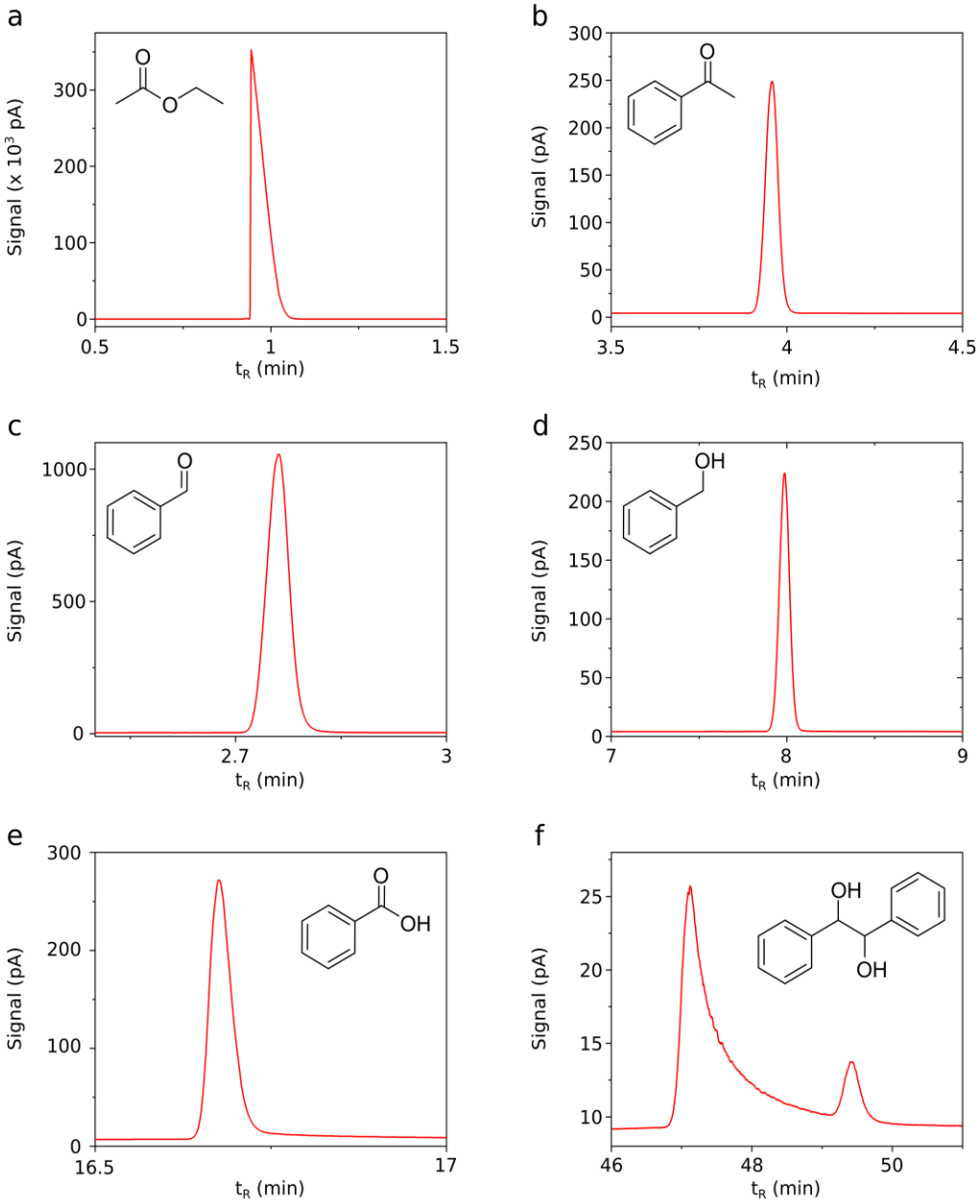

Figure A.7 Peaks obtained from the gas chromatography for (a)ethyl acetate, (b) acetophenone, (c) benzaldehyde, (d) benzyl alcohol, (e) benzoic acid and (f) hydrobenzoin.

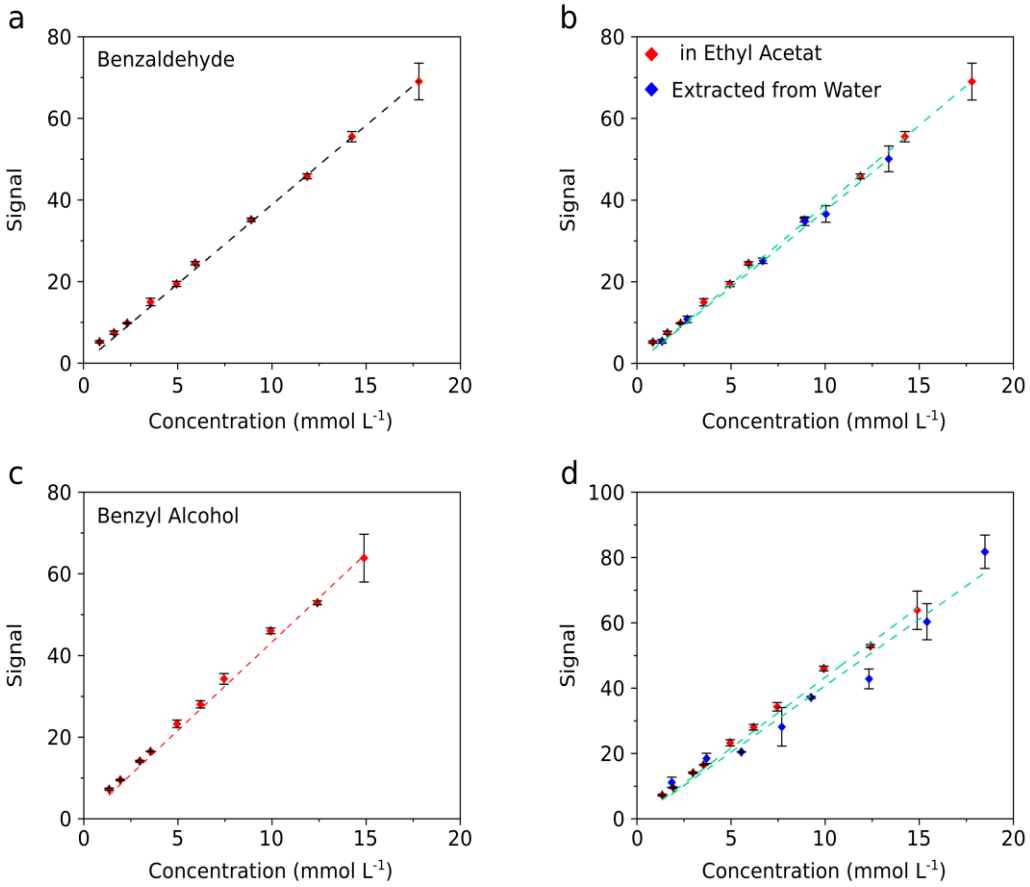

Figure A.8 Calibration and extraction of (a, b) benzaldehyde and (c, d) benzyl alcohol.

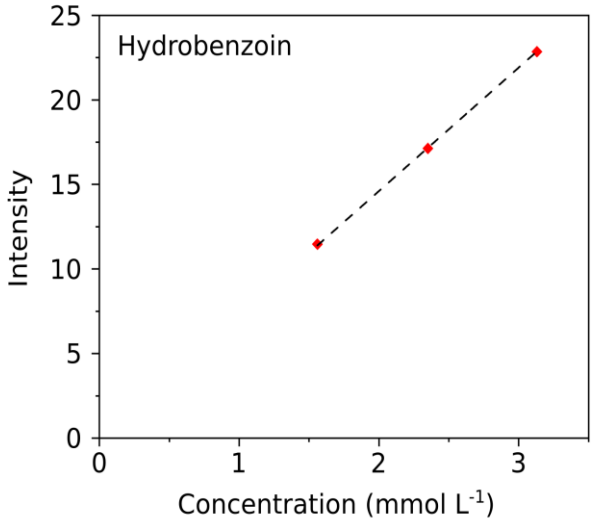

Figure A.9 Calibration of hydrobenzoin.

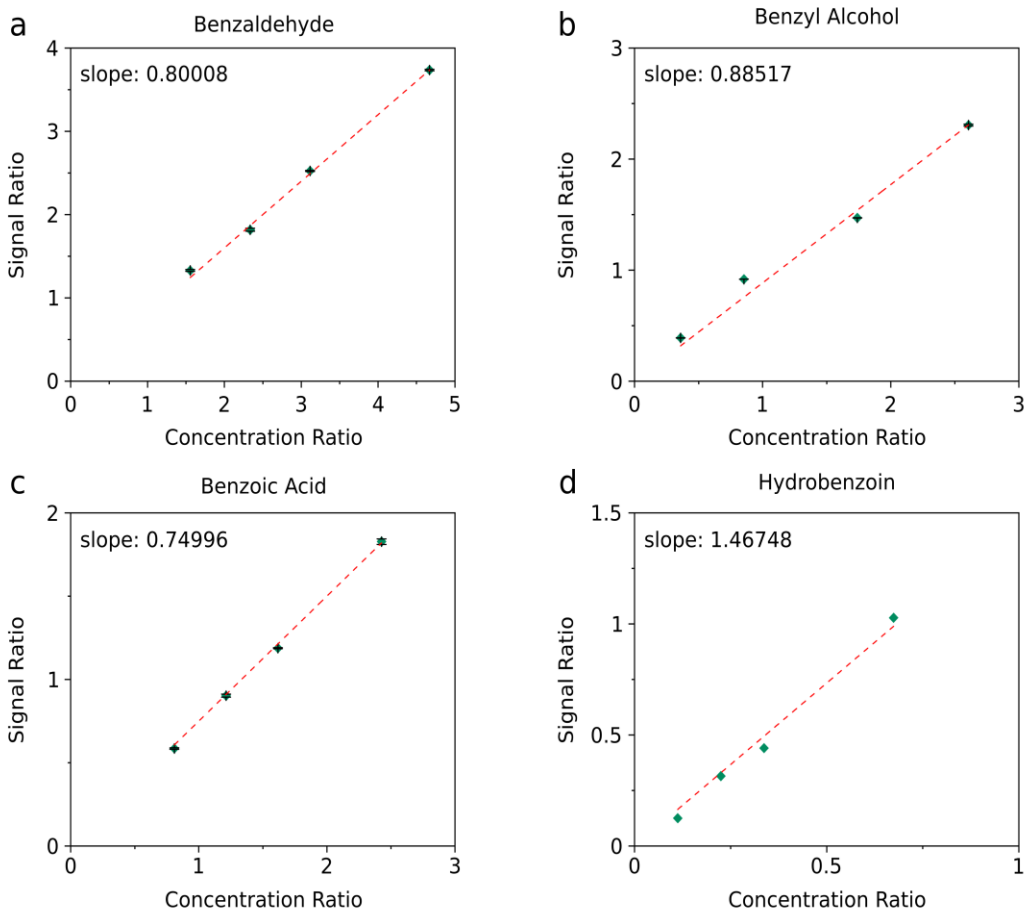

Figure A.10 Calibration of (a) benzaldehyde, (b) benzyl alcohol, (c) benzoic acid and (d) hydrobenzoin using acetophenone as an internal standard.

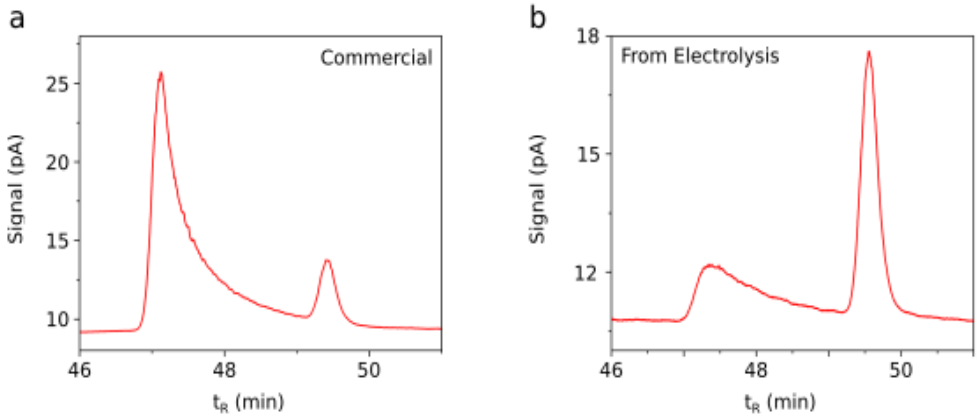

Figure A.11 Hydrobenzoin peak obtained from (a) commercial source and (b) from electrolysis.

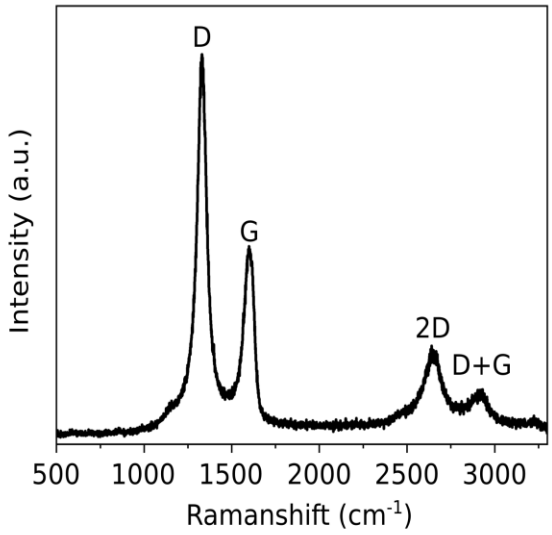

Figure A.12 Raman spectrum obtained for glassy carbon.

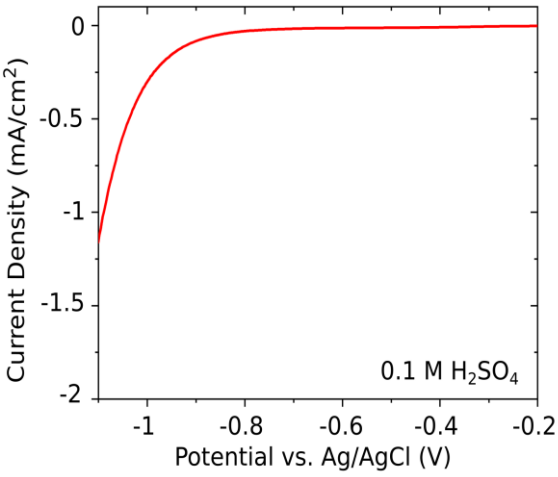

Figure A.13 Current response of a LSV (2 mV/s) on a sputtered a-C film in 0.1 M H_2SO_4.

Appendix II

Presentations and Published Work

Peer Reviewed Publications

- Victor Manuel Villapun Puzas, Luke N. Carter, **Christian Schröder**, Paula E. Colavita, David A. Hoey, Mark A. Webber, Owen Addison, Duncan E. T. Shepherd, Moataz M. Attallah, Liam M. Grover, Sophie C. Cox: "Surface Free Energy Dominates the Biological Interactions of Postprocessed Additively Manufactured Ti-6Al-4V", ACS Biomaterials Science & Engineering, **2022**, 8, 10, 4311-4326.
- Hugo Nolan, **Christian Schröder**, Marc Brunet Cabré, Filippo Pota, Neill McEvoy, Kim McKelvey, Tatiana S. Perova, Paula E. Colavita: "MoS2/carbon heterostructured catalysts for the hydrogen evolution reaction: N-doping modulation of substrate effects in acid and alkaline electrolytes", Carbon, **2023**, 202, 70-80.
- Marc Brunet Cabré, Dahnan Spurling, Pietro Martinuz, Mariangela Longhi, **Christian Schröder**, Hugo Nolan, Valeria Nicolosi, Paula E. Colavita, Kim McKelvey: "Isolation of pseudocapacitive surface processes at monolayer MXene flakes reveals delocalized charging mechanism", Nature Communications, **2023**, 14, 374.
- Marc Brunet Cabré, **Christian Schröder**, Filippo Pota, Maida A. Costa de Oliveira, Hugo Nolan, Lua Henderson, Laurence Brazel, Dahnan Spurling, Valeria Nicolosi, Pietro Martinuz, Mariangela Longhi, Faidra Amargianou, Peer Bärmann, Tristan Petit, Kim McKelvey, Paula E. Colavita: "Carbon Thin-Film Electrodes as High-Performing Substrates for Correlative Single Entity Electrochemistry", Small Methods, **2024**, 2400639.
- Maida A. Costa de Oliveira, **Christian Schröder**, Marc Brunet Cabré, Hugo Nolan, Antoni Forner-Cuenca, Tatiana S. Perova, Kim McKelvey, Paula E. Colavita: "Effects of N-functional groups on the electron transfer kinetics of VO2+/VO2+ at carbon: Decoupling morphology from chemical effects using model systems", Electrochimica Acta, **2024**, 475, 143640.
- Filippo Pota, Maida A. Costa de Oliveira, **Christian Schröder**, Marc Brunet Cabré, Hugo Nolan, Aran Rafferty, Olivier Jeannin, Franck Camerel, James A. Behan, Frédéric Barrière, Paula E. Colavita: "Porous N-doped carbon-encapsulated iron as a novel catalyst architecture for the electrocatalytic hydrogenation of benzaldehyde", ChemSusChem, **2024**, e202400546.

- Hugo Nolan, Federico Zen, Alican Gençer, Lua Henderson, Martin Kelly, Filippo Pota, **Christian Schröder**, Eoin M. Scanlan, Paula E. Colavita: "Functional organic adlayers for controlling the adhesion strength of electrolessly deposited copper on super-engineering plastics", Applied Surface Science, **2024**, 682, 161700.
- Maida Aysla Costa de Oliveira, Marc Brunet Cabré, **Christian Schröder**, Hugo Nolan, Filippo Pota, James A. Behan, Frédéric Barrière, Kim McKelvey, Paula E. Colavita: "Single-Entity Electrochemistry of N-Doped Graphene Oxide Nanostructures for Improved Kinetics of Vanadyl Oxidation", Small, **2024**, 2405220.
- **Christian Schröder**, Lua Henderson, Filippo Pota, Kiaya Doyle, Paula E. Colavita: "Modulating the Electrocatalytic Hydrogenation of Benzaldehyde on Cu@ C Electrode Materials", The Journal of Physical Chemistry C, **2025**, 129(15), 7217-7224.
- Filippo Pota, Maida A. Costa de Oliveira, **Christian Schröder**, Aran Rafferty, Clara De Castro, Ludivine Rault, James A. Behan, Frédéric Barrière, Paula E. Colavita: "Electrocatalytic hydrogenation of unsaturated organics using Mo and W porous carbon-encapsulated nanostructures: impact of metal type on properties and performances", Journal of Materials Chemistry A, **2025**, 13, 12383-12396.

Conference Contributions

Oral Presentations

- Hugo Nolan, **Christian Schröder**, Marc Brunet-Cabré, Niall McEvoy, Kim McKelvey, Paula E. Colavita: "Influence of N-doped Carbon Supports on Heterostructured MoS_2 Electrocatalysts for the Hydrogen Evolution Reaction." 32nd International Conference on Diamond and Carbon Materials 2022, Lisbon, Portugal.
- **Christian Schröder**, Hugo Nolan, Marc Brunet-Cabré, Kim McKelvey, Paula E. Colavita: "Nitrogenated carbon materials for electrocatalytic transformations." 33rd International Conference on Diamond and Carbon Materials 2023, Palma de Mallorca, Spain.
- **Christian Schröder**, Hugo Nolan, Marc Brunet-Cabré, Kim McKelvey, Paula E. Colavita: "Novel Carbon Heterostructures for Electrocatalytic Transformations." EMRS 2023 Fall Meeting, Warsaw, Poland
- **Christian Schröder**, Hugo Nolan, Marc Brunet-Cabré, Niall McEvoy, Kim McKelvey, Paula E. Colavita: "Carbon-Based Electrode Materials for Electrocatalytic Transformations." 244th biannual ECS meeting 2023, Gothenburg, Sweden.
- **Christian Schröder**, Hugo Nolan, Marc Brunet-Cabré, Filippo Pota, Kim McKelvey, Paula E. Colavita: "Nitrogenated-Carbon heterostructures for electrocatalytic hydrogenation reactions." EMRS 2024 Spring Meeting, Strasbourg, France.

Poster Presentations

- **Christian Schröder**, Hugo Nolan, Marc Brunet Cabré, Kim McKelvey Paula Colavita: "Electrocatalysis of complex transformations at advanced carbon electrodes." 15th International conference on materials chemistry (MC15), 2021, Online.
- **Christian Schröder**, Hugo Nolan, Marc Brunet-Cabré, Kim McKelvey, Paula E. Colavita: "Novel Carbon Electrodes for Complex Electrocatalytic Transformations of Organic Compounds" 32nd International Conference on Diamond and Carbon Materials 2022, Lisbon, Portugal.

- **Christian Schröder**, Hugo Nolan, Marc Brunet-Cabré, Filippo Pota, Niall McEvoy, Kim McKelvey, Tatiana S Perova, Paula E Colavita: "Nitrogenated carbon electrodes as cathode materials for electrocatalytic transformations of organic compounds." 16th International conference on materials chemistry (MC16), 2023, Dublin, Ireland.

Awards

Best Paper Award

E-MRS Fall Meeting 2023 Symposium B: Advanced catalytic materials for (photo)electrochemical energy conversion IV for the presentation on "Novel Carbon Heterostructures for Electrocatalytic Transformations."

Trinity Trust Travel Grant

For attending the 244th biannual ECS meeting in Gothenburg.

And for attending the E-MRS spring meeting 2024 in Strasbourg.